



**University of  
Nottingham**  
UK | CHINA | MALAYSIA

**Understanding the Evolution of Superalloy  
Microstructure During Inertia Friction  
Welding Using In-situ X-ray Diffraction  
and Cellular Automata**

Matthew Rowson, MEng. (Hons)

Thesis submitted for the degree of Doctor of Philosophy in Mechanical Engineering

Gas Turbines and Transmissions Research Centre,

University of Nottingham,

NG7 2TU,

UK

March 2021

*“For the rest of your life, nobody can ever tell you that you couldn’t do it, ‘cause you did it.”*

-Bill Parcells

## **Abstract**

There is a constant drive within the gas turbine industry to improve the efficiency of engines through the increase of operating temperatures at which these machines perform. Such demands require materials capable of maintaining their mechanical properties at these elevated temperatures, alongside having excellent oxidation and corrosion resistance during operation. Nickel-based superalloys are renowned for their excellent material properties at both ambient and elevated temperatures. The current generation of these materials make use of complex alloy chemistry and intricate heat treatment processes are employed to produce a microstructure which provides optimal mechanical properties over an extremely wide range of temperatures.

The utilisation of Nickel-based superalloys to attain these properties in critical applications creates many significant challenges in joining these materials. When welding processes which involve bulk melting are used, these materials are susceptible to solidification cracking as the contraction stresses produced by shrinking of the dual-phase microstructure are often higher than the strength of the filler metal. Therefore, solid-state joining processes such as Inertia Friction Welding (IFW) are often used for these materials as they significantly reduce the likelihood of these defects.

Although solid-state welding techniques such as IFW are well-established, they are still relatively novel as there is an incomplete understanding of the driving forces which control the process evolution. There are clear trends between the welding parameters and the macro-scale process behaviour, yet it is not fully understood how the highly coupled thermal, mechanical and microstructural effects which occur govern the evolution of the process.

The present work describes the development of a novel in-situ synchrotron diffraction technique for the characterisation of the microstructure evolution which occurs during IFW. These studies have quantified, for the first time, the spatial and temporal evolution of phase fractions which is produced by this process. This novel experimental methodology has been implemented for IFW of a tool steel, and the phase fractions of parent ferrite and high-temperature austenite have been quantified throughout the process. Additionally, the formation and evolution of the TMAZ and HAZ during IFW have been observed and characterised for the first time.

The in-situ diffraction experiments have also been employed for IFW of the Nickel-based disc alloy RR1000. The phase fraction of the precipitate strengthening  $\gamma'$  phase has been quantified with both spatial and temporal resolution. For this material, a range of weld parameters have been investigated to assess the sensitivity of the microstructure evolution to design changes in the process parameters. Here, the macro-scale sensitivity to the process parameters has been linked to the thermal and microstructural effects which have been observed.

In addition to the novel experimental techniques developed and implemented in this thesis, numerical methods have been investigated as a means of evaluating the microstructure evolution. Coupled thermo-mechanical Finite Element Analysis (FEA) models have been produced to evaluate the thermal response of IFW for a range of process parameters, alongside the macro-scale process outputs. Thermal history data has been extracted from these FEA models and used as input data into novel Cellular Automata (CA) models which have been used to evaluate the microstructure evolution. The CA models used first-principles atomic thermodynamics through the CALPHAD approach to define local equilibrium values and evaluate diffusion element driving forces. Fick's law has been implemented to calculate the diffusive fluxes in the dual phase microstructure and the subsequent phase composition due to these has been evaluated by the local equilibrium approach.

Future developments have been recommended based on the research conducted in this thesis. Whilst this work has improved the understanding of the microstructure evolution which occurs during IFW, there is still a large knowledge gap surrounding the fundamental nature of deformation mechanics for Nickel-based superalloys. The coupling of thermal, mechanical and microstructural effects which are known to combine to produce deformation in processes such as IFW are not fully understood. Investigation into the thermal and mechanical influence on microstructure and subsequent deformation mechanics under compressive and shear loading could be linked with this work to assist explanation of the deformation mechanisms which occur during IFW. Experimentally, it has been suggested that developments to the IFW apparatus may be performed to expand the range of geometries which can be investigated. Continued developments and improvements of synchrotron beamline technologies will permit increased X-ray fluxes in the future, which would permit acquisition of more coherent diffraction patterns which are less susceptible to the

influences of background noise. This will allow for more accurate characterisation of phase fractions, alongside refined temporal and spatial resolution. Numerically, it is suggested that the CA modelling capabilities may be expanded to include mechanical driving forces on atomic diffusion for the purpose of phase transformations, given the fact that high strains and strain rates are present in IFW.

The work presented in this thesis utilises two analysis techniques to improve the understanding of microstructure evolution during IFW. In-situ diffraction experiments have been performed on laboratory-scale weld geometries and it is expected that the behaviour observed in these investigations would scale-up to larger geometries. The numerical modelling approach developed has provided a foundation for modelling the evolution of microstructure during IFW, which could be applied to any weld geometry or material.

## **Acknowledgements**

Firstly, I would like to thank my principal supervisor, Dr. Chris Bennett. Without your support and guidance, I would not have started this Ph.D., and without your continued commitment over the past four years, I would not be writing this thesis. I would like to extend that gratitude to my second supervisor, Dr. James Rouse. James offered a great wealth of knowledge and a different perspective to the project. Without that, this research would not have been a success.

There are a range of people working under the wider research project of which this work forms only a small part, but unfortunately all of whom would not fit on a single page of text. Special thanks go to Simon Bray, Ph.D. (Rolls-Royce), Professor Hector Basoalto (University of Sheffield) and Dr. Andrew McBride (University of Glasgow) for many interesting and fruitful discussions which have helped shape this research.

This work would not have been possible without the hard work of the GDM Group which designed and built the experimental apparatus used in this research. That gratitude must be extended to the Engineering and Design team at the Gas Turbines and Transmissions Research Centre (G2TRC), who provided a great amount of support with experimental rig design.

I would also like to thank the technical staff from the Wolfson Building and Nanoscale and Microscale Research Centre at the University of Nottingham. Your support provided me with the essential laboratory experience for the experimental work which has formed part of this thesis.

My warmest gratitude is extended to my partner, Erin. Without your continued patience and encouragement, this thesis would have never been completed. You have been there for me throughout this journey and experienced every single high and low point by my side. I will forever cherish the love and support you have given me over the past few years.

Finally, I would like to dedicate this work to my mother. To say that this would not have been possible without you would be an understatement. The sacrifices you made to provide me with the best possible foundation in life are the only reason why I am here today, and that is something I will hold closely for the rest of my life.

# Nomenclature

## Symbols

### General

$A$	Area
$E$	Energy
$I$	Inertia
$n$	Rotational speed
$P, p$	Pressure
$Q, q$	Heat flux
$r, r_o, r_i$	Radius (absolute, outer, inner)
$T$	Temperature
$t$	Time
$U$	Upset
$V_s$	Sliding velocity
$W_s$	Strain energy
$z$	Axial position
$\alpha$	Thermal diffusivity
$\varepsilon$	Strain
$\dot{\varepsilon}$	Strain rate
$\eta$	Efficiency
$\mu$	Coefficient of friction
$\sigma$	Stress
$\tau, \tau_f$	Shear stress (absolute, frictional)
$\omega$	Rotational speed

### X-ray Diffraction

$a$	Lattice parameter
$d$	d-spacing
$\varepsilon$	Strain
$\theta$	Diffraction angle
$\lambda$	X-ray wavelength
$\varphi$	Azimuthal angle

## CALPHAD & Atomic Diffusion

$c_B$	Atomic concentration of species B
$D_B$	Diffusion coefficient of species B
$G$	Gibbs free energy
$\Delta H_m$	Enthalpy of phase transformation
$J_B$	Atomic flux of species B
$M_B$	Atomic mobility of species B
$m_B$	Mole fraction of species B
$Q_B$	Activation energy
$R$	Universal gas constant
$T$	Temperature
$V_M$	Molar volume
$x_B$	Atomic fraction of species B
$z$	Distance
$\varepsilon$	Strain
$\mu_B$	Chemical potential of species B

## Abbreviations

1D	One dimensional
2D	Two dimensional
CA	Cellular Automata
BCC	Body Centred Cubic
CALPHAD	Calculation of Phase Diagrams
FCC	Face Centred Cubic
FD	Finite Difference
FEA	Finite Element Analysis
HAZ	Heat Affected Zone
IFW	Inertia Friction Welding
LVDT	Linear Variable Differential Transformer
MC	Monte Carlo
PC	Primitive Cubic
SEM	Scanning Electron Microscopy
TEM	Transmission Electron Microscopy
TMAZ	Thermo-Mechanically Affected Zone
XRD	X-Ray Diffraction

## **Publications**

Rowson, M., Bennett, C.J., Azeem, M.A., Magdysyuk, O., Rouse, J., Lye, R., Davies, J., Bray, S., Lee, P.D., *Observation of microstructure evolution during inertia friction welding using in-situ synchrotron X-ray diffraction*. Journal of Synchrotron Radiation, 2021. **28**:3. <https://doi.org/10.1107/S1600577521001569>

## List of Tables

<b>Table 2.1:</b> Nominal composition of RR1000 in at %.....	10
<b>Table 2.2:</b> A summary of microstructure and mechanical property techniques investigated for the IFW process in relevant literature.....	26
<b>Table 2.3:</b> A summary modelling approaches for the IFW process in relevant literature.....	37
<b>Table 3.1:</b> Elemental composition of BS1407 steel.....	54
<b>Table 3.2:</b> Chemical composition of the RR1000 nickel-based superalloy.....	55
<b>Table 3.3:</b> Characteristics of the parent microstructure of RR1000 nickel-based superalloy used in the experimental methodology.....	56
<b>Table 3.4:</b> Conversion of maximum absolute weld input parameters to maximum specific parameters for the two specimen geometries used in the experiments.....	59
<b>Table 3.5:</b> IFW input parameters for BS1407 welds.....	64
<b>Table 3.6:</b> The five axial offset distances between the centre of the synchrotron beam and initial weld interface for BS1407 welds.....	64
<b>Table 3.7:</b> IFW input parameters for Nickel-based superalloy welds.....	65
<b>Table 3.8:</b> The axial offset positions between initial contact interface and X-ray beam centre for the nickel-based superalloy IFWs.....	66
<b>Table 3.9:</b> Permitted diffraction peaks from primitive cubic (PC) and face centred cubic (FCC) phases in X-ray diffraction.....	69
<b>Table 3.10:</b> $\gamma'$ precipitate sizes simulated in the 1D ternary CA model and the respective volume fractions applied to the dissolution profile of each precipitate....	86
<b>Table 4.1:</b> Comparison of diffraction images for assessment of the microstructural symmetry about the contact interface.....	104
<b>Table 5.1:</b> IFW input parameters for Nickel-based superalloy welds.....	123
<b>Table 5.2:</b> The axial offset positions between initial contact interface and X-ray beam centre for the nickel-based superalloy IFWs.....	124

**Table 5.3:** Mean volume fractions of primary and secondary  $\gamma'$  for four samples and the standard deviation for each sample.....144

**Table 5.4:** Summary of measured and calculated  $\gamma'$  volume fractions for RR1000...145

## List of Figures

<b>Figure 1.1:</b> Schematic of the IFW process and typical process output data.....	2
<b>Figure 2.1:</b> Schematic representation of the microstructure of the turbine disc alloy Udimet720.....	9
<b>Figure 2.2:</b> Low-magnification SEM image presenting the distribution of $\gamma$ grains and primary $\gamma'$ precipitates in RR1000.....	11
<b>Figure 2.3:</b> High-magnification SEM image presenting the distribution of primary and secondary $\gamma'$ precipitates in RR1000. Inset: ultra-high-magnification image showing the population of tertiary $\gamma'$ .....	12
<b>Figure 2.4:</b> SEM image of a cracked grain boundary due to liquation of $\gamma'$ and $\gamma$ - $\gamma'$ eutectic.....	14
<b>Figure 2.5:</b> Schematic of the IFW process.....	16
<b>Figure 2.6:</b> The three stages of the IFW process as defined through transitions in the upset data. ....	18
<b>Figure 2.7:</b> Representative peak temperature curve aligned with a schematic of the microstructurally affected zones produced by the inertia friction welding process...	19
<b>Figure 2.8:</b> Classical 2D CA neighbourhoods with a 1 cell radius.....	49
<b>Figure 2.9:</b> Classical 2D CA neighbourhoods with a various cell radii.....	49
<b>Figure 3.1:</b> Specimen geometry for IFW of BS1407 steel.....	56
<b>Figure 3.2:</b> Specimen geometry for IFW of nickel-based superalloy RR1000.....	57
<b>Figure 3.3:</b> Annotated CAD render of the IFW apparatus produced to conduct the in-situ synchrotron diffraction experiments.....	58
<b>Figure 3.4:</b> Schematic of the IFW setup at Diamond Light Source.....	61
<b>Figure 3.5:</b> Schematic of the axial offset distance between the initial weld interface and synchrotron beam.....	62
<b>Figure 3.6:</b> SEM image of parent RR1000 to analyse the primary $\gamma'$ precipitates....	68

<b>Figure 3.7:</b> Comparison of X-ray diffraction profiles highlighting the influence of background noise on low intensity PC $\gamma'$ peaks.....	70
<b>Figure 3.8:</b> Schematic of the IFW problem as modelled in DEFORM.....	75
<b>Figure 3.9:</b> Flow chart of the optimisation procedure for the material model in DEFORM .....	78
<b>Figure 3.10:</b> Flow chart describing the procedures performed by the 1D CA model..	84
<b>Figure 3.11:</b> Equilibrium volume fraction data evaluated from Thermo-Calc for the representative material.....	86
<b>Figure 3.12:</b> The processing of SEM images to produce a digital material representation for the 2D CA modelling approach.....	88
<b>Figure 3.13:</b> Flow chart describing the procedures performed by the 2D CA model..	90
<b>Figure 4.1:</b> Weld outputs for the five BS1407 repeat welds.....	92
<b>Figure 4.2:</b> Weld interface position relative to the synchrotron beam centre for the five BS1407 welds conducted.....	93
<b>Figure 4.3:</b> Debye-Scherrer diffraction rings recorded during weld S1, P4.....	94
<b>Figure 4.4:</b> The diffraction pattern of BCC ferrite at 1 ° intervals in the Azimuth range.....	95
<b>Figure 4.5:</b> Variation in peak parameters throughout weld P4 for the (110) BCC Ferrite peak.....	96
<b>Figure 4.6:</b> Variation in peak parameters throughout weld P4 for the (111) FCC Austenite peak.....	97
<b>Figure 4.7:</b> Waterfall plot of the XRD data series produced during weld P1, where every 20 <sup>th</sup> image of the 100 fps diffraction acquisition is presented for clarity.....	98
<b>Figure 4.8:</b> Comparison of weld interface position relative to the synchrotron beam, alongside diffraction data for 4 welds.....	100
<b>Figure 4.9:</b> GSAS-II refinement for diffraction images.....	101
<b>Figure 4.10:</b> Evolution of the austenite phase fraction at the contact interface throughout IFW.....	102

<b>Figure 4.11:</b> Axial evolution of the austenite fraction observed during IFW .....	105
<b>Figure 4.12:</b> Percent change of the lattice parameters of ferrite and austenite measured from the in-situ diffraction images.....	106
<b>Figure 4.13:</b> An annotated radial section of weld P5 showing the region surrounding the contact interface.....	107
<b>Figure 4.14:</b> Austenite volume fraction recorded from in-situ X-ray diffraction at the end of the weld, and after 100 s of post weld cooling.....	108
<b>Figure 4.15:</b> Axial variation in the lattice parameter calculated from in-situ diffraction data after welding.....	109
<b>Figure 4.16:</b> Comparison of weld output data for in-situ XRD weld P5 and the repeat weld with ex-situ thermocouple measurements.....	110
<b>Figure 4.17:</b> Temperature measurements recorded during the repeat weld, with a K type thermocouple spot-welded 0.6 mm from the initial weld interface.....	111
<b>Figure 4.18:</b> The austenite phase fraction evolution from weld S1, P5, presented alongside the estimated austenite fraction evaluated from thermal measurements of the repeat weld.....	112
<b>Figure 4.19:</b> The position of the thermocouple during the weld, showing how the thermocouple is consumed at the weld interface.....	113
<b>Figure 4.20:</b> Comparison of the desired thermal measurement at the centre of the thermocouple, and the mean temperature recorded across the axial profile at which the thermocouple is in contact with the specimen OD.....	114
<b>Figure 4.21:</b> Estimated experimental strain and the strain required to form austenite calculated from temperatures recorded during the repeat weld.....	116
<b>Figure 4.22:</b> The microstrain calculated from the lattice parameter evolution of ferrite and austenite.....	117
<b>Figure 4.23:</b> The position of the weld interface relative to the synchrotron beam for weld P5.....	118
<b>Figure 5.1:</b> The three stages of the IFW process as defined through transitions in the upset data.....	120

<b>Figure 5.2:</b> A representative IFW weld section showing approximate sizes of the primary $\gamma'$ free zone (PGPFZ) and secondary $\gamma'$ free zone (SGPFZ).....	122
<b>Figure 5.3:</b> Weld outputs for the four repeat welds of parameter set N1 and the mean value calculated from these.....	125
<b>Figure 5.4:</b> Position of the weld interface relative to the stationary beamline for the four RR1000 welds performed with input parameter set N1.....	125
<b>Figure 5.5:</b> Weld outputs for the RR1000 repeat welds performed with input parameter set N2, alongside the mean values calculated from welds N2, P1; N2, P2 and N2, P3.....	126
<b>Figure 5.6:</b> Position of the weld interface relative to the stationary beamline for the four RR1000 welds performed with input parameter set N2.....	127
<b>Figure 5.7:</b> Weld outputs for the RR1000 repeat welds performed with input parameter set N3, and the mean outputs calculated from these.....	128
<b>Figure 5.8:</b> Position of the weld interface relative to the stationary beamline for the four RR1000 welds performed with input parameter set N3.....	128
<b>Figure 5.9:</b> Weld outputs for the RR1000 repeat welds performed with input parameter set N4 and the mean outputs calculated from these.....	129
<b>Figure 5.10:</b> Position of the weld interface relative to the stationary beamline for the three RR1000 welds performed with input parameter set N4.....	130
<b>Figure 5.11:</b> Energy input rate for each weld input parameter set derived from rundown curves.....	130
<b>Figure 5.12:</b> Debye-Scherrer diffraction rings acquired from the parent RR1000 microstructure.....	133
<b>Figure 5.13:</b> Comparison of X-ray diffraction profiles highlighting the influence of background noise on low intensity peaks.....	134
<b>Figure 5.14:</b> Analysis of the results when summing images to form lower acquisition rates.....	134

<b>Figure 5.15:</b> Rietveld refinement of diffraction images recorded during weld N4, P2.....	136
<b>Figure 5.16:</b> Lattice parameter evaluated from the [111] composite peak for 10 randomly selected pre-weld diffraction images.....	138
<b>Figure 5.17:</b> Data evaluated from summed images recorded during weld N1, P3...	139
<b>Figure 5.18:</b> SEM image of parent RR1000 to analyse the primary $\gamma'$ precipitates..	140
<b>Figure 5.19:</b> Comparison of the primary $\gamma'$ size distribution measured by SEM with published data.....	141
<b>Figure 5.20:</b> Example of image processing for a high magnification image for secondary $\gamma'$ analysis.....	142
<b>Figure 5.21:</b> Comparison of the secondary $\gamma'$ size distribution measured by SEM with published data.....	143
<b>Figure 5.22:</b> Comparison of the axial $\gamma'$ volume fraction profiles measured by XRD and imaged via SEM.....	145
<b>Figure 5.23:</b> Calculation of the sensitivity of the lattice parameter to temperature evaluated using thermal expansion coefficient data.....	147
<b>Figure 5.24:</b> The mean upset curve for weld parameter set N1.....	148
<b>Figure 5.25:</b> Microstructure evolution during the start of conditioning for weld parameter set N1.....	149
<b>Figure 5.26:</b> Microstructure evolution during the middle stage of conditioning for weld parameter set N1.....	150
<b>Figure 5.27:</b> Microstructure evolution during the end stage of conditioning for weld parameter set N1.....	151
<b>Figure 5.28:</b> Microstructure evolution during the early stage of burn-off for weld parameter set N1.....	152
<b>Figure 5.29:</b> Microstructure evolution during the middle period of burn-off for weld parameter set N1.....	153

<b>Figure 5.30:</b> Microstructure evolution during the final period of burn-off for weld parameter set N1.....	154
<b>Figure 5.31:</b> All $\gamma'$ volume fraction data acquired during steady-state burn-off.....	154
<b>Figure 5.32:</b> Microstructure evolution during the early period of transition between burn-off and consolidation for weld parameter set N1.....	155
<b>Figure 5.33:</b> Microstructure evolution during the end of the transition between burn-off and consolidation for weld parameter set N1.....	156
<b>Figure 5.34:</b> Microstructure evolution during the start of consolidation for weld parameter set N1.....	157
<b>Figure 5.35:</b> Microstructure evolution during the middle period of consolidation for weld parameter set N1.....	158
<b>Figure 5.36:</b> Microstructure evolution during the end of consolidation for weld parameter set N1.....	159
<b>Figure 5.37:</b> All $\gamma'$ volume fraction data acquired during steady-state consolidation.....	161
<b>Figure 5.38:</b> Microstructure evolution during the start of weld stall for weld parameter set N1.....	161
<b>Figure 5.39:</b> Microstructure evolution during the end of weld stall for weld parameter set N1.....	162
<b>Figure 5.40:</b> Weld output data from the validation welds compared with the mean experimental weld.....	163
<b>Figure 5.41:</b> Thermocouple positions relative to the contact interface for the two validation welds performed.....	164
<b>Figure 5.42:</b> Thermocouple measurements recorded during the two repeat welds performed.....	165
<b>Figure 5.43:</b> Thermal validation of diffraction data for the middle of the conditioning stage.....	166

<b>Figure 5.44:</b> Thermal validation of diffraction data for the middle of the burn-off stage.....	167
<b>Figure 5.45:</b> Thermal validation of diffraction data for the middle of the transition from burn-off to consolidation.....	167
<b>Figure 5.46:</b> Thermal validation of diffraction data for the middle of the consolidation stage.....	168
<b>Figure 5.47:</b> Thermal validation of diffraction data at weld stall.....	169
<b>Figure 5.48:</b> Mean upset data for the low speed welds with defined weld stages...	171
<b>Figure 5.49:</b> $\gamma'$ volume fraction evolution during conditioning of the low speed welds.....	172
<b>Figure 5.50:</b> $\gamma'$ volume fraction evolution during the burn-off stage of the low speed welds.....	173
<b>Figure 5.51:</b> $\gamma'$ volume fraction evolution during the consolidation stage of the low speed welds. ....	174
<b>Figure 5.52:</b> $\gamma'$ volume fraction at the weld stall of the low speed welds.....	174
<b>Figure 5.53:</b> Mean upset data for the high speed welds with defined weld stages....	175
<b>Figure 5.54:</b> $\gamma'$ volume fraction evolution during conditioning of the high speed welds.....	176
<b>Figure 5.55:</b> $\gamma'$ volume fraction evolution during the burn-off stage of the high speed welds.....	176
<b>Figure 5.56:</b> $\gamma'$ volume fraction evolution during the consolidation stage of the high speed welds.....	177
<b>Figure 5.57:</b> Axial profile of $\gamma'$ volume fraction at the end of the high speed welds..	178
<b>Figure 5.58:</b> Mean upset data for the low pressure welds with defined weld stages..	179
<b>Figure 5.59:</b> Axial profile of $\gamma'$ volume fraction during conditioning of the low pressure welds.....	179

<b>Figure 5.60:</b> Axial profile of $\gamma'$ volume fraction during the burn-off stage of the low pressure welds.....	180
<b>Figure 5.61:</b> Axial profile of $\gamma'$ volume fraction during the consolidation stage of the low pressure welds.....	181
<b>Figure 5.62:</b> Axial profile of $\gamma'$ volume fraction produced at the end of welding for the low pressure welds.....	182
<b>Figure 5.63:</b> Mean upset data for the high pressure welds with defined weld stages.....	183
<b>Figure 5.64:</b> Axial profile of $\gamma'$ volume fraction during conditioning of the high pressure welds. ....	183
<b>Figure 5.65:</b> Axial profile of $\gamma'$ volume fraction during the burn-off stage of the high pressure welds. ....	184
<b>Figure 5.66:</b> Axial profile of $\gamma'$ volume fraction during the consolidation stage of the high pressure welds.....	185
<b>Figure 5.67:</b> Axial profile of $\gamma'$ volume fraction for high pressure welds at the end of the process.....	186
<b>Figure 5.68:</b> Relationship between the measured width of the $\gamma'$ dissolved zone during burn-off and the burn-off rate for each weld parameter set.....	187
<b>Figure 5.69:</b> Relationship between the measured width of the $\gamma'$ dissolved zone during consolidation and the consolidation upset rate for each weld parameter set.....	187
<b>Figure 5.70:</b> Polynomial fitting of the relationship between axial position and $\gamma'$ volume fraction for the measurement of the $\gamma'$ dissolved zone at the end of conditioning of weld parameter set N1.....	189
<b>Figure 5.71:</b> Size of the $\gamma'$ dissolved zone relative to the IFW process for the four sets of weld parameters investigated in this study.....	189
<b>Figure 6.1:</b> Outputs of the baseline and optimised DEFORM FE models compared with the experimental mean weld data.....	196
<b>Figure 6.2:</b> Flow stress input data produced by the optimisation routine.....	197

<b>Figure 6.3:</b> Process outputs of the validation welds compared with the mean experimental weld.....	202
<b>Figure 6.4:</b> Thermocouple measurements from validation weld 1 presented alongside FEA temperature values at consistent axial positions.....	203
<b>Figure 6.5:</b> Thermocouple measurements from validation weld 2 presented alongside FEA temperature values at consistent axial positions.....	204
<b>Figure 6.6:</b> Verification of the CA model through comparison of $\gamma'$ dissolution kinetics with the DICTRA diffusion module.....	207
<b>Figure 6.7:</b> Verification of the CA model for the ternary alloy system through comparison of $\gamma'$ dissolution kinetics with the DICTRA diffusion module.....	209
<b>Figure 6.8:</b> Thermal history data extracted from the FEA model for three axial locations at a weld time of 0.62 s for IFW of weld parameter set N1.....	210
<b>Figure 6.9:</b> Combined results of the 1D CA simulation for temperatures extracted from FEA modelling of weld parameter set N1 at $t = 0.62$ s.....	212
<b>Figure 6.10:</b> Comparison of microstructure evolution data evaluated from in-situ synchrotron diffraction and cellular automata models for weld parameter set N1 at $t = 0.62$ s.....	213
<b>Figure 6.11:</b> Comparison of microstructure evolution data evaluated from in-situ synchrotron diffraction and cellular automata models for weld parameter set N1 at $t = 1.25$ s.....	214
<b>Figure 6.12:</b> Comparison of microstructure evolution data evaluated from in-situ synchrotron diffraction and cellular automata models for weld parameter set N1 at $t = 2.37$ s.....	215
<b>Figure 6.13:</b> Comparison of $\gamma'$ volume fraction data evaluated from in-situ synchrotron diffraction and cellular automata models for weld parameter set N2...	217
<b>Figure 6.14:</b> Comparison of $\gamma'$ volume fraction data evaluated from in-situ synchrotron diffraction and cellular automata models for weld parameter set N3...	219
<b>Figure 6.15:</b> Comparison of $\gamma'$ volume fraction data evaluated from in-situ synchrotron diffraction and cellular automata models for weld parameter set N4...	221

<b>Figure 6.16:</b> Verification of the 2D CA model through comparison of $\gamma'$ dissolution kinetics with the DICTRA diffusion module.....	223
<b>Figure 6.17:</b> A small region of the microstructure modelled in the 2D CA model highlighting the benefits of 2D modelling.....	225
<b>Figure 6.18:</b> The evolution of the atomic fraction of Aluminium at position x in the simulation presented in Figure 6.17.....	226
<b>Figure 6.19:</b> Comparison of microstructure evolution data evaluated from in-situ synchrotron diffraction and cellular automata models for weld parameter set N1 at t = 0.62 s.....	227
<b>Figure 6.20:</b> Comparison of microstructure evolution data evaluated from in-situ synchrotron diffraction and cellular automata models for weld parameter set N1 at t = 1.25 s.....	228
<b>Figure 6.21:</b> Comparison of microstructure evolution data evaluated from in-situ synchrotron diffraction and cellular automata models for weld parameter set N1 at t = 2.37 s.....	229

# Contents

<b>Abstract</b> .....	x
<b>Acknowledgements</b> .....	vi
<b>Nomenclature</b> .....	vii
<b>Publications</b> .....	ix
<b>List of Tables</b> .....	x
<b>List of Figures</b> .....	xii
<b>Contents</b> .....	xxii
<b>Chapter 1 – Introduction</b> .....	1
1.1 Background.....	1
1.2 Inertia friction welding.....	2
1.3 Microstructure evolution during IFW.....	3
1.4 Research aims.....	4
1.5 Thesis structure.....	4
<b>Chapter 2 – Literature Review</b> .....	6
2.1 Introduction.....	6
2.2 Nickel-based superalloys.....	7
2.2.1 Disc alloy RR1000.....	10
2.2.2 Challenges in welding of Nickel-based superalloys.....	12
2.2.3 Concluding remarks.....	15
2.3 Inertia friction welding.....	16
2.3.1 Variation in microstructure and mechanical properties across an IFW.....	25
2.3.2 Concluding remarks.....	28
2.4 Synchrotron diffraction.....	31
2.4.1 Advantages of synchrotron diffraction.....	31
2.4.2 Characterisation of microstructure evolution using in-situ synchrotron radiation.....	33
2.4.3 Concluding remarks.....	35
2.5 Modelling of IFW.....	36
2.5.1 Thermal modelling.....	38
2.5.2 Thermo-mechanical modelling.....	40
2.5.3 Microstructure modelling.....	43
2.5.4 Concluding remarks.....	45
2.6 Techniques for modelling microstructure evolution.....	46
2.6.1 Overview of numerical modelling approaches.....	46
2.6.2 Concluding remarks.....	49
2.7. Knowledge gaps.....	51
<b>Chapter 3 – Research Methodology</b> .....	53
3.1 Background.....	53
3.2 Experimental methods.....	54
3.2.1 Materials.....	54

3.2.2	Weld specimens.....	56
3.2.3	Inertia friction welding machine.....	57
3.2.4	In-situ synchrotron X-ray diffraction of IFW.....	60
3.2.5	Weld input parameters.....	63
3.2.6	Microscopic examination of post-weld microstructure.....	66
3.2.7	Summing of diffraction images.....	68
3.2.8	Diffraction data analysis techniques.....	70
3.2.3	Thermal validation of XRD data.....	73
3.3	Numerical methods.....	74
3.3.1	Finite element analysis.....	74
3.3.2	Cellular automata.....	78
3.3.2.1	Cellular automata fundamentals.....	79
3.3.2.2	Thermodynamic fundamentals.....	79
3.3.2.3	The physics of atomic diffusion.....	80
3.3.2.4	Binary Ni-Al model.....	83
3.3.2.5	Ternary Ni-Al-Cr model.....	85
3.3.2.5.1	1-dimensional cellular automata.....	86
3.3.2.5.2	2-dimensional cellular automata.....	87
<b>Chapter 4</b>	<b>– Characterisation of Steel Microstructure Evolution During IFW</b> ..	<b>91</b>
4.1	Introduction.....	91
4.2	IFW process data.....	92
4.2.1	Weld outputs and repeatability assessment.....	92
4.3	Phase transformations.....	94
4.3.1	Analysis of directional strain.....	94
4.3.2	Time-resolved XRD spectra.....	97
4.3.3	Process-resolved XRD spectra.....	98
4.3.4	Position-resolved XRD spectra.....	101
4.4	Comparison with microscopic examination.....	107
4.4.1	HAZ size.....	107
4.4.2	TMAZ size.....	108
4.5	Thermal validation.....	110
4.5.1	Assessment of weld repeatability.....	110
4.5.2	Comparison of thermal response and diffraction data.....	111
4.5.3	Methods of understanding the influence of strain on phase transformations.....	115
4.6	Conclusions.....	119
<b>Chapter 5</b>	<b>– Characterisation of Nickel-Based Superalloy Microstructure Evolution During IFW</b> .....	<b>120</b>
5.1	Introduction.....	120
5.2	IFW process data.....	123
5.2.1	Weld outputs.....	124
5.2.1.1	Parameter set N1.....	124
5.2.1.2	Parameter set N2.....	125
5.2.1.3	Parameter set N3.....	127

5.2.1.4	Parameter set N4.....	128
5.2.1.5	Energy input.....	130
5.3	Diffraction data analysis.....	132
5.3.1	Introduction.....	132
5.3.2	Analysis of phase fractions.....	135
5.3.3	Evaluation of uncertainty in diffraction profiles.....	136
5.3.4	Evaluation of directional strain.....	137
5.4	Post-weld diffraction analysis.....	140
5.5	Microstructure evolution during IFW.....	147
5.5.1	Introduction.....	147
5.5.2	Microstructure evolution during conditioning.....	149
5.5.3	Microstructure evolution during burn-off.....	152
5.5.4	Microstructure evolution during the transition from burn-off to consolidation.....	155
5.5.5	Microstructure evolution during consolidation.....	157
5.5.6	Microstructure evolution during weld stall.....	161
5.5.7	Thermal validation of diffraction data.....	163
5.6	Sensitivity of microstructure evolution to process parameters.....	171
5.6.1	Sensitivity to weld pressure.....	171
5.6.2	Sensitivity to initial rotational velocity.....	178
5.6.3	Assessment of microstructural control of macro-scale process behaviour.....	186
5.7	Conclusions.....	191
<b>Chapter 6</b>	<b>– Cellular Automata Modelling of Microstructure Evolution During IFW.....</b>	<b>193</b>
6.1	Introduction.....	193
6.2	Finite element analysis.....	194
6.2.1	Assessment of process outputs.....	195
6.2.2	Analysis of thermal response.....	201
6.3	1D Finite difference.....	206
6.3.1	Binary Ni-Al system.....	206
6.3.1	Ternary Ni-Al-Cr system.....	208
6.4	2D Cellular automata.....	223
6.5	Conclusions.....	230
<b>Chapter 7</b>	<b>– Conclusions.....</b>	<b>231</b>
7.1	Conclusions.....	231
7.2	Suggestions for future work.....	233
<b>References.....</b>		<b>235</b>
<b>Appendix A</b>	<b>– Microstructure Evolution of RR1000 During IFW Using Weld Parameter Sets N2, N3 and N4.....</b>	<b>246</b>
A1	Microstructure evolution using weld parameter set N2.....	246
A2	Microstructure evolution using weld parameter set N3.....	252
A2	Microstructure evolution using weld parameter set N3.....	261
<b>Appendix B</b>	<b>– Reference Input Data for CA Models.....</b>	<b>268</b>

B1 Binary Ni-Al system.....	268
B2 Ternary Ni-Al-Cr system.....	272

# Chapter 1

## Introduction

### 1.1 Background

There is a constant drive within the aerospace industry to increase the efficiency of turbine engines. The most common approach of achieving improved efficiency is through increasing the operating temperatures throughout the engine [1]. This in turn produces a requirement for the development and production of materials with optimal mechanical properties at both ambient and elevated temperatures.

Nickel-based superalloys are regularly used in high-temperature turbine components due to their increased strength and corrosion resistance at elevated temperatures. The superalloys used can be separated into two sub-categories, depending on their desired use. These are precipitation-strengthened alloys for use in disc components, and directionally solidified or single crystal alloys for turbine blades.

This work primarily concerns the Nickel-based superalloy RR1000, a precipitation-strengthened disc alloy used in high-pressure turbine and compressor discs [2]. The microstructure of this material consists of a  $\gamma$  matrix phase, strengthened by  $\gamma'$  precipitates at grain boundaries and within matrix grains. The  $\gamma'$  phase has a volume fraction of approximately 45 % and exists in a size distribution which provides optimum mechanical properties. Due to this, the alloy can operate at temperatures up to 1000K.

Due to the increased volume fraction of  $\gamma'$  in the current generation of precipitation-strengthened Nickel-based superalloys, they are very difficult to weld via conventional welding processes, as microcracks are often produced during solidification of the weld [3]. Therefore, solid-state joining technologies, such as diffusion bonding and fusion welding, are attractive for these materials due to the lack of melting during the process. Rolls-Royce plc currently use Inertia Friction Welding (IFW) to join RR1000 components in high-pressure turbine and compressor components. This research is focussed on novel methods of evaluating the evolution of microstructure during IFW, utilising bespoke experimental methods and novel numerical analysis approaches.

## 1.2 Inertia friction welding

Inertia Friction Welding (IFW) is a solid-state welding process used to join axisymmetric components. It is known to be a fast, repeatable and efficient process which produces a very narrow Heat Affected Zone (HAZ), which makes it a very attractive joining method. A schematic of the process is shown in Figure 1.1. The process outputs of interest are the rundown in rotational velocity, and the upset (axial shortening), which are presented in Figure 1.1d and Figure 1.1e, respectively.

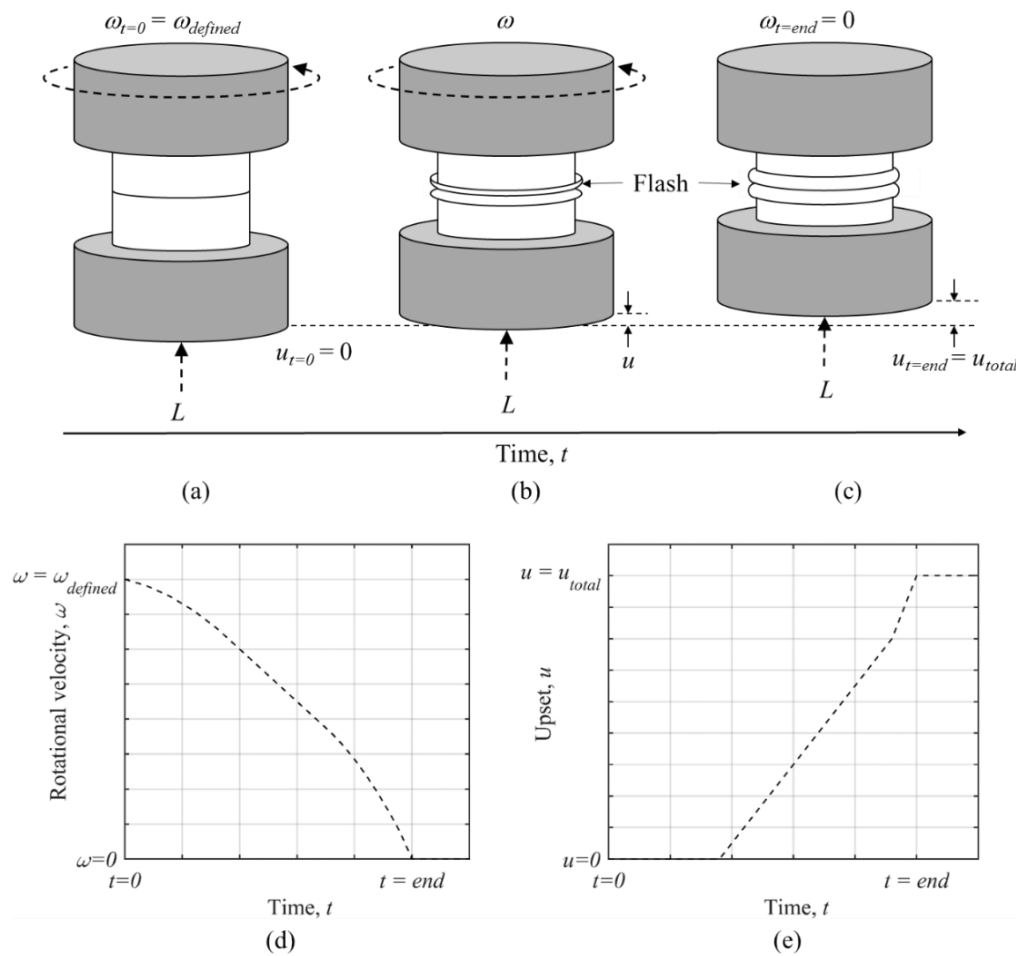


**Figure 1.1:** Schematic of the IFW process and typical process output data.

The two workpieces in IFW are known as the spindle and fixture workpieces. The spindle workpiece is attached to a flywheel of inertia  $I$  and rotated to a pre-defined rotational velocity ( $\omega_{initial}$ ). This stores energy ( $E$ ) for welding which can be calculated

using Equation 1.1. The fixture workpiece is non-rotating, and an axial load is applied from this workpiece to allow for joining of the two components.

$$E = \frac{1}{2} I \omega_{initial}^2 \quad (\text{Eq. 1.1})$$

The process starts when the spindle drive is disengaged, and the load is applied from the fixture workpiece simultaneously (Figure 1.1 (a)). This brings the workpieces into contact, and the relative rotational motion at the contact interface causes frictional heating, converting kinetic energy from the flywheel into heat. The material around the contact interface increases in temperature until it is high enough to allow for plastic deformation of the material, which is expelled outwards as ‘flash’ (Figure 1.1 (b)). The end of the weld occurs when all the kinetic energy has been dissipated into the workpieces, and there is no further rotation of the spindle workpiece (Figure 1.1 (c)). The two process outputs of interest are the rundown in rotational velocity and upset. The rundown curve (Figure 1.1. (d)) allows for understanding of the energy input rate throughout the weld duration, which can be used to define the frictional behaviour at the contact interface. The upset, or axial shortening (Figure 1.1. (e)) shows the amount of plastic deformation through measurement of shortening of the workpieces through the process. Here, the total upset ( $u_{total}$ ) is a measure of the total amount of mechanical shortening produced by the process.

IFW requires a thorough understanding of the input parameters (initial rotational velocity, flywheel inertia and axial load) to produce an optimal weld in which substantial mechanical deformation has occurred to produce a sound joint, without excessive heat input which would produce a large HAZ.

### **1.3 Microstructure evolution during IFW**

The high strength of precipitation-strengthened superalloys is primarily attributed to the presence of  $\gamma'$  precipitates. To join these alloys via IFW, there is a requirement to dissolve these precipitates in order to reduce the strength of the material sufficiently so plastic deformation can occur.  $\gamma'$  precipitates typically dissolve at temperatures in excess of 800 [4], whilst the solidus of these alloys typically exceeds 1200 °C [5]. This makes the processing window for these alloys extremely small.

Due to the nature of the IFW process, where a combination of high temperatures and heating rates are produced, alongside extremely high rotational velocities and pressures, there are a range of factors which must be considered when evaluating the evolution of the microstructure of Nickel-based superalloys during IFW. The effects of temperature and strain on both the  $\gamma$  grains and  $\gamma'$  precipitates must be understood in order to produce models capable of predicting evolution of the microstructure.

## **1.4 Research aims**

The primary aim of this research is to develop the understanding of the microstructure evolution of Nickel-based superalloys during IFW.

To achieve this, a novel experimental IFW machine has been produced to facilitate acquisition of in-situ X-ray diffraction data. An analysis procedure has been developed to allow for quantified analysis of the diffraction patterns produced.

Cellular Automata modelling approaches have also been investigated as a means of predicting the microstructure evolution which occurs during IFW. This model evaluates the diffusion of atoms between phases due to changes in weld temperature and the subsequent phase transformations produced by this. CALPHAD approaches are linked to the model to define local equilibria and evaluate thermodynamic properties.

Comparison of experimental and numerical modelling results allows for a development of understanding of the microstructure evolution which occurs during IFW. The in-situ diffraction data provides novel experimental data, and the numerical model assesses whether the physics implemented can correctly represent these experimental results.

## **1.5 Thesis structure**

Relevant literature for this body of work is reviewed in Chapter 2.

Chapter 3 outlines both the experimental and numerical research methodologies used in this body of work.

In Chapter 4, the results from the novel in-situ synchrotron diffraction experiments are analysed for BS1407 steel.

Chapter 5 expands the analysis of the in-situ diffraction experiments to Nickel-based superalloys, using a variety of additional analysis methods to provide more detail on the evolution of microstructure for these materials.

The novel Cellular Automata modelling approach for prediction of microstructure evolution is shown in Chapter 6, alongside validation against experimental results.

Chapter 7 draws some conclusions from this body of work and suggests possible directions for future research in this area.

## **Chapter 2**

### **Literature Review**

#### **2.1 Introduction**

The goal of this work is to improve the understanding of the evolution of Nickel based superalloy microstructure during Inertia Friction Welding (IFW). Developing the understanding of microstructure evolution which occurs during IFW is required to allow for a better understanding of the physics which govern the evolution of the process. Improvement in this understanding will allow for easier prediction of optimised process parameters which produce an optimal weld joint with minimum detriment to the microstructure and mechanical properties.

To develop the understanding of microstructure evolution during IFW, novel experimental methods have been implemented that provide quantified microstructural data from experimental welds. Additionally, numerical modelling approaches have been developed to assess whether the thermal history produced by the process can accurately evaluate the microstructure due to atomic diffusion and subsequent phase transformations.

What follows is a review of the state of the art in the fields of Nickel-based superalloy materials, experimental analysis of Inertia Friction Welding and numerical modelling of the IFW process.

## 2.2 Nickel-based superalloys

In gas turbine aircraft engines, components are subjected to exceptional mechanical loads at extremely high temperatures. There is a constant drive to increase the rotational speeds and temperatures within the engine to improve the efficiency of these machines, thus reducing fuel waste and the environmental impact of their operation. Therefore, to produce components for these engines, there is a requirement for a material with exceptional strength, toughness, oxidation and corrosion resistance, at both ambient and elevated temperatures.

In a modern gas turbine engine, approximately 40 – 50 % of the weight is made-up by Nickel-based superalloys [6]. These alloys are primarily implemented in combustor and turbine components, where the operating temperatures are highest. Nickel-based superalloys provide exceptional high-temperature strength and toughness, alongside excellent resistance to oxidation, which makes them ideal for use in combustor and turbine components.

Most Nickel-based superalloys exhibit excellent high-temperature mechanical properties due to the presence of a precipitate phase,  $\gamma'$  which coexists with the face-centred-cubic  $\gamma$  matrix. The two phases exhibit extremely similar lattice parameters and are often referred to as a superlattice. The  $\gamma'$  phase primarily acts as a barrier to dislocation motion, as dislocations cannot permeate the boundary between the phases, providing increased yield strength and creep performance. The high-temperature excellence of these materials is attributed to the fact that these precipitates do not dissolve until temperatures very close to the alloy melting temperature are reached.

Within the definition of Nickel-based superalloys, there are specific sub-classes which can be primarily defined based on their intended use. Taking the gas turbine engine as an example, the temperatures and stresses exerted on a turbine blade and turbine disc during standard operation differ due to their positions in the engine. Therefore, different alloy compositions and microstructural control methods are implemented to produce optimal properties for these components.

For turbine blade components, it was discovered in the 1960s that investment casting offers better process control than the previously used extrusion and forging processes [7]. The first turbine blades produced by investment casting consisted of an equiaxed

grain structure. However, the casting process was developed in the 1970s to produce directionally solidified alloys with long columnar grains and single crystal microstructures [8].

The production of columnar and single crystal blade alloys improved the creep life of these components greatly, due to the lack of grain boundaries in the traverse direction, which were a common path for dislocation motion during creep evolution.

The  $\gamma'$  volume fraction in blade alloys is usually around 70 % [9]. This is a very high volume fraction when compared to other superalloy classes. However, this is required due to the creep deformation mechanisms which present themselves in this class of materials. At small length scales, dislocation motion is known to occur in the matrix phase, however creep dislocations do not penetrate the precipitate phase. Therefore, a high  $\gamma'$  volume fraction inhibits the motion of dislocations.

It is also known that there is a strengthening effect produced by the  $\gamma/\gamma'$  interfaces, which is why these alloys are not made up of 100 %  $\gamma'$  volume fraction. The optimal microstructure for creep resistance includes a fine dispersion of small  $\gamma'$  precipitates with narrow channels of  $\gamma$  matrix between them, to best inhibit the motion of dislocations.

On the other hand, turbine disc components require different alloy compositions and microstructures based on their unique operating conditions. As an example, a typical temperature for blade disc operation is 650 °C, which is much lower than that of 1550 °C experienced by the turbine blades [7]. Additionally, it is known that the mechanical loading on the disc is greater than that of the turbine blade, due to the small geometry of these in comparison, and their requirement to transmit power from the blades to the shaft.

In turbine disc alloys, the  $\gamma'$  volume fraction is usually in the region of 45 – 55 %, which is designed by alloy content, processing path and heat treatments. This provides strength and fatigue resistance at high temperatures. To achieve this, high amounts of Aluminium, Titanium and Tantalum are added to these alloys.

The increasing alloy content required to produce the desired  $\gamma'$  volume fraction creates challenges with conventional cast and wrought processing routes, as segregation and chemical inhomogeneity throughout a billet become likely [10]. This results in

uncontrollable microstructural features such as  $\gamma$  grain size growth and undesirable phases. To overcome this, powder metallurgy superalloys are now used [11].

The total volume fraction of  $\gamma'$  alone does not control the mechanical properties of disc alloys. The size and distribution of the  $\gamma'$  precipitates provide the optimal material strength. In most disc alloys, the microstructure consists of a trimodal distribution of  $\gamma'$ , which is produced by the heat treatment route. Primary  $\gamma'$  precipitates reside at grain boundaries and triple points and increase the strength of the material by inhibiting grain growth through Zener pinning. The large primary  $\gamma'$  precipitates are produced due to incomplete solutioning during the first stage of heat treatment, which is carried out below the  $\gamma'$  solvus temperature [12].

Secondary and tertiary  $\gamma'$  precipitates are formed at much lower temperatures. Here, a slower cooling rate produces this bimodal distribution of fine precipitates which had solutioned during the solutioning heat treatment phase. The slow cooling permits diffusion of  $\gamma'$ -forming elements to nucleate and grow the precipitates. The secondary and tertiary  $\gamma'$  are termed intergranular precipitates, as they reside in the  $\gamma$  grains. These precipitates prevent dislocation motion, increasing the yield strength of these alloys by preventing plasticity. A schematic of the tri-modal distribution of  $\gamma'$  precipitates is presented in Figure 2.1 [13].

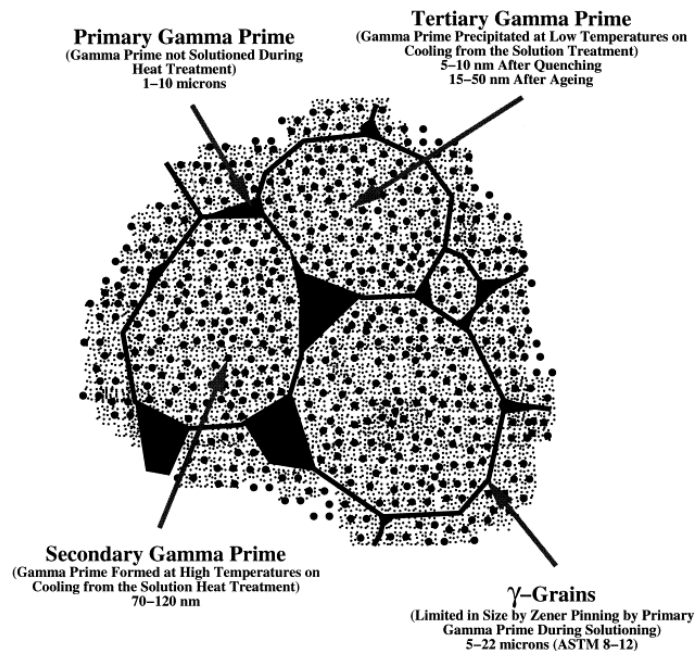


**Figure 2.1:** Schematic representation of the microstructure of the turbine disc alloy Udimet720 [13].

### 2.2.1 Disc alloy RR1000

RR1000 is a high strength powder metallurgy disc alloy produced by Rolls-Royce plc. There are various forms of this alloy present in the literature, namely the fine-grained and coarse-grained variants [12]. The fine-grained variant has an approximate grain size of 6  $\mu\text{m}$ , with a trimodal distribution of primary, secondary and tertiary  $\gamma'$  precipitates. The coarse-grain variant of RR1000 has an average grain size of 33  $\mu\text{m}$ , and the precipitate phase exists in a bimodal distribution of secondary and tertiary  $\gamma'$ . This work focuses on the fine-grained variant, which is intended for use in high pressure compressor and turbine disc components [14]. The nominal composition of fine-grained RR1000 is presented in Table 2.1 [15].

**Table 2.1:** Nominal composition of fine-grained RR1000 in at % [15].

Element	Ni	Cr	Co	Mo	Al	Ti	Ta	B	Hf
at%	50.9	17.6	16.5	3.0	6.35	4.3	0.63	0.08	0.16

This alloy is produced by hot isostatic pressing, extrusion and isothermal forming. A sub-solvus solution heat treatment is applied for production of the primary  $\gamma'$  precipitates. A subsequent precipitation aging treatment is used to produce the secondary and tertiary  $\gamma'$  precipitates and refine the  $\gamma$  grain size.

The total  $\gamma'$  volume fraction present in RR1000 is approximately 50 % [16], although this does vary by  $\pm 2$  % within the literature depending on the characterisation method used [17]. There is also variation in the volume fraction of the different precipitate sizes, which is caused by variations in the bounds used to define the sizes of precipitate sizes. Reported data shows primary  $\gamma'$  volume fractions from 10 % [18] to values as high as 17 % [19].

A common assumption defines primary  $\gamma'$  precipitates as those with an equivalent diameter greater than 0.5  $\mu\text{m}$  [10, 14]. Tertiary  $\gamma'$  precipitates may be defined as those with a diameter lower than 50 nm [15], although this again may vary depending on the characterisation methods used, with some references defining tertiary  $\gamma'$  up to 90 nm

in diameter [16]. Secondary  $\gamma'$  is usually defined by the sizes which fall between those of primary and tertiary  $\gamma'$ .

A low magnification Scanning Electron Microscope (SEM) image presenting the distribution of  $\gamma$  grains and  $\gamma'$  precipitates is shown in Figure 2.2 [19]. In this study, the  $\gamma$  grain size was found to be  $3.0 \mu\text{m} \pm 0.2 \mu\text{m}$ . The mean diameter of primary  $\gamma'$  precipitates was evaluated as  $0.78 \mu\text{m}$ .

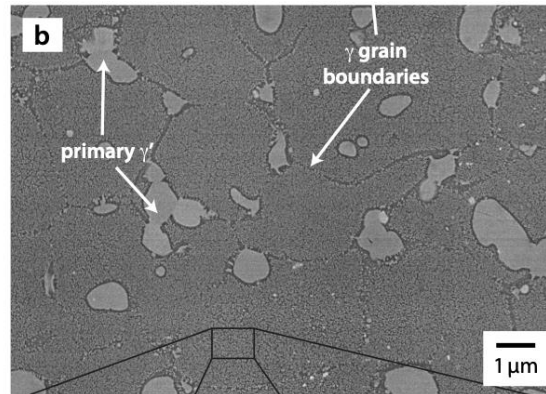


**Figure 2.2:** Low-magnification SEM image presenting the distribution of  $\gamma$  grains and primary  $\gamma'$  precipitates in RR1000.

In Figure 2.3, a high-magnification SEM image is presented, showing the distribution of small-scale secondary and tertiary  $\gamma'$  precipitates [16]. Here, the respective average precipitate diameters were calculated as follows; primary  $1.25 \mu\text{m} \pm 0.18 \mu\text{m}$ , secondary  $125 \text{nm} \pm 10 \text{nm}$ , tertiary  $42 \text{nm} \pm 5 \text{nm}$ .

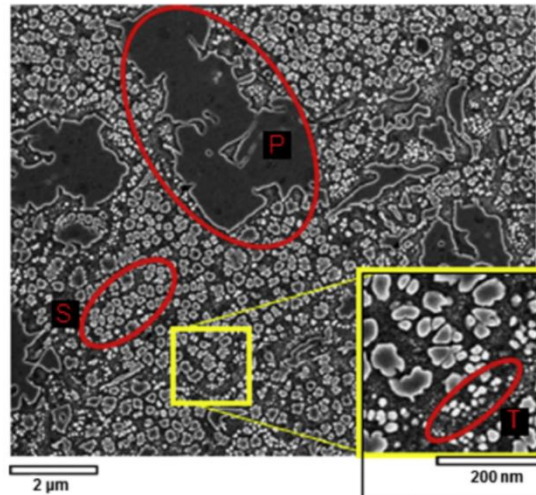


**Figure 2.3:** High-magnification SEM image presenting the distribution of primary and secondary  $\gamma'$  precipitates in RR1000. Inset: ultra-high-magnification image showing the population of tertiary  $\gamma'$ .

The exact volume fractions and precipitate sizes vary between different references available in the literature. This is in part due to the ways in which researchers have characterised the microstructure. As an example, utilisation of SEM in which even the highest magnifications may have difficulty resolving nm-scale precipitates would provide different results to transmission electron microscopy, where smaller length scales can be analysed in greater detail. There is also the possibility that alloy development over time has slightly altered the chemistry and heat treatment routes, and so data published in the early stages of alloy development would likely differ from recent studies.

### 2.2.2 Challenges in welding of Nickel-based superalloys

The production and validation of materials which can withstand the extreme operating conditions of the high-pressure turbine only provides part of the solution for increasing engine performance and efficiency. These components must be in some way machined to produce their final shape. Additionally, these components must be joined together, either by mechanical fixings or more often via some form of bonding or welding process, in order to produce a complete assembly.

This provides a significant challenge for the manufacture of turbines. Since the superalloys employed in these machines offer excellent strength and toughness at ambient and elevated temperatures, machining and joining of these alloys are extremely difficult. The machinability of Nickel-based superalloys is not of interest here, but a comprehensive review of this topic can be found in the literature [20].

Welding of Nickel-based superalloys can cause a range of defects which impact the material properties and life of the welded joint. For precipitation strengthened superalloys, the main concerns are solidification cracking, liquation cracking and strain age cracking [21].

Solidification cracking occurs due to the difference in chemistry between the  $\gamma$  and  $\gamma'$  phase. When cooling from the liquid form, the  $\gamma$  and  $\gamma'$  phases resolidify at different temperatures [3]. In general, the  $\gamma$  phase will solidify first, prior to the  $\gamma'$  phase. When the  $\gamma'$  phase solidifies, it also shrinks due to thermal contraction. This shrinkage causes tensile strain between the  $\gamma$  and  $\gamma'$  phases, which in the most extreme cases will immediately form a crack. The problem of solidification cracking means that weld processes which involve bulk melting of the alloy cannot be implemented.

Additionally, the chemistry of superalloys also causes defects when welding below the melting temperature of the alloy. In processes such as Gas Tungsten Arc (GTA) welding, in which a filler wire is used to join the material, liquation cracking has been observed in the Heat Affected Zone (HAZ) [22]. Liquation cracks occur in a similar fashion to solidification cracks, despite the avoidance of bulk melting. Liquation is likely in processes in which a rapid heat input is utilised. Here, the  $\gamma'$  solvus temperature may be exceeded in a very short time, which limits the time permitted for the  $\gamma'$  phase to dissolve into the  $\gamma$  matrix. Once the  $\gamma'$  solvus temperature is exceeded, any remaining  $\gamma'$  will melt. The same issue as presented in solidification melting then occurs, by which the solidification of the liquid  $\gamma'$  causes contraction and cracking at the  $\gamma/\gamma'$  interface.

The problem of liquation cracking can also be extended to the field of constitutional liquation, or eutectic melting [23]. Here, the dissolution of the  $\gamma'$  phase causes diffusion of  $\gamma'$ -forming elements (Al, Ti, Ta) into the  $\gamma$  matrix. There is limited time for these elements to dissolve outwards from the precipitate and homogenise in the  $\gamma$  matrix, and so some para-equilibrium eutectic phase forms around the  $\gamma/\gamma'$  interface.

This eutectic phase has a lower melting point than either of the  $\gamma$  or  $\gamma'$  phases. Similar to liquation cracking, this eutectic can then melt at lower temperatures than the bulk melting temperature, and therefore solidification cracks may form. Figure 2.4 presents an SEM image in which both eutectic melting of a  $\gamma$ - $\gamma'$  eutectic and liquation of individual  $\gamma'$  precipitates are observed on a cracked grain boundary of Inconel 738 [24].

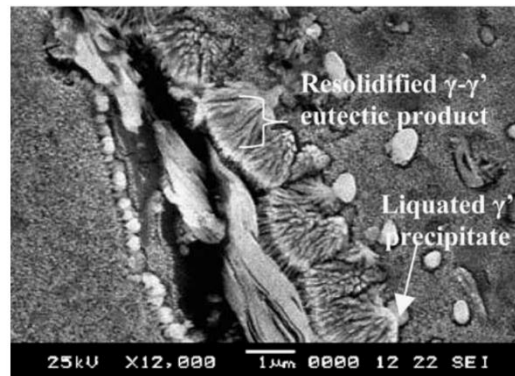


**Figure 2.4:** SEM image of a cracked grain boundary due to liquation of  $\gamma'$  and  $\gamma$ - $\gamma'$  eutectic [24].

There are two possible causes of strain-age cracking [25]. Firstly,  $\gamma'$  re-precipitation may occur due to the heat applied to weld the superalloy. This is unlikely in most cases, but depending on the parent microstructure and alloy composition, the equilibrium microstructure at elevated temperatures may present a driving force for re-precipitation of  $\gamma'$ . Secondly, a long process duration may present an opportunity for solidification strains to transfer to the grain boundaries due to dislocation motion at elevated temperatures. Depending on the nature of the residual stresses present from solidification, transfer of these to grain boundaries may permit intergranular cracking.

There are a range of possible defects which may arise during the joining of Nickel-based superalloys. The problems which present themselves indicate that there is an extremely small 'process window' in which defect-free welds can be produced. Great care must be taken when selecting weld parameters to avoid the formation of these defects, however these tend to lead to longer process times in order to avoid melting of the  $\gamma'$  phase. This in turn produces a larger HAZ due to the increased time for heat input and conduction through the weld workpieces.

### **2.2.3 Concluding remarks**

Nickel-based superalloys have been produced and developed over time to produce materials with exceptional mechanical properties at ambient and elevated temperatures. This has allowed for an increase in performance of gas-turbine engines during this time. There is a continued drive to increase performance and efficiency of gas turbines, to reduce fuel waste and the environmental impact associated with this, which in turn drives continued development of these superalloys.

Precipitation-strengthened superalloys are susceptible to a range of defects during high temperature processing which limits the joining methods which can be used to bond these materials together. As the high-temperature properties of these materials improved due to continued alloy development, the process window in which a defect-free joint can be produced becomes smaller.

### 2.3 Inertia friction welding

Inertia friction welding (IFW) is a solid-state joining process which is used to join axisymmetric components. One component is attached to a flywheel and rotated to a pre-defined initial rotational velocity ( $\omega_{initial}$ ) to store energy for welding, while the other component is held stationary, as shown schematically in Figure 2.5.

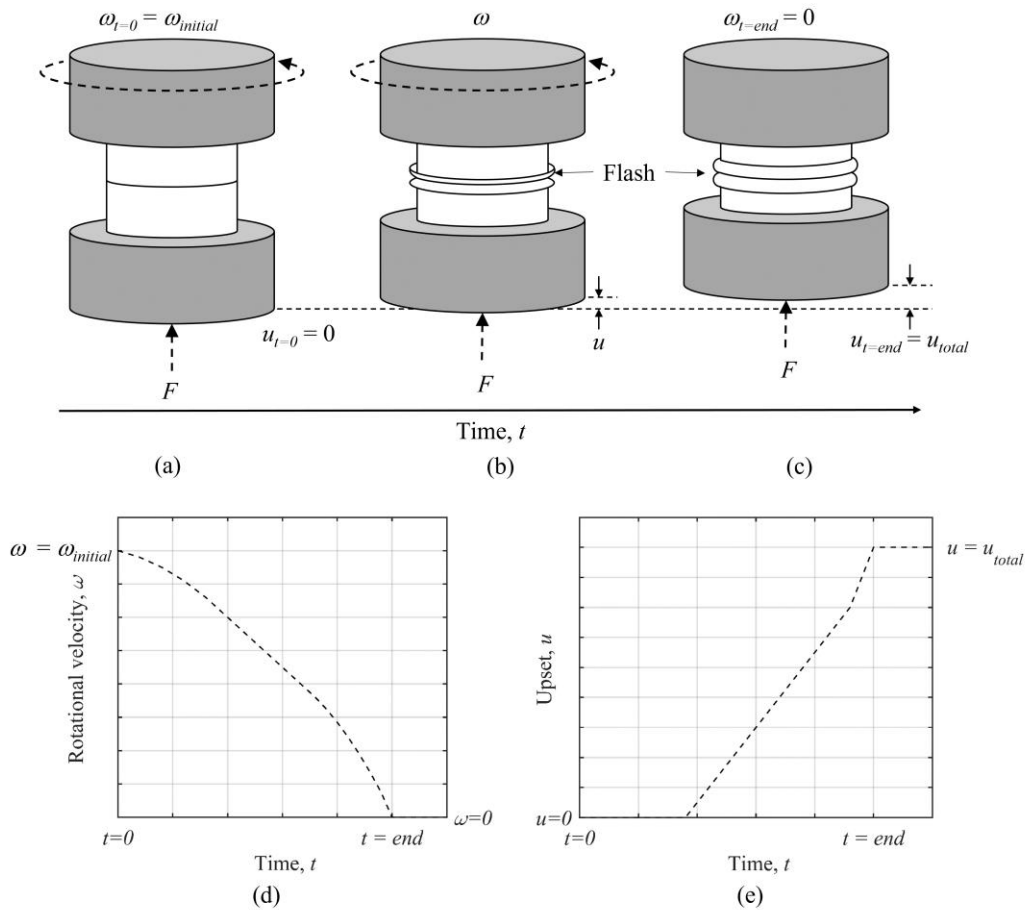


**Figure 2.5:** Schematic of the IFW process; (a) workpieces brought into contact to start the process, generating heat at the weld interface due to friction at the contact interface; (b) upsetting begins due to continued application of the axial load, where soft material around the weld interface is expelled as ‘flash’; (c) the end of the weld indicated by ceasing of the rotational velocity. (d) and (e) show the rundown in rotational velocity and upset (axial shortening), respectively, for clarification.

The process starts when the drive is disengaged, and the components are brought together under an axial load ( $F$ ) applied to the stationary component. The relative rotational motion between the workpieces causes frictional heating at the contact interface, thereby softening the surrounding material which is expelled as ‘flash’ under the axial load. The expulsion of ‘flash’ causes axial shortening of the specimens, known as upset ( $u$ ). As kinetic energy is converted to heat at the weld interface, the rotational velocity of the rotating specimen reduces throughout the process. The process is complete when the rotational velocity reaches zero. The two process outputs are the rundown in rotational velocity (Figure 2.5d) and the upset profile (Figure 2.5e) produced as the specimens shorten through the process.

The combination of initial rotational velocity ( $\omega_{initial}$ ) and flywheel inertia ( $I$ ) produce energy ( $E$ ) for welding; however, to scale between weld geometries, this is better presented as specific energy ( $S.E.$ ) as shown in Equation 2.2, where  $A$  is the initial contact area between specimens.

$$E = \frac{1}{2} I \omega_{initial}^2 \quad (\text{Eq. 2.1})$$

$$S.E. = \frac{E}{A} \quad (\text{Eq. 2.2})$$

The IFW process is commonly defined into three stages; conditioning, burn-off and consolidation as outlined in Figure 2.6. These stages are defined by the upset response of the material. The early portion of the weld in which no upset occurs is defined as conditioning. The conditioning stage is followed by a stage in which a constant upset rate is produced, which is known as steady state burn off. Towards the end of the weld, there is a sharp increase in the upset rate during the consolidation stage.

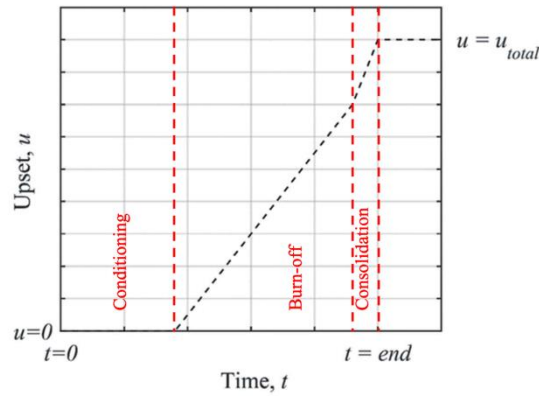


**Figure 2.6:** The three stages of the IFW process as defined through transitions in the upset data.

IFW offers a range of benefits for all materials. It is a fast and repeatable process which occurs over extremely short time scales (the weld duration is often less than 10s). For Nickel-based superalloys, the fact that the process is performed in the solid state greatly reduces the probability of micro-cracking. However, the process is limited by the fact that only axisymmetric cylindrical/tubular specimens can be welded. Additionally, there is a large equipment cost associated with IFW machines, and so it is generally only implemented when other welding processes are not viable. Often, components of large radial geometry are welded via IFW as there are difficulties in generating a homogenous radial heat input with more general welding techniques, which results in a non-uniform heat affected zone.

Microscopic examination of as-welded IFWs has revealed that there are two distinct zones produced by inertia friction welding [26]. These are the thermo-mechanically affected zone (TMAZ) and the heat affected zone (HAZ). Far from the contact interface, the parent material (PM) remains unaltered. A schematic of these regions relative to an IFW is presented in Figure 2.7.

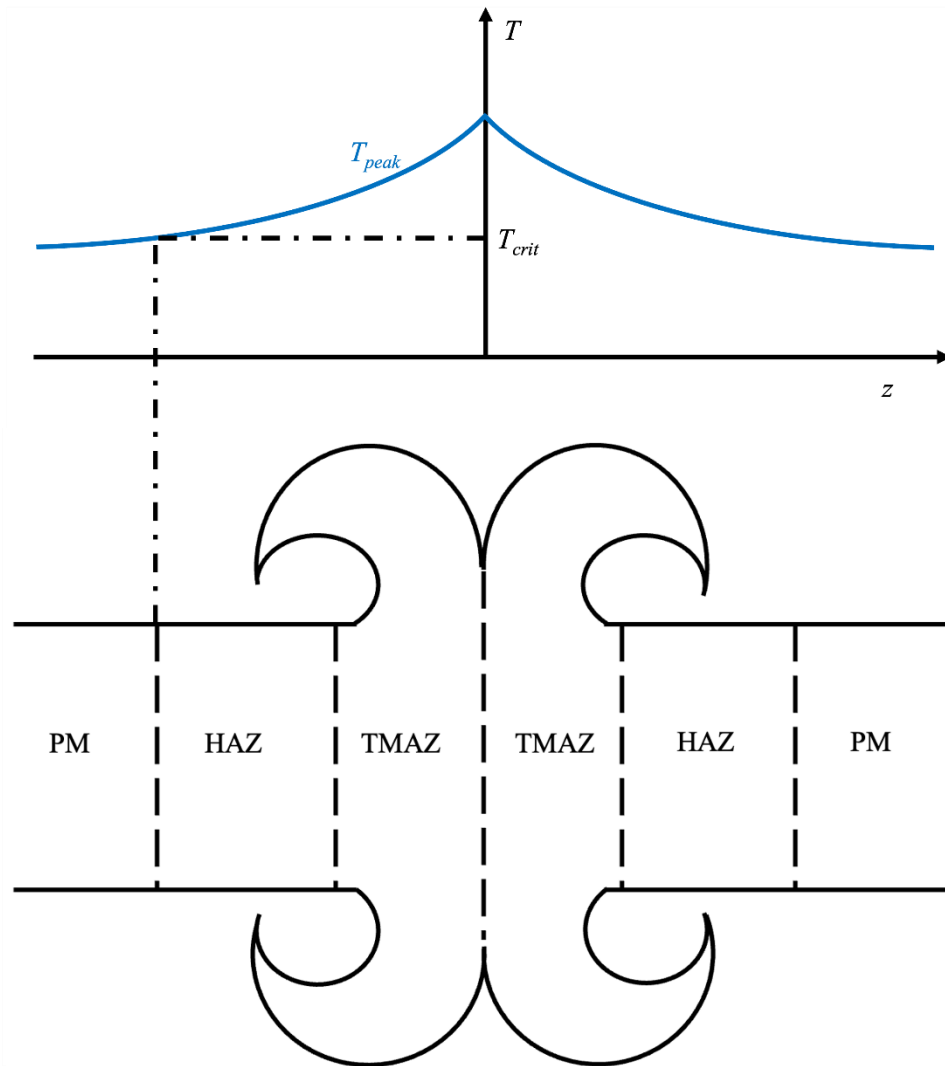


**Figure 2.7:** Representative peak temperature curve aligned with a schematic of the microstructurally affected zones produced by the inertia friction welding process.  $T_{crit}$  is the temperature at which a phase transformation occurs.

The TMAZ is a region in which significant mechanical influence on the microstructure is observed, primarily through the mechanism of dynamic recrystallisation. The HAZ contains a microstructure which has clearly been altered by the thermal history produced by the process. Here, phase transformations are often seen, however, grain refinement is limited due to the limited mechanical strain in this region.

In IFW, the combination of localised heating and pressure joins the materials. However, to produce a successful weld with complete bonding across the weld

interface, a thorough understanding of the sensitivity of process response to variations in rotational velocity, flywheel inertia and axial pressure is required.

The IFW technique relies on a combination of initial rotational velocity and flywheel inertia to provide energy for welding, with the components brought together and forged under an axial pressure. Designed variations in process parameters effect the physics of the process, as the conversion from stored energy to heat at the weld interface occurs at different rates dependent on the combination of input parameters selected. This influences the macro-scale behaviour of the process, as the rundown in rotational velocity and mechanical deformation (upset) are affected by the variation in energy input rate.

Experimental assessments of the sensitivity of IFW to the process inputs were traditionally carried out to understand the behaviour and response of the technique. For newly developed materials, parametric studies are performed to understand the magnitude by which input parameters must be varied to cause substantial change in the macroscale outputs. Over time, parametric studies have also been carried out to assist understanding in the microstructural response, and to facilitate the development of numerical modelling approaches through improved process understanding.

One of the first published parametric studies of IFW was carried out by Tumuluru in 1984 [27]. This study analysed the effect of welding variables on the process outputs and microstructural response for dissimilar low alloy steel pipes. Each parameter was varied in turn whilst the remaining parameters were kept constant. Doubling the initial rotational velocity provided increased total upset and extended the weld duration to 5 times its original value due to the increased energy available for welding. Increasing the axial pressure produced an increase in the total upset, and a slight reduction in weld duration. The flywheel inertia was increased by a factor of 5 which tripled the length of the weld duration, and increased the total upset, again due to the increased energy available for welding.

Daus *et al.* [28] investigated the effect of process parameter combinations on the mechanical properties and fatigue strength of dissimilar IFWs of alloys RR1000 and Inconel 718. Three input parameter combinations were tested, and all three welds showed a trough in hardness on the Inconel 718 side, due to the reduced volume fraction of  $\gamma'$  in Inconel 718 which can be completely dissolved. Reducing the weld

pressure was shown to increase the axial length of this hardness trough, which occurs due to the increased time for heat generation and conduction which occurs with the reduced deformation at lower weld pressures. It was concluded from this research that the variation in process parameters had no significant influence on the crack growth rate, and that any changes in crack growth rate were attributed to variations in the local crack path.

Guo *et al.* studied the influence of weld pressure on dissimilar welds of Aluminium and Magnesium alloys [29]. Weld pressures ranging from 77 MPa to 125 MPa were investigated and it was observed that at this range of pressures, the upset values produced were in the range of 6 mm to 23 mm, with increased pressure causing a larger amount of total upset. Across the range of parameters studied, it was seen consistently that the deformation mainly occurred on the Magnesium specimen however, with the largest weld pressures, some limited flash formation was observed on the Aluminium workpiece. All welds showed the formation of an intermetallic layer at the contact interface, which was prominent on the Magnesium specimen. It was observed that the axial thickness of this intermetallic layer decreased when the weld pressure was increased. This was attributed to the increased deformation and reduced process time at higher weld pressures. Tensile tests were performed which showed that welds conducted with increased weld pressure produced a larger tensile strength, which was attributed to the thinner intermetallic layer at the contact interface.

A process parameter study was performed across a broad range of process parameters for IFW of AISI 4140 steel by Kessler *et al.* [30]. This work aimed to assess the effect of weld parameters on the total upset and torsional moment produced by the process. It was observed that the total weld energy and weld pressure both caused an increase in the torsional moment and upset when these weld parameters were increased. Welds performed with a greater specimen wall thickness caused an increase in the torsional moment and a reduction in total upset, due to the larger flow path of material required to form flash and thus permit axial deformation. A broad range of weld process parameters were investigated, with pressures of 100 MPa – 160 MPa and specific energies of 80 J/mm<sup>2</sup> to 150 J/mm<sup>2</sup>. However, it was observed that all weld specimens exhibited similar tensile behaviour.

A sensitivity study of the effects of process variables on IFW of dissimilar Nickel-based superalloys LSHR and Mar-M247 was carried out by Mahaffey *et al.* [31]. This investigation consisted of three welds with various combinations of initial rotational velocity and flywheel inertia which produced the same initial kinetic energy for welding. It was demonstrated that increasing the flywheel inertia extended the weld duration and increased the amount of total upset. Additionally, increasing the flywheel inertia provided a greater amount of chemical mixing between the two alloys. It was concluded that higher inertia, which increased the temperature and weld duration, promoted dynamic recrystallisation on the stronger Mar-M247 side, which promoted deformation. On the contrary, welds with low inertia, which had shorter durations and lower temperatures, had insufficient time to dissolve  $\gamma'$  or sufficiently recrystallise the Mar-M247 side. This research was concluded with a hypothesis that increasing the inertia may increase process efficiency, as a lower portion of weld energy is consumed by the IFW machine. This hypothesis was investigated by Senkov *et al.* [32]. Various combinations of inertia, rotational velocity, kinetic energy, and pressure were investigated whilst the friction torque on the sample surfaces and machine bearings was measured to assess the efficiency of the process. Free rundown tests of the IFW machine showed that increasing the flywheel inertia reduced losses, as the spindle side takes longer to rundown naturally, thus the process was more efficient. When the axial pressure was increased (and all other process variables remained constant), the process duration reduced, which increased the efficiency of the process due to reduction of time in which the machine can consume weld energy. Increasing the total energy available for welding was found to reduce efficiency, as a greater portion of the weld energy was consumed by the machine bearings. A trend was produced to calculate the process efficiency as a function of inertia, rotational velocity and axial pressure, and when compared with experimental data, the coefficient of determination of this function was found to be 0.976. It was concluded that a new variable, the sample energy (simply the efficiency multiplied by flywheel energy) should be considered as a critical parameter for IFW. Senkov *et al.* [33] also extended the research into this hypothesis, conducting a process parameter analysis study on the behaviour of LSHR to Mar-M247 IFWs. It was found that upset increased with increasing pressure, inertia and total kinetic energy. Additionally, weld duration increased with increased inertia and total kinetic energy, and with reduced pressure. Both the upset rate and weld durations were fit to functions of inertia, pressure and weld energy. Furthermore, the

varying upset on both the LSHR and Mar-M247 workpieces was described with empirical equations.

In some more recent investigations, Finite Element (FE) models have been implemented as a method of investigating the sensitivity of the IFW process response to input parameters. These have been implemented in some cases to show the variation of effects that are extremely difficult to measure experimentally, such as the interface temperature. In other cases, FE analysis has been performed for very large ranges of process parameters, which would be extremely costly to conduct experimentally.

Chen *et al.* investigated the effect of initial rotational speed on the interface temperature and weld upset [34]. In this study, a 2D axisymmetric model was produced in Abaqus to model IFW of the Nickel-based superalloy GH4169. It was observed that by increasing the initial rotational velocity, a greater amount of total upset was produced due to the larger amount of weld energy available. This agrees with the data seen in various experimental studies. Furthermore, it was seen that the increase in rotational speed caused a faster heating rate at the contact interface. This was attributed to the greater relative rotational motion at the contact interface which produced an increased apparent friction coefficient.

Wang *et al.* [35] simulated a range of finite element models to evaluate the sensitivity of interface temperature and mechanical upset to variations in axial pressure, flywheel inertia and initial rotational speed for IFW of the superalloy GH4169. The range of weld pressures investigated were as follows; weld pressure 250 MPa – 500 MPa, initial rotational speed 120 rad/s – 170 rad/s, flywheel inertia 0.92 kg.m<sup>2</sup> – 1.55 kg.m<sup>2</sup>. It was observed that the upset was proportional to the square of the initial rotational speed and logarithmically proportional to the weld pressure. It was concluded that an increase in the axial pressure improved the conversion efficiency of mechanical energy to heat. Furthermore, an increase in pressure produced a narrower high temperature zone, due to the larger upset. A weldability criterion was defined in which a critical pressure was defined to produce upset at a given initial rotational speed and vice versa.

A study of the weld energy required to undergo the conditioning stage of IFW, and its relationship with varying process parameters was performed by Turner *et al.* [36]. Finite element analysis was implemented to model IFW of a titanium alloy, and the modelling results were validated against experimental data. The variation in the

conditioning time was measured due to variations in axial pressure (40 MPa – 150 MPa) and initial rotational speed (115 rad/s – 180 rad/s). It was observed that for both weld parameters, a reduction in the parameter produced an increase in conditioning time. Additionally, the weld energy required to form the thermal profile in the weld which permits steady state burn off was investigated. Due to the longer conditioning time, it was observed that lower values of weld pressure and initial rotational velocity used a greater portion of the total weld energy to perform the conditioning stage. This in turn resulted in reduced upset in these welds due to the lower amount of weld energy remaining for the burn-off and conditioning stages.

Turner *et al.* also used FE modelling to evaluate the size of the TMAZ and HAZ during IFW of a Titanium alloy through analysis of thermal histories and plastic strain [37]. The results showed that an increase in the weld pressure produced a narrower HAZ, which is to be expected given the greater total upset and reduction in weld duration. An increase in the total weld energy through a larger initial rotational velocity produced a wider HAZ, and the size of the HAZ was shown to be more sensitive to the rotational speed than weld pressure. Definition of the TMAZ size from the plastic strain during steady-state burn-off showed reasonable agreement with experimental data but it was concluded that the approach used was a great simplification of the range of phenomena which may influence the TMAZ size.

Liu *et al.* utilised a radial basis function neural network to predict the total upset of IFW using training data from a set of FE models [38]. The neural network predicted the upset response with an error of approximately 8 % when compared with the FE simulations. The sensitivity of upset to axial pressures of 200 MPa - 500 MPa and rotational speeds of 120 rad/s - 200 rad/s were produced by the model, which showed a general trend that an increase in these parameters produced greater total upset, due to the larger amount of total energy available and more effective conversion of this energy to heat. The neural network also predicted a weldability criterion, similar to the results produced by Wang *et al.*, in which a critical relationship between speed and pressure required to produce axial shortening was defined.

### **2.3.1 Variation in microstructure and mechanical properties across an IFW**

Understanding of the connection between the resultant microstructure and mechanical properties after IFW is essential for determining optimised process parameters which produce a joint with mechanical properties close to the parent material(s).

Further to this, it is desirable to attempt to gain some information regarding the process behaviour from the resultant microstructure, and the variation of this with changing input parameters. It has been presented in the previous section that changing the weld parameters produces different process behaviour, such as conditioning time, weld duration and total upset, but it is not known whether the process behaviour is dominated by the microstructure produced due to thermal and mechanical loads applied throughout the process.

A variety of methods have been investigated to analyse both the microstructure produced by IFW, and the mechanical properties produced axially across the welded joint. A table summarising the methods used and the materials investigated is presented in Table 2.2.

**Table 2.2:** A summary of microstructure and mechanical property techniques investigated for the IFW process in relevant literature.

<b>Authors</b>	<b>Material(s)</b>	<b>OM</b>	<b>SEM</b>	<b>TEM</b>	<b>Lab. XRD</b>	<b>SXRD</b>	<b>Hardness</b>
Preuss <i>et al.</i> [39]	RR1000		✓	✓		✓	✓
Preuss <i>et al.</i> [40]	RR1000, U720Li IN718					✓	✓
Roder <i>et al.</i> [41]	Incoloy 909 – Inconel 718 dissimilar welds.	✓		✓			✓
Huang <i>et al.</i> [42]	Inconel 718 – U720Li dissimilar welds		✓	✓			✓
Moat <i>et al.</i> [43]	Aermet100 – SCMV dissimilar welds	✓	✓		✓	✓	✓
Taban <i>et al.</i> [44]	Aluminium – steel dissimilar welds		✓	✓			✓
Huang <i>et al.</i> [12]	RR1000 CG, FG and dissimilar CG – FG welds		✓	✓			✓
Senkov <i>et al.</i> [45]	LSHR – Mar M247 dissimilar welds		✓				✓

It can be seen in Table 2.2 that for Inertia Friction Welding, previous ex-situ work investigating the resultant microstructure produced by the process involves mechanical hardness/microhardness testing coupled with some form of imaging technique to correlate the mechanical response to the microstructure variation across the weld joint.

Many publications available in the literature utilise Scanning Electron Microscopy (SEM) and Transmission Electron Microscopy (TEM) to evaluate the resultant microstructure produced by IFW [7, 35, 38, 40]. An investigation into the axial variation in microstructure produced by IFW of RR1000 in the as-welded condition and through three different post-weld heat-treatments (PWHTs) can be found in the work of Preuss *et al.* [39]. SEM and TEM were implemented to characterise sizes of  $\gamma$  grains and  $\gamma'$  precipitates, and this was compared with microhardness tests to correlate the two. The study concluded that the most important features in determining the strength of the weld joint were tertiary  $\gamma'$  volume fraction, work hardening and grain boundary strengthening. Additionally, in the as-welded condition and for one PWHT, the influence of each of these factors was summed to show how these combine to produce the hardness profiles seen in each state. Characterisation of the weld line zone produced by IFW of RR1000 was carried out by Huang *et al.* [12]. This study investigated the effects of the parent grain size on the resultant microstructure. Coarse grain (CG) and fine grain (FG) variants of RR1000 were welded in CG-CG, FG-FG and CG-FG combinations. All welds were also heat treated and cooled in air. It was concluded that irrespective of parent grain size, the weld line microstructure consisted of very fine recrystallised grains with smooth and straight boundaries. Similar work has been performed for dissimilar IFW of superalloys 720Li and Inconel 718 [42]. The morphology of the  $\gamma'$  and  $\gamma''$  (in the case of Inconel 718) were linked to the hardness profiles produced in the as-welded and PWHT states. The interesting conclusion from this work was the larger HAZ on the 720Li specimen, the cause of which was the superior strength of alloy 720Li producing reduced deformation and subjecting the material to higher temperatures for longer durations. The four PWHTs investigated in this study were all found to produce joints of greater strength than the weaker parent material. Dissimilar Nickel superalloy IFWs were also investigated by Senkov *et al.* [45], for welding of solid cylinders of LSHR and Mar-M247. In addition to microhardness and electron microscopy, tensile specimens were extracted from two radial locations in the weld (centre and rim). Tensile testing of these samples showed an increased yield strength and ductility in the samples extracted from the centre of the weld. This was attributed to the clean, defect-free bondline produced in the centre of the bars. On the contrary, tensile specimens extracted from the rim showed limited recrystallisation and plastic deformation and contained agglomerated carbide and

oxide clusters at the weld interface. These interface defects were found to act as crack initiation sites during tensile testing.

Similar processes have been implemented in the analysis of dissimilar steel to Aluminium IFWs by Taban *et al.* [44]. In this study, additional techniques such as X-ray elemental mapping and Energy Dispersive Spectroscopy (EDS) were used to analyse the mixing of material at the contact interface. The hardness profiles showed very little change in each material, with a steep gradient occurring over the weld interface. The weld temperatures of 400 °C were deemed insufficient to change the microstructure of steel, however the lack of HAZ in the Aluminium specimen was surprising. EDS line scans showed steep gradients in element compositions over the weld interface, consistent with the microhardness profiles. An intermetallic layer with an average width of 250 nm was seen at the interface, which through compositional analysis was deemed to be made up of FeAl and Fe<sub>2</sub>Al<sub>5</sub> intermetallics.

Other investigations available in the literature implement a variety of microscopic techniques dependent on the size of the microstructural effects of interest [37, 39]. Roder *et al.* performed optical microscopy and TEM to assess the microstructure of dissimilar superalloy IFW of Incoloy 909 and Inconel 718 [41]. Here, TEM was used to assess the effect of nm-scale  $\delta$  and  $\epsilon''$  phases on the resultant mechanical properties produced by IFW. Three PWHTs were investigated as methods to improve the mechanical response of the welds. However, it was concluded that the PWHT did not improve the ductility or creep response of the Incoloy 909 specimen, which was attributed to the high volume fraction of the  $\epsilon''$  phase on the grain boundaries in the heat affected zone.

SEM was performed on dissimilar IFWs of Aermet100 and SCMV to assess carbide precipitation before and after a PWHT by Moat *et al.* [43]. The size and distribution of the carbide precipitates was analysed to assess the correlation between carbide precipitation and the hardness increase in the Aermet100 workpiece produced by the PWHT. This study also used laboratory and synchrotron X-ray diffraction techniques to measure the volume fractions of retained austenite in the as-welded and PWHT cases for further analysis of the resultant microstructure and mechanical properties.

Synchrotron diffraction techniques have also been investigated for Nickel-based superalloys [35, 36]. The first of these studies used synchrotron diffraction to

characterise the axial variation in  $\gamma'$  volume fraction in the as-welded and PWHT conditions for IFW of RR1000. The phase fraction data was used alongside the SEM and TEM analyses to characterise the relationships between microstructure and mechanical response. The second study compared microstructure and mechanical response in the as-welded condition RR1000, 720Li and Inconel 718 [40]. This study used synchrotron diffraction to quantify the  $\gamma'$  volume fractions in each superalloy and related this to the axial profile produced by microhardness testing. The 25% volume fraction of  $\gamma'$  in Inconel 718 was found to dissolve completely near the weld interface, which reduced the hardness of the joint significantly. On the contrary, alloys 720Li and RR1000 produced harder weld joints, as their increased volume fraction of  $\gamma'$  did not completely dissolve. Additionally, the increased atomic fraction of  $\gamma'$ -forming Al and Ti in these alloys created a stronger driving force for reprecipitation of  $\gamma'$  on cooling of the weld, which strengthened these welds near the interface.

### **2.3.2 Concluding remarks**

Experimental investigations of the IFW process have allowed for a development in the understanding of the process. Analysis of the process parameters have produced a thorough understanding of the sensitivity of the process response to input parameters. Beyond this, experimental analyses have been carried out to assess the influence of process parameters on the behaviour of IFWs of dissimilar materials, and the process efficiency.

Metallurgical and mechanical analysis of as-welded IFWs have facilitated the formation of the understanding of the effects of process parameters of the microstructural response. Further to this, these investigations allow for correlation between microstructure and mechanical response, allowing for analysis of optimum process parameters which provide minimal detriment to material properties.

Whilst the experimental methods utilised to date have allowed for large amounts of developments in the field of IFW, there are limitations to the amount of information which can be gained from ex-situ analyses. Despite the experimental investigations carried out, there is a significant lack of understanding of the physical occurrences which dictate the evolution of the IFW process. Furthermore, it is not known whether the response of the process, in particular the three stages (conditioning, burn-off and

consolidation) are dictated by a combination of thermal and mechanical effects, or whether the evolution of microstructure which occurs during IFW also assists transitions between the weld stages. This limitation in process understanding is believed to restrict more widespread usage of the process.

Currently, new materials require parametric investigation and microstructural analysis prior to comparison with previous generation materials to assist the recommendation of optimal process parameters. With an improved understanding of process evolution, numerical models can be developed and tested for a range of materials and weld parameters, providing a reduction in both time and experimental resources. The aim of the work conducted here is to provide novel experimental data which quantifies the microstructure evolution during IFW. This data will provide a foundation for the development and validation of numerical models which can predict the evolution of this microstructure due to thermal and mechanical influences.

## 2.4 Synchrotron diffraction

X-ray diffraction is a commonly used material characterisation method within the fields of materials science and engineering. In 1912, Max von Laue discovered that passing X-rays through crystal structures produced diffraction patterns [46]. A year later, W. L. and W. H. Bragg expanded on this [47], establishing the relationship which links the X-ray wavelength, incident angle and the spacing between atomic layers in the crystal structures. This fundamental relationship is known as Bragg's Law and is shown in Equation 2.3.

$$n\lambda = 2d\sin(\theta) \quad (\text{Eq. 2.3})$$

where  $n$  is an integer,  $\lambda$  is the X-ray wavelength,  $\theta$  is the incident angle between X-rays and atomic layer, and  $d$  is the spacing of the crystal layers. Over time, Bragg's law has been expanded to progress the information which can be acquired from X-ray diffraction data, allowing for analysis of phase fractions, crystallite sizes and microstrains to be analysed in simple laboratory environments.

The first reported synchrotron experiments were conducted almost 35 years after Bragg's discovery [48], and were at first dismissed, due to the fact that the synchrotron caused the X-ray photons to lose energy. However, over time, synchrotrons have since been recognised to have exceptional properties over conventional X-ray tubes [49].

### 2.4.1 Advantages of synchrotron facilities

To understand the benefits of synchrotron diffraction, the fundamentals of X-ray diffraction must be outlined. As discovered by von Laue and Bragg, when X-rays pass through a crystalline structure, they produce a diffraction pattern, which can be analysed for microstructural characterisation. The diffraction pattern is produced due to constructive interference of waveforms which are in-phase.

The diffraction pattern produced will depend on multiple factors, which are primarily linked to the characteristics of the incident X-rays. The first of these is the photon flux, which is the number of photons passing through the unit of bandwidth per second [50]. The benefit of increased photon flux in an X-ray source is simple, increasing the

number of X-ray photons into the source will increase the number of diffracted X-rays.

The second beam characteristic is the X-ray photon energy, which is inversely proportional to the X-ray wavelength [51]. As a photon collides with an electron, the elastic scattering which occurs reduces the energy of the diffracted X-rays. Generally speaking, a larger photon energy increases the depth of material which an X-ray source can penetrate.

Another variable which must be considered is the X-ray spot size, i.e., the size of the region which the X-ray source can be focussed down to using beam optics [52]. The spot size is also related to any beam divergence, which may be introduced at the photon source or during any beam optics.

These features are often combined into the term brilliance. To understand the term brilliance, it is useful to shift X-rays to the visible light region of the electromagnetic spectrum. Brilliance is the beam brightness per unit area and is increased by increasing the photon flux or reducing the X-ray spot size [53].

In general terms, increasing the X-ray brilliance means there are more photons penetrating the source, leading to an increased number of diffracted photons. Increasing the number of diffracted photons can be useful in many ways. For example, the sample geometry can be increased to allow for a larger gauge volume for acquisition of diffraction data. The beam size may be reduced further to improve the spatial resolution of diffraction measurements, or the acquisition time of diffracted X-rays could be reduced.

The X-rays produced at a synchrotron light source have a flux which is typically 6-8 orders of magnitude larger than those available in laboratory facilities [54]. When this is coupled with the optic capabilities which can reduce the beam spot to less than 1  $\mu\text{m}$ , the brilliance of a synchrotron source is over a billion times larger than that of a laboratory source [55].

Laboratory X-ray facilities often require a vacuum to reduce any losses of X-ray flux due to the atoms present in air. The increased flux available at a synchrotron light source minimises these losses, allowing for diffraction experiments to be recorded in an ambient atmosphere. This in turn reduces the size limitations of the X-ray chamber,

as a vacuum is no longer required. The X-ray chambers at synchrotron light sources are extremely large, allowing for installation of experimental equipment such as engine blocks [56], which provides the facility to conduct in-situ diffraction experiments.

#### **2.4.2 Characterisation of microstructure evolution using in-situ synchrotron radiation**

As X-ray diffraction occurs due to the atomic structure(s) present in a material, the diffraction data acquired can be analysed to characterise the composition of the material on a microstructural level. The peak structure of a diffraction pattern provides information regarding the crystal structure which has been analysed, and the distance between the peaks can be characterised to define the size of the lattice structure. In-situ synchrotron diffraction experiments often aim to characterise the evolution of the microstructure of a material by recording successive diffraction images as a process is performed. The diffraction data can then be analysed to assess how the microstructure evolves during this process. This is the case for a wide range of processes, for which there is a wealth of literature. In this section relevant literature has been analysed to assess the benefits of synchrotron diffraction which make the in-situ diffraction experiments performed in this body of work possible.

Elmer *et al.* observed the  $\alpha \rightarrow \beta$  phase transformation of Ti-6Al-4V in the heat affected zone of gas tungsten arc welds [57]. The experimental set up utilised a 12 keV beam energy with a flux of  $10^{10}$  photons/s, narrowed to a beam spot size of 250  $\mu\text{m}$ . Measurements were taken across the heat affected zone (HAZ) for 6 different sets of welding conditions, in which the heat input per unit weld length varied by a factor of 2. The results obtained were compared with thermal calculations and equilibrium thermodynamics, with the comparison showing that the transformation to  $\beta$ -Ti took an average of 4 s longer to achieve than predicted. This was attributed to the relatively high heating rates which material is subjected to in the HAZ, with non-isothermal heating of 43  $^{\circ}\text{C/s}$  present. The non-isothermal heating required superheating of approximately 154 – 195  $^{\circ}\text{C}$  to fully complete the phase transformation.

This work was expanded to include the phase transformations which occur in the fusion zone (FZ) alongside the HAZ [58]. Analysis of diffraction data acquired from the FZ showed the  $\beta \rightarrow L$  transformation occurring as no crystal structure was seen in the diffraction patterns when complete melting was observed. Again, comparisons between the diffraction data and computational predictions of thermal evolution and equilibrium thermodynamics were carried out. The resultant microstructure showed an increased fraction of martensite in the FZ, which was concluded to be due to the lower temperature at which the transformation began upon cooling in the FZ.

Wong *et al.* implemented a similar experimental set-up to investigate the dynamics of phase transformations in carbon-manganese gas tungsten arc spot welds [59]. An acquisition time of 50 ms was used to show the dynamics of the phase transformation in both the fusion zone (FZ) and HAZ. It was seen that the transformation from parent ferrite to high-temperature austenite in both the FZ and HAZ took twice as long as the reverse transformation on cooling, indicating the cooling rate was higher than the heating rate. The results also showed the occurrence of melting in the FZ, prior to solidification and solid-state phase transformations. Interestingly, at temperatures close to the phase transformation temperature, a contraction in the lattice was seen through the calculation of d-spacing, which was attributed to carbide precipitation or residual stress relaxation. However, it should be noted that these measurements were only taken from the single major peak, as opposed to the full pattern.

Stone *et al.* investigated the temporal evolution of phases during isothermal growth of bainite [60]. The results of this study showed once the austenite  $\rightarrow$  bainite transformation had started, two unique populations of austenite were present in the material. One form of austenite was the same as that of the parent austenite, whilst the other was shown to be a carbon-enriched form of austenite linked to the formation of bainite. Furthermore, the carbon-enriched austenite peaks showed an asymmetry which could not be attributed to any instrumental effects, however, the heterogeneous distribution of carbon present accounted for this peak asymmetry.

An investigation into the feasibility of using Low Transformation Temperature (LTT) alloys to generate compressive residual stresses was conducted by Kromm and Kannengiesser [61]. Here, a synchrotron light source was used in-situ with a simulated weld cycle, in which heating and cooling rates in the region of 500 °C/s were used.

Various LTT filler materials were investigated with varying Nickel content from 8 - 12 %. A 1 mm<sup>2</sup> beam was used with an acquisition rate of 0.125 fps. The results were used to calculate phase transformation temperatures which occurred due to the simulated weld cycles, and it was seen that the cooling conditions did not affect the martensite transformation temperatures. Additionally, it was demonstrated that the start temperature of martensite formation was strongly linked to the alloy content, with increased concentrations of Nickel providing a large reduction in the martensite start temperature.

Kenel *et al.* implemented X-ray diffraction in-situ with laser melting to simulate additive manufacture conditions for Ti-6Al-4V [62]. In these experiments, rapid cyclic heating and cooling was used to approximate the conditions of additive manufacture. A beam area of 9 x 30 µm was used with beam energy was 17.3 keV. The detector acquisition rate was 1 kHz. The spatial and temporal resolution provided by the synchrotron beamline allowed for analysis of the effects influenced by solid and liquid phases. The reversible  $\alpha' \leftrightarrow \beta$  transformation occurred repeatedly during the heating and cooling cycles, with a single  $\alpha'$  phase present after cooling. During cooling of the simulated weld, as the  $\alpha'$  phase formed, a secondary  $\beta$  phase was also seen in the diffraction data, which was attributed to partitioning of Vanadium to the beta phase.

Similarly, in-situ synchrotron diffraction was conducted for the Wire Arc Additive Manufacture (WA-AM) process of stainless steels by Brown *et al.* [63]. Here, a 71keV beam energy with a beam area of 0.2 x 0.2 mm<sup>2</sup> was used with a detector acquisition rate of 0.877 Hz throughout cooling of the AM build. Due to the method of which the build was constructed, the substrate was moved relative to the beam throughout cooling, to analyse both temporal and spatial evolution of phase fractions. A quantitative analysis of ferrite and austenite fractions was produced throughout the cooling; however, the liquid fraction could not be quantitatively analysed as it does not produce a lattice structure

### **2.4.3 Concluding remarks**

Synchrotron diffraction is a materials characterisation methodology which can be tailored to a wide range of requirements. The brilliance of a synchrotron beamline allows for high photon fluxes and beam energies, with focussing optics which can

provide extremely fine spatial resolutions. With the high flux and beam energy, diffraction images can be acquired at extremely high rates, providing highly dynamic data regarding microstructural evolution.

The flexibility of synchrotron diffraction offers itself to in-situ characterisation of IFW. The high acquisition rate is of great benefit considering the short process duration, and the spatial resolution is desirable considering the localisation of the HAZ about the contact interface in the process. The beam flux and energy available at synchrotron facilities is also required, given the high attenuation coefficients of the materials which are welded by IFW, particularly aerospace grade steel alloys and Nickel-based superalloys.

## 2.5 Modelling of IFW

Similar to many joining and manufacturing processes, numerical modelling has been investigated as a means of reducing the experimental cost of IFW. Analytical models have been built, historically as part of the development and understanding of thermal evolution, but recently as a means of having simplistic models which can guide parametric decision in short times.

Further to these, Finite Element Analysis has been developed to represent and predict the thermal and mechanical evolution of weld specimens during IFW. Over time, this has led to the production of numerical models with the ability to accurately predict macro-scale process outputs, and residual stress accumulation due to post-weld cooling and machining. An overview of modelling approaches implemented and the novelty of these models is presented in Table 2.3.

**Table 2.3:** A summary modelling approaches for the IFW process in relevant literature.

<b>Authors</b>	<b>Model Type</b>	<b>Novel Outputs</b>
Wang & Nagappan [64]	Analytical thermal evolution	Thermal response of IFW as functions of position and time
Dave <i>et al.</i> [65]	Analytical thermal evolution	Thermal response of IFW as functions of position and time
Balasubramanian <i>et al.</i> [66]	Finite element model of heat generation and conduction	Thermal predictions of the IFW process
Moal & Massoni [67]	Coupled thermo-mechanical FE simulation	Temperature-dependent material rheology
D'Alvise <i>et al.</i> [68]	Coupled thermo-mechanical FE simulation	Thermal response, weld time and upset predictions
Fu <i>et al.</i> [69]	Coupled thermo-mechanical FE simulation	Thermal response, final weld geometry predictions

**Table 2.3 (cont'd):** A summary modelling approaches for the IFW process in relevant literature.

<b>Authors</b>	<b>Model Type</b>	<b>Novel Outputs</b>
Bennett <i>et al.</i> [70]	Coupled thermo-mechanical FE simulation with elastoplastic material model	Interface contact evolution, sensitivity to process parameters
Wang <i>et al.</i> [35]	Coupled thermo-mechanical FE simulation	Sensitivity of FE simulation outputs to the three weld input parameters
Yang <i>et al.</i> [71]	Analytical thermal and mechanical analysis	Estimate of thermal history and mechanical upset
Bennett <i>et al.</i> [72]	Coupled thermo-mechanical- FE simulations with volumetric expansion of the austenite → martensite transformation	Residual stress predictions and the effect of volumetric phase transformations on these
Bennett <i>et al.</i> [73]	Coupled thermo-mechanical- FE simulations with two-way volumetric phase transformations	Residual stress predictions and the effect of volumetric phase transformations on these
Iracheta <i>et al.</i> [74]	Coupled thermo-mechanical- FE simulations with inclusion of multiple volume-dependent phase transformation models	Residual stress predictions and the effect of the phase transformations modelled on these.

### 2.5.1 Thermal modelling

Wang and Nagappan [64] investigated the transient temperature distribution of AISI 1020 steel during IFW with an analytical model and experimental measurements. The heat input across the contact interface was calculated based on experimental data, in which the heat input  $q$  was a product of the angular deceleration, coefficient of friction ( $\mu$ ), axial pressure ( $P$ ) and radial distance from the centre of the cylinder ( $r$ ), as shown in Equation 2.4.

$$q = \frac{1440 \pi}{778} \mu P r n(t) \quad (\text{Eq. 2.4})$$

where  $n(t)$  is the rotational speed of the spindle workpiece as a function of time  $t$ . A 2D finite difference network was used to solve the heat equation, where heat generated at the interface was conducted in the axial and radial directions, as follows.

$$\frac{\partial^2 T}{\partial r^2} + \frac{1}{r} \frac{\partial T}{\partial r} + \frac{\partial^2 T}{\partial z^2} = \frac{1}{\alpha} \frac{\partial T}{\partial t} \quad (\text{Eq. 2.5})$$

where  $T$  is the temperature,  $r$  and  $z$  are coordinates in the radial and axial directions, respectively, and  $\alpha$  is the thermal diffusivity.

When compared with thermocouple measurements from experimental welds, the model was shown to over-predict the heat input at the weld interface. This was thought to be caused by the experimental equipment, which applied the pressure slowly. It was concluded that use of a hydraulic power unit would apply the pressure faster, bringing the experimental method closer towards the ideal solution and thus reducing the discrepancy in the initial heating rate. The temperature profiles later in the weld showed good agreement between analytical models and experimental data.

Dave *et al.* modified the analytical model produced by Wang and Nagappan to model the thermal response of dissimilar welded stainless steel and niobium [65]. In this study, use of tube geometries with thin wall thickness provided the assumption that there was negligible radial effect on the heat generation across the interface, and so this was ignored. In this approach, the speed curve was fit to an empirical relationship as shown in Equation 2.6, so the heat input could be assumed from Equation 2.7.

$$\omega(t) = \omega_0 \exp \left[ -m \cdot \left( \frac{t}{\tau} \right)^n \right] \quad (\text{Eq. 2.6})$$

$$Q(t) = A_0 \omega(t) \quad (\text{Eq. 2.7})$$

In Equation 2.6,  $\omega(t)$  is the rotational speed as a function of time.  $m$  and  $n$  are constants,  $t$  is the weld time and  $\tau$  is defined as the characteristic time (the time taken for the rotational speed to decay to 10 % of its original value). In Equation 2.7,  $Q(t)$  is the heat input and  $A_0$  is a constant based on the conservation of energy.

Another analytical solution was proposed which was based on the initial flywheel kinetic energy and the energy used to plastically deform material around the interface and form the flash. The remaining energy was used to calculate the heat input at the weld interface. Comparing both models with experimental measurements showed that the approach based on Wang and Nagappan's model was more accurate over longer weld durations. In contrast, the model which accounted for the energy required to form the flash produced better agreement with experimental data in the first 0.15 s of the process.

Finite element modelling was used to investigate the temperature distributions of similar Inconel 718 and dissimilar Inconel 718 to 1045 steel welds by Balasubramanian *et al.* [66]. Here, Fourier's heat conduction equation was used to solve the conduction problem, similar to Equation 6.5. This study used an energy balance method in which flywheel energy throughout the process was converted to a power input, applied to a 1mm region about the weld interface. The power input ( $P$ ) was evaluated using Equation 2.8.

$$P = \frac{dE}{dt} = I\omega \frac{d\omega}{dt} \quad (\text{Eq. 2.8})$$

Where  $I$  is the flywheel inertia. This approach showed good agreement between the experimental and model results at different axial positions in the weld workpieces. However, this modelling approach did not account for deformation of material about the interface and subsequent shortening of the workpieces.

### 2.5.2 Thermo-mechanical modelling

With the advent of finite element analysis, simulations of the IFW process were no longer limited to thermal analyses. The ability to model plastic deformation in FEA brought about an opportunity to develop a modelling process which could accurately represent the mechanical upset which occurs in IFW, thus reducing the requirement for experimental trials.

Coupled thermo-mechanical modelling was desirable for the IFW process given the large amount of heat input in the process, and the requirement for mechanical

deformation to form a weld. The coupling of thermal and mechanical effects was required to simulate the changing material rheology at the range of temperatures which occur in IFW.

The first reported use of FEA to model IFW is presented by Moal and Massoni in 1995 [67]. The authors produced a coupled thermo-mechanical model for simulating IFW of similar materials. A viscoplastic incompressible Norton-Hoff material model was implemented in which the material rheology was temperature dependent. To model the effects of torsion; axial, radial and rotational velocity components were computed at each node. However, an axisymmetric model was used to reduce computational time.

Heat generation was produced by the frictional behaviour at the interface, this was modelled in two stages. At low temperatures, a Coulomb law in which the friction is proportional to the contact pressure was implemented, as shown in Equation 2.9.

$$\tau_f = -\alpha p \frac{\Delta V_s}{|\Delta V_s|} \quad (\text{Eq. 2.9})$$

where  $\tau_f$  is the frictional shear stress,  $\alpha$  is the coefficient of friction,  $p$  is the pressure and  $\Delta V_s$  is the sliding velocity. At higher temperatures, the friction became dependent on the viscous shear flow, as follows.

$$\tau_f = -\alpha p K(T) \frac{\Delta V_s}{|\Delta V_s|} \quad (\text{Eq. 2.10})$$

where  $K(T)$  is thermal-dependent material parameter. Validation of the model against experimental data showed a good match with the rotational velocity curve. The model overpredicted the total upset by approximately 20%, which was caused by a poor definition of the material model.

D'Alvise *et al.* developed a new formulation to solve IFW in FEA [68]. The mechanical equations in this model accounted for inertia, pressure and friction. These were solved by a novel P1+/P1 formulation, which used linear interpolation in velocity and pressure, as opposed to the traditional P2/P0 formulation; however, the results were proven to be more numerically stable. This two-workpiece model was used to predict the outputs of 7 welds with different weld parameters. The FE simulations underestimated the weld duration slightly, and also underestimated the total upset.

However, the numerical model showed the same sensitivity to process parameters when predicting rundown time and total upset. Furthermore, comparison of temperature history with experimental measurements showed a maximum error of 6.6 %. Measurements of the axial and radial dimensions of the flash showed errors of 3.8 % and 1.1 % respectively.

Fu *et al.* [69] used the analytical heat generation model proposed by Wang and Nagappan to model the IFW process in FEA. The temperature, stress and strain response of the model was investigated. Due to the radial sensitivity of the heat flux input, a variation in material properties across the weld interface was seen, which produced an asymmetric flash profile. The temperature distributions produced by the model showed good agreement with the experimental measurements taken with an infrared sensor. The upset and rundown data was not presented.

Bennett *et al.* [70] investigated the effects of thermal expansion at the weld interface during IFW of tubular components. Modelling of thermoelastic effects showed that the initial heat generation causes a reduction in contact area and a non-uniform pressure distribution at the weld interface. The effects of weld pressure and initial rotational velocity on the amount by which the contact area reduced and the time taken for sufficient plastic deformation to recover 90 % of the contact area were investigated. It was found that increasing the weld pressure would reduce the amount by which the contact area reduced, and additionally reduced the time taken to recover 90 % of the contact area. Similarly, increasing the initial rotational velocity also reduced the change in contact area and recovery duration. However, the measured variables were shown to be much more sensitive to pressure than initial rotational speed. It was concluded that the thermoelastic effects are significant and would cause variation in energy input rates and thermal profiles across the weld walls.

A parametric study for IFW of a Nickel-based superalloy was conducted by Wang *et al.* [35]. The influence of rotational velocity, flywheel inertia and pressure on the interface temperature and total upset were investigated. It was shown that by increasing pressure, the heating rate and total upset were increased. Increasing the flywheel inertia was shown to reduce the heating rate and total upset. The total upset was found to be approximately proportional to the square of the rotational speed and logarithmically proportional to weld pressure. The study concluded that a critical

combination of rotational velocity and weld pressure which will produce upset, providing a weldability criterion to produce a successful weld.

In 2013, a simple analytical model was produced by Yang *et al.* [71] to predict the process outputs of IFW of Inconel 718. The model assumed a 1D heat flow in the vicinity of the joint which was calculated from the rundown of experimental welds. The thermal response was coupled with a mechanical model which used Hill's general method to predict the upset. The lambda model was implemented as the constitutive model as it contains a small number of variables. The model was shown to produce a reasonable estimate of upset, and whilst this was not as accurate as FE models when compared with experimental data, the analytical solution can be acquired much faster which is useful for guiding process parameters.

### 2.5.3 Microstructure modelling

With the development of FEA leading to the formulation of models which could accurately represent and predict the macro-scale outputs of IFW, the attention turned to expanding the capabilities of these models. Particular attention was provided to the modelling of phase transformations in steels, and the influence of the volumetric changes which accompanied these phase transformations on the formation of residual stresses during post weld cooling.

Bennett *et al.* investigated the effects of modelling the volumetric expansion of the austenite  $\rightarrow$  martensite transformation upon cooling of the weld on the residual stress formation [72]. Dissimilar welds of Aermet100 to SCMV were modelled here. In this study, both representative and predictive friction behaviour was implemented. The predictive approach was based on that of Moal and Massoni [67], in which a two stage, temperature dependent friction law was implemented. The representative friction coefficient ( $\mu(t)$ ) was calculated from experimental weld data, as shown in Equation 2.11.

$$\mu(t) = \eta \frac{(E^{n+1} - E^n)}{-\omega \Delta t P \left( \frac{2\pi}{3} [r_o^3 - r_i^3] \right)} \quad (\text{Eq. 2.11})$$

Where  $\eta$  is the process efficiency, defined as a constant.  $E$  is the energy available for welding in two time points,  $n$  and  $n + 1$ , which are separated by a time step  $\Delta t$ .  $\omega$  is the

rotational velocity at time  $t$ ,  $P$  is the weld pressure.  $r_o$  and  $r_i$  are the outer and inner radii of the weld specimen, respectively. The phase fraction of Martensite present due to cooling was calculated using a modified Magee equation, as shown in Equation 2.12.

$$\xi_M = 1 - \exp(\psi_1 T + \psi_4) \quad (\text{Eq. 2.12})$$

Where  $\xi_M$  is the phase fraction of Martensite.  $\psi_1$  and  $\psi_4$  are constants which describe the phase transformations defined from experimental data using a least-squares fit. It was observed that inclusion of the volumetric expansion due to the formation of Martensite reduced the residual stress formation in the FEA prediction by approximately 40 %, when compared with the evaluation of residual stresses without inclusion of the phase transformation.

This work was extended to include the volumetric reduction produced by the martensite  $\rightarrow$  austenite phase transformation during heating of the weld, alongside the reverse transformation upon cooling [73]. The residual stresses were compared with experimental measurements. The magnitudes of residual stresses and the trends of these produced by the FEA model were in good agreement with the experimental data.

Iracheta *et al.* performed a sensitivity study of the residual stresses to the parameters modelled in FEA [74]. Within this study, the variation of residual stress predictions was assessed using four different material models. The first model included the definition of parent martensite in the SCM material at low temperatures. The second material model included the reversible transformation of tempered martensite  $\leftrightarrow$  austenite, however both phases did not have temperature-dependent material properties. The third material model included this same transformation; however, the temperature-dependent material properties of the austenite phase were included. The final material definition contained three phases in which the transformations were irreversible, as follows: tempered martensite (parent)  $\rightarrow$  austenite  $\rightarrow$  quenched martensite. It was concluded that the three-phase model offered little benefit over the reversible transformation represented in the two-phase model, and so the two-phase model produced a simplified approach to representing the transformation strains which occur during IFW of steel components.

#### 2.5.4 Concluding remarks

Modelling of the Inertia Friction Welding process has seen significant development, particularly in the last 20 years, which has seen expansion from limited thermal analysis to fully coupled thermo-mechanical-microstructure models. Finite Element models have been produced with the capability of accurately modelling the thermal response, which is highly coupled to the mechanical response, alongside the rundown and upset process behaviour, given a suitable material definition.

Recent work has expanded the capability of these numerical solutions to incorporate the effects of phase transformations, which shows that the microstructure evolution can be modelled in these approaches. However, the microstructure modelling coupled to these simulations is currently limited to the application of steels, as the phase transformations which occur in these materials are present amongst a discrete transformation temperature range. This cannot be applied to Nickel-based superalloys as the dissolution of  $\gamma'$  is a diffusion-based transformation, and therefore is dependent not only on temperature, but the rate of temperature change. Additionally, the range of precipitate sizes present in turbine disc superalloys present another difficulty, as the different precipitate sizes will dissolve under different thermal conditions. Therefore, the evolution of a Nickel-based superalloy microstructure during IFW must utilise some other form of numerical model to provide an accurate result.

## 2.6 Techniques for modelling microstructure evolution

There are a range of numerical approaches which have been investigated in the field of modelling microstructure evolution. These models are mostly implemented in the areas of recrystallisation and solidification microstructures. The most-commonly accepted modelling approaches; phase-field, Monte-Carlo and Cellular Automata are reviewed and their limitations assessed with respect to the application of modelling solid-state diffusion-based phase transformations.

### 2.6.1 Overview of numerical modelling approaches

One commonly implemented numerical modelling approach to calculate the evolution of microstructures is the phase-field methodology. This formulation solves the equations relevant at the interface between phases. The interfacial boundary condition is replaced by a partial derivative which is solved to approximate the interface physics.

Phase-field modelling is most commonly implemented in the modelling of solidification microstructures [71, 72]. In these approaches, phase-field variables are used in conjunction with material definitions which describe the state of the material with respect to position and time. The phase-field variables allow for the solution of diffusion equations without the requirement of interface tracking. Phase-field modelling has been less intensively explored for the modelling of recrystallisation, but there are some investigations which have been performed [77].

Singer-Loginova *et al.* [78] conducted a thorough review of the applications of the phase-field process; including solidification microstructures, grain boundary analysis, and solid-state phase transformations. The phase-field modelling approach was found to be limited in many areas, such as modelling multicomponent systems, as multiple phase-fields would be required for modelling each constituent element. Recent attempts at modelling multicomponent systems using phase-field modelling had relied heavily on approximations or thorough linking with thermodynamic software, which is computationally expensive. Additionally, phase-field models for solidification microstructures, which are highly dependent on diffusion, were difficult to replicate when the thermal gradients modelled was large. Whilst the process is very flexible,

the solution is relatively simple, and does not provide the level of accuracy required for this investigation.

Sieradzki *et al.* [79] conducted a comparison of Monte-Carlo (MC) and Cellular Automata (CA) modelling for static recrystallisation of steels. The MC approach utilises a discrete lattice of cells, which store state variables which are randomly assigned to give the correct global average. For modelling of recrystallisation, each cell has an associated energy which depends on the number of different grains present in the local neighbourhood. At the start of a step, a cell is randomly chosen and its state is changed to match that of one of its neighbours. Then, the energy is recalculated for this cell to assess whether a reduction in energy has occurred. If the energy in the cell has reduced, the change is accepted, otherwise, it is returned to its original state. Therefore, it can be said that the MC model works in a trial-and-error manner, such that the model will randomly select cells and perform the same computation until the defining criteria is met. This defines the Monte-Carlo step (the number of iterations required to meet the condition) and thus there is no binding to physical time in this model. The basic rule of the model is to minimise energy, and to do so, arbitrary units are used. On the contrary, the CA model was defined by parameters which have physical units, and so the dislocation density, temperature and stored energy values have a physical definition, which could be compared with an experimental process. Additionally, the CA model was bound to real time units.

CA models are algorithms which are used to describe how a system evolves by applying a set of global and local transformation rules to matrix cells. They consist of a discrete lattice of cells, which have a defined cell size and store a set of state variables. The response of the system is evaluated between timesteps  $t$  and  $t + \Delta t$ , which varies due to the change in global inputs (for example, temperature/strain), and the variation in state variables between the cell of interest and its neighbouring cells.

Whilst both models produced reasonable results, it was concluded that the MC model was limited as it was based on arbitrary units. Whilst the results could be approximated by MC, it required additional data analysis and would still be limited to the estimation of the recrystallisation process, as the input parameters had no physical meaning. As the CA model was built from analytical equations, it was deemed that this was the more powerful numerical tool.

MC modelling has also been investigated for solidification microstructures [76, 77]. In these cases, the solidification and resultant grain structure produced showed good agreement with experimental data. However, it is observed that only one set of process parameters are investigated. It can be questioned whether variation of input parameters would produce an equally accurate result, or whether the limitation of the model to not represent real time would then present issues in the feasibility of the modelling approach. The fact that the MC approach cannot represent time means that it cannot be used for the case of diffusion-based transformations, as the diffusion of elements is based on the time permitted for the diffusive process to occur.

CA has also been used extensively to model solidification microstructures. Zhan *et al.* [82] modelled the simulation of grain growth during solidification using the cellular automata approach. The CA model used implemented analytical equations for the nucleation of solid due to undercooling, and grain growth (via the solidification front velocity) due to the cell size and concentration gradient. The model was found to be able to reproduce the formation of dendritic structures at various angles due to the implementation of a limited angles method, and additionally had no orientation preference based on the CA lattice. The solidification was modelled using a single grain and multiple grains, to represent the ability of the model to represent competition between solidification fronts.

There is a wealth of literature available in which CA has been implemented to monitor different forms of microstructure evolution [79-81]. The common theme in the success of these models is the coupling of the state variables to constitutive equations which provide the correct definition of physics. The storage of all state variables allows for these to be correctly defined, and so they are not approximated or recorded from a position- or time-based function. Furthermore, the neighbourhood effects in CA can be varied, to model local or far-field effects, as shown in Figure 2.8 and 2.9 [86].

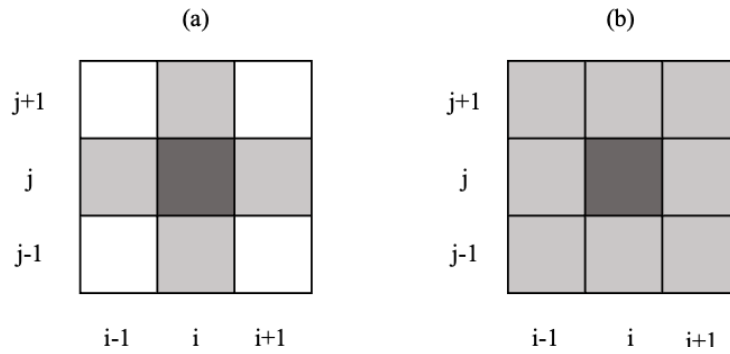


**Figure 2.8:** Classical 2D CA neighbourhoods with a 1 cell radius: (a) von Neumann; (b) Moore [86].

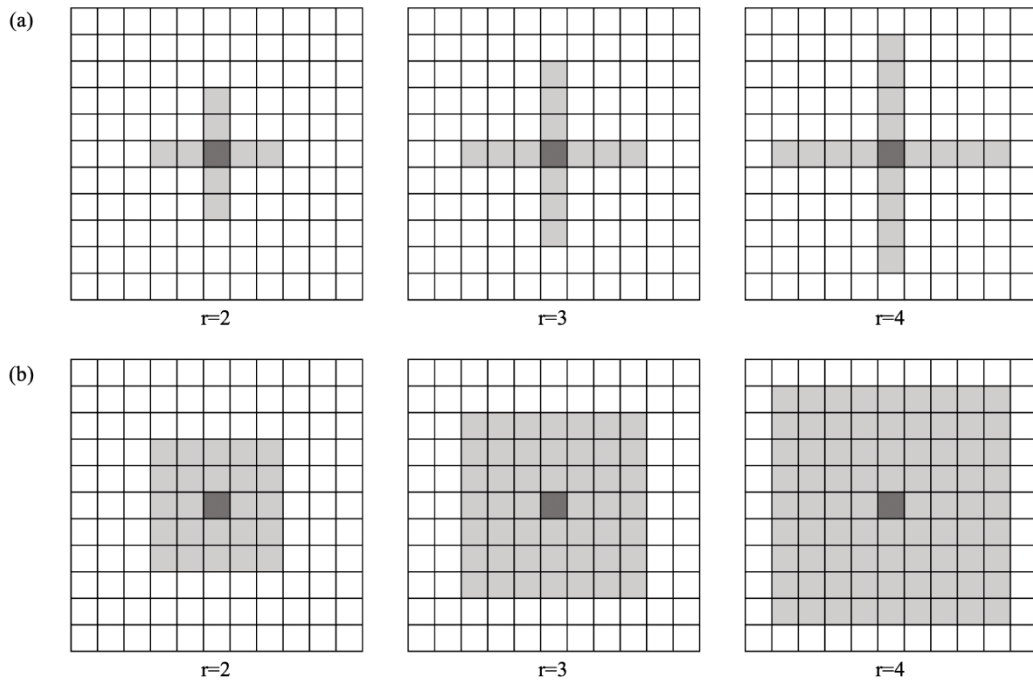


**Figure 2.9:** Classical 2D CA neighbourhoods with a various cell radii: (a) von Neumann; (b) Moore [86].

### 2.6.2 Concluding remarks

There are a variety of numerical modelling approaches which have been implemented to predict the evolution of microstructure in a variety of processes. Phase-field, Monte-Carlo and Cellular Automata are the modelling approaches most accepted for

microstructure evolution mapping. Each of the three modelling approaches offer benefits to the modelling of atomic diffusion and phase transformations due to thermal histories, however the phase-field and Monte-Carlo approaches both present possible drawbacks which may limit the accuracy of the desired analysis.

Phase-field models have been shown to be computationally expensive for the modelling of multi-component systems like RR1000, as a different phase-field is required for each component. Monte-Carlo simulations appear to produce representative microstructures which agree well with experimental analysis; however, they are limited by the fact they are not physically linked to time. This causes issues when modelling of diffusive processes due to the requirement for time to be modelled to resolve the amount of diffusion of respective species.

Cellular Automata appears to provide a sturdy foundation for modelling of diffusion-based phase transformations. An unlimited number of state variables can be evaluated, and the evolution of these can be linked to the defining constitutive physics. Additionally, the reliance on local neighbourhood effects to monitor the evolution of a cell lends itself well to diffusive phase transformations, as features such as concentration gradients which act as diffusion driving forces can be evaluated using local neighbourhoods. Hence, Cellular Automata has been selected as the numerical modelling approach which will be investigated in this work.

## 2.7 Knowledge gaps

For the Inertia Friction Welding process, there is large knowledge gap regarding the incomplete understanding of microstructure evolution. A range of experimental approaches have been implemented to characterise the post-weld microstructure and mechanical properties; however, these are limited by the fact they must be performed *ex-situ*. The nature of deformation in IFW causes the historical evidence of microstructure evolution to be ejected from the contact interface during upsetting. Hence, the resultant microstructure which is characterised only presents evidence of the process behaviour in the end stage of the weld.

There is a clear trend in how Inertia Friction Welds evolve on the macroscale. For any material, the process exhibits discrete conditioning, burn-off and consolidation phases. The unanswered question in this field surrounds the driving forces for transitions between these phases. It would be simple to assume that these are driven by macro-scale process behaviour, given the fact that all materials show these stages. However, it is known that the strength of a material is controlled by its microstructure, and so it is also feasible to suggest that the microstructure controls these regions.

There is evidence in the current understanding of the process sensitivity to input parameters which logically link to the evolution of IFW to microstructural effects. As an example, it is known that increasing weld pressure will cause a shorter conditioning phase. Considering the effects of increased pressure on the process, there is an increased mechanical load and interface friction coefficient, leading to larger a larger amount of heat generation. These physics can be correlated, somewhat simplistically, to the microstructure evolution. Larger thermal and mechanical loads provide greater driving forces for microstructure evolution, be it in the form of phase transformations or grain refinement processes such as recrystallisation. These changes in the microstructure would reduce the strength of the weld, permitting the onset of burn-off in a shorter time, hence reducing conditioning time. However, the physical changes which the microstructure undergo during the process have not been measured and cannot be measured using conventional *ex-situ* analysis techniques.

Numerical models are becoming increasingly popular and more widely used across a range of fields. Finite Element Analysis has been developed for the IFW process and models are available which can accurately predict process outputs and post-weld

effects such as residual stress formation. FEA has been investigated as a means of evaluating the microstructure evolution, and this has been implemented for more simple phase transformations such as the martensite  $\rightarrow$  austenite transformation in high-strength steels.

The limitations of FEA to predict microstructure evolution are dependent on the materials which the IFW process is used for. Precipitate-strengthened Nickel-based superalloys such as RR1000 are some of the most used materials in IFW. The microstructure evolution of these alloys is complex as the dissolution of the  $\gamma'$  precipitates is diffusion-dependent. Hence, the transformation cannot be simply defined as a function of time. Factors such as temperature, thermal history and diffusive time must be accounted for in the modelling of  $\gamma'$  dissolution. Thus, to accurately evaluate this in a process such as IFW, numerical models which expand beyond the current capabilities of FEA are required.

## **Chapter 3**

### **Research Methodology**

#### **3.1 Background**

In this chapter, the research methods utilised in this body of work are introduced. Firstly, the experimental methods are presented, detailing the methodology of the in-situ synchrotron diffraction experiments conducted at Diamond Light Source. Alongside this, details of the materials investigated and supplementary experimental procedures such as sample preparation and Scanning Electron Microscopy (SEM) are outlined. Following this, the numerical modelling approaches used in this study are explained in detail. Firstly, the details of the Finite Element Analysis (FEA) models are provided, outlining the model set-up, material data and boundary conditions. Secondly, the details of the Cellular Automata (CA) modelling approach are outlined.

## 3.2 Experimental methods

The experimental approaches used in this study primarily utilise the in-situ X-ray diffraction experiments performed. However, some supplementary experiments and analyses have been carried out to support and reinforce the results provided by the synchrotron diffraction experiments, and so these are explained here also.

### 3.2.1 Materials

Whilst the primary focus of this body of work was the microstructure evolution of the Nickel-based superalloy RR1000, the microstructure of this alloy is extremely complex, consisting of a tri-modal distribution of  $\gamma'$  precipitates in a crystalline  $\gamma$  matrix. Subsequently, the X-ray diffraction patterns produced by this material are highly convoluted, making analysis of phase fractions and phase transformations extremely difficult. To facilitate understanding of the experimental methodology and data analysis techniques, BS1407 steel was also investigated in the in-situ diffraction experiments due to its simpler microstructure and more clear phase transformations. The composition of this material was measured by spark emission testing and is presented alongside the typical analysis in Table 3.1.

**Table 3.1:** Elemental composition of BS1407 steel.

Element	Fe	C	Cr	Mn	Si	Other
Spark emission testing (%)	97.500	1.2	0.413	0.350	0.220	0.307
BS1407 Typical composition (%) [87]	Bal.	0.95 – 1.25	0.35 – 0.45	0.25 – 0.45	< 0.40	<0.09

BS1407 is a tool steel which consists of a body-centred-cubic (BCC) ferrite phase at ambient temperatures and a face-centred-cubic (FCC) austenite phase at elevated temperatures. Due to the nature of X-ray diffraction, the two different lattice structures

produced by BS1407 at different temperatures permit different peak reflections, and so the phase transformation which occurs is extremely clear. The Thermo-Calc software [88] has been used to calculate the equilibrium transformation temperature range for the ferrite to austenite transformation for this composition, which was predicted to occur between 725 °C and 734 °C.

The Nickel-based superalloy RR1000 has also been investigated as part of the experimental methodology. For this material, a range of weld input parameters have been investigated to analyse the sensitivity of microstructure evolution to the weld parameters. The composition of RR1000 is presented in Table 3.2.

**Table 3.2:** Chemical composition of the RR1000 Nickel-based superalloy [15].

Element	Ni	Cr	Co	Mo	Al	Ti	Ta	Hf	Zr	C	B
Wt. %	Bal	13.5	14	3.8	2.5	3.4	0.0	0.0	0.055	0.035	0.01
		-	-	-	-	-	-	-	-	-	-
		17	20	5.5	4.0	5.0	3.0	0.4	0.075	0.07	0.04

In Table 3.3 the features of the parent microstructure of RR1000 are presented, showing the  $\gamma'$  volume fraction, comprising of primary, secondary and tertiary  $\gamma'$ . The values for primary and secondary  $\gamma'$  have been acquired from Scanning Electron Microscopy (SEM). As the tertiary  $\gamma'$  precipitates are extremely small in size, they cannot be resolved under SEM. To evaluate the tertiary  $\gamma'$  volume fraction, the difference between total  $\gamma'$  volume fraction evaluated from X-ray diffraction and sum of primary and secondary precipitates observed under SEM have been compared. The uncertainties in Table 3.4 are evaluated from standard deviation between different SEM or XRD images used to characterise the parent microstructure.

**Table 3.3:** Characteristics of the parent microstructure of RR1000 Nickel-based superalloy used in the experimental methodology.

$\gamma'$ precipitate size	Volume fraction (%)	Uncertainty (%)
Primary (SEM)	9.49	$\pm 0.90$
Secondary (SEM)	28.80	$\pm 2.18$
Tertiary (Calculated)	9.23	$\pm 5.48$
TOTAL (XRD)	47.43	$\pm 2.49$

### 3.2.2 Weld specimens

Two weld specimen geometries have been utilised in the experimental methodology which account for the two classes of materials used, BS1407 steel and RR1000. Firstly, the specimen geometry used for welding of BS1407 steels was produced from a rod of 16 mm diameter. The rod was parted to a length of 22 mm using a lathe, before a drill hole of 12 mm diameter was produced with a depth of 4 mm at full drill diameter. A final facing operation was performed on both ends of the sample, to ensure the seated surface and the weld face were parallel; this provided a final length of 20 mm. This specimen geometry is shown in Figure 3.1.

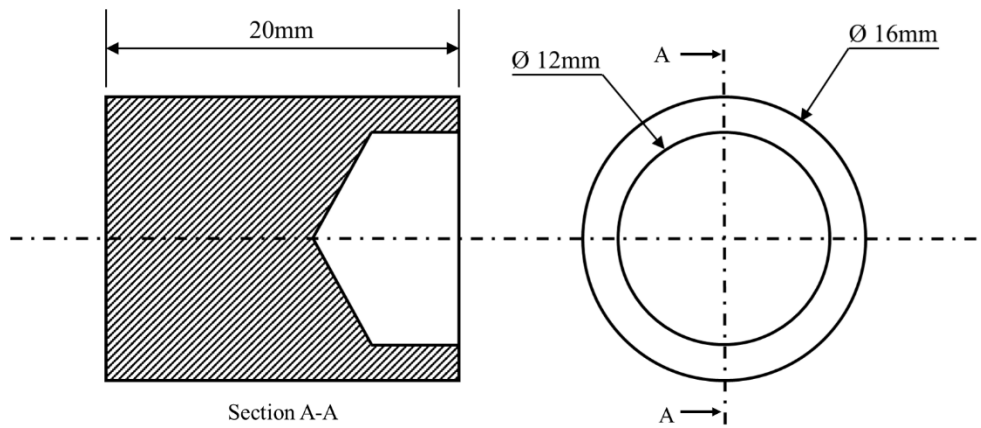


**Figure 3.1:** Specimen geometry for IFW of BS1407 steel.

In comparison to BS1407 steel, RR1000 attributes significantly greater strength at elevated temperatures. Due to this, the superalloy is more difficult to weld via IFW, often requiring larger specific energy and weld pressure to form a successful joint.

Additionally, Nickel-based superalloys exhibit a larger absorption coefficient for X-rays than tool steels. This means for an identical gauge volume, RR1000 permits diffraction of fewer X-rays. Due to these factors, the specimen geometry was reduced to provide a smaller contact area (allowing for increased specific energy and weld pressure) and a shorter gauge length for the intersection of the X-ray beam line.

The RR1000 weld specimens were manufactured from ‘blanks’ produced by Hot Isostatic Pressing (HIP) which have been provided by Rolls-Royce. These specimens were turned down to 16 mm diameter bar using a lathe and carbide workpiece. A weld nose feature of 10 mm OD, 8mm ID and 4mm axial length was produced by lathe. A final facing operation was carried out on both ends of the specimen. The geometry of the IFW specimens for Nickel-based superalloys is presented in Figure 3.2.

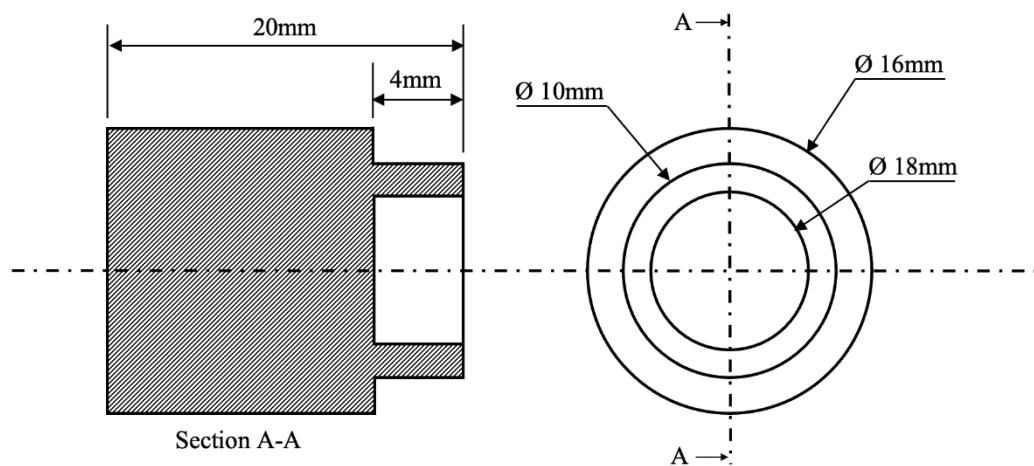


**Figure 3.2:** Specimen geometry for IFW of Nickel-based superalloy RR1000.

### 3.2.3 Inertia friction welding machine

Despite the high flux and beam energy available at synchrotron facilities, conventional weld specimen geometries are too large for X-rays to penetrate. Conducting the novel in-situ X-ray diffraction experiments required a method of performing inertia friction welding with a sufficiently small sample geometry to allow for penetration of X-rays from the synchrotron source. A bespoke, small-scale IFW machine was produced in

order to perform welds at the scale required. This machine was designed by an undergraduate project group. A schematic of the machine is presented in Figure 3.3.

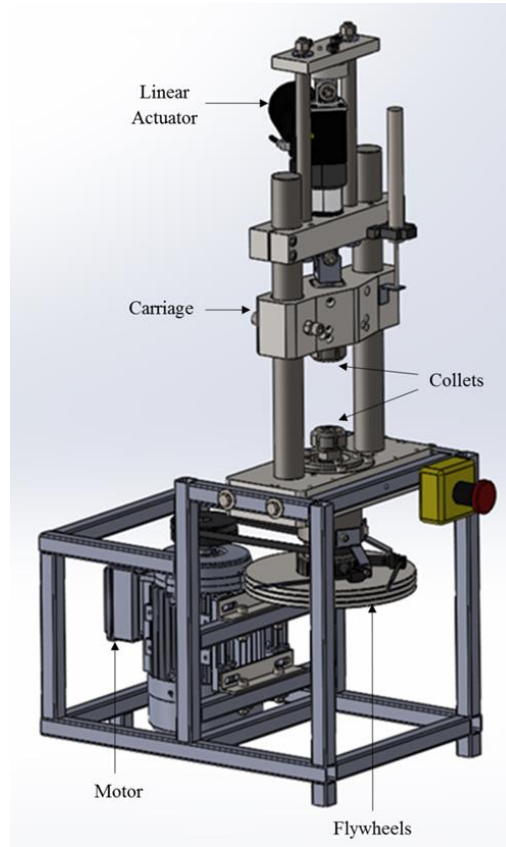


**Figure 3.3:** Annotated CAD render of the IFW apparatus produced to conduct the in-situ synchrotron diffraction experiments.

The weld specimens were held in collets throughout the process. The collet nuts were tightened to a torque of 84 Nm, which exceeded the specification to ensure no axial or rotational slipping of the specimens occurred during welding. In the spindle assembly, the collet nut was threaded onto a shaft on which up to three flywheels, each providing  $0.0176 \text{ kg}\cdot\text{m}^2$  inertia, could be mounted. A three-phase motor was used to drive the shaft, providing a rotational speed of up to 4140 rpm. The combination of rotational speed and flywheel inertia produced a maximum of 4950 J of weld input energy. In the fixture assembly, the collet was fitted to a carriage which was free to move axially upon two tie bars. A linear actuator was mounted to the rear of the carriage, applying

an axial load of up to 4000 N. The conversions of these parameters to specific energy and pressure for the two weld specimen geometries are provided in Table 3.4.

**Table 3.4:** Conversion of maximum absolute weld input parameters to maximum specific parameters for the two specimen geometries used in the experiments.

<b>Specimen Geometry</b>	<b>Absolute Energy (J)</b>	<b>Specific Energy (MJ/m<sup>2</sup>)</b>	<b>Axial Load (N)</b>	<b>Weld pressure (MPa)</b>
BS1407 specimen	4950	56.27	4000	45.47
RR1000 superalloy specimen	4950	143.24	4000	115.75

To measure process inputs and outputs, such as axial load, rotational velocity and upset throughout the process, a set of sensors were attached to the IFW apparatus. The signals recorded by the sensors were processed by a National Instruments CompactDAQ and recorded via LabView software. The LabView interface also provided external control of the IFW device from the control hutch at the beamline. Data was recorded at 10 kHz for optimal resolution during welds which occurred over short time scales. The data was stored in the form of Time-Voltage arrays, and the voltage data was post-processed via MATLAB in accordance with the respective conversion values for each sensor.

The rotational velocity rundown was measured using an RLS GTS35 gear tooth sensor [89]. A gear wheel was mounted onto the spindle shaft assembly, and the sensor produced a voltage pulse when a gear tooth passed the sensor. This produced a square wave signal, the frequency of which was converted to a rotational velocity. A TE FC23 load cell [90] was fitted to the rear of the linear actuator. This sensor is a strain gauge, which was compressed when the actuator was engaged. Upset measurements were recorded using an LVDT. The LVDT was fixed to the linear actuator mount, and the ball tip rested on the carriage, providing a position of the carriage and fixture specimen throughout the process. A pre-weld pressure test was performed to find the position of

the weld interface, which provided a position of zero upset, and the change in position from this point was recorded as upset.

As part of the post-processing of the IFW machine outputs, the processed outputs were filtered using a 3<sup>rd</sup> order Butterworth filter with a cutoff frequency of 10 Hz. These filter parameters were tested and proven to remove high-frequency noise from the signals without impacting the magnitude of the outputs. Additionally, the filter was proven to cause no phase shift, ensuring that the outputs measured were correctly synchronised with the time counter.

To synchronise the weld data with the diffraction data recorded, a voltage pulse was produced by the diffraction sensor with each image captured. This voltage pulse was recorded by the IFW machine alongside the process outputs. The pulses were then aligned with the weld data acquisition to define the time at which each image was recorded. This was of great use when evaluating diffraction images of interest during the weld process.

#### **3.2.4 In-situ synchrotron X-ray diffraction of IFW**

The in-situ synchrotron diffraction experiments were conducted at Experimental Hutch 1 of Beamline I12 at Diamond Light Source, Oxford, UK. The IFW apparatus was mounted onto the beamline sample stage, which allowed for translation in the x, y and z directions. The translational motion of the sample stage was used to align the weld specimens with the synchrotron beam, and subsequently apply any required offset to this.

A Dectris Pilatus3 X CdTe 2M detector was used for the acquisition of Debye-Scherrer diffraction rings. This detector had a resolution of 1475 x 1679 pixels, with a pixel size of 172  $\mu\text{m}^2$ . This provided an extremely high resolution resulting in sharp diffraction peaks for further processing and analysis. The maximum acquisition rate of this detector was 250fps. The sample-to-detector distance used throughout these experiments was 880 mm. In this study, two acquisition rates were used. For BS1407 steel welds, an acquisition rate of 100 fps was used to facilitate acquisition of complete Debye-Scherrer diffraction rings to be recorded for the material, X-ray beam energy and penetration depth. For the superalloy RR1000, the acquisition rate was set to

150fps. This increased acquisition rate aimed to capture highly dynamic events which occurred in the microstructure evolution.

At the specimen geometry used to conduct these experiments, it was expected that axial gradients in temperature and strain during the process would be extremely high, with deformation localised over a very narrow region about the contact interface. Therefore, to capture the microstructure evolution, and the axial gradient in this, a  $100\ \mu\text{m} \times 100\ \mu\text{m}$  monochromatic X-ray beam with 89 keV energy was used. The X-ray beam intersected a chord of the weld specimen, which minimised path length and prevented absorption of X-rays. However, it was ensured that the X-ray beam intersected the centre of the specimen wall thickness, where temperatures and strains were expected to be largest at the contact interface. A schematic of this set-up is presented in Figure 3.4.

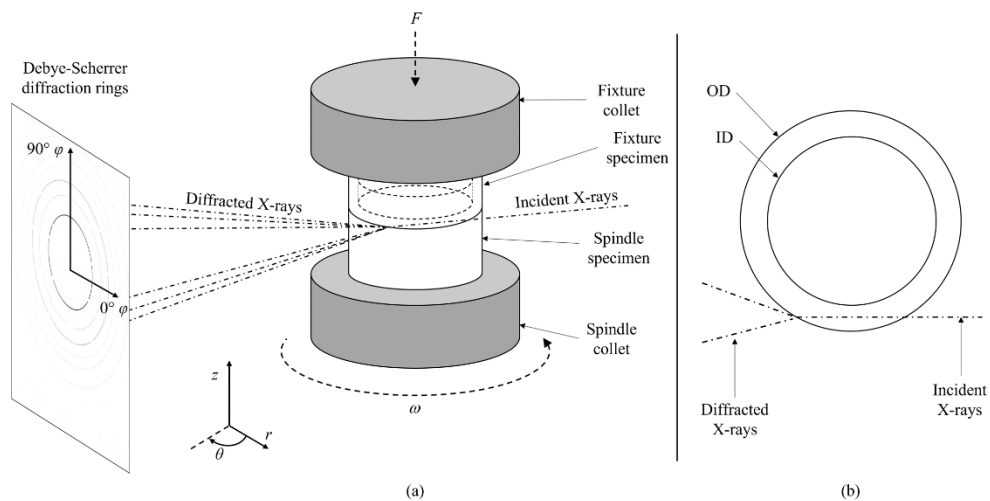


**Figure 3.4:** Schematic of the IFW setup at Diamond Light Source; (a) overview of the experimental methodology showing the relationship between weld system and diffraction rings; (b) plan view of the weld specimens to show the X-ray path in detail.

A characteristic of the IFW process is the axial shortening of specimens as they bond during the weld. As the axial load is applied from a single specimen, the contact interface moves axially as the specimens shorten. Prior testing and parametric investigation indicated a total upset value of approximately one order of magnitude larger than the X-ray beam height, and so diffraction patterns at a single axial point could not be recorded throughout the process with a stationary X-ray beam.

To allow for quantification of the microstructure at a single axial position (for example, the contact interface) throughout the process, several welds were performed with identical process parameters. For each weld, the axial position of the synchrotron beam was varied with respect to the initial contact interface, as shown in Figure 3.5. The axial distance between the initial contact interface and the centre of the synchrotron beam is denoted  $z_0$ .

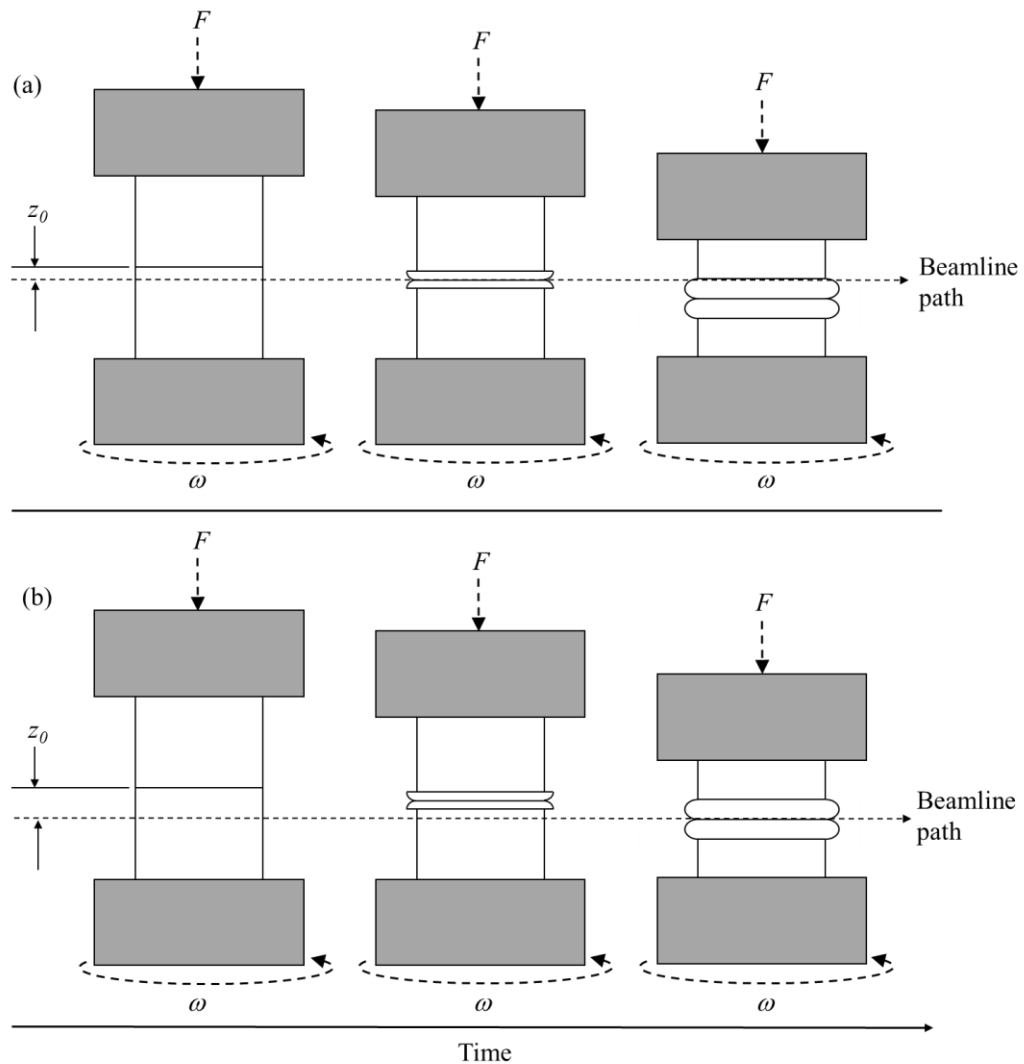


**Figure 3.5:** Schematic of the axial offset distance between the initial weld interface and synchrotron beam. The offset allowed for diffraction data to be gathered from the weld interface at various time points during the weld; (a) a small axial offset caused intersection of the weld interface and synchrotron beam at the beginning of the weld; (b) a larger axial offset required more deformation of the weld specimens to move the contact interface into the stationary beam, and so intersection between the weld interface and synchrotron beam did not occur until the end of the weld.

Using the contact interface as the point of interest, varying the value of  $z_0$  provided alignment of the centre of the X-ray beam and the contact interface at different points in time during the weld. Increasing the value of  $z_0$  caused the intersection of the contact interface and synchrotron beam to occur later in the process.

To provide quantitative diffraction data analysis, it was important to understand the position of the weld interface relative to the stationary X-ray beam throughout the process. To calculate the position of the weld interface throughout IFW, it was assumed that both specimens deform symmetrically about the weld interface. Thus, the axial distance of the weld interface relative to the centre of the beam area can be determined using Equation 3.1.

$$z(t) = z_0 - \frac{u(t)}{2} \quad (\text{Eq. 3.1})$$

where  $z(t)$  is the position of the weld interface relative to the centre of the synchrotron beam area.  $z_0$  is the relative X-ray beam offset from the initial weld interface and  $u(t)$  is the weld upset. When  $z(t)$  was positive, the weld interface is positioned above the synchrotron beam centre, and negative values indicate that the weld interface was below the synchrotron beam. This relationship allowed the axial position of the beamline relative to the contact interface to be tracked throughout the process.

### 3.2.5 Weld input parameters

Due to the variation in material properties between BS1407 and the four Nickel-based superalloys investigated in the experimental procedure, the IFW input parameters were varied to ensure complete bonding at the interface. One set of weld parameters (S1) was used for the BS1407 welds, and these are presented in Table 3.5. For weld parameter set S1, five individual axial offset values ( $z_0$ ) were used. These are presented in Table 3.6.

**Table 3.5:** IFW input parameters for BS1407 welds.

<b>Parameter Set</b>	<b>Rotational Velocity (rpm)</b>	<b>Flywheel Inertia (kg.m<sup>2</sup>)</b>	<b>Specific Energy (MJ/m<sup>2</sup>)</b>	<b>Axial Load (N)</b>	<b>Axial Pressure (MPa)</b>
S1	4000	0.0344	34.31	4000	45.47

**Table 3.6:** The five axial offset distances between the centre of the synchrotron beam and initial weld interface for BS1407 welds.

<b>Position Name</b>	<b>Axial offset from initial weld interface, <math>z_o</math> (mm)</b>
P1	0.05
P2	0.1
P3	0.15
P4	0.375
P5	0.6

As the microstructure evolution of Nickel-based superalloys are the primary focus of this work, four sets of input parameters were investigated to assess the sensitivity of the microstructure evolution to the weld input parameters. A combination of two initial rotational speed values and two axial load values were used to produce the four input parameter sets. These parameter sets are denoted N1 – N4, and commonly referred to by the combination of speed and pressure used when comparing the variation in microstructure evolution due to the different weld parameters. The weld input parameters for RR1000 are presented in Table 3.7.

**Table 3.7:** IFW input parameters for Nickel-based superalloy welds.

<b>Parameter Set</b>	<b>Rotational Velocity (rpm)</b>	<b>Flywheel Inertia (kg.m<sup>2</sup>)</b>	<b>Specific Energy (MJ/m<sup>2</sup>)</b>	<b>Axial Load (N)</b>	<b>Axial Pressure (MPa)</b>
N1 (LS, HP)	2800	0.0344	42.79	3000	106.1
N2 (LS, LP)	2800	0.0344	42.79	1300	45.98
N3 (HS, LP)	4000	0.0344	87.33	1300	45.98
N4 (HS, HP)	4000	0.0344	87.33	3000	106.1

For each parameter set, the RR1000 welds produced different sets of process outputs, rundown and upset. Due to this, the axial offset positions used were varied for each parameter set with the aim of providing a good representation of the axial profile of microstructure throughout the process. The axial offset values used for the RR1000 welds at four different input parameter sets are presented in Table 3.8. It should be noted here that while it was desired that four welds of each input parameter set were completed to produce a clear response in the axial evolution of the microstructure, only three welds could be performed for parameter set N4. This was due to the limited number of specimens available. Whilst ‘spare’ samples were prepared for the experiments, unforeseen beamline errors and failures caused these to be used up prior to performing welds of parameter set N4.

**Table 3.8:** The axial offset positions between initial contact interface and X-ray beam centre for the Nickel-based superalloy IFWs.

<b>Axial offset name</b>	<b>N1 Offset (mm)</b>	<b>N2 Offset (mm)</b>	<b>N3 Offset (mm)</b>	<b>N4 Offset (mm)</b>
P1	0.05	0.05	0.05	0.05
P2	0.20	0.15	0.15	0.75
P3	0.55	0.40	0.30	1.65
P4	0.85	0.45	0.50	-

### 3.2.6 Microscopic examination of post-weld microstructure

In addition to the in-situ diffraction measurements, a set of X-ray diffraction (XRD) measurements were taken in the post-weld state for Nickel-based superalloy IFWs. For each material and parameter set, 20 post-weld measurements were recorded at axial increments of 100  $\mu\text{m}$  across the weld interface. These measurements allowed for comparison with post-weld microscopic examination, and calibration of diffraction data analysis techniques to ensure confidence in the in-situ microstructure evolution.

BS1407 welds were prepared for microscopic examination as follows. Welds were sectioned with a carbide cutting disc. The clamped ends of the specimens were removed first, prior to axial sectioning of the remaining weld material. The weld section was mounted in Bakelite conductive resin, using a heating time of 9 minutes and a cooling time of 2 minutes. The mounted weld section was ground using Silicon Carbide grinding discs of grits 60 to 1200. The final polishing was carried out using diamond polishing wheels of 6  $\mu\text{m}$  and 1  $\mu\text{m}$ . Etching was carried out using a 2% Nital solution, which was carefully swabbed over the surface of the weld section until the austenite region surrounding the weld interface was revealed.

Nickel-based superalloy IFWs were sectioned via Electro-Discharge Machining (EDM) due to their increased hardness. For mounting, grinding and polishing, the same procedures used on BS1407 welds were also used for RR1000. The superalloy weld sections were electro-chemically etched using oxalic acid, with a voltage of 5 V for 4 - 6 s. This etching procedure preferentially reacts with the  $\gamma$  phase, revealing the distribution of  $\gamma'$  precipitates.

Optical Microscopy (OM) was used throughout the grinding and polishing processes to ensure that each grit was used for an adequate time, removing all scratches produced by the previous grit size. Additionally, OM images were recorded after etching to ensure that the etch was successful, and the etch reaction was homogenous across the specimens.

For the Nickel-based superalloy RR1000, the microstructural features present occur over shorter length scales. To resolve these, high magnification images were acquired using a FEI Quanta600 Scanning Electron Microscope. Images were recorded in Secondary Electron (SE) mode using an electron voltage of 15 kV and a spot size of 5.

For comparison with the post-weld XRD images recorded, SEM images were acquired at 0.1mm increments from the contact interface, to a distance of 1mm. SEM images were recorded from both specimens, to assess for symmetry in the Heat Affected Zone (HAZ) about the interface. Image magnifications of 2,000 x and 10,000 x were used, with the low magnification images analysed for primary  $\gamma'$  volume fractions, and the higher magnification used to assess the secondary  $\gamma'$  volume fraction.

To characterise the parent material, both XRD and SEM were used. Five diffraction images recorded from each of four individual stationary weld specimens were used to characterise an average  $\gamma'$  volume fraction and standard deviation. Three low- and high- magnification SEM images were recorded from four separate weld specimens to analyse the primary and secondary  $\gamma'$  volume fraction and deviation across a specimen, alongside the mean primary and secondary  $\gamma'$  volume fractions.

To evaluate the volume fraction of  $\gamma'$  from the SEM images, the image processing methodology outlined by Payton et. al [91] has been used. The image processing software FIJI ImageJ has been used to process all SEM images. Firstly, a median filter using a 3 pixel radius was applied. The radius of 3 pixels has been chosen as this value gave the best filtering of noise in the image without smoothing the edges of the precipitates. Next, an unsharp mask was applied with a radius of 3 pixels and a mask weight of 0.6 to enhance the contrast between precipitates and matrix, before a Gaussian blur filter was used (radius 3 pixels) to minimise the loss of contrast in the centre of the precipitates. Outliers were removed based on the precipitate sizes of interest (< 500 nm diameter for primary  $\gamma'$  at 2,000 x magnification, < 50 nm diameter

for secondary  $\gamma'$  at 10,000x magnification). A binary threshold was applied to the filtered image, with Otsu's method used to automatically find the threshold value. A 2 pixel erosion was applied, before a hole-filling operation and dilation of 2 pixels. An example is provided in Figure 3.6 showing the conversion of a raw SEM image to the processed image for statistical analysis of primary  $\gamma'$  volume fraction and size distribution.

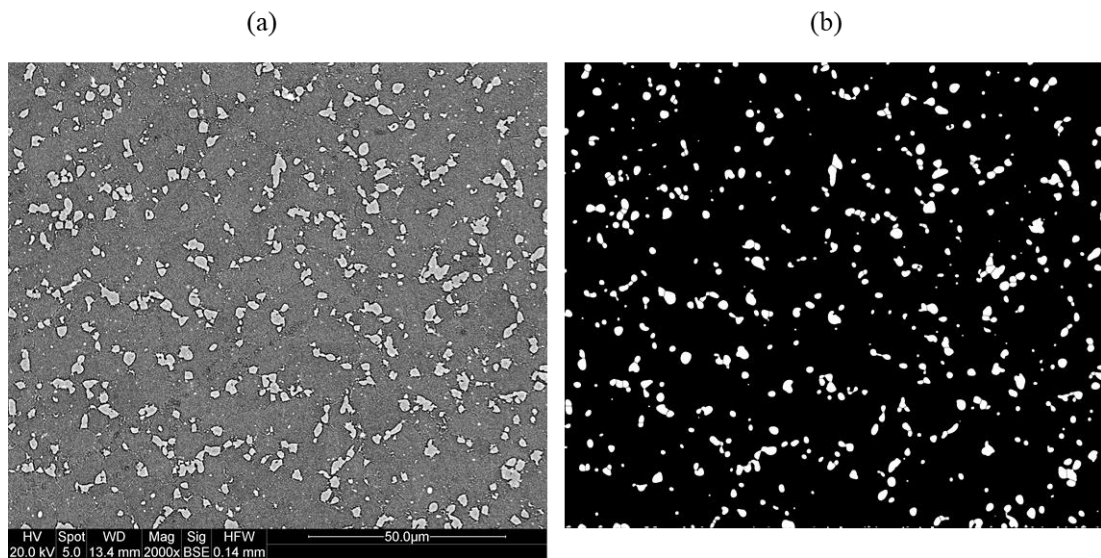


**Figure 3.6:** SEM image of parent RR1000 to analyse the primary  $\gamma'$  precipitates. (a) Raw SEM image, (b) Processed image for statistical analysis.

### 3.2.7 Summing of diffraction images

For all superalloys which consist of a  $\gamma/\gamma'$  superlattice, both phases exist with the same FCC crystal structure. The size of the cubic lattice of both phases is often very similar. This presented difficulties when processing diffraction data for RR1000 as the permitted diffraction peaks from the two phases have the same crystal structure, and these reside at similar  $2\theta$  values due to the similar lattice size.

However, it is known that despite both phases existing in FCC form, the  $\gamma'$  phase diffracts X-rays as a primitive cubic crystal. Primitive cubic phases permit diffraction of additional peaks when compared with the FCC diffraction patterns. A comparison of the permitted peaks is provided in Table 3.9.

**Table 3.9:** Permitted diffraction peaks from primitive cubic (PC) and face centred cubic (FCC) phases in X-ray diffraction.

Peak number ( $h^2 + k^2 + l^2$ )	Primitive Cubic (PC)	Face Centred Cubic (FCC)
1	[100]	-
2	[110]	-
3	[111]	[111]
4	[200]	[200]
5	[210]	-
6	[211]	-
7	-	-
8	[220]	[220]
9	[221]/[300]	-
10	[310]	-
11	[311]	[311]
12	[222]	[222]

The additional reflections permitted by the primitive cubic  $\gamma'$  crystal structure are often called 'superlattice reflections'. These additional peaks are often very low in intensity when compared with the peaks also produced by the FCC  $\gamma$  phase, due to the low difference in X-ray scattering ability of Nickel and Aluminium. When accounting for a two-phase system with one primitive cubic and one FCC phase of the same lattice parameter, the relative intensity of the peaks only permitted by the PC phase is much lower than the composite peaks produced by the two phases (e.g. [111], [200], [220]). It is often observed that only the [100] and [110] peaks produced by the  $\gamma'$  phase can be resolved in X-ray diffraction, unless very large acquisition times are used.

Due to the extremely high acquisition rate of 150 fps used in the RR1000 experiments, the impact of the background noise on the diffraction patterns was significant. Due to this, it was impossible to accurately define the [100] and [110] diffraction peaks produced by the  $\gamma'$  phase. Without the ability to resolve these peaks, accurate phase fraction analysis could not be performed.

To overcome this issue, the raw (142 fps) Debye-Scherrer diffraction rings were combined chronologically to simulate increased acquisition times. Images were combined in sets of various integers, and the phase fractions and Rietveld residual analysed to assess an appropriate number of diffraction images which provided accurate phase analysis. As an example, a comparison of diffraction images from the parent material are presented in Figure 3.7, at the original acquisition rate of 142 fps and a summed acquisition rate of 14.2 fps.

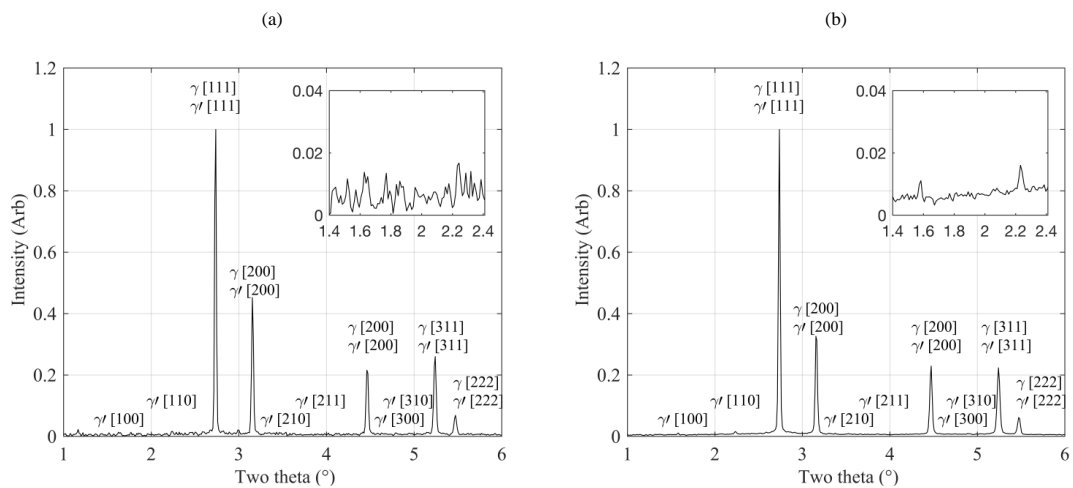


**Figure 3.7:** Comparison of X-ray diffraction profiles highlighting the influence of background noise on low intensity PC  $\gamma'$  peaks. (a) Original 142 fps acquisition, (b) Summed 14.2 fps acquisition. The inset in both figures shows the  $2\theta$  range between  $1.4$  and  $2.4^\circ$  where the  $[100]$  and  $[110]$  primitive cubic  $\gamma'$  peaks reside to highlight how the reduced acquisition rate allows for these peaks to be resolved.

### 3.2.8 Diffraction data analysis techniques

The diffraction data analysis techniques used for BS1407 steel and RR1000 are similar in principal but there are slight differences in application due to the superlattice nature of RR1000. For BS1407 steel, the microstructure features of interest are the phase fractions of ferrite and austenite, and the lattice strain present in each phase. For RR1000, the phase fractions of  $\gamma$  and  $\gamma'$  are of interest, alongside the lattice strain of the  $\gamma$  matrix.

For all diffraction patterns, the Data Analysis WorkbeNch (DAWN) software [92] was used for azimuthal integration of the Debye-Scherrer diffraction rings. This software

was produced by Diamond Light Source, and beamline support staff provided processing scripts for diffraction images. To calibrate synchrotron instrument parameters, diffraction images were recorded using a standard sample of ceria ( $\text{CeO}_2$ ).

For both materials the crystallographic data analysis software GSAS-II [93] has been used to perform full Rietveld refinement and quantitative phase analysis. The refinement procedure was limited to fitting of the background function, phase fraction, lattice parameter and sample parameters (Gaussian and Lorentzian peak width).

BS1407 IFW diffraction patterns were processed via DAWN and GSAS-II software as mentioned above. In the analysis of phase fractions, only the BCC ferrite and FCC austenite phases were included in the refinement, as negligible phases such as carbides and graphite were not of interest. Additionally, the texture parameters were not refined for BS1407 steel. The atomic data for the ferrite and austenite phases in the GSAS refinement was only dependent on the compositions of iron and carbon, as these atoms dictate the equilibrium phase composition more than trace elements such as chromium, manganese and silicon.

In the analysis of X-ray diffraction data of RR1000 Inertia Friction Welds, Debye-Scherrer diffraction rings were converted to diffraction patterns using DAWN, and full Rietveld refinement was performed using GSAS-II. In the Rietveld refinement process, the phases included were primitive cubic  $\gamma'$  and FCC  $\gamma$ . Negligible phases such as carbides were ignored in this analysis as they exist in a variety of lattice structures, but also exhibit very little sensitivity to the temperature range produced by IFW. For RR1000, literature values for atomic concentrations of the  $\gamma$  and  $\gamma'$  phases evaluated by Atom Probe Tomography [15] were applied to the phases used in the refinement. This is of great importance here due to the sensitivity of the peak intensities of  $\gamma$  and  $\gamma'$  to the composition of the phases. In RR1000, there are many alloying elements of significant concentration which must be accounted for. The importance of correctly including these in the refinement process is especially important due to the reliance on low intensity [100] and [110]  $\gamma'$  peaks to evaluate the  $\gamma'$  volume fraction in the in-situ diffraction images. For RR1000, the texture of the  $\gamma$  phase was refined once the phase fractions had been defined. As the texture parameter of a phase influences the peak intensity of the peaks produced, it was seen as

inappropriate to refine the texture for the  $\gamma'$  phase, due to the reliance on low-intensity [100] and [110] peaks to accurately define the phase fractions.

Analysis of micro strain has been carried out through measurement of the evolution of lattice parameter of the separate phases. Due to the low intensity of the primitive cubic [100] and [110]  $\gamma'$  peaks and thus the susceptibility of these peaks to be influenced by background noise, particularly at low phase fractions, the strain evolution of this phase has not been evaluated. The strain evolution for each phase is calculated using equation 3.2.

$$\varepsilon(t) = \frac{a_{weld}(t) - a_{parent}}{a_{parent}} \quad (\text{Eq. 3.2})$$

where  $a_{parent}$  is the lattice parameter of the phase evaluated from the parent material prior to welding and  $a_{weld}$  is the lattice parameter calculated from a diffraction image recorded at time  $t$  during IFW. The evaluation of the parent lattice parameter is simple in the case of phases which are present in significant fractions in the parent material, such as the ferrite phase in BS1407 and the  $\gamma$  phase in RR1000. These lattice parameters were simply evaluated from pre-weld diffraction images.

However, in the case of BS1407, austenite only forms at elevated temperatures and so this phase was not present in pre-weld diffraction images. Therefore, the parent value of the austenite lattice parameter had to be evaluated from post-weld data, where a significant phase fraction of austenite was retained in the microstructure. The parent austenite lattice parameter was evaluated from diffraction images recorded at the furthest axial distances from the contact interface at which retained austenite was present after welding, to ensure the parent value was free from any residual strain which may have formed around the interface due to high amounts of deformation.

As IFW is a coupled thermo-mechanical problem at the macro-scale, both thermal and mechanical strains have an effect on the lattice parameter. These strains have been de-convoluted using temperature measurements recorded from repeat welds. Here, reference data for the lattice parameter evolution of ferrite and austenite at a range of temperatures [94] has been normalised and applied to the parent lattice parameters of BS1407. For RR1000, thermal expansion coefficient data has been applied to the parent lattice parameter to estimate the volumetric expansion of the cubic lattice. These relationships have been applied to thermal measurements taken from repeat

welds to estimate lattice parameter evolution across the temperature range recorded during IFW. The mechanical and thermal strains can then be de-convoluted using equation 3.3.

$$\varepsilon(t) = \frac{a_{weld}(t) - a_{thermal}(t)}{a_{parent}} \quad (\text{Eq. 3.3})$$

Where  $\varepsilon(t)$  is the strain in the phase,  $a_{weld}$  is the lattice parameter of the phase recorded during IFW,  $a_{thermal}$  is the estimated lattice parameter of the phase at the recorded temperature and  $a_{parent}$  is the lattice parameter of the phase in the parent material. For BS1407 steel,  $a_{weld}$  was calculated from the mean lattice parameter derived from the peak position of the four peaks with lowest diffraction angle (BCC ferrite: [110], [200], [211], [220] and FCC austenite: [111], [200], [220], [311]). The  $a_{weld}$  of RR1000 was derived from the lattice parameter of the [111] composite peak alone. This peak was used as it is the composite peak which resides at the lowest two theta value. The misfit between the  $\gamma$  and  $\gamma'$  is exaggerated at larger  $2\theta$  values, which causes broadening of the composite peak and may possibly shift the lattice parameter from the true value.

### 3.2.9 Thermal validation of XRD data

To validate the phase evolution seen in processed diffraction data, selected welds have been repeated, with a spot-welded K type thermocouple attached to the fixture specimen. Type K thermocouples have a sensitivity of  $41 \mu\text{V}/^\circ\text{C}$ , with uncertainty of  $\pm 2.2^\circ\text{C}$  at ambient temperature and  $\pm 7.5^\circ\text{C}$  at  $1000^\circ\text{C}$ , allowing for accurate thermal measurements. The axial position of the thermocouple was kept consistent with the  $z_0$  values used for welds of interest. Furthermore, the repeatability of the weld outputs were checked to ensure that the welds could be treated as identical, and thus the diffraction data could be shown to correlate with the thermal data.

### 3.3 Numerical methods

The second part of this chapter involves the development of a novel numerical modelling methodology to represent the microstructure evolution of RR1000 during IFW. To do so, a validated macro-scale process model is required to provide accurate thermal outputs. Here, Finite Element Analysis (FEA) has been utilised to model the process response, and the details of this approach are presented first.

The thermal response of the Finite Element model is used as input data for the Cellular Automata (CA) numerical model. This model predicts the diffusion of elements between the  $\gamma$  and  $\gamma'$  phases and the subsequent phase transformations which occur due to these. Due to the novelty of this application of CA, the model details and underlying physics have been explained in greater detail.

#### 3.3.1 Finite element analysis

Finite Element modelling has been performed in the commercial FE code DEFORM v11.1. This code has a velocity-based formulation and is commonly used to model metal forming processes where high temperatures and deformations are present. Within this code, there is a 2.5D torsion environment in which 2D elements are modelled to reduce computational time. However, each node has a 3-component velocity vector which allows the out-of-plane circumferential deformations and shear behaviour to be evaluated. Thus, the process can be accurately modelled without the computational expense of running full 3D models.

A schematic of the model set-up is presented in Figure 3.8. The workpiece is modelled as a rigid plastic material, with a tabular material definition. The tabular flow stress is defined as functions of temperature, strain and strain rate. This flow stress definition was evaluated using Gleeble compression tests and provided by Rolls-Royce. The workpiece is seated in a rigid die, upon which the weld energy and inertia inputs are defined. From this, the initial rotational velocity is calculated. There is a sticking friction condition applied between the workpiece and rigid die, which ensures there is no slipping of the specimen throughout the process simulation. The fixture workpiece is simulated using a symmetry boundary, upon which the axial load is applied. The use of a symmetry boundary reduces the number of elements modelled by negating

the requirement to model the fixture workpiece. The outputs of the model have been compared with a full model in which both workpieces are simulated, and the macro-scale outputs are consistent between the two models.

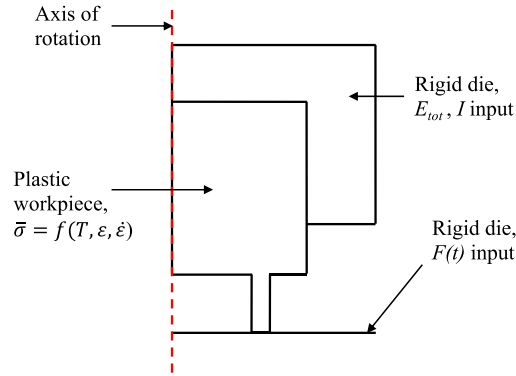


**Figure 3.8:** Schematic of the IFW problem as modelled in DEFORM.

Between the spindle workpiece and the symmetry boundary the representative friction coefficient  $\mu(t)$  is applied. This is calculated from experimental data using equation 3.4 and applied to all workpiece nodes which are in contact with the symmetry boundary.

$$\mu(t) = \eta \cdot \frac{E_{t+1} - E_t}{-\omega \Delta t P \left( \frac{2\pi}{3} [r_o^3 - r_i^3] \right)} \quad (\text{Eq. 3.4})$$

Where  $\eta$  is the process efficiency, assumed as a constant value of 0.95.  $E$  is the total energy available for welding at times of  $t$  and  $t+1$ , which are separated by a time step of  $\Delta t$ .  $\omega$  is the rotational velocity at time  $t$ ,  $P$  is the weld pressure and  $r_o$  and  $r_i$  are the outer and inner radii, respectively.

Initial tests of the FE code for the weld geometry and weld parameters used in the experimental methodology showed an extremely inaccurate mechanical response. Whilst the rundown curves produced by the model were consistent with experimental data due to the experimentally defined friction coefficient, the upset response was approximately 1 order of magnitude lower than the upset produced in the experimental welds. This was surprising considering the fact the same FEA software and material model have been shown to produce very accurate results when modelling larger weld

geometries. However, considering the large reduction in specimen geometry, it is possible that heating rates, strains and strain rates are drastically different to those experienced in conventional weld geometries.

The main output of interest of these models is the thermal data, which is provided into the CA models to predict the microstructure evolution. The mechanical deformation is of great importance to this for two reasons. Firstly, the upsetting process removes hot material from the contact interface. When considering the axial profile of temperature at any point in the process, the difference between a model in which upset occurs and one which does not would be large, due to the ejection of hot material from the interface. Secondly, this data will be directly compared with experimental data in which the axial profile of microstructure evolution is evaluated. If the mechanical response is not accurate, the uncertainty in the position at which temperatures are extracted from increases greatly.

To improve the mechanical response of the FEA approach, an optimisation routine has been performed. The tabular material data at high temperatures (deemed as equal to and greater than 900 °C in this case) have been extracted from the DEFORM software. At each temperature point for which data is input, the flow stress variation with strain rate has been fit to a power law of the following form.

$$\sigma = K \dot{\epsilon}^m \quad (\text{Eq. 3.5})$$

This produces a different value of  $K$  and  $m$  for each temperature. The relationship between temperature and  $K$  can also be fit to a power law as follows.

$$K = JT^n \quad (\text{Eq. 3.6})$$

The relationship between temperature and the power factor  $m$  is linear and is fit as follows.

$$m = IT + p \quad (\text{Eq. 3.7})$$

It can be seen that the four variables,  $J$ ,  $n$ ,  $I$  and  $p$ , describe the variation in the power law with temperature. The  $K$  and  $m$  values calculated from these four variables describe the flow stress variation with strain rate.

A Matlab code was developed which automated the creation and submission of DEFORM files, and subsequently analysed the output data. Within this code, the

Matlab function *lsqnonlin* was used. This is a non-linear least-squares optimisation function which methodically varies input parameters to minimise the variation in the output when compared with the ideal case. Here, the objective function was the FEA upset curve, and the ideal case was the mean upset response of the experimental welds of that parameter set. The variables ( $J, n, I, p$ ) were set as the input parameters, and these were varied by the *lsqnonlin* function to minimise the difference between FEA model upset and experimental upset.

As the objective of this optimisation procedure was not to produce a new material model for this scale of weld geometries, the optimisation was performed separately for each weld parameter set. Whilst this produced different material models for each weld parameter set, it is believed that this method produced more accurate upset responses when compared with a single material model. A flow chart detailing the steps of the optimisation procedure is presented in Figure 3.9.

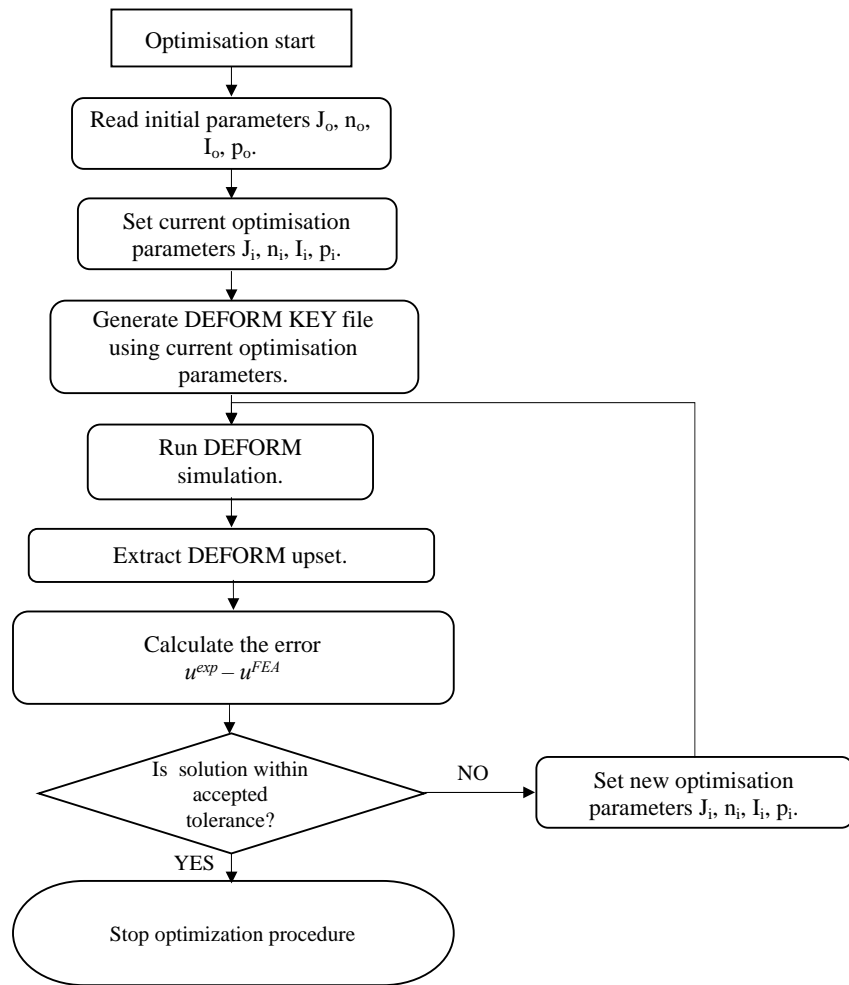


**Figure 3.9:** Flow chart of the optimisation procedure for the material model in DEFORM.

### 3.3.2 Cellular automata

Cellular Automata (CA) is a commonly used numerical modelling methodology for the evaluation of microstructure evolution. In this research, the CA approach has been applied to predict the diffusion of elements between phases and the phase transformations which occur due to these. The CA approach is well-suited to this problem due to its inclusion of local ‘neighbourhood’ effects which are evaluated between adjacent cells. This provides a method to evaluate gradients in concentration and chemical potential which are required for the calculation of diffusion coefficients and atomic fluxes.

Further to this, the CA modelling methodology can be used to evaluate multiple state variables across the cellular matrix, and many physical equations can be defined to calculate the evolution of these between time steps. In this case, the sensitivity of thermodynamic parameters to temperature can be evaluated and stored at each time step, alongside the atomic fluxes of the constituent elements modelled.

### 3.3.2.1. Cellular automata fundamentals

In Cellular Automata, a matrix of cells is used to represent small regions of the microstructure. It is assumed that each cell is at local equilibrium, that being that the phase fraction in each cell is evaluated from the equilibrium phase diagram at the system temperature and the composition within the cell. The initial state variables defined across this matrix are the cell state and chemical composition. The cell state definition defines a cell of  $\gamma$  with a value of 0 and a cell of  $\gamma'$  with a value of 1. These definitions are used to evaluate the phase fractions and are updated at each time step based on the equilibrium value evaluated from the composition present in each cell. The chemical compositions are defined as atomic fractions,  $x_B$ , where B represents the element defined. In the initial condition of the model, the atomic fractions are evaluated from the equilibrium phase diagram at the start temperature, where the atomic compositions of  $\gamma$  and  $\gamma'$  are calculated separately and applied to their respective cells.

### 3.3.2.2. Thermodynamic fundamentals

There are multiple thermodynamic parameters which must be evaluated for input into the diffusion calculation. In the initial condition for the CA model, the molar volume of the representative material is evaluated at equilibrium volume fractions and the start temperature of the system. The molar volume is useful for calculation of chemical concentration from the atomic fraction present in a cell, as shown in equation 3.8.

$$c_B = \frac{x_B}{V_m} \quad (\text{Eq. 3.8})$$

where  $c_B$  is the concentration of element B in mol/m<sup>3</sup>,  $x_B$  is the atomic fraction of element B in the cell, where the sum of atomic fractions in each cell is equal to unity.  $V_m$  is the molar volume of the system in m<sup>3</sup>/mol. For simplicity, it is assumed that the

molar volume of the  $\gamma$  and  $\gamma'$  phases are equal, which is a common assumption given the low misfit between the two phases in superalloys [95].

Another thermodynamic variable required for the diffusion calculation is the chemical potential. The chemical potential is commonly known as the partial molar Gibbs function and defines how the Gibbs function or free energy of the system varies due to compositional changes, as shown in equation 3.9.

$$\mu_B = \left( \frac{\partial G}{\partial m_B} \right)_{p,T} \quad (\text{Eq. 3.9})$$

where  $\mu_B$  is the chemical potential of element B in a mixture, often defined in J/mol.  $G$  is the Gibbs free energy of the cell and  $m_B$  is the number of moles of B present in the cell. It can be seen in Equation 3.9 that the chemical potential is sensitive to composition, temperature and pressure, although the pressure is assumed as constant (atmospheric) for the purpose of these calculations.

The chemical potential provides the second driving force for diffusion, alongside the concentration gradient. At any given composition, temperature and pressure, the equilibrium phase composition occurs where the Gibbs free energy is minimised. Therefore, the derivative of the Gibbs free energy with system composition defines the free energy associated with that species, and thus the driving force towards equilibrium.

For the calculation of the diffusive flux of an element, the atomic mobility must also be defined. The atomic mobility is defined as functions of temperature and chemical concentration. The atomic mobilities,  $M_B$ , are evaluated from a frequency factor,  $M_B^0$  and an activation energy  $Q_B$ , as defined by absolute rate reaction theory. This is shown in Equation 3.10.

$$M_B = M_B^0 \exp\left(-\frac{Q_B}{RT}\right) \frac{1}{RT} \Gamma^{mg} \quad (\text{Eq. 3.10})$$

Where  $\Gamma^{mg}$  is the ferromagnetic transition factor, which accounts for the effect of magnetic ordering on the atomic mobility of transition metals.

The thermodynamic values required for the diffusion calculation have been calculated using the thermodynamic software Thermo-Calc. These have been evaluated at equilibrium for intervals of 0.01 (or 1 %) in atomic fraction and 10 °C across the range

of compositions and temperatures required. These data have been stored in the form of reference tables. During the diffusion calculation, the reference tables are interpolated from to acquire equilibrium thermodynamic data at the system temperature and cell composition. This reduces the requirement to couple the diffusion model with thermodynamic software, reducing the computational time of the model.

### 3.3.2.3. The physics of atomic diffusion

Diffusion can be described using Fick's first law. In the one-dimensional case, the flux of element B,  $J_B$ , is calculated from the diffusion coefficient  $D_B$  and the concentration gradient,  $dc_B/dz$ . This is presented in equation 3.11.

$$J_B = -D_B \frac{dc_B}{dz} \quad (\text{Eq. 3.11})$$

where the flux is calculated in mol/m<sup>2</sup>/s when the diffusion coefficient is provided in m<sup>2</sup>/s, the concentration in m<sup>3</sup>/mol and the distance in m. The flux value  $J_B$  represents the transport of element B through an area perpendicular to the diffusing direction per unit time. This is more appropriately represented in equation 3.12.

$$J_B = \frac{\Delta m_B}{dt} \frac{1}{A} \quad (\text{Eq. 3.12})$$

$$\Delta m_B = J_B A dt \quad (\text{Eq. 3.13})$$

where  $\Delta m_B$  is the number of moles diffusing through a defined cross-sectional area  $A$  during a time step  $dt$ .

In extremely simple cases the diffusion coefficient can be defined as constant, however in more complex systems where multiple elements are present, and there are discrete changes in temperature, these must be evaluated based on the current equilibrium thermodynamics.

For interdiffusion in multicomponent systems, the continuity equation must be introduced, to ensure that the amount of matter in the system is conserved.

$$\frac{\partial c_B}{\partial t} = \frac{\partial}{\partial z} \left( D_B \frac{dc_B}{dz} \right) \quad (\text{Eq. 3.14})$$

At a given concentration of element B, equilibrium values of element mobility and chemical potential can be used to calculate the diffusion coefficient of B as shown in equation 3.15.

$$D_B = c_B M_B \frac{\partial \mu_B}{\partial c_B} \quad (\text{Eq. 3.15})$$

However, this relationship only holds for a simple case. In multicomponent systems, where two or more elements are present, interdiffusion must also be considered. Onsager first hypothesised that the flux of an element B was not only dependent on the concentration gradient of B, but also the concentration gradients of other elements in the system [96]. This is commonly expressed as shown in Equation 3.16.

$$J_k = - \sum_{j=1}^N D_{kj} \frac{\partial c_j}{\partial z} \quad (\text{Eq. 3.15})$$

where  $k$  is the diffusing element,  $j$  is the independent concentration and  $N$  is the total number of elements in the system. However, in reality the sum of the concentrations (when treated as atomic fractions), sum to unity, and so the sum of the concentration gradients is equal to zero. Therefore, the summation is only performed across  $N-1$  elements, with the remaining element labelled the dependent concentration.

Taking a ternary system A-B-C as an example. If element C is chosen as the dependent concentration, the fluxes are evaluated as follows.

$$J_A = \left( -D_{AA}^C \frac{\partial c_A}{\partial z} \right) + \left( -D_{AB}^C \frac{\partial c_B}{\partial z} \right) \quad (\text{Eq. 3.16})$$

$$J_B = \left( -D_{BA}^C \frac{\partial c_A}{\partial z} \right) + \left( -D_{BB}^C \frac{\partial c_B}{\partial z} \right) \quad (\text{Eq. 3.17})$$

$$J_C = \left( -D_{CA}^C \frac{\partial c_A}{\partial z} \right) + \left( -D_{CB}^C \frac{\partial c_B}{\partial z} \right) \quad (\text{Eq. 3.18})$$

Note how in Equations 3.16 – 3.18, none of the fluxes are dependent on the concentration gradient of C. As an example, the diffusion coefficient  $D_{BA}^C$  is defined as the diffusion coefficient for a flux of element B, based on the concentration gradient of A, where C is the dependent concentration. The calculation of this interdiffusion coefficient is shown in Equation 3.19.

$$D_{BA}^C = c_B M_B \frac{\partial \mu_B}{\partial c_A} \quad (\text{Eq. 3.19})$$

#### 3.3.2.4. Binary Ni-Al model

To verify that the Cellular Automata model produced accurately evaluates the diffusion of elements, a 1D model has been tested first. For simplicity, this model contains a binary system of Nickel and Aluminium. The mass fraction of Aluminium is 9 % for consistency with literature data. This model has been implemented to assess the dissolution of a single  $\gamma'$  precipitate of 1  $\mu\text{m}$  radius due to various heating rates, similar to the investigation conducted by Tancret [97].

The results produced by the 1D CA model have been compared with a 1D DICTRA simulation. In both cases, the cell size was set to 50 nm, to produce 20 cells across the precipitate radius. It was found this value produced a good balance of computational accuracy and simulation time.

The 1D model for verification of the diffusion calculation starts with loading of the thermodynamic reference data. The state variables matrices are created for a defined number of nodes. The  $\gamma'$  precipitate volume fraction is defined, consistent with equilibrium values at 1000 °C. The precipitate size is input and from this the cell size is calculated. The cell state variable is then updated, and the local composition applied to each cell based on this.

The diffusion calculation begins with the interpolation of thermodynamic reference values for the composition present in each cell. Each cell is passed over and the diffusive flux of each element is calculated using the local neighbourhood, which in the 1D case is cells directly adjacent of the cell of interest.

The conservation of matter is applied and the rate of change of cell composition is calculated. The concentration gradient present at the start of the time step is divided by the rate of change of concentration to define a maximum time step. This maximum time step ensures that the concentration gradient does not switch directions in any time step. The cell concentrations are then updated based on the maximum allowable time step. Local equilibrium is applied in each cell to calculate the  $\gamma'$  volume fraction in each cell and the total volume fraction over the system.

At the end of the time step the system time is updated, and the new temperature derived from the constant heating rate. The model checks whether complete dissolution has occurred, or whether the maximum temperature ( $T_{Melting}$ ) has been exceeded. If neither of these conditions are met, the next time step begins, and the diffusion calculation repeats. When the  $\gamma'$  volume fraction reaches 0 or a temperature of 1369 °C is exceeded, the simulation terminates. A flowchart for the 1D CA model is shown in Figure 3.10.

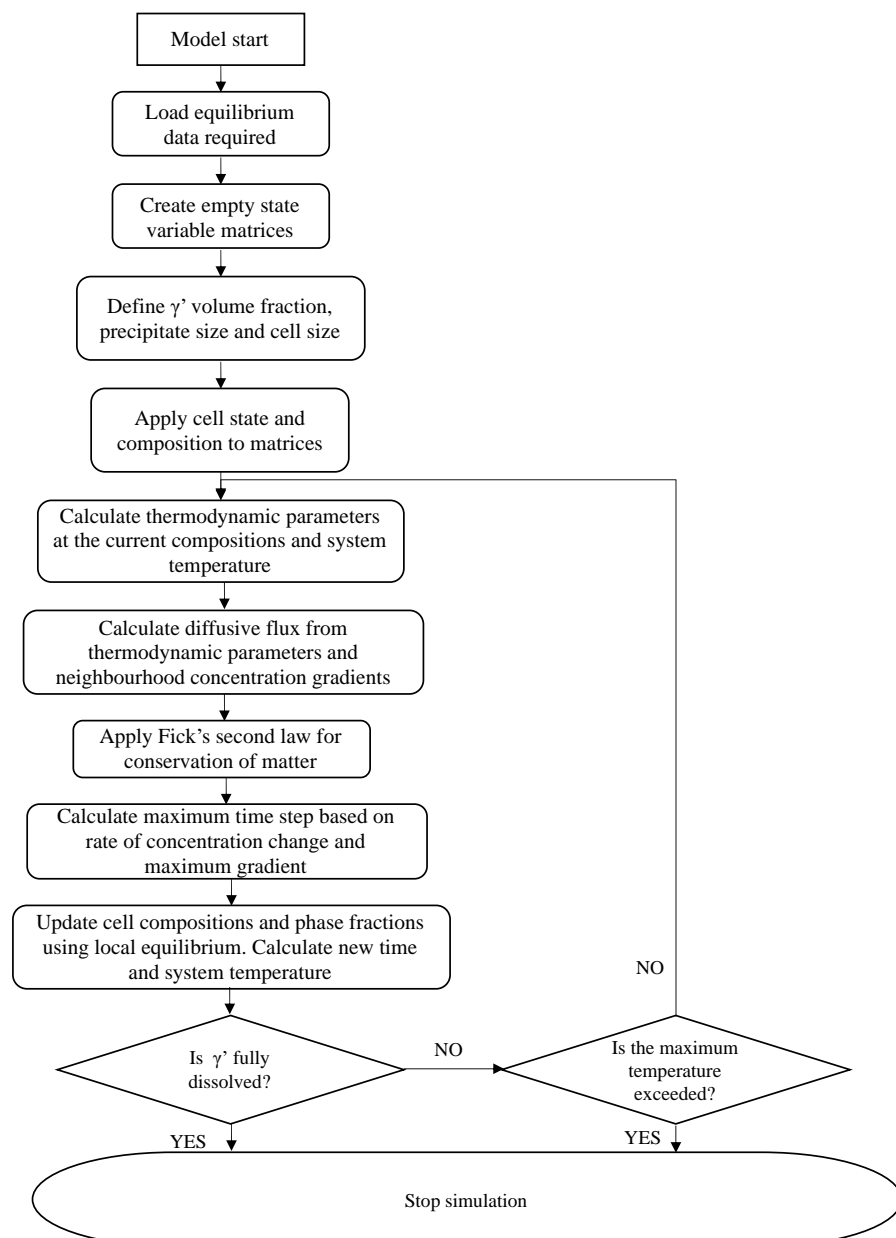


**Figure 3.10:** Flow chart describing the procedures performed by the 1D CA model.

### 3.3.2.5. Ternary Ni-Al-Cr model

To provide a representative system of RR1000, CA models have been produced which model the ternary Ni-Al-Cr system. Whilst this does not model the diffusivity of all constituent elements present in RR1000, it is known that in most superalloys, Chromium is the slowest diffusing element [98]. Therefore, the rate of phase transformations is heavily dependent on the diffusion of Chromium between phases. Thus, the ternary model implemented here offers an accurate representation of  $\gamma'$  dissolution behaviour with a large reduction in the computational expense required for modelling of all 11 constituent elements.

To provide a representative composition of RR1000, reference data for the composition of  $\gamma$  and  $\gamma'$  has been used to evaluate the primary elements which act as  $\gamma'$  formers, and those which reside in the matrix [15]. It is observed that Aluminium, Titanium and Tantalum are present in large fractions in the  $\gamma'$  phase. As shown in Table 3.3, these elements sum to a weight fraction of 8.6 % in RR1000. Elements that reside in the  $\gamma$  phase have been defined as Chromium, Cobalt and Molybdenum, and these sum to a weight fraction of 38.5 % in RR1000.

In the ternary system, Aluminium has been defined as the  $\gamma'$  forming element, and Chromium as the element which resides in  $\gamma$ . As a starting point, the equilibrium phase fractions of  $\gamma$  and  $\gamma'$  with temperature have been analysed for the Ni-0.086Al-0.385Cr system. The final system chosen had wt. % of 8.6 % for Aluminium and 23 % for Chromium. This composition was chosen due to the equilibrium dissolution trend shown by the material, in which at the known dissolution temperature range in RR1000 (850 – 900 °C), the equilibrium phase fractions were roughly consistent with parent RR1000. However, most importantly, this composition provided a similar  $\gamma'$  solvus temperature to RR1000. As is shown in Figure 3.11, the  $\gamma'$  solvus temperature in the representative material was 1130 °C, which is similar to the value of 1145 °C produced by RR1000.

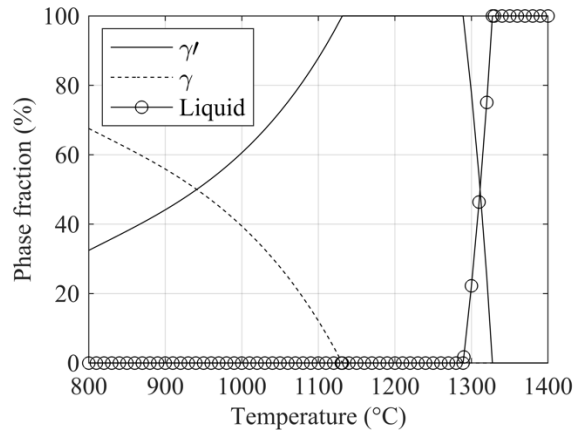


**Figure 3.11:** Equilibrium volume fraction data evaluated from Thermo-Calc for the representative material.

### 3.3.2.5.1 1-dimensional cellular automata

As a simplified case, the 1D binary CA model has been expanded to model the ternary Ni-Al-Cr system used to represent RR1000. In this case, three precipitate sizes have been simulated in the single precipitate model. These precipitate sizes have been selected to simulate dissolution of primary, secondary and tertiary  $\gamma'$ . The precipitate radii for primary and secondary  $\gamma'$  have been taken from the mean values measured under SEM, and the tertiary  $\gamma'$  was estimated from the expected diameter range of 5 – 30 nm. The dissolution profile of each precipitate has been normalised against the volume fraction of each precipitate. The sizes and representative volume fractions simulated are presented in Table 3.10.

**Table 3.10:**  $\gamma'$  precipitate sizes simulated in the 1D ternary CA model and the respective volume fractions applied to the dissolution profile of each precipitate.

$\gamma'$ precipitate	Precipitate radius ( $\mu\text{m}$ )	Precipitate Volume fraction (%)
Primary	0.4825	9.49
Secondary	0.143	28.80
Tertiary	0.0125	9.23

As the 1D ternary simulation utilised multiple precipitate sizes, it was not feasible to keep the cell size consistent for each of the three precipitate sizes. Hence, the number of cells across the precipitate radius was set to a constant value of 20, consistent with the 1D binary simulation. Again, the purpose of this was to balance computational accuracy, ensuring the geometry was sufficiently discretised, whilst optimising simulation time.

### **3.3.2.5.2 2-dimensional cellular automata**

Whilst the 1D model can be used to quickly evaluate trends in dissolution behaviour at different thermal histories, it lacks the effects of precipitate interaction that are present in the microstructure of RR1000. Dissolution of  $\gamma'$  precipitates is reliant on diffusion, and as an example, dissolution of the  $\gamma'$  phase would cause diffusion of Aluminium out of the precipitate, enriching the matrix in the surrounding area. Should there be another  $\gamma'$  precipitate in this area, the local enrichment of Aluminium in the matrix would reduce the concentration gradient of Aluminium and reduce the driving force for dissolution. Therefore, the modelling of a 2D region in which a statistical representation of the microstructure is included allows for these effects to be evaluated. This in turn provides a more accurate description of the dissolution behaviour of  $\gamma'$  precipitates in RR1000.

For the 2D model, SEM images are used to generate the representation of parent microstructure. An SEM image is taken and processed using the same methodology as for the experimental analysis of  $\gamma'$  volume fraction and distribution. This image can then be imported in full, or a smaller region can be extracted to investigate an area of interest. An SEM image, processed image and parent microstructure representation in Matlab are presented in Figure 3.12.

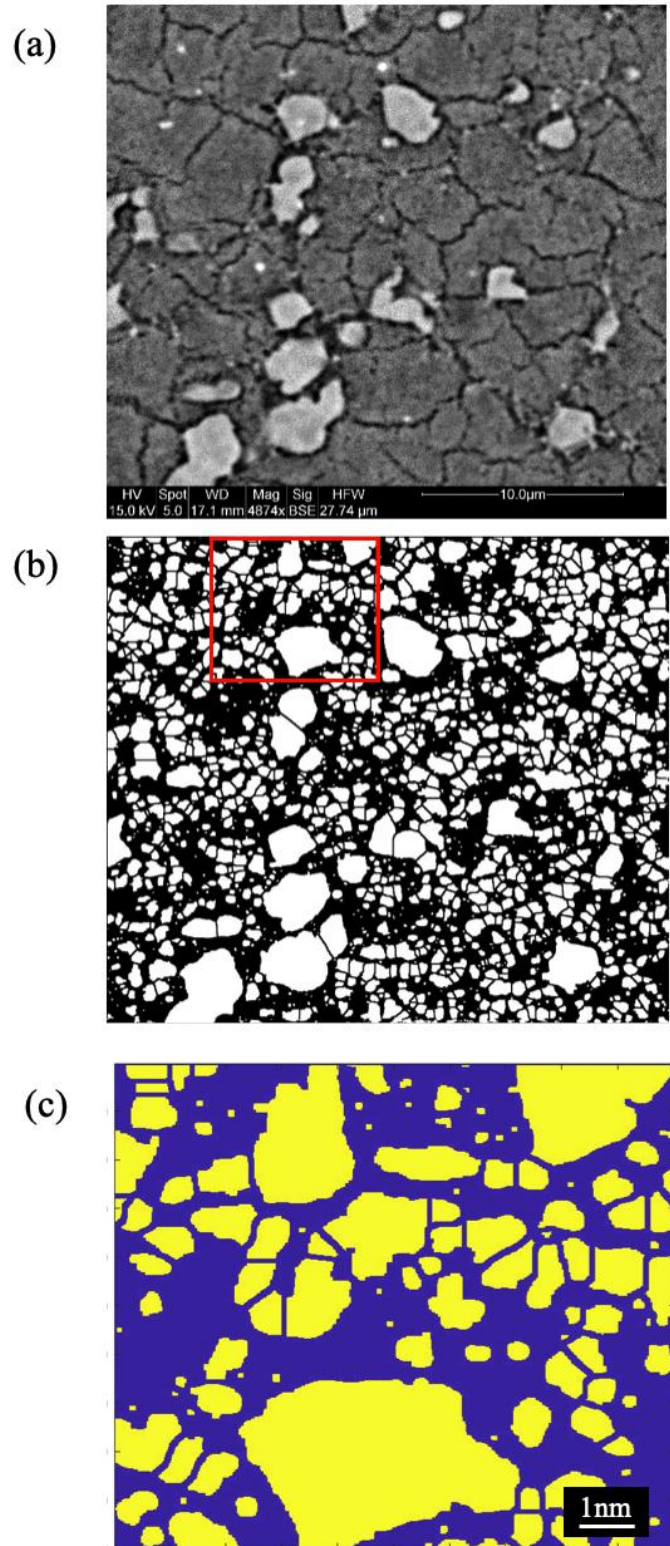


**Figure 3.12:** The processing of SEM images to produce a digital material representation for the 2D CA modelling approach. (a) Raw SEM image, (b) processed SEM image in which the red box highlights the region of interest, (c) the digital material representation in Matlab.

It should be noted that the digital material representation used in the 2D CA model does not account for tertiary  $\gamma'$ , as these cannot be resolved by SEM. As tertiary  $\gamma'$  precipitates are smallest, it is assumed that these dissolve fully and their chemical composition homogenises across the matrix phase. To account for this, the composition of  $\gamma'$  for the estimated 9.23 % tertiary  $\gamma'$  is added to the composition of the matrix phase when a temperature of 950 °C is exceeded.

The 2D CA model starts with the importing of the digital material representation. The scale on the SEM image is used to define the cell size as the size of each pixel. If desired, a smaller region of the digital material representation can be selected. In the representative case presented in Figure 3.12c, the secondary  $\gamma'$  precipitates were found to contain a minimum of 20 pixels across the width of the precipitate, ensuring that the resolution was high enough to ensure computational accuracy, similar to the 1D simulations.

The cell state matrix is imported from the binary image imported at the start of the matrix. Equilibrium compositions of the three constituents are defined dependent on the cell state. Empty state variables are created consistent in size with the imported image, and thermodynamic reference data is imported. The temperature data extracted from FEA analysis is also imported as input data for this model.

The diffusion model begins with the interpolation of thermodynamic values from their reference tables. These values are input into the flux equations alongside the concentration gradients. In the 2D case, the neighbouring cells are defined as those directly adjacent to the cell of interest (for example; N, S, E, W).

Fick's second law is applied to ensure matter is conserved and the rate of change of concentration is evaluated for all cells and for the three elements modelled. The maximum time step is defined using the concentration gradients present at the start of the time step and the rate of concentration change, to ensure the flux direction does not flip during a time step. The concentrations of each element in each cell are updated based on the maximum time step evaluated.

The resulting phase fractions from the diffusion of elements are calculated from the local equilibrium approach. The model repeats the diffusion calculation until the total simulation time is completed, such that the full thermal history extracted from FEA has been evaluated. This procedure is presented in a flow chart in Figure 3.13.

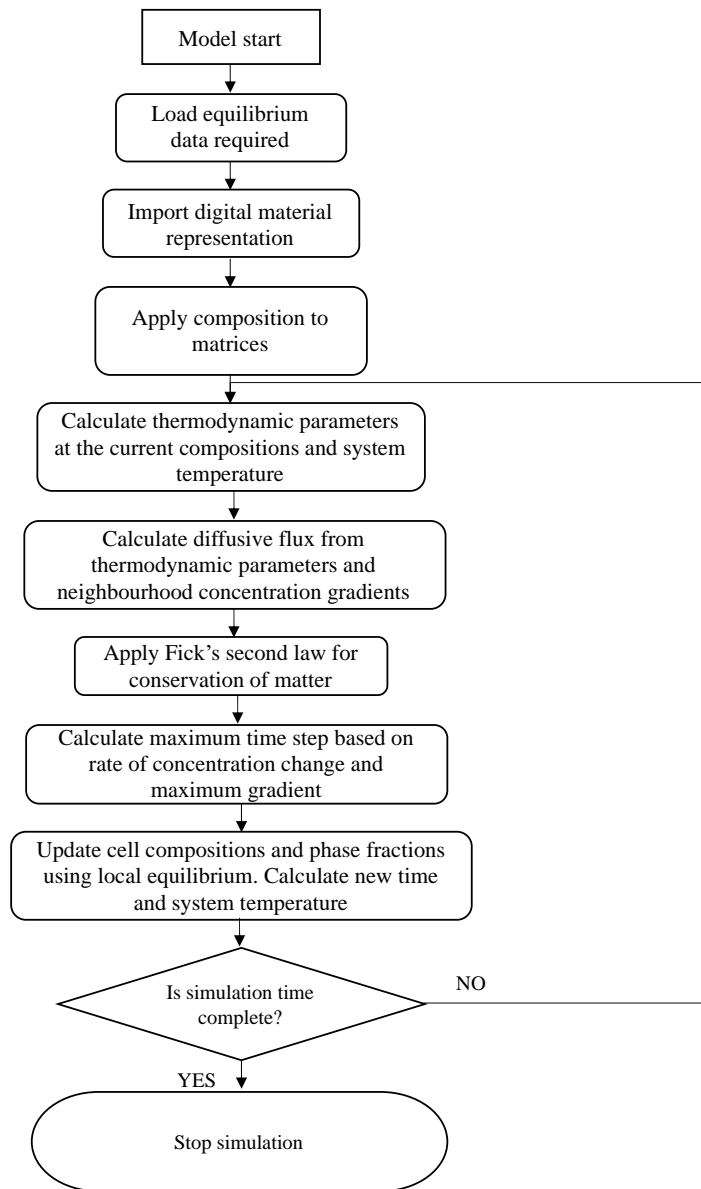


**Figure 3.13:** Flow chart describing the procedures performed by the 2D CA model.

## **Chapter 4**

# **Characterisation of Steel Microstructure Evolution During IFW**

### **4.1 Introduction**

This chapter presents the results obtained from the experiments analysing the in-situ microstructural evolution of BS1407 during IFW. As highlighted in the methodology, the in-situ synchrotron diffraction experiments performed to obtain these results were extremely complex. Beyond the experimental challenges, the combination of thermal and mechanical effects which occurred during IFW produced changes in the diffraction data that required de-convolution in order to form some understanding of the mechanical influence on the phase transformations.

The current understanding of the heat evolution in the IFW process would lead to the logical expectation that phase transformations would occur at the contact interface first, as this is the location at which heat is generated. Conduction of this heat axially through the specimens would then cause phase transformations further from the interface, as the Heat Affected Zone (HAZ) formed and evolved.

## **4.2 IFW process data**

For each weld performed during the in-situ synchrotron diffraction experiments, the rundown in rotational velocity and the upset have been recorded. The energy input rate can be derived from the rundown curve, and the upset response can allow for thermal, mechanical and microstructural predictions to be made based on deformation rates, conditioning time, total burn-off upset and consolidation. Furthermore, when performing welds using the same process parameters, an assessment of the repeatability of the process and material used can be conducted.

Here, the repeatability of the weld outputs is of extreme importance. The evolution of microstructure at a single axial location, such as the contact interface, could not be evaluated from a single weld due to the fact that the specimens shorten during the process. Therefore, repeat welds using different initial synchrotron beam positions were performed to allow for this information to be captured at different points in time, thus allowing for this evolution to be characterised. Therefore, it was desirable for the process outputs to be identical for the repeat welds, so that the process behaviour for each weld could be treated as identical permitting the assumption that variations in diffraction data are not caused by differences in process response.

### **4.2.1 Weld outputs and repeatability assessment**

The rotational velocity and upset of the five BS1407 repeat welds (P1-P5) are presented in Figure 4.1. Here, the weld durations have been evaluated as the time at which the rotational velocity reading reached zero. The total upset has been measured from the LVDT recording at a time 0.5 s after the end of the weld.

The rundown data shows a mean weld duration of 1.14 s, and the standard deviation of the five welds was 0.010 s. The standard deviation in weld duration accounts for 8.76 % of the mean value. The upset curves presented in Figure 4.1b provide a mean total upset value of 1.54 mm. The standard deviation of the five repeat welds was 0.087 mm, which is 5.66 % of the mean value.

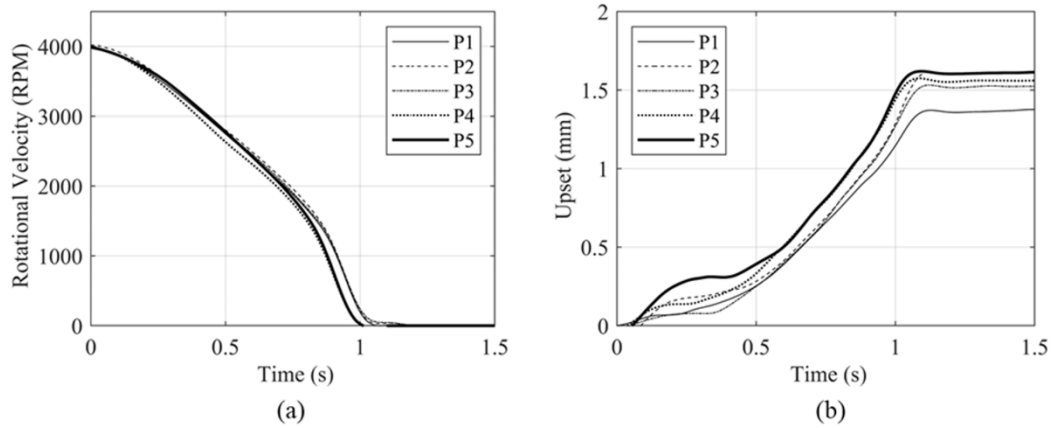


**Figure 4.1:** Weld outputs for the five BS1407 repeat welds. (a) Rundown, (b) Upset.

Here, an allowable scatter of 10 % variation in weld outputs has been defined, due to the small specimen geometry at which these welds were performed. As the standard deviation of repeat welds was within 10 % of the mean value for both measured weld outputs, the welds can be treated as equivalent for the purpose of this study.

For each weld, Equation 3.1 has been used to convert the upset data into the position of the weld interface relative to the centre of the synchrotron beam. This is presented in Figure 4.2. For each individual weld, the weld interface is aligned with the centre of the synchrotron beam at a different time. Note that the weld interface positions at the start of each weld,  $t = 0$ s, were consistent with the axial offset positions presented in Table 3.7.

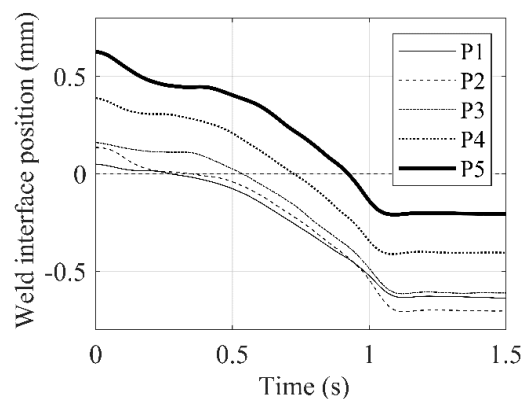


**Figure 4.2:** Weld interface position relative to the synchrotron beam centre for the five BS1407 welds conducted.

## 4.3 Phase transformations

### 4.3.1 Analysis of directional strain

When using Debye-Scherrer diffraction rings for diffraction data analysis, it is desirable to perform full Azimuthal integration over the diffraction rings to utilise all of the available data. However, in cases where directional strains may be present, Azimuthal integration may not be feasible due to the different behaviour exhibited at different  $\psi$  angles in the diffraction rings. To show the difference in the FCC and BCC phase structures, two sets of Debye-Scherrer diffraction rings are presented in Figure 4.3. These were recorded during weld S1, P4. Figure 4.3a was recorded at a weld time of 0 s and shows the parent BCC ferrite phase. Figure 4.3b was recorded at a time of 0.6 s and shows the FCC austenite phase structure.

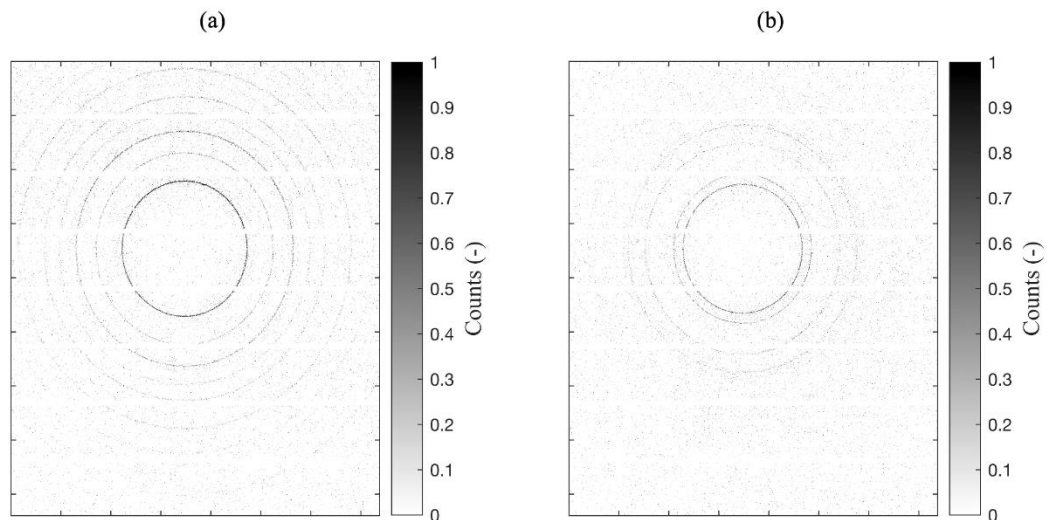


**Figure 4.3:** Debye-Scherrer diffraction rings recorded during weld S1, P4. (a)  $t = 0$  s, (b)  $t = 0.6$  s.

To ensure that full Azimuthal integration was feasible, the variation in the diffraction pattern with the Azimuth angle in the diffraction rings has been investigated. Using a pre-weld diffraction image of BCC ferrite recorded from weld P4 at  $t = 0$  s, the diffraction rings have been divided into bins of  $1^\circ$  in the Azimuth and plotted for the full  $360^\circ$  rings. This is presented in Figure 4.4.

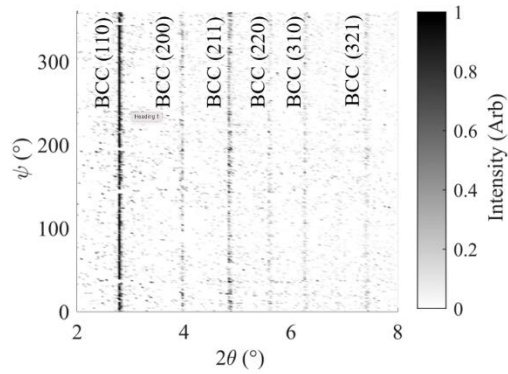


**Figure 4.4:** The diffraction pattern of BCC ferrite at  $1^\circ$  intervals in the Azimuth range.

It can be seen in Figure 4.4 that there is very little variation in the diffraction angle of the BCC ferrite peaks across the  $360^\circ$   $\psi$  range. This shows that there is minimal directional effect in the material prior to welding, and full Azimuthal integration can be performed for these images. It should be noted that the noise present in Figure 4.4 is attributed to the high acquisition rate and high detector sensitivity.

However, the study presented in Figure 4.4 only accounts for one image recorded prior to welding. Therefore, to ensure that any directional effects did not become prominent during the whole welding process, images were extracted at 0.05 s increments from weld P4. Weld P4 was chosen for this analysis as both ferrite and austenite were present for a significant portion of the weld duration. For each diffraction image,  $10^\circ$  slices at the principal axes  $0^\circ$  and  $90^\circ$   $\psi$  were extracted, alongside full Azimuthal integration, producing three unique diffraction patterns. For each diffraction pattern, the BCC (110) and FCC (111) peaks, when present, were fitted. The variation in  $2\theta$  and d-spacing for each peak throughout the duration of welding was recorded and is presented in Figure 4.5 for the BCC (110) peak.

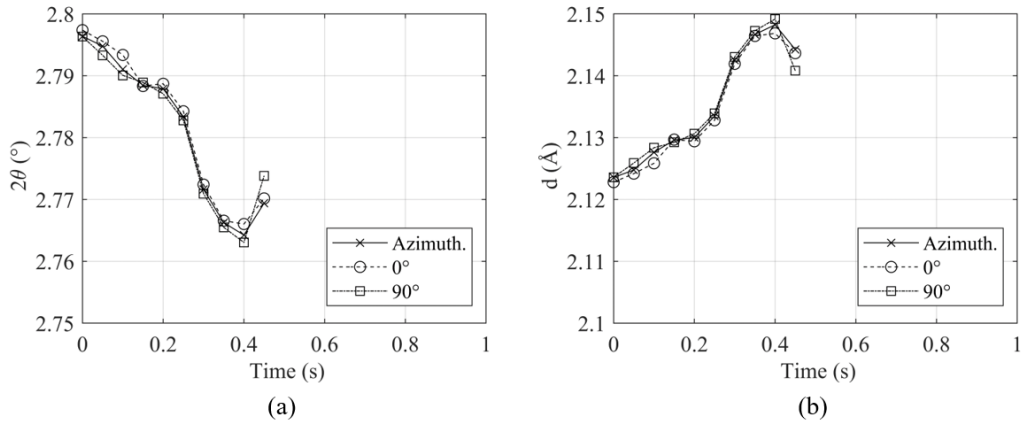


**Figure 4.5:** Variation in peak parameters throughout weld P4 for the (110) BCC Ferrite peak. (a) Diffraction angle,  $2\theta$ . (b) d-spacing.

Figure 4.5 shows that despite there being fluctuations in the peak values during the process, there is little difference in the value shown by full Azimuthal integration when compared to the principal angles. When comparing against the Azimuthal integration, there was no more than 0.16 % difference between the value measured in either principal direction, for either variable.

Figure 4.6 presents the variation in peak parameters throughout weld P4 for the Austenitic FCC (111) peak. Similar to the BCC (110) peak, there is little variation between the principal directions and the full Azimuthal integration values. The maximum difference measured was between the 0 ° direction and full integration at  $t = 0.6$  s, with a difference of 0.15 %.

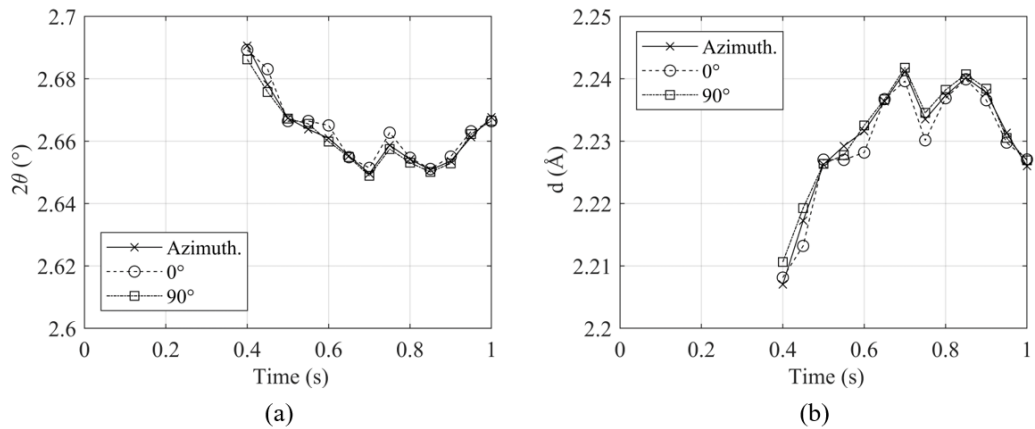


**Figure 4.6:** Variation in peak parameters throughout weld P4 for the (111) FCC Austenite peak. (a) Diffraction angle,  $2\theta$ . (b) d-spacing.

### 4.3.2 Time-resolved XRD spectra

Whilst an understanding of the weld interface position and a set of repeat welds are required to fully understand the microstructure evolution throughout IFW, plotting of a single series of diffraction data does highlight some interesting artefacts. In Figure 4.7, the time-resolved diffraction patterns recorded during weld P1 are presented. Here, every 20<sup>th</sup> image of the 100 fps diffraction data is plotted for clarity.

The peaks present in the pre-weld diffraction data highlight the presence of Body Centred Cubic (BCC) ferrite. At  $t = 0$  s, the parts come into contact and the weld commences. A phase transformation can be seen approximately 0.2 s into the weld process, as the systematic presence of peaks changes. The phase which forms is Face Centred Cubic (FCC) austenite.

Once the weld completed at 1.1 s, no further heat generation occurred in the weld and the effects of cooling can be seen in the diffraction data. After 1.1 s, the intensity of the FCC austenite peaks decreases, and re-formation of the BCC ferrite peaks occurs simultaneously. After approximately 3 s, no further changes are observed in the diffraction profile. Both FCC austenite and BCC ferrite are present in the post-weld microstructure.

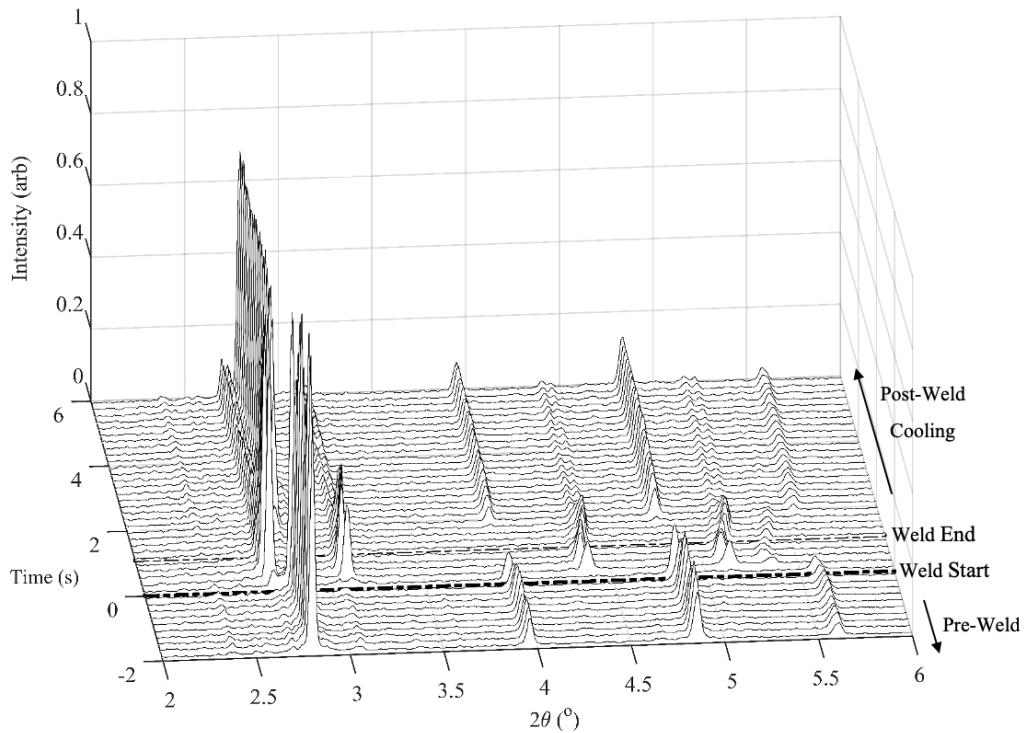


**Figure 4.7:** Waterfall plot of the XRD data series produced during weld P1, where every 20<sup>th</sup> image of the 100 fps diffraction acquisition is presented for clarity.

### 4.3.3 Process-resolved XRD spectra

The raw diffraction patterns processed from each weld can be compared to show some initial trends in the results. In this analysis, weld P2 has been omitted due to the small variation in initial axial offset ( $z_0$ ) between this weld and the neighbouring welds. Figure 4.8 presents the weld interface position for each weld alongside the diffraction data series for each individual weld. The dashed line in each plot of diffraction data series represents the intersection of the weld interface and synchrotron beam. It is recommended that this Figure is used in conjunction with Figure 3.5 to assist the understanding of the microstructure evolution.

In each series of diffraction data, the phase transformation from BCC ferrite to FCC austenite can be seen. Comparing welds side-by-side shows that by increasing the axial offset ( $z_0$ ) value, the time taken for the transformation to occur increases. This is due

to the larger amount of upset required to bring the region surrounding the contact interface, where temperatures are highest, into the synchrotron beam.

During IFW, heat is generated at the weld interface and conducted axially through the specimens. This causes production of the Heat Affected Zone (HAZ), which is defined as the region in which the temperature history is extreme enough to cause substantial changes to the microstructure (i.e., for phase transformations to occur). Therefore, in the set of diffraction data presented in Figure 4.8b, the presence of austenite is expected to occur when the HAZ enters the beamline. In Figure 4.8a, the value of  $z(t)$  at which the first formation of austenite is seen in the diffraction data is marked with a cross. The evolution of the HAZ is seen through this approach, as welds with larger  $z_0$  values display the presence of austenite in the microstructure at larger values of  $z(t)$ , when the weld interface is further from the beamline centre.

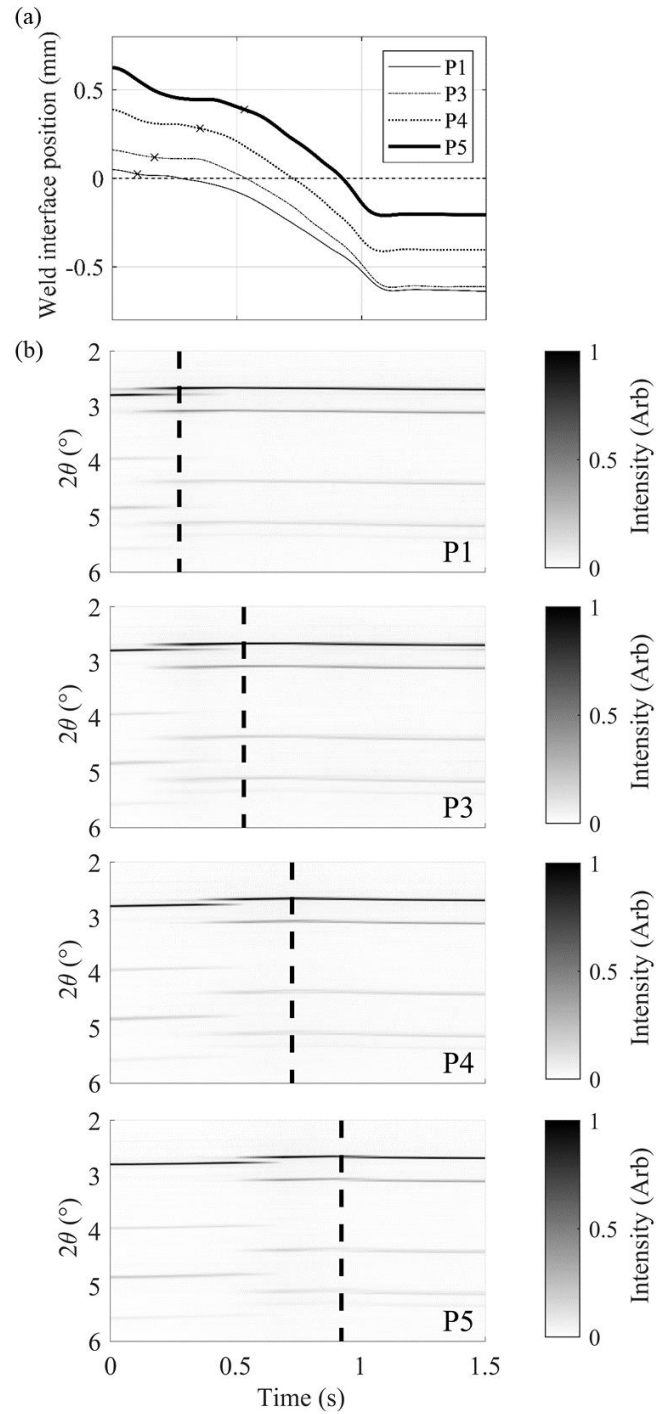


**Figure 4.8:** Comparison of weld interface position relative to the synchrotron beam, alongside diffraction data for 4 welds; (a) Position of the weld interface relative to the beam; (b) X-ray diffraction data labelled for repeat welds. The dashed line in each plot of (b) represents the intersection of the weld interface and the synchrotron beam centre presented in (a). Each position curve in part (a) is marked with a cross at the time at which the transformation from ferrite to austenite occurs in the respective series of diffraction data, showing the increasing size of the HAZ during welding.

#### 4.3.4 Position-resolved XRD spectra

To quantify phase evolution throughout the IFW process, Rietveld refinement has been performed on a selection of images recorded during the in-situ diffraction experiments. Two diffraction patterns are presented in Figure 4.9, alongside the refined calculation produced by GSAS-II. Figure 4.9a shows a diffraction pattern recorded prior to welding, which consists of BCC ferrite with a lattice parameter of  $3.0038 \text{ \AA}$ , and a phase fraction of 99.8 %. In Figure 4.9b, the diffraction pattern presented is that from weld S1, P1, at a weld time of 0.28 s, when the contact interface and synchrotron beam centre were aligned. In this image, the phase fractions were calculated to be 30.2 % austenite and 59.8 % ferrite. The lattice parameter of FCC austenite in this image was calculated as  $3.8431 \text{ \AA}$ .

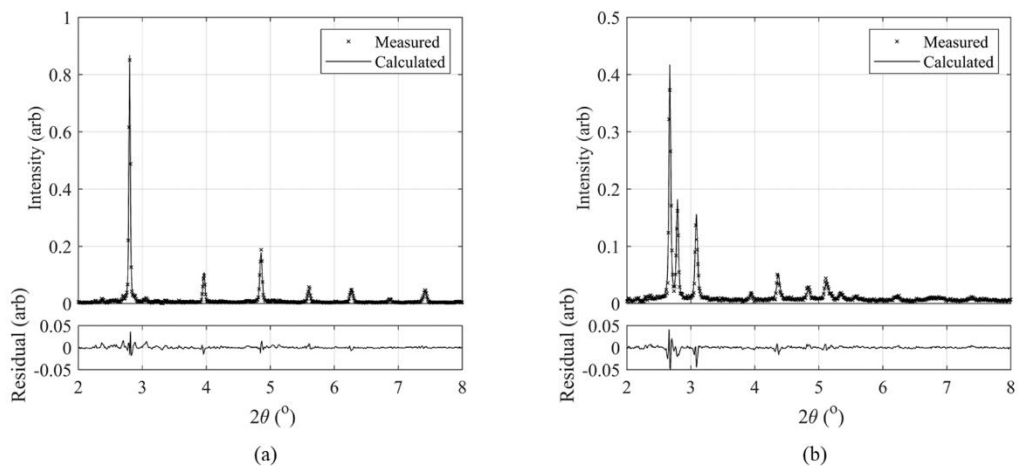


**Figure 4.9:** GSAS-II refinement for diffraction images from (a) the parent material prior to welding; (b) the weld interface 0.28 s into weld S1, P1.

For each repeat weld, the IFW machine data was processed to highlight the diffraction image acquired when the weld interface was aligned with the centre of the synchrotron beam. These images have been extracted and full Rietveld analysis has been performed to estimate the phase fractions of ferrite and austenite in each image. This allows for quantification of the austenite phase fraction at the contact interface throughout IFW and is presented in Figure 4.10.

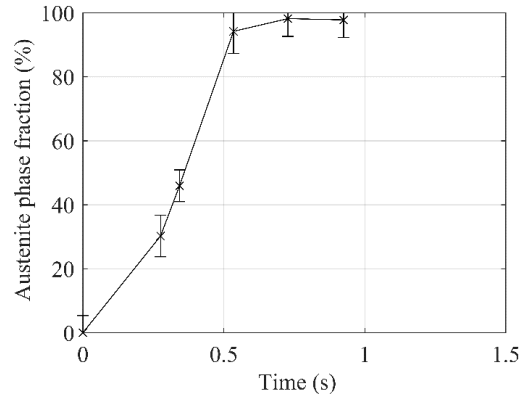


**Figure 4.10:** Evolution of the austenite phase fraction at the contact interface throughout IFW. Each data point is taken from a repeat weld of parameter set S1, refined from the diffraction image recorded when the weld interface and synchrotron beam centre were coincident. The point at  $t = 0$  s was evaluated from a pre-weld diffraction pattern of the parent microstructure.

The contact interface microstructure transformed from fully ferritic at the start of the weld, to an austenite fraction of 30.2 % at a weld time of 0.28 s. Using the calculation of the ferrite to austenite transformation temperature produced by ThermoCalc (725 °C - 734 °C), formation of austenite in this time suggests heating rates in excess of 2000 °C/s at the contact interface. After a weld time of 0.5 s, the weld interface phase fraction remained in excess of 95 %, however, at no point was this seen to reach the expected value of 100 %. It is thought that the high acquisition rate used when acquiring images has increased the contribution of background noise in these diffraction patterns. Due to this, there still appeared to be a small [110] BCC peak of similar lattice parameter to the ferrite phase, which contributed up to 5 % fraction of ferrite. The error bars plotted in Figure 4.10 are assessed from the residual produced by the Rietveld refinement, and it provides confidence that the anticipated error extends to 100% austenite fraction in the diffraction images recorded after a weld time of 0.5 s.

It is commonly assumed that during IFW, the thermal and mechanical (and thus microstructural) evolution is axially symmetrical about the contact interface. This has been shown by post-weld hardness assessments and microstructural examination. The data collected in these novel experiments allows for an assessment of the symmetry

of the microstructure evolution during the process. Figure 4.2 has been used to highlight time points during the process at which two of the repeat welds have equal and opposite distances between beamline centre and contact interface. The images recorded from these points have then been extracted and processed using the methods discussed previously.

Table 4.1 presents four pairs of diffraction images. For each image, the weld from which it was recorded is noted alongside the weld time and axial offset from beamline centre to contact interface. For each image, the austenite volume fraction is presented, alongside the error which has been calculated from the residual of the Rietveld refinement. Finally, the change in lattice parameter from the parent values is presented. Note, when the phase fraction of a phase is less than 5 %, its lattice parameter has been omitted from the results due to the large influence of background noise as mentioned previously.

The parent lattice parameters have been calculated as follows. For ferrite, this has been taken from pre-weld data, producing a value of 3.0038 Å. As the austenite forms during the process, temperature and strain have an influence on the lattice parameter. Therefore, post-weld data has been analysed for weld P2, as the position of the beamline at the end of the weld is furthest from the weld interface, and so effects of temperature and strain on the lattice parameter will be least significant. The average value of the austenite lattice parameter in the post weld state was 3.7747 Å.

**Table 4.1:** Comparison of diffraction images for assessment of the microstructural symmetry about the contact interface.

<b>Weld</b>	<b>Time (s)</b>	<b>Weld interface position (mm)</b>	<b><math>\Delta a_{\text{ferrite}}</math> (%)</b>	<b><math>\Delta a_{\text{austenite}}</math> (%)</b>	<b>Austenite phase fraction (%)</b>
P1	0.451	-0.0526	-	2.112	95.9 ± 8.1
P3	0.455	0.0542	-	2.280	100.0 ± 4.1
P3	0.645	-0.0885	-	2.343	95.8 ± 8.0
P4	0.640	0.0817	-	2.258	100.0 ± 7.8
P1	0.711	-0.2432	1.054	2.076	90.6 ± 7.1
P5	0.711	0.2342	0.9456	2.285	91.0 ± 5.3
P4	0.830	-0.1090	-	2.712	100.0 ± 7.2
P5	0.831	0.1092	-	2.542	98.2 ± 9.2

A good agreement is shown between the diffraction images recorded on the two specimens at similar times and positions. Firstly, the phase fractions of ferrite and austenite are consistent, and both values calculated are within the error for each of the four pairs. Across the four pairs of images, the difference between change in lattice parameter from the parent values is no more than 0.209 % in any case. This is a promising result considering the slight differences in weld time and weld position that the images were recorded at. These results suggest that at the scale tested, IFW shows microstructural symmetry about the contact interface, and so the IFW rig produced did not cause any undesired effects on the specimens.

The symmetry of the microstructure about the contact interface allows for a map of the microstructure evolution to be produced by inverting the contact interface position about the beamline, for all five repeat welds. This provides a range of points in time and position, at which the microstructure can be quantified. The values can be interpolated between the data points, to provide a full map of the evolution of the microstructure across the weld specimens.

Figure 4.11 presents the austenite fraction quantified from a range of images processed from the five repeat welds performed. The microstructure at the contact interface transforms from fully ferritic to 100 % austenite within 0.6s, consistent with Figure 4.10. Furthermore, the microstructure is seen to transform to full austenite at a distance 0.5 mm from the contact interface at a weld time of 0.95 s. This shows the rapid conduction of heat axially through the specimens. The increase in size of the austenite zone shows the growth of the HAZ throughout the process.

Between 0.5 s and 1 s, the HAZ grows axially at a rate of 2 mm/s across the two specimens. This is surprising considering the upset rate of 1 mm/s occurring during this time. This highlights the extremely large amount of heat generated at the contact interface during IFW, and the rapid rate at which it is conducted axially along the specimens.

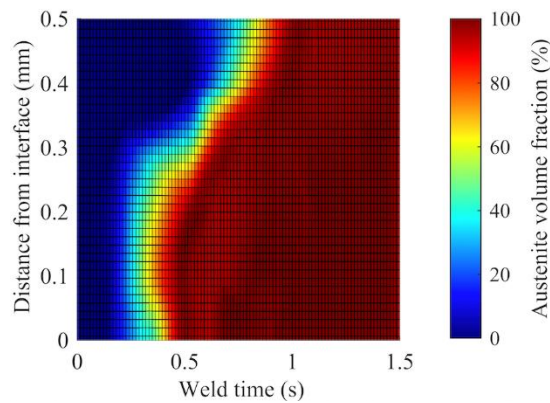


**Figure 4.11:** Axial evolution of the austenite fraction observed during IFW.

In the same manner, the evolution of the lattice parameters of the ferrite and austenite phases can be presented. Here, the percent change in lattice parameter from the predefined parent values is presented. Again, the lattice parameter has been omitted from these results if the phase fraction of the phase is less than 5 %, due to the significant inaccuracies presented by the contribution of background noise on low intensity peaks. In the cases where a composite microstructure is present (i.e., both ferrite and austenite exist), the change in both lattice parameters has been calculated and the mean value presented in the results. The evolution of the lattice parameters is shown in Figure 4.12.

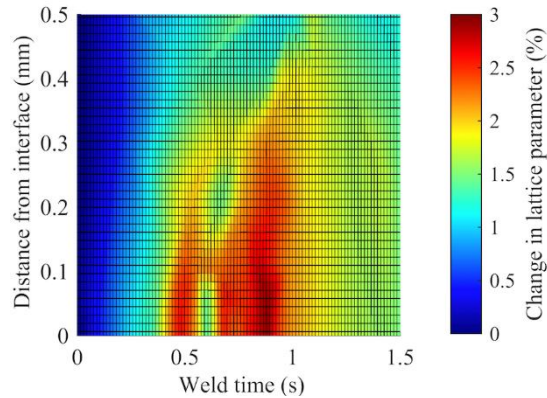


**Figure 4.12:** Percent change of the lattice parameters of ferrite and austenite measured from the in-situ diffraction images.

Figure 4.12 shows a similar trend to that seen in Figure 4.11. The shape of the fully austenitic region in Figure 4.11 correlates to a region in which the lattice parameter increases approximately 1.5 % above the parent values in Figure 4.12. This is expected due to the influence of temperature on the lattice parameter. The increase in temperature leads to thermal expansion, which in turn increases the size of the lattice by increasing the mean distance between atoms. Further to this, a region of increased change in lattice parameter is seen. This region is shown to form at the weld interface at approximately 0.45 s, and this increases in size to an axial length of 0.8 mm at 1.0 s. The lattice parameter in this region shows a 3 % increase above parent values. This is likely indicative of increased strain in this region, showing the formation and evolution of the Thermo-Mechanically Affected Zone (TMAZ). After a weld time of 1.0 s, the end of the weld is shown by a reduction in lattice parameter back towards the parent values, showing the occurrence of post-weld cooling and the ceasing of rotation, reducing the shear strain present in the specimens.

## 4.4 Comparison with microscopic examination

Due to the repeatability of the five welds conducted in this study, a single weld (S1, P5) has been used for comparison with the XRD data analysed. This weld has been prepared as outlined in section 3.2.6 and microscope images taken at 100 x magnification. This image is presented in Figure 4.13 and is annotated for clarification of the different regions produced by the process.

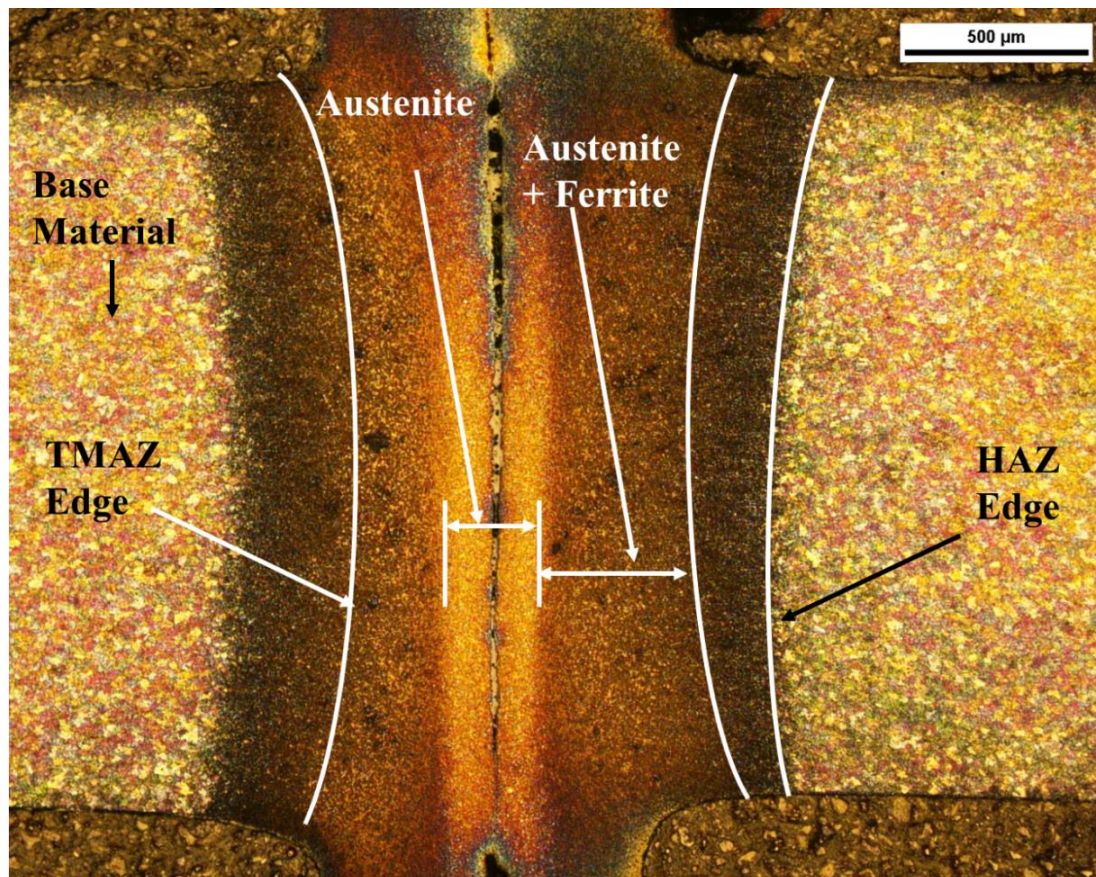


**Figure 4.13:** An annotated radial section of weld P5 showing the region surrounding the contact interface.

### 4.4.1 HAZ size

For comparison with the post-weld optical microscope measurements, in-situ diffraction images recorded for all welds at times of 1.1 s and 100 s have been processed. The austenite phase fraction has been presented alongside the mean size of each relevant region in Figure 4.14.

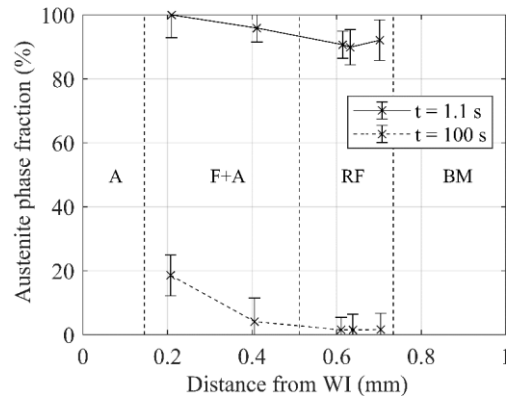


**Figure 4.14:** Austenite volume fraction recorded from in-situ X-ray diffraction at the end of the weld, and after 100 s of post weld cooling. (A = austenite, F+A = ferrite and austenite, RF = reformed ferrite, BM = base material)

The edge of the HAZ is seen to occur 0.73 mm from the weld interface in Figure 4.13. It is shown in Figure 4.14 that at the end of the weld, the microstructure at distances of 0.6 – 0.7 mm from the weld line were approximately 90 % austenite. After post-weld cooling, this transformed back to ferrite (reformed ferrite), shown by the negligible austenite fraction at  $t = 100$  s.

A region with a length of 0.29 mm is seen to contain pure austenite in the optical microscope images. However, no welds were completed with a final weld interface within this range, and so there is no XRD data available to validate this. The axial region between  $z = 0.15$  mm and  $z = 0.51$  mm shows a reduction in austenite fraction with distance from the weld interface. This is seen in the optical microscope images with more reformed ferrite occurring as the distance from the weld interface increases.

#### 4.4.2 TMAZ size

Using Figure 4.13, the mean size of the TMAZ has been calculated as 0.86 mm, which accounts for 0.43 mm on each of the two specimens. To assess whether the lattice parameter variation shows the size of the TMAZ in the post weld state, the variation of the lattice parameters from the parent material have been plotted against the distance from the weld interface. Here, the austenite lattice parameter variation is plotted for  $t = 1.1$ s and the ferrite lattice parameter for  $t = 100$  s, due to the increased phase fraction of each at the respective time points. This is presented in Figure 4.15.

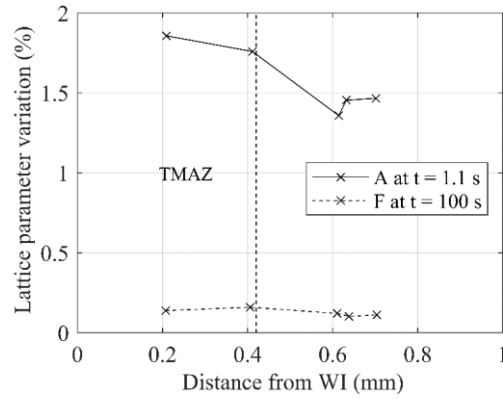


**Figure 4.15:** Axial variation in the lattice parameter calculated from in-situ diffraction data after welding.

There is little evidence of the TMAZ in the post weld state. Whilst there is a slight increase in the ferrite lattice parameter at axial positions of 0.2 and 0.4 mm, there is not enough variation from the values outside the TMAZ to suggest significant strain. However, the lattice parameters recorded at a weld time of 1.1 s show significant evidence of the TMAZ. The lattice parameter outside the TMAZ is approximately 1.4 % above the parent value, due to increased temperature. However, the austenite lattice parameters recorded inside the TMAZ at 1.1 s show a 1.75 % increase above the parent value. This data aligns with the results presented in Figure 4.12, which shows the formation of a highly strained region, which increases in size to approximately 0.4 mm either side of the interface by the end of the weld.

## 4.5 Thermal validation

### 4.5.1 Assessment of weld repeatability

As outlined in Section 3.2.8, a repeat weld was conducted with a spot-welded thermocouple attached to the outer wall of the weld specimen. The axial position of this thermocouple was 0.6 mm from the contact interface, consistent with the  $z_0$  value of weld S1, P5. Similar to the repeatability assessment carried out for welds S1, P1 – S1, P5, the outputs of the repeat weld have been analysed to ensure the welds can be considered similar, and thus the temperature data can be considered to be consistent with the XRD data. The outputs of welds S1, P5 and the repeat weld (RW) are presented in Figure 4.16.

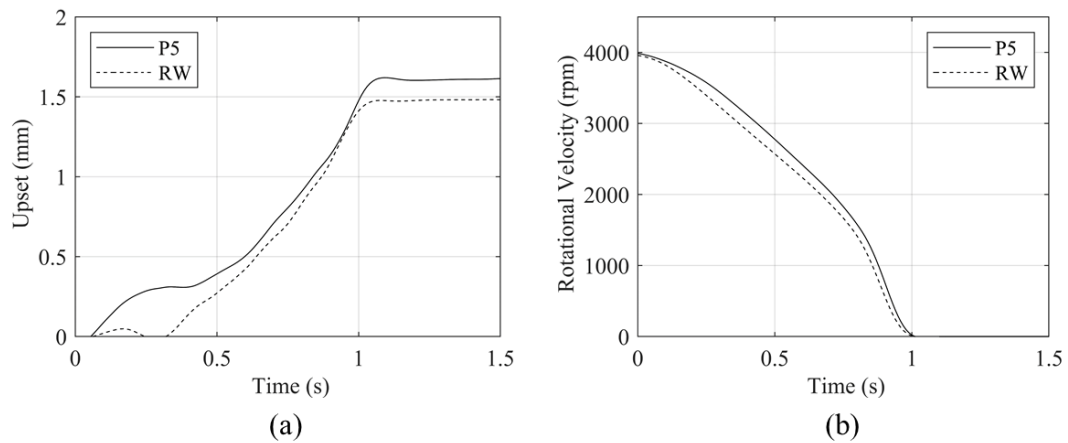


**Figure 4.16:** Comparison of weld output data for in-situ XRD weld P5 and the repeat weld with ex-situ thermocouple measurements; (a) upset; (b) rundown.

For the repeat weld, the weld duration and total upset had variations of -0.960 % and -8.19% respectively, from weld S1, P5. Additionally, there is close agreement in the profiles of the two rundown curves, which indicates that the energy input rates and thus the heat input rates were similar for the two welds. The slight inconsistency between the two upset curves between 0.1 and 0.5 s is anticipated to have occurred due to differences in surface finish at the contact interface of the weld specimens. Another possible source of this difference is friction between the carriage sleeves and tie bars, which may cause unstable movement of the carriage, particularly as the load is ramping up in the early portion of the weld.

#### 4.5.2 Comparison of thermal response and diffraction data.

The thermal measurements recorded during the repeat weld are presented in Figure 4.17.

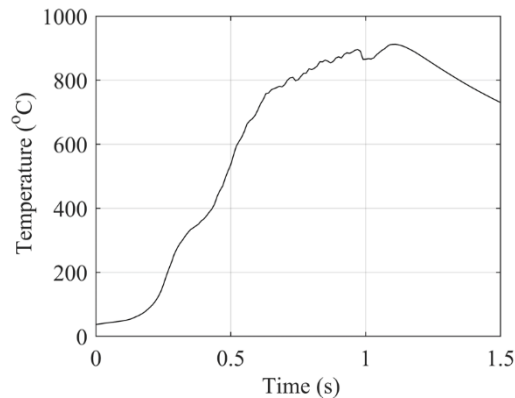


**Figure 4.17:** Temperature measurements recorded during the repeat weld, with a K type thermocouple spot-welded 0.6 mm from the initial weld interface.

The ThermoCalc prediction of the ferrite to austenite transformation temperature range (725 °C to 734 °C) has been used to calculate the equilibrium phase fractions which would be produced at the temperatures recorded during welding. Here, temperatures below 725 °C are completely ferritic, and temperatures above 734 °C produce a 100 % austenitic microstructure. At temperatures between 725 °C and 734 °C, a linear interpolation has been used to estimate the phase composition. In Figure 4.18, the estimated equilibrium austenite fraction is presented alongside the austenite fraction calculated from the diffraction data of weld P5, where each diffraction image has been processed and refined as outlined in Section 3.2.8.

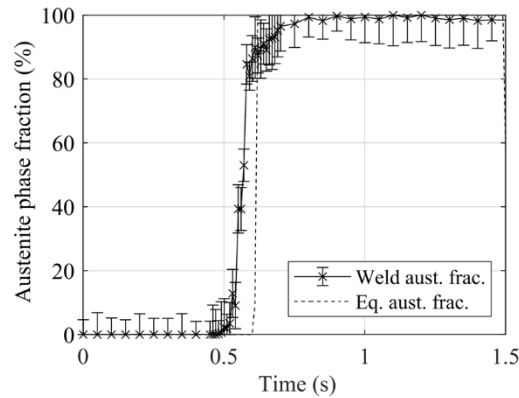


**Figure 4.18:** The austenite phase fraction evolution from weld S1, P5, presented alongside the estimated austenite fraction evaluated from thermal measurements of the repeat weld.

Figure 4.18 shows that the transformation from ferrite to austenite in the diffraction data for weld S1, P5 occurred prior to equilibrium estimations evaluated from thermal measurements of the repeat weld. The transformation is seen to occur approximately 0.12 s prior to the equilibrium transformation. Directly comparing the processed diffraction data and the thermal measurements reveals that the first presence of austenite occurs when the weld temperature is 495 °C, which is 230 °C below the equilibrium start temperature.

There are some possible sources of error which may influence the temperature recording. Firstly, the sensitivity of a K type thermocouple is  $\pm 2.2$  °C or  $\pm 0.75$  % of the temperature. Assuming the phase transformation present in the diffraction data is occurring at equilibrium, the presence of austenite would require a weld temperature of 725 °C, providing a maximum systematic error of  $\pm 5.44$  °C. Additionally, the measurement location was different for the XRD measurements and the thermocouple recordings. The synchrotron beam penetrated a chord of the weld specimen, which cannot be replicated by the thermocouple, which was spot-welded to the outer diameter of the specimen. However, due to the small radial wall thickness of the weld specimens, any radial gradients in temperature were expected to be negligible. Therefore, the XRD measurements should match up to the thermal history, as the microstructure should have a negligible gradient in the radial direction.

Another possible source of error was the differences in the gauge volume. The synchrotron beam area was  $100\ \mu\text{m} \times 100\ \mu\text{m}$ , whilst the spot-size of the thermocouple tip was measured to be a circle of 0.6 mm diameter. FE modelling has been used to assess the temperature gradient over this spot size, and any influence of this gradient on the value produced. As the thermocouple is spot-welded to a single weld specimen, as the weld progresses the thermocouple is consumed by the interface. Therefore, to understand the temperature gradient across the thermocouple, the evolution of the weld must be considered. Presented in Figure 4.19 is the position of the thermocouple, starting with an offset of 0.6 mm from the weld interface. The diameter of the thermocouple is accounted for by the dashed lines  $\pm 0.3\ \text{mm}$  from the desired position. It is shown that the thermocouple is likely to enter the interface at approximately 0.7s, where it will be consumed due to the compressive loading at the contact interface. This shows how the size of the measurement location of the thermocouple reduces during welding.

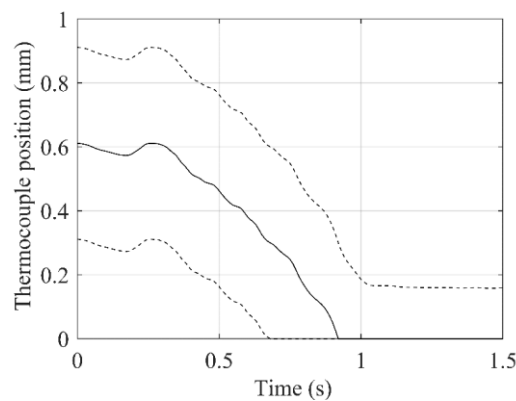


**Figure 4.19:** The position of the thermocouple during the weld, showing how the thermocouple is consumed at the weld interface.

The thermal response from FE modelling has been extracted across the range of axial locations at which the thermocouple and specimen OD are in contact. The temperature at the desired location (spot centre) and the mean temperature across the thermocouple spot are presented in Figure 4.20.

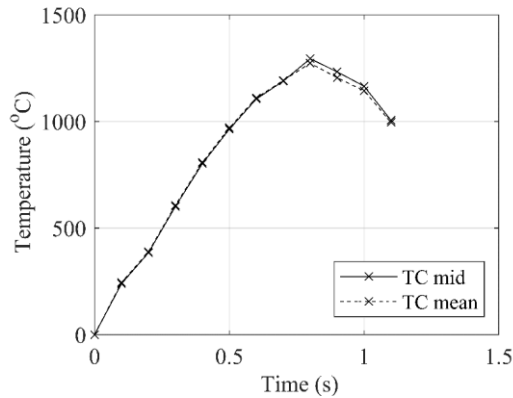


**Figure 4.20:** Comparison of the desired thermal measurement at the centre of the thermocouple, and the mean temperature recorded across the axial profile at which the thermocouple is in contact with the specimen OD.

The thermal profile along the axial profile of the thermocouple spot is almost linear throughout the weld. Therefore, when taking the mean temperature across the axial dimension of the thermocouple spot, there is little variation from the desired measurement, at the spot centre. The maximum difference between desired measurement and mean temperature in the spot is 2.52 %.

Another possible source of error in the temperature recordings arises from positioning of the thermocouple. A 0.2 mm difference in the position of the thermocouple gave rise to an 11 % difference in the temperature calculated in the FE model.

Austenite is first seen in the diffraction data at a weld time of 0.48 s. At this time, the temperature measurement of the repeat weld was 495 °C. Applying the combination of possible error sources to this temperature measurement gives an error of  $\pm 70.6$  °C. With the inclusion of possible errors, the temperature recorded when austenite formation begins is still below the equilibrium transformation temperature. This reveals that non-equilibrium phase transformations are occurring in BS1407 welds. To assess the possible cause of these non-equilibrium phase transformations, the strain in the region surrounding the weld interface has been investigated.

### 4.5.3 Methods of understanding the influence of strain on phase transformations

The results produced clearly show that the transformation from ferrite to austenite occurred below the equilibrium transformation temperature; however, there is a combination of thermal and mechanical effects which occur during IFW which can assist the occurrence of non-equilibrium phase transformations. To investigate this, the approach proposed by Ramesh & Melkote for predicting white layer formation during high-speed machining of tool steels has been used [99]. This method estimates the temperature of a phase transformation based on the stress and strain energy which the material is subjected to, as shown in Equation 4.1:

$$T = T_0 \exp\left(\frac{\Delta_\alpha^\gamma V_m \cdot \sigma - W_S}{\Delta_\alpha^\gamma H_m}\right) \quad (\text{Eq. 4.1})$$

where  $T$  is the transformation temperature which occurs under a stress,  $\sigma$  and strain energy,  $W_S$ .  $T_0$  is the equilibrium transformation temperature,  $\Delta_\alpha^\gamma V_m$  is the molar volume change, and  $\Delta_\alpha^\gamma H_m$  is the molar enthalpy of the transformation from  $\alpha$  to  $\gamma$ .

The temperature data recorded from the repeat weld was used as the transformation temperature,  $T$ . The stress,  $\sigma$ , was calculated from the axial pressure from the weld. Equation 4.1 has then been rearranged to calculate the strain energy required to cause the transformation from ferrite to austenite at the stress and temperature recorded in the weld. Using stress-strain data for BS1407, the strain energy was converted into a strain value for comparison with experimental data.

To estimate the strain which occurs during the process, the size of the deformed zone of a radially cross-sectioned weld has been measured using optical microscopy as shown in Figure 4.13. From this, the minimum and maximum thickness were determined as 0.76 mm and 1.04 mm, respectively. Across the weld specimen chord which the beamline intersects, the average deformed zone thickness was calculated to be 0.86 mm. Assuming the total upset occurred over the deformed zone, the experimental strain was estimated using Equation 4.2:

$$\varepsilon(t) = \frac{u(t)}{z_{def}} \quad (\text{Eq. 4.2})$$

Where  $\varepsilon(t)$  is the strain at time  $t$ ,  $u(t)$  is the upset at time  $t$ , and  $z_{def}$  is the mean axial length of the deformed zone. The comparison between the experimental strain data and the strain required to form austenite at reduced temperatures is shown in Figure 4.21. This suggests that the magnitude of strain in the deformed zone was large enough to assist non-equilibrium austenite formation at a weld time of 0.25 s, which is earlier than the time at which austenite is seen in the diffraction data of weld P5.

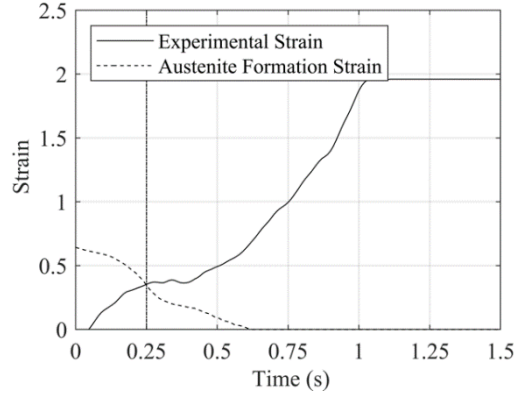


**Figure 4.21:** Estimated experimental strain and the strain required to form austenite calculated from temperatures recorded during the repeat weld. The vertical line at  $t = 0.25$  s indicates the point at which these lines intersect.

To verify the estimated experimental strain profile, the variation of ferrite and austenite lattice parameters have been analysed to estimate the microstrain during the process. The parent lattice parameters are defined as  $3.0038 \text{ \AA}$  for ferrite and  $3.7747 \text{ \AA}$  for austenite, as shown previously. To correctly understand the evolution of the lattice parameters of both phases present, the effects of temperature and strain must be de-convoluted. To do so, reference data for the lattice parameters of ferrite and austenite at difference temperatures [94] has been normalised and applied to the parent lattice parameters found in this experiment, to produce relationships between the lattice parameters and temperature. These relationships have been applied to the temperature data presented in Figure 4.17 to estimate the ferrite and austenite lattice parameters produced at the temperatures experienced in this weld. The microstrain was calculated using Equation 4.3:

$$\varepsilon(t) = \frac{a_{weld}(t) - a_{thermal}(t)}{a_{parent}} \quad (\text{Eq. 4.3})$$

where  $\varepsilon(t)$  is the strain in the phase,  $\alpha_{weld}$  is the lattice parameter of the phase recorded during IFW,  $\alpha_{thermal}$  is the estimated lattice parameter of the phase at the recorded temperature and  $\alpha_{parent}$  is the lattice parameter of the parent material. Here,  $\alpha_{weld}$  is calculated from the mean lattice parameter derived from the peak position of the four peaks with lowest diffraction angle (BCC ferrite: [110], [200], [211], [220] and FCC austenite: [111], [200], [220], [311]).

The strain of both the ferrite and austenite phases is presented in Figure 4.22, alongside the time at which the centre of the X-ray beamline intersects the outer and inner bounds of the deformed zone. This experimental microstrain data matches the trends of the estimated macrostrain, and so there is confidence in the assumptions made here.

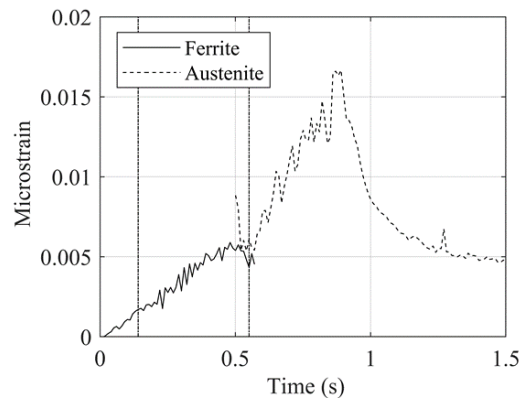


**Figure 4.22:** The microstrain calculated from the lattice parameter evolution of ferrite and austenite. The vertical dashed lines show the time points at which the centre of the X-ray beamline intersects the outer and inner bounds of the deformed zone.

The approach used has estimated that the strain produced in the deformed zone was high enough to assist non-equilibrium austenite formation at a weld time of 0.25 s. However, austenite was not present in the diffraction data until a weld time of 0.48 s. To fully understand this, the position of the weld interface relative to the synchrotron beamline throughout the process must be considered. This is presented in Figure 4.23. In addition, position data at  $\pm 0.43$  mm from the weld interface is presented to show the size of the deformed zone. The size of the deformed zone is presented from a weld time of 0.35 s onwards, as this coincides with the onset of steady-state deformation as

seen in Figure 4.16a. Prior to the occurrence mechanical deformation, it is assumed that the deformed zone developed in size, and that during steady-state deformation the deformed zone size remained constant due to the linear energy input rate and upset rate. It can be seen that the mean deformed zone length intersects the centre of the synchrotron beam at 0.46 s.

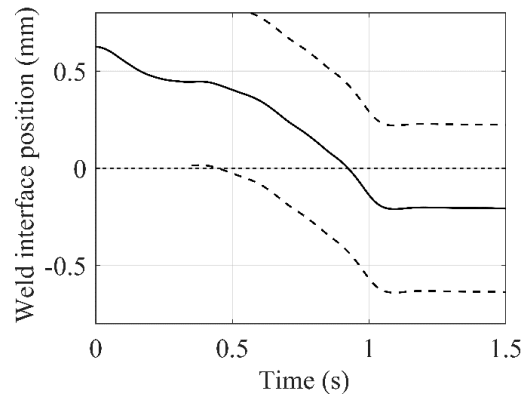


**Figure 4.23:** The position of the weld interface relative to the synchrotron beam for weld P5. The dashed lines show the average thickness of the deformed zone from a time of 0.35 s.

Utilising justifiable and reasonable assumptions, it has been estimated that the strain present in the deformed zone of this weld was large enough to assist non-equilibrium austenite formation at a weld time of 0.25 s. As the weld progressed, the deformed zone was pushed into the stationary X-ray beamline at 0.46 s, which in turn displayed the presence of austenite in the diffraction data at 0.48 s.

## 4.6 Conclusions

The novel implementation of in-situ synchrotron diffraction for the IFW process has quantified the microstructure evolution which occurs during welding of BS1407 steel. The phase fractions of ferrite and austenite have been quantified at the contact interface, which showed that the microstructure at the interface was fully austenitic within 0.52 s of the weld commencing. Additionally, it was observed that at 0.27 s, the austenite phase fraction was 52 %, which suggest heating rates at the interface are in excess of 2000 °C/s.

These analysis approaches have been extended across a range of axial positions from which diffraction data was recorded for the five welds. Phase fraction data has been analysed to quantify the evolution of the HAZ during IFW. The HAZ was first observed at 0.27 s, and was shown to rapidly grow axially, exceeding an axial length of 1 mm 0.87 s into the weld.

Analysis of the lattice parameter evolution during IFW showed two discrete regions which formed and evolved. The first region was consistent in size with the HAZ, indicating the effect of thermal expansion on the lattice. A smaller region with a larger change from parent lattice parameter was also observed, which was attributed to mechanical strain in the TMAZ. This region was first observed at a weld time of 0.42 s and was seen to increase to an axial size of 0.8 mm at the end of the process.

Ex-situ thermal validation of the processed diffraction data highlighted the existence of non-equilibrium phase transformations occurring in the TMAZ. The localisation of strain in the TMAZ during upsetting of the specimens has been proven to be significant enough to assist the transformation from ferrite to austenite at temperatures below the equilibrium transformation temperature.

## Chapter 5

# Characterisation of Nickel-Based Superalloy

## Microstructure Evolution During IFW

### 5.1 Introduction

There is an incomplete understanding regarding the mechanisms which drive the macro-scale evolution of the Inertia Friction Welding process. In order to develop the understanding of the microstructure evolution of Nickel-based superalloys during IFW, in-situ synchrotron diffraction experiments were performed for RR1000. The purpose of these experiments was to produce novel information regarding the dissolution behaviour of  $\gamma'$  phase throughout the IFW process, and the sensitivity of this behaviour to weld parameters.

To characterise the microstructure evolution and assess whether this may drive the evolution of the process seen on the macroscale, the three stages of the process; conditioning, burn-off and consolidation, were analysed separately. The evolution of the HAZ and the spatial distribution of  $\gamma'$  are evaluated for these three stages. These weld stages are defined from the upset behaviour of a weld and are presented for an example upset curve in Figure 5.1.

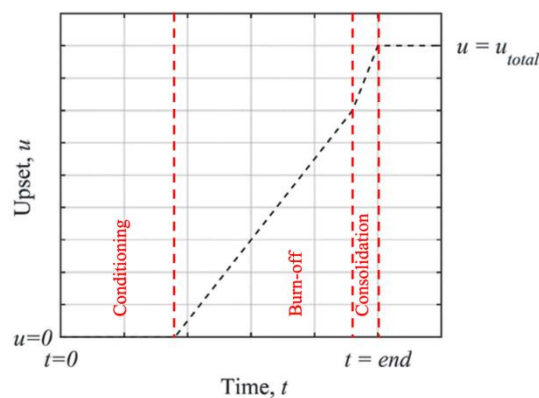


**Figure 5.1:** The three stages of the IFW process as defined through transitions in the upset data.

In the conditioning stage, there is no upset. However, it is observed that this stage very quickly transitions into the burn-off stage at which steady-state mechanical deformation occurs at a significant rate. It is expected that during the conditioning stage the generation of heat at the interface and conduction of this axially through the specimen causes dissolution of the  $\gamma'$  precipitates around the contact interface. This stage is expected to continue until there is enough material which has sufficiently reduced in strength to allow the onset of mechanical upset under the axial load applied. However, the axial length of this region is unknown, as is whether this region is sensitive to the process parameters.

During burn-off, the upset rate is constant. It is expected that during this stage, the energy input and mechanical upset will offset one another, producing an axial profile in the microstructure which is also steady-state. Further to this, there is an expectation that the axial length of the region in which  $\gamma'$  is dissolved from the microstructure will be somewhat proportional to the rate of upset, with a wider zone allowing for increased mechanical deformation and a larger upset rate.

The upset rate is largest during the consolidation stage. This is usually coupled with an increase in energy input rate at the end of the weld. During this stage, it is expected that the broad zone in which the  $\gamma'$  volume fraction is reduced will be rapidly ejected from the contact interface, bringing cooler material with an increased  $\gamma'$  volume fraction into the weld interface. Whilst it is known that there is a HAZ present in the as-welded condition, it would be logical that this has a smaller axial length than its size measured during burn-off, as this is ejected during consolidation.

Post-weld investigation of as-welded IFWs often define two discrete zones within the HAZ. These are named the primary  $\gamma'$  free zone (PGPFZ) and the secondary  $\gamma'$  free zone (SGPFZ). A typical weld section is presented in Figure 5.2 with these regions labelled. The PGPFZ is located closest to the interface, as the primary  $\gamma'$  precipitates require temperatures in excess of 1000 °C for dissolution to occur. Additionally, the primary precipitates are largest and so require a longer time at elevated temperatures to fully dissolve. On the contrary, secondary  $\gamma'$  precipitates can dissolve at lower temperatures (approximately 800 °C) and their smaller size permits the occurrence of full dissolution in shorter times. Due to these factors, the SGPFZ has a much larger axial length. Unfortunately, the two distributions of precipitates cannot be resolved

from one another using X-ray diffraction, however, the in-situ measurements of  $\gamma'$  volume fraction have been used alongside this understanding to evaluate which of the precipitate distributions may have dissolved in the process.

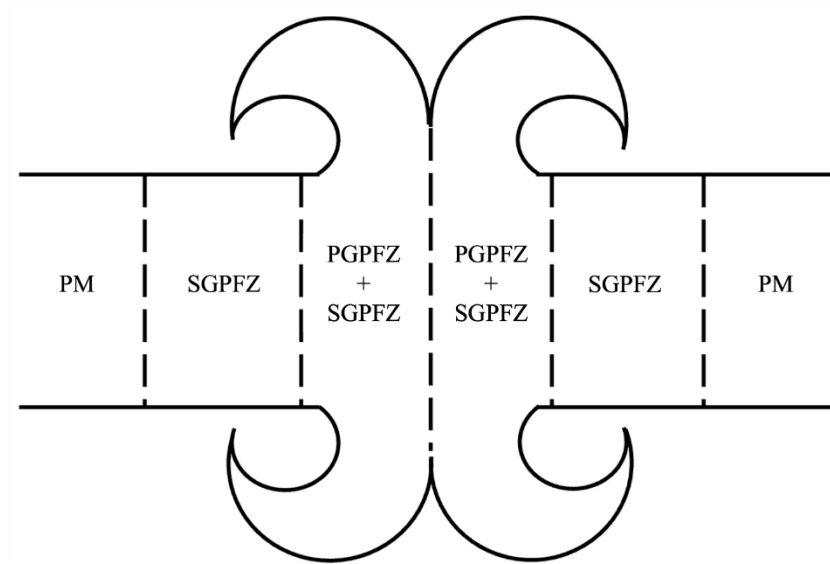


**Figure 5.2:** A representative IFW weld section showing approximate sizes of the primary  $\gamma'$  free zone (PGPFZ) and secondary  $\gamma'$  free zone (SGPFZ).

## 5.2 IFW process data

Due to the complex nature of the experimental methodology, multiple repeat welds of identical input parameters were required to assess the axial profile of microstructure evolution during IFW. For each repeat weld, the stationary synchrotron beamline was offset by a different axial distance from the initial contact interface.

The four sets of process parameters investigated in this study produced varying amounts of upset. Therefore, to acquire microstructural data from an appropriate range of axial positions, the axial offset distances between the beamline and contact interface were varied for each set of process parameters.

The four sets of weld parameters investigated for RR1000 inertia friction welding are presented in Table 5.1, and the axial offset of the beamline from the initial contact interface are provided in Table 5.2

**Table 5.1:** IFW input parameters for Nickel-based superalloy welds.

<b>Parameter Set</b>	<b>Rotational Velocity (rpm)</b>	<b>Flywheel Inertia (kg.m<sup>2</sup>)</b>	<b>Specific Energy (MJ/m<sup>2</sup>)</b>	<b>Axial Load (N)</b>	<b>Axial Pressure (MPa)</b>
N1 (LS, HP)	2800	0.0344	42.79	1300	106.1
N2 (LS, LP)	2800	0.0344	42.79	3000	45.98
N3 (HS, LP)	4000	0.0344	87.33	1300	45.98
N4 (HS, HP)	4000	0.0344	87.33	3000	106.1

**Table 5.2:** The axial offset positions between initial contact interface and X-ray beam centre for the Nickel-based superalloy IFWs.

<b>Axial offset name</b>	<b>N1 Offset (mm)</b>	<b>N2 Offset (mm)</b>	<b>N3 Offset (mm)</b>	<b>N4 Offset (mm)</b>
P1	0.05	0.05	0.05	0.05
P2	0.20	0.15	0.15	0.75
P3	0.55	0.40	0.30	1.65
P4	0.85	0.45	0.50	-

### 5.2.1 Weld outputs

For each set of process parameters, the welds were grouped, and the macro-scale process outputs were used to calculate a mean profile of rundown and upset. This provides an average weld for each set of process parameters. The upset profiles of the individual welds can then be compared with that of the mean weld, to evaluate the difference in upset, and thus any error in axial position when plotting the axial profile of microstructure.

#### 5.2.1.1 Parameter set N1

The rundown and upset for the RR1000 repeat welds of parameter set N1 are presented in Figure 5.3, alongside the mean data for this parameter set. Additionally, the position of the weld interface relative to the stationary X-ray beamline for each of the four repeat welds is presented in Figure 5.4. For the four welds performed using these input parameters, the mean duration was 2.54 s, with a standard deviation of 0.06 s. The mean total upset value for the four welds was 1.690 mm, with a standard deviation of 0.123 mm. For the weld duration and total upset, the standard deviation was 2.27 % and 8.06 %, respectively, of the mean values.

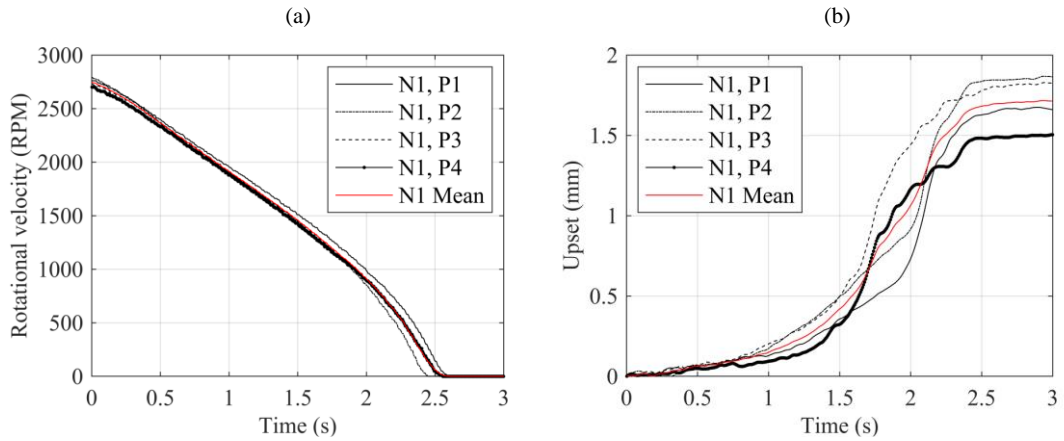


**Figure 5.3:** Weld outputs for the four repeat welds of parameter set N1 and the mean value calculated from these. (a) Rundown, (b) Upset.

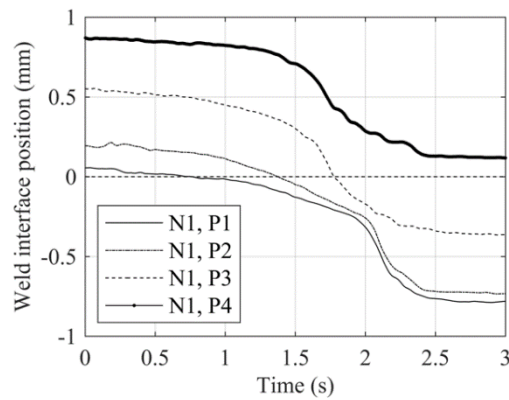


**Figure 5.4:** Position of the weld interface relative to the stationary beamline for the four RR1000 welds performed with input parameter set N1.

### 5.2.1.2 Parameter set N2

The weld outputs for the four RR1000 IFWs conducted with input parameter set N2 are shown in Figure 5.5. The position of the weld interface relative to the X-ray beam is presented in Figure 5.6. In Figure 5.5b, it can be seen that the upset of weld N2, P4 was approximately 40 % lower than that of the other welds, despite having a rundown curve which was consistent with the other welds of parameter set N2.

Due to this, weld N2, P4 was omitted from the calculation of the mean rundown and upset values. However, this weld is still included in the analysis of diffraction data to

assess whether the microstructural information acquired can assist the understanding of why this weld produced a smaller upset response.

After removal of weld N2, P4, the remaining welds had a mean duration of 3.20 s, and a standard deviation of 0.21 s. The mean total upset of the three welds was 0.912 mm, with a standard deviation of 0.055 mm. For the weld duration and total upset, the standard deviation was 6.48 % and 6.08 % of the respective mean values.

It is observed in Figure 5.5a that the averaging of the weld rundown curves produced an unnatural artefact at the end of the process. Due to the fact that the weld durations were slightly different for each weld, at a weld time of 3 s, some of the welds had been completed whilst others were still ongoing. The averaging in this region appears to produce an effect in which the rundown appears to ‘tail off’ with a slower deceleration than is seen in the raw weld data. Whilst this is not true to the actual process behaviour, it was expected that this would not cause any inaccuracies in data processing as it occurred at the end of the process and thus has a very insignificant effect.

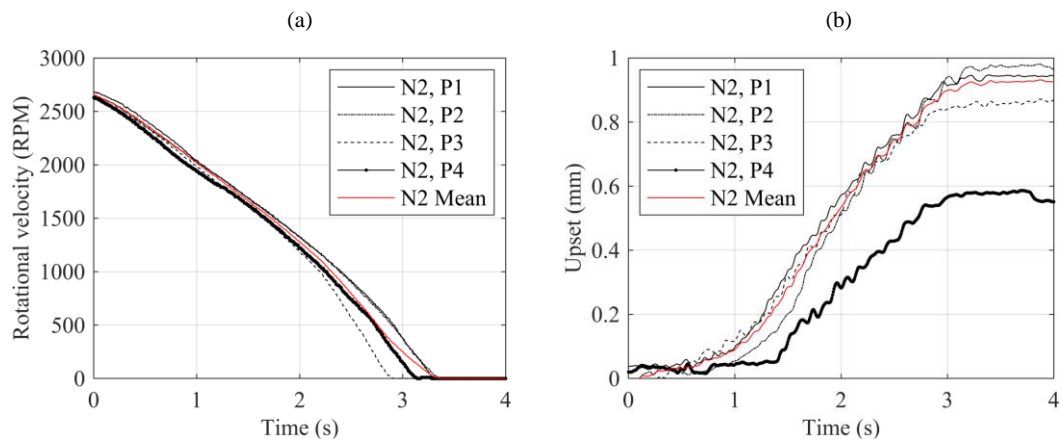


**Figure 5.5:** Weld outputs for the RR1000 repeat welds performed with input parameter set N2, alongside the mean values calculated from welds N2, P1; N2, P2 and N2, P3. (a) Rundown, (b) Upset.

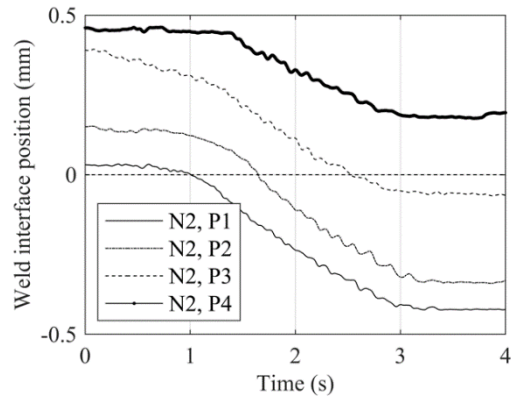


**Figure 5.6:** Position of the weld interface relative to the stationary beamline for the four RR1000 welds performed with input parameter set N2.

### 5.2.1.3 Parameter set N3

For IFW input parameter set N3, the rundown and upset curves are presented in Figure 5.7. Furthermore, the position of the weld interface relative to the beamline for each repeat weld is shown in Figure 5.8. For this parameter set, the mean outputs were calculated from all four repeat welds. The effect of increasing the total energy input for parameter set N3 is prominent here, as the duration of these welds was much greater than those of parameter sets N1 or N2.

For these four welds, the mean weld duration and total upset were 6.03 s and 0.987 mm, respectively. For the weld duration, the standard deviation was 0.21 s, or 3.48 % of the mean value. The standard deviation of the total upset was 0.138 mm, or 14.0 % of the mean value.

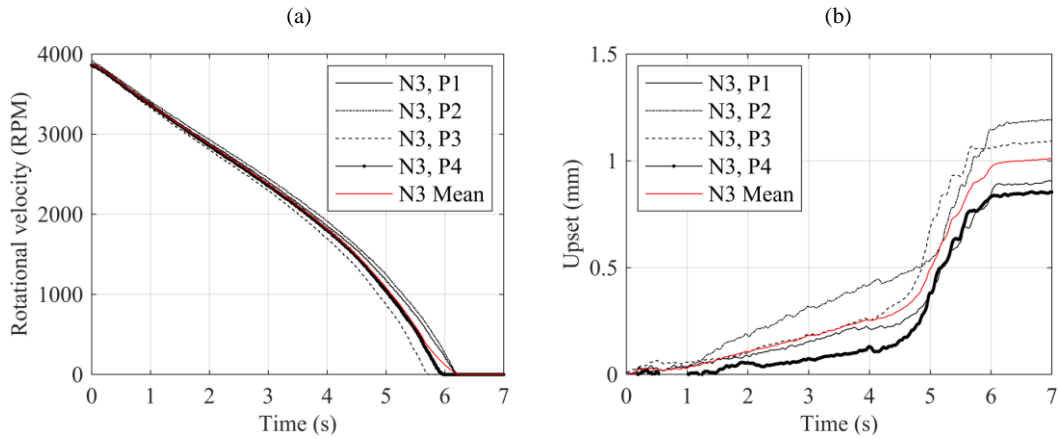


**Figure 5.7:** Weld outputs for the RR1000 repeat welds performed with input parameter set N3, and the mean outputs calculated from these. (a) Rundown, (b) Upset.

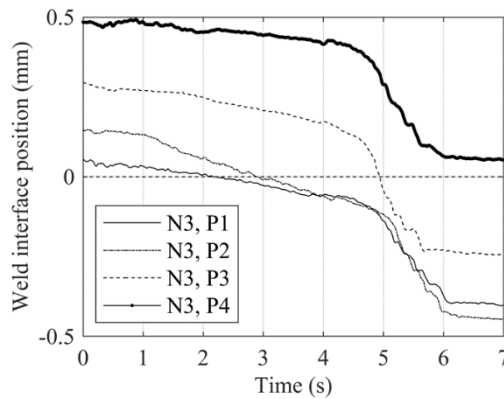


**Figure 5.8:** Position of the weld interface relative to the stationary beamline for the four RR1000 welds performed with input parameter set N3.

#### 5.2.1.4 Parameter set N4

Due to the limited availability of specimens, only three repeat welds of parameter set N4 could be performed. For these three welds, the rundown and upset are presented in Figure 5.9, and the weld interface positions are shown in Figure 5.10. The mean values of rotational velocity and upset were calculated from all three repeat welds conducted.

The three welds of parameter set N4 had a mean weld duration of 4.87 s and a standard deviation of 0.153 s, or 3.14 % of the mean value. The mean total upset was 3.85 mm, with a standard deviation of 0.511 mm, or 13.3 % of the mean value.

It can be seen in Figure 5.9b that the total upset of welds are parameter set N4 were much larger than those of the other three parameter sets used, which was due to the increased energy and pressure used. Increasing the weld pressure is known to increase the interface friction coefficient, in turn generating heat more rapidly at the interface. Additionally, an increase in weld pressure provides larger mechanical loading, which means less softening of the material around the interface is required prior to it being ejected from the interface.

In Figure 5.10, it can be seen that the range of axial positions from which diffraction data was recorded was much greater than the other three parameter sets. However, it is expected that any microstructural changes which occur in this parameter set will occur over larger axial distances, due to the larger upset which occurred.

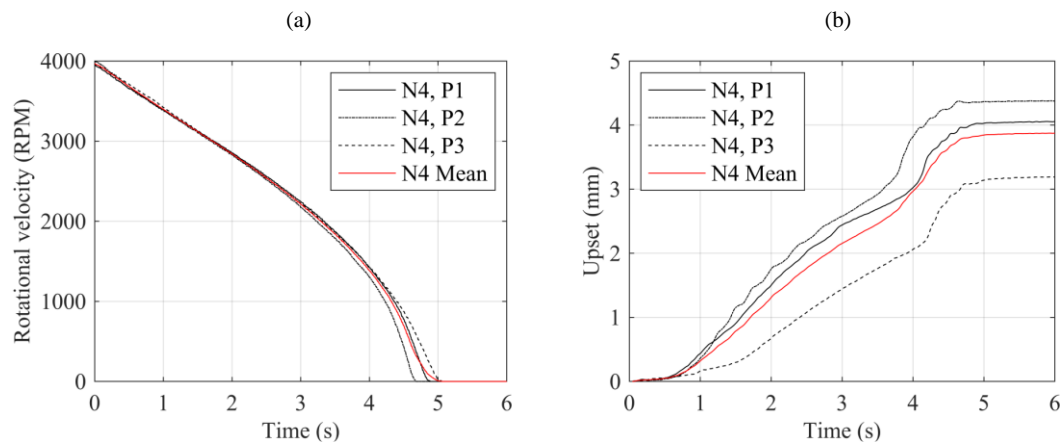


**Figure 5.9:** Weld outputs for the RR1000 repeat welds performed with input parameter set N4 and the mean outputs calculated from these. (a) Rundown, (b) Upset.

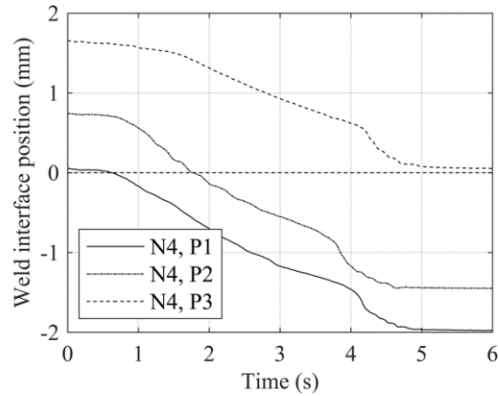


**Figure 5.10:** Position of the weld interface relative to the stationary beamline for the three RR1000 welds performed with input parameter set N4.

### 5.2.1.5 Energy input

For each set of input parameters, the mean rundown curve was input into Equation 1.1 to calculate the energy input rate into the weld. This data is shown in Figure 5.11.

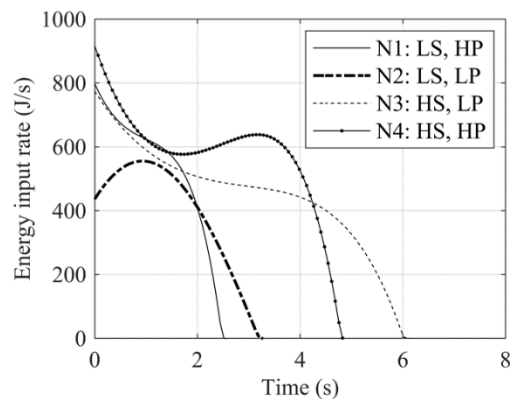


**Figure 5.11:** Energy input rate for each weld input parameter set derived from rundown curves.

Comparing parameter sets N3 and N4, it can be seen that the welds with increased axial pressure (N4) had a larger energy input rate for the majority of the weld duration. This was due to the larger weld pressure increasing frictional heat generation at the contact interface. The same trend is seen when comparing parameter sets N1 and N2, which had the same initial rotational velocity. Parameter set N1 had a higher energy

input rate than N2, due to the increased axial pressure, which additionally resulted in a shorter weld duration.

When comparing input parameter sets with the same axial pressure, such as sets N1 and N4 (or N2 and N3), it is seen that the energy input rate is not constant. In both cases, the parameter set with increased initial rotational velocity had a faster energy input rate. However, the welds with increased initial rotational velocity also have an increased weld duration, due to the larger total energy input.

It is thought that the consistent energy input rates seen in the first 0.5 s of welding for parameter sets N1 and N3 is purely coincidental, as the initial rotational velocity and axial pressure were both different between these input parameter sets.

## 5.3 Diffraction data analysis

There are a range of analysis techniques for X-ray diffraction spectra which can be applied dependent on the microstructural information required. In this study, the phase fractions and lattice parameters are the features of interest.

### 5.3.1 Introduction

The superlattice nature of Nickel-based superalloys causes difficulties when processing X-ray diffraction data. The  $\gamma$  and  $\gamma'$  phases which form the superlattice have similar lattice sizes and so their diffraction peaks overlap. Despite both phases existing with a face-centred-cubic (FCC) lattice structure, the  $\gamma'$  phase exhibits a primitive cubic structure. The permitted reflections from a primitive structure provide additional diffraction peaks, predominantly the [100] and [110] peaks, which can be used to calculate the volume fraction of the  $\gamma'$  phase. However, due to the multiplicity factor of the primitive cubic structure, the intensity of these additional peaks is much smaller than those which are also permitted by the FCC lattice structure.

In this study, an extremely high acquisition rate was used to capture rapid changes in the RR1000 microstructure during IFW. However, with increasing acquisition rate, the influence of background noise to the diffraction profile is increased, due to the reduced exposure time for acquisition of diffracted X-rays. When peaks with low relative intensity are present, such as the [100] and [110] primitive cubic  $\gamma'$  peaks exhibited by RR1000, the influence of the background noise is greater.

Due to the low intensity of the primitive cubic peaks produced by the  $\gamma'$  phase, these cannot be distinguished from the background noise at the acquisition rate of 142 fps used for these welds. To overcome this, the Debye-Scherrer diffraction images recorded from the parent RR1000 were summed together in sets of various integers. This produced a range of new acquisition rates from 71 fps to 2.84 fps.

The raw Debye-Scherrer rings acquired at the original rate of 142 fps and the summed rate of 14.2 fps are presented in Figure 5.12. It can be seen that summing the diffraction images provides much clearer and coherent diffraction rings for subsequent processing and analysis.

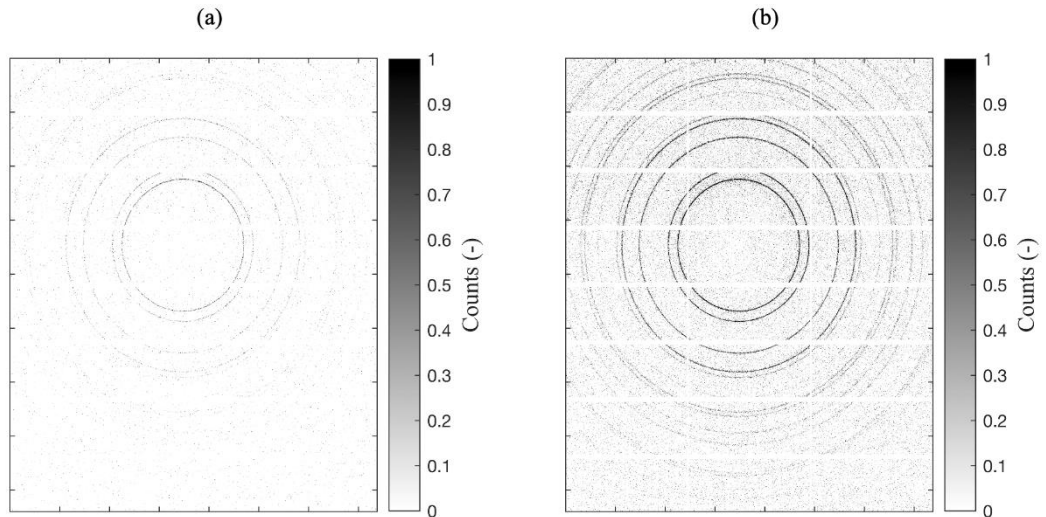


**Figure 5.12:** Debye-Scherrer diffraction rings acquired from the parent RR1000 microstructure. (a) Original 142 fps acquisition rate, (b) Summed 14.2 fps acquisition rate.

Azimuthal integration has been performed on the diffraction images presented in Figure 5.12, providing diffraction spectra for analysis of phase composition. These are presented in Figure 5.13. Whilst there is little difference in the general structure of the diffraction profiles, it is clear that the low intensity  $\gamma'$  primitive peaks ( $2\theta = 1.6^\circ$ ,  $2\theta = 2.2^\circ$ ) cannot be resolved with the higher acquisition rate (Figure 5.10a). Reduction of the acquisition rate to 14.2 fps provides clear peaks that can be resolved for accurate analysis of the  $\gamma'$  volume fraction.

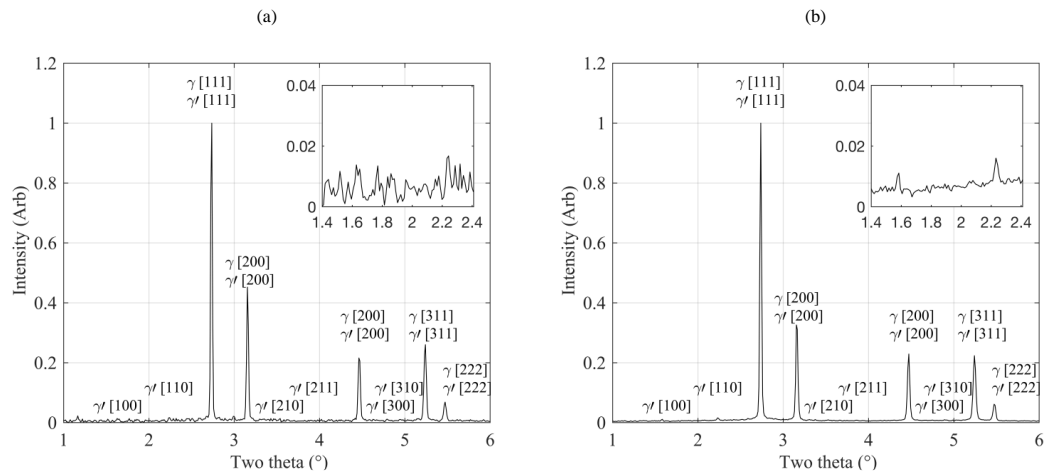


**Figure 5.13:** Comparison of X-ray diffraction profiles highlighting the influence of background noise on low intensity peaks. (a) Original 142 fps acquisition, (b) Summed 14.2 fps acquisition. The inset in both figures shows the  $2\theta$  range between  $1.4$  and  $2.4^\circ$  where the [100] and [110] primitive cubic  $\gamma'$  peaks reside to highlight how the reduced acquisition rate allows for these peaks to be resolved.

A full Rietveld refinement analysis was performed on the range of summed images, and the parent  $\gamma'$  volume fraction and residual were extracted to evaluate the ability to resolve the primitive cubic  $\gamma'$  peaks, and the accuracy in the volume fraction measurement obtained. This data is presented in Figure 5.14.

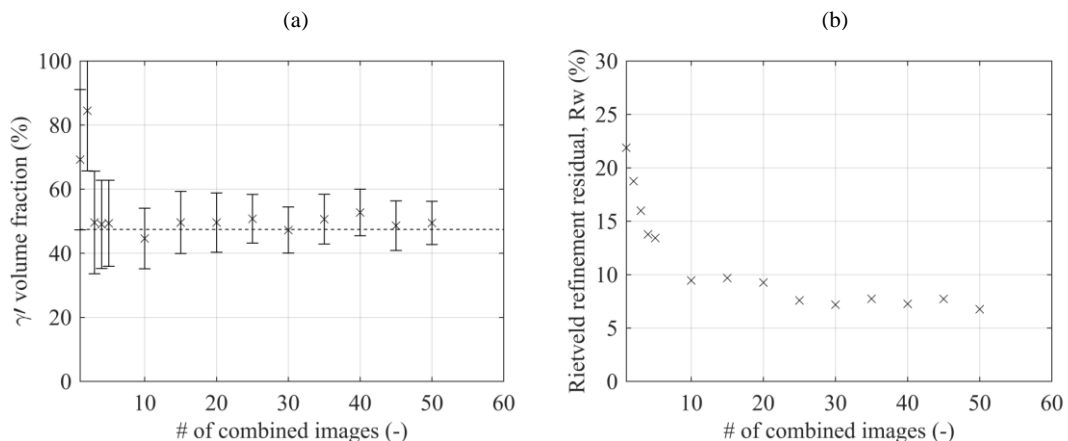


**Figure 5.14:** Analysis of the results when summing images to form lower acquisition rates. (a)  $\gamma'$  volume fraction, (b) Rietveld residual,  $R_w$ .

It can be seen in Figure 5.14a that the  $\gamma'$  volume fraction calculated from the diffraction data appears to be consistent with the parent volume fraction when 3 or more images are summed (47.3 fps). However, the residual of the refinement procedure is in excess of 15 % when 3 images are combined. The residual of the refinement reaches an appropriate value of less than 10 % when 10 or more images are summed.

In Figure 5.14b, it is seen that when summing larger sets of raw data, the residual reduced to approximately 6 %, providing an increase in the accuracy of the analysis. Whilst it is important to ensure that there is a high level of accuracy in the measurements taken from the in-situ diffraction data, there is also value in having an increased acquisition rate to provide dynamicity in the data acquired and subsequently processed. Summing the raw images in sets of 10 provides an excellent balance of accuracy and dynamicity in the diffraction data.

The argument can be made that there is value to having a higher acquisition rate of 47.3 fps. However, it is important to remember that the  $\gamma'$  volume fraction will decrease during the process. At higher acquisition rates, reduced  $\gamma'$  volume fractions would be more significantly impacted the background noise. When summing images in sets of 10, to provide an acquisition rate of 14.2 fps, it was seen that  $\gamma'$  volume fractions as low as 10 % can still be seen and resolved in the diffraction data. Hence, images were summed to provide an acquisition rate of 14.2 fps.

### **5.3.2 Analysis of phase fractions**

A full Rietveld refinement was performed on the summed diffraction images to analyse the evolution of phase fractions throughout IFW. The phases refined in the analysis are  $\gamma$  and  $\gamma'$ . Negligible phases such as carbides which may exist are not included as they have a very small volume fraction and show minimal evolution at the temperature ranges expected during IFW. Figure 5.15 shows two refined diffraction patterns recorded during weld N1, T2.

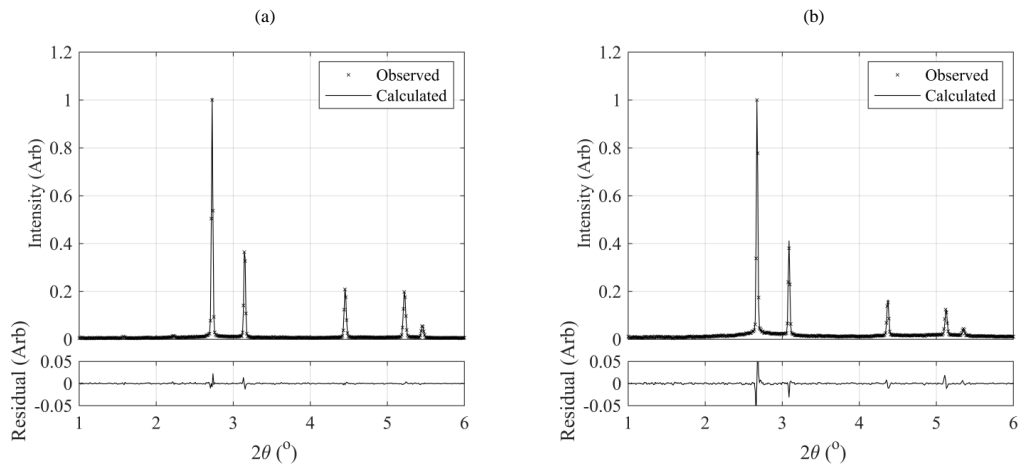


**Figure 5.15:** Rietveld refinement of diffraction images recorded during weld N4, P2. (a) Parent material prior to welding. (b) Image recorded at a weld time of 2.16 s with a beamline position 0.18 mm from the weld interface.

In Figure 5.15a, the diffraction pattern was recorded prior to welding. The refinement procedure calculated the parent  $\gamma'$  volume fraction from this image as 47.43 %, with a residual of 7.212 %. The refinement calculated the lattice parameters of the  $\gamma'$  precipitates and  $\gamma$  matrix to be 3.7595 Å and 3.7628 Å, respectively.

The diffraction image shown in Figure 5.15b was recorded at a weld time of 2 s, at a distance 0.0229 mm below the weld interface. Here, the  $\gamma'$  volume fraction was calculated as 5.03 %, with a residual of 9.77 %. The lattice parameter of the primitive cubic  $\gamma'$  and face-centred-cubic  $\gamma$  phases were calculated as 3.8426 Å and 3.8455 Å, respectively.

### 5.3.3 Evaluation of uncertainty in diffraction profiles

Whilst X-ray diffraction analysis techniques can provide a range of information about the microstructure of a material, it is an experimental technique and so the results have an uncertainty associated with them. Some of the uncertainties arise from the experimental set-up and others from data processing techniques.

The Rietveld refinement process calculates the phase fractions of  $\gamma$  and  $\gamma'$  present in the microstructure. The analysis technique is based on the minimisation of an error function between the experimental data and a model prediction. For each refinement

there is a residual, which is the sum of squared errors across the whole diffraction pattern. The uncertainty associated with the phase fraction calculation was set to the value of the residual, as this provides an analysis of multiple peaks, intensities and widths, which all factor into the calculation of phase fractions.

Each phase has an associated lattice parameter, which shows the size of the crystal lattice structure. In XRD, this is calculated based on the  $2\theta$  values of each peak present in a phase. After Azimuthal integration of the Debye-Scherrer diffraction rings, there is a resolution of  $0.010983^\circ$  on the  $2\theta$  axis. This provides an uncertainty of  $\pm 0.005492^\circ$  for any peak position. Calculation of the  $\gamma'$  lattice parameter from the [100] and [110] primitive cubic peaks whilst accounting for the uncertainty in peak position produces a value of  $3.7595 \pm 0.0113 \text{ \AA}$ . For the  $\gamma$  phase, the uncertainty is lower, due to the increased  $2\theta$  values which the FCC peaks occupy. The  $\gamma$  lattice parameter is calculated to be  $3.7628 \pm 0.0047 \text{ \AA}$ . As the lattice parameters of both phases vary due to strain and thermal effects during IFW, the uncertainties were converted to percentage values for each phase. This gives errors of  $\pm 0.2986 \%$  for  $\gamma'$  and  $\pm 0.1249 \%$  for the  $\gamma$  phase.

#### 5.3.4 Evaluation of directional strain

To assess whether any directional strain effects were present in the diffraction data,  $10^\circ$  slices of the Debye-Scherrer diffraction rings were extracted at the principal system axes,  $0^\circ$  and  $90^\circ$ . In these experiments, the  $0^\circ$  Azimuthal direction would present effects present in the  $r$ - $\theta$  plane of the weld coordinate system, and the  $90^\circ$  Azimuth would present effects in the axial  $z$  direction of the system.

The [111] peak was fit with a Gaussian function to evaluate the  $2\theta$  position of the peak, and from this the lattice parameter was evaluated. Any variation in the lattice parameter of the [111] peak between the principal axes and full Azimuthal integration would highlight directional strains in the horizontal and vertical directions.

Firstly, 10 summed diffraction images recorded prior to welding were evaluated to assess whether any directionality is present in the parent material. This is presented in Figure 5.16.

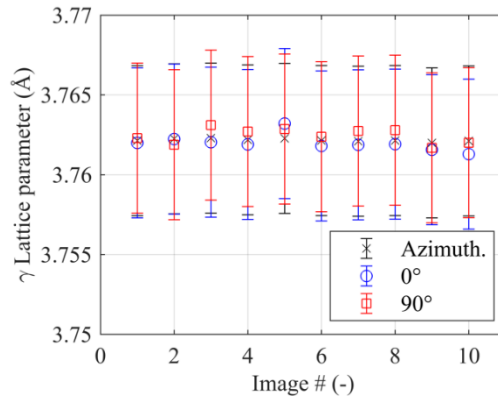


**Figure 5.16:** Lattice parameter evaluated from the [111] composite peak for 10 randomly selected pre-weld diffraction images.

Figure 5.16 shows that there were different lattice parameters evaluated from the [111] peak using the three different sets of data. However, when accounting for the uncertainty when calculating the lattice parameter, the variation between the principal directions and the full integration was much smaller than the uncertainty of each value. Therefore, it can be said that there is no clear directional strain present in the parent material.

It would be expected that any directional strains would most likely occur during welding, specifically when the beamline and contact interface were aligned and large amounts of shear stress were present due to the relative rotational motion at the contact interface. To assess whether any directionality was present during IFW, weld N1, P3 was randomly selected and the same analysis performed. The results of this are presented in Figure 5.17.

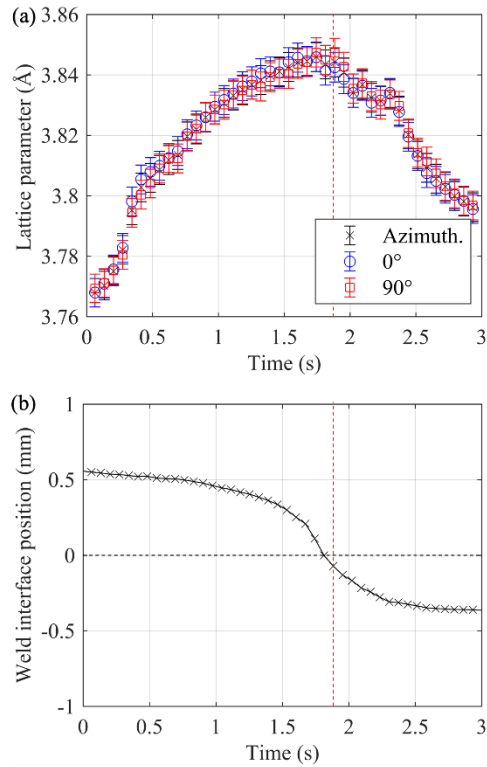


**Figure 5.17:** Data evaluated from summed images recorded during weld N1, P3. (a) Lattice parameter evaluated from the [111] composite ( $\gamma + \gamma'$ ) peak at  $0^\circ$ ,  $90^\circ$  and after full Azimuthal integration. (b) Position of the weld interface relative to the stationary beamline. The vertical dashed red line in each plot shows the time in which the contact interface was coincident with the centre of the synchrotron beam

In Figure 5.17a, there was a large variation in the lattice parameter values evaluated as the process evolved. Using Figure 5.17b, it can be seen that the lattice parameter was largest when the contact interface and beamline were aligned, as the temperatures and strains were largest around the contact interface. However, there are no clear directional effects which occur. At no point was the difference between the lattice parameter evaluated from the two principal directions large enough to exceed the bounds of the uncertainty of the lattice parameter analysis. Therefore, it can be concluded that there was no significant directional strain present during the process.

## 5.4 Post-weld diffraction analysis

To increase the confidence in the processing methods used to analyse the in-situ synchrotron diffraction data, X-ray diffraction experiments were also conducted on the welded samples. For each weld, 20 diffraction images were recorded axially across the Heat Affected Zone (HAZ) of the weld after 100 s of cooling. This provided an axial profile of the microstructure for comparison with microscopic analysis.

Welded specimens of parameter sets N2 and N4 were axially sectioned by electro-discharge machining. The sections were then mounted in Bakelite, mechanically polished and electrochemically etched prior to Scanning Electron Microscope (SEM) imaging. SEM images were acquired at axial increments of 0.1mm from the contact interface, and magnifications of 2,000x and 10,000x were used to investigate the distributions of both primary and secondary  $\gamma'$  precipitates.

The SEM images were processed using ImageJ, and an example of the raw image and processed image for the analysis of primary  $\gamma'$  precipitates are shown in Figure 5.18.

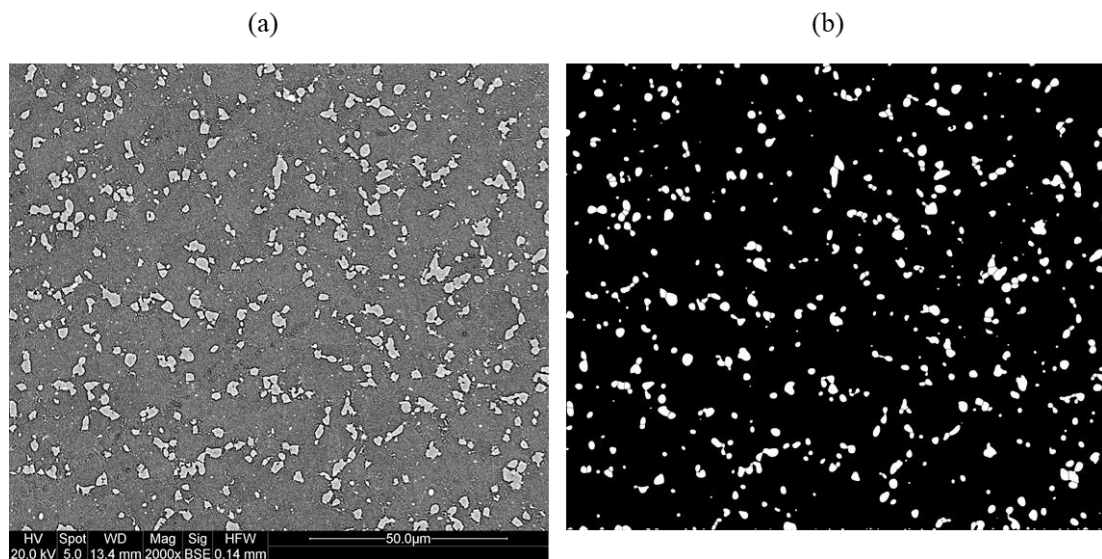


**Figure 5.18:** SEM image of parent RR1000 to analyse the primary  $\gamma'$  precipitates. (a) Raw image, (b) Processed image for statistical analysis.

To validate that the image processing technique used was appropriate for this material, the size distribution of the precipitates shown in Figure 5.18b was compared with the primary  $\gamma'$  distribution reported by Collins *et al.* [19], which is shown in Figure 5.19.

The 566 precipitates analysed in this image had an equivalent circular radius between 0.25 and 1.125  $\mu\text{m}$ . Statistically, the mean radius was 0.4825  $\mu\text{m}$ , and the mode 0.376  $\mu\text{m}$ . Figure 5.14 shows an excellent agreement between the distribution which was measured by SEM and that of the published data.

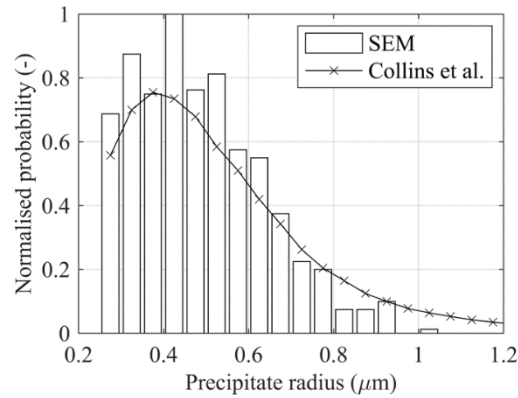


**Figure 5.19:** Comparison of the primary  $\gamma'$  size distribution measured by SEM with published data. SEM data was separated into 0.05  $\mu\text{m}$  bins (i.e., 0.20 – 0.25  $\mu\text{m}$ , 0.25 – 0.30  $\mu\text{m}$ , etc.) and normalised such that the maximum probability is equal to 1.

To measure the volume fraction and distribution of the secondary  $\gamma'$  precipitates, 10,000x magnification images were processed using the same imaging approach. Unfortunately, the resolution of the SEM limits the quality of images at very high magnification, and so a region of the  $\gamma$  grain had to be selected in each high magnification image for subsequent processing. Figure 5.20 shows the raw SEM image and the processed image used for analysis of secondary  $\gamma'$  distribution.

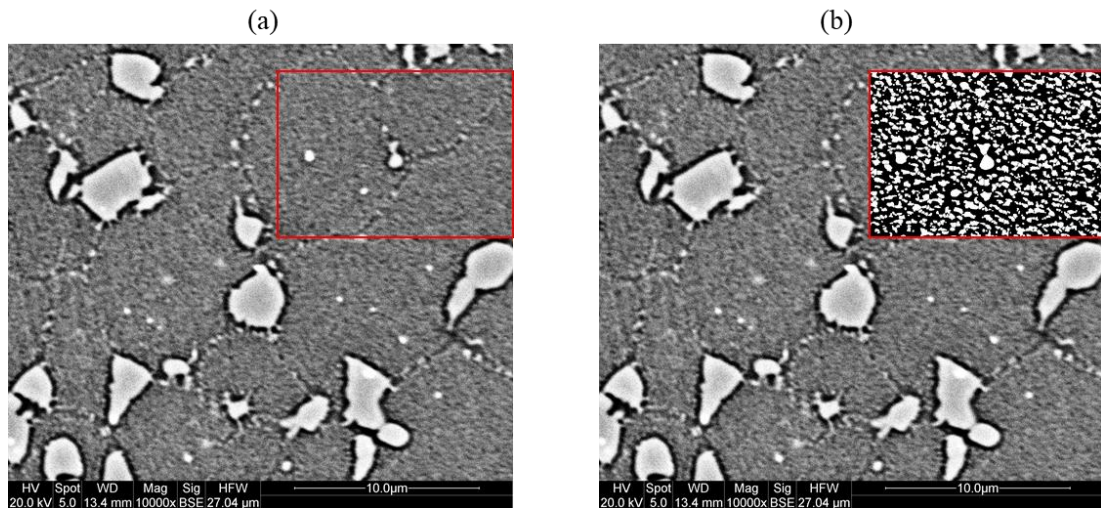


**Figure 5.20:** Example of image processing for a high magnification image for secondary  $\gamma'$  analysis. (a) Raw image, (b) Processed image for statistical analysis. Note the red box shows the bounds of the region processed and analysed.

The 976 secondary  $\gamma'$  precipitates measured in Figure 5.20b had equivalent circular radii between 30 and 290 nm, although only one precipitate exceeded the secondary  $\gamma'$  upper limit of 250 nm radius. The mean radii was 143 nm, and the mode 65 nm. The distribution measured in Figure 5.20b is presented alongside the size distribution of small-scale precipitates documented by Chen *et al.* [16] in Figure 5.21. Note that in this figure, precipitates with radii below 25 nm in the literature were excluded from the plot as these are categorised as tertiary  $\gamma'$ . The data produced here was normalised against the maximum value of the remaining range from the literature.

In Figure 5.21, it is shown that there is good agreement between the data produced via SEM analysis and the published data. For precipitate radii below 150 nm, the two sets of data align well, but there are some minor discrepancies above 150 nm.

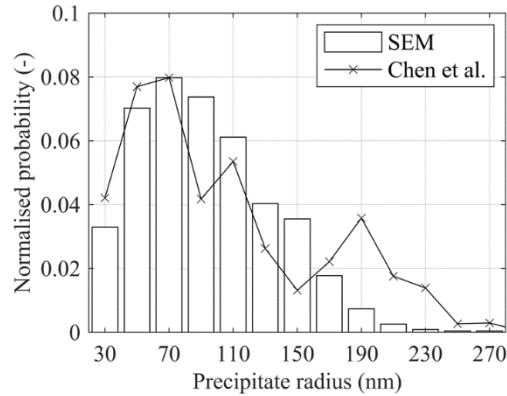


**Figure 5.21:** Comparison of the secondary  $\gamma'$  size distribution measured by SEM with published data. SEM data was separated into 20 nm bins (i.e., 0.20 – 0.40 nm, 0.40 – 0.60 nm, etc.) and normalised against the published data such that the maximum probabilities in both datasets are equal.

After comparison between the precipitate size distributions measured by SEM analysis and published data in the literature, the processing technique was applied to 12 high and low magnification images. The images were taken from 4 separate specimens to account for the variations in the location which the sample was extracted from the forging. Three images were recorded for each specimen to ensure a representative average was measured. The results are provided in Table 5.3.

It is seen that the primary  $\gamma'$  area fraction differs slightly between specimens. However, for each specimen, the standard deviation is low, showing that the magnification used provides a large enough image area to provide a representative distribution of primary  $\gamma'$ . For the four specimens examined, the mean primary  $\gamma'$  area fraction was derived as  $9.49 \pm 0.90 \%$ , where the uncertainty is defined as the standard deviation.

Similarly, it is seen that there is variation in the secondary  $\gamma'$  area fractions between samples. However, despite only analysing a small area of each image, the standard deviation in each sample is still relatively low, which shows that a large enough sample size is being analysed to provide information about the whole distribution. The average secondary  $\gamma'$  area fraction was calculated to be  $28.80 \pm 2.18 \%$ .

**Table 5.3:** Mean volume fractions of primary and secondary  $\gamma'$  for four samples and the standard deviation for each sample.

<b>Sample No.</b>	<b>Mean primary <math>\gamma'</math> area fraction (%)</b>	<b>Standard Deviation (%)</b>	<b>Mean secondary <math>\gamma'</math> area fraction (%)</b>	<b>Standard Deviation (%)</b>
1	9.00	0.22	30.00	0.7
2	8.29	0.11	31.48	0.95
3	10.45	0.04	27.20	0.88
4	10.21	0.12	26.50	0.57

To define the parent total  $\gamma'$  volume fraction, a full Rietveld refinement was performed on 20 X-ray diffraction images recorded from a range of stationary samples. The total gamma prime volume fraction calculated from this approach is  $47.43 \pm 2.49$  %.

Tertiary  $\gamma'$  precipitates are too small to be resolved under SEM, even at the highest magnifications. Due to their small size, they are expected to dissolve fully at lower temperatures during IFW. As the smallest precipitates, these dissolve first and therefore it is expected that the  $\gamma'$  forming elements stored in tertiary  $\gamma'$  will diffuse and homogenise across the  $\gamma$  grains.

Due to this, it was decided that tertiary  $\gamma'$  precipitates are not of interest to this study. However, the tertiary  $\gamma'$  volume fraction can be derived using the other analyses carried out. Using the total  $\gamma'$  volume fraction from XRD, and the primary and secondary  $\gamma'$  volume fractions from SEM, the tertiary  $\gamma'$  volume fraction is calculated as  $9.23 \pm 5.48$  %. Note, the increased error here is due to the stacking of errors from the other analyses. A summary of the  $\gamma'$  volume fractions and uncertainties is presented in Table 5.4.

**Table 5.4:** Summary of measured and calculated  $\gamma'$  volume fractions for RR1000.

$\gamma'$ precipitate size	Volume fraction (%)	Uncertainty (%)
Primary (SEM)	9.49	$\pm 0.90$
Secondary (SEM)	28.80	$\pm 2.18$
Tertiary (Calculated)	9.23	$\pm 5.48$
TOTAL (XRD)	47.43	$\pm 2.49$

With the parent material characterised and the SEM image processing validated against published data, the SEM images taken from the welded specimens were processed and compared with the post-weld diffraction data. The comparison of SEM and XRD analysis for welds N2, P2 and N4, P1 are presented in Figure 5.22.

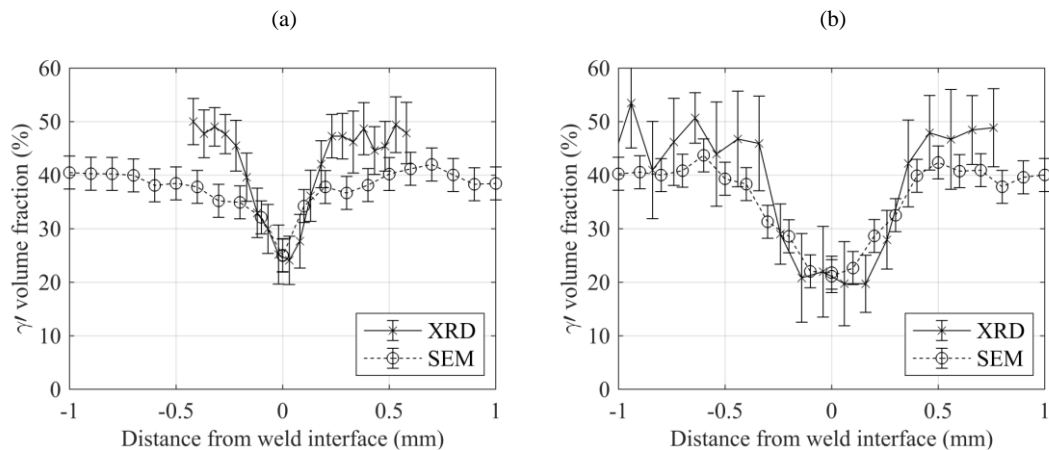


**Figure 5.22:** Comparison of the axial  $\gamma'$  volume fraction profiles measured by XRD and imaged via SEM. (a) Weld N2, P2. (b) Weld N4, P1.

The axial volume fraction profiles measured by the two analysis techniques are in good agreement for both sets of weld parameters. It should be noted that the SEM analysis approach does not account for tertiary  $\gamma'$ , as it is too small to resolve. However, this explains why the measurements made by SEM and XRD are closer at distances close to the weld interface. Near the weld interface, tertiary  $\gamma'$  will be completely dissolved from the microstructure, and so only the primary and secondary  $\gamma'$  remain. These can be measured by SEM, and so the two techniques produce similar results. Further from the weld interface, where the temperatures were lower, tertiary  $\gamma'$  does not dissolve. As these tertiary precipitates cannot be measured by SEM, the

SEM measurement of volume fraction is approximately 10 % below that of the XRD measurement.

## 5.5 Microstructure evolution during IFW

### 5.5.1 Introduction

The Rietveld refinement process has been shown to be accurate when used to measure the  $\gamma'$  volume fraction of welded samples. The same data processing methodology was applied to the in-situ diffraction data to analyse the  $\gamma'$  volume fraction evolution throughout IFW. Further to this, the  $\gamma$  lattice parameter was evaluated to assess the thermal response and support the explanation of the  $\gamma'$  volume fraction evolution.

To estimate the thermal response from the lattice parameter values, thermal expansion coefficient data for RR1000 was applied to the parent lattice parameter of the  $\gamma$  phase to calculate the increase in lattice size based on the temperature. This data was only available for the temperature range of 20 – 900 °C, and so a second-order polynomial was fit to the data to allow for extrapolation to 1200 °C. This is presented in Figure 5.23. The primary point of interest here is at 850 °C, above which there is a driving force for dissolution of  $\gamma'$ . This temperature coincides with a lattice parameter of 3.81 Å.

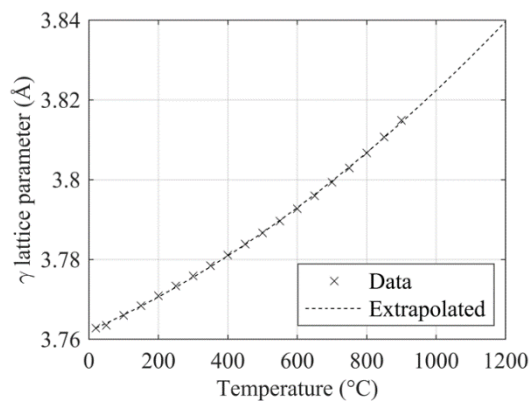


**Figure 5.23:** Calculation of the sensitivity of the lattice parameter to temperature evaluated using thermal expansion coefficient data.

The IFW process is controlled by a combination of thermal and mechanical effects. Therefore, it cannot be assumed that the change in lattice parameter is due to thermal effects alone. To evaluate the possible magnitude by which the lattice parameter would vary under mechanical strain, the axial strain component was calculated using the weld pressures and Young's Modulus data at ambient and elevated temperatures. At the

maximum weld pressure investigated in this study, the axial strain can be calculated as 0.00038 at ambient temperatures, and 0.00063 at 1200 °C. Using the larger of the two strain values, the shift in lattice parameter due to mechanical loading was -0.00237 Å. As this is much smaller than the possible changes due to increasing temperatures, the mechanical strain effects can be ignored for the purpose of this analysis.

For weld parameter set N1, the mean weld was divided into the primary stages of welding; conditioning, burn-off and consolidation. Additionally, a transition stage was defined between burn-off and consolidation, alongside a weld stall stage, which is between the linear consolidation and the end of the weld. The mean upset data is presented in Figure 5.24, with these stages defined.

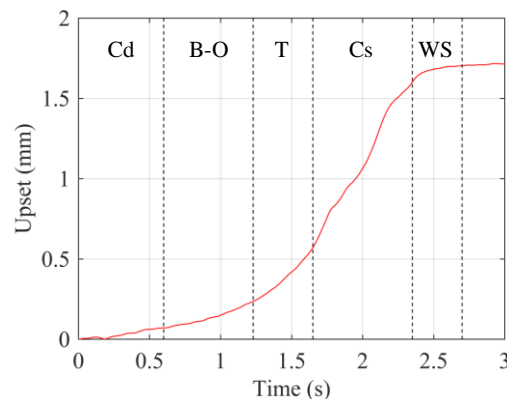


**Figure 5.24:** The mean upset curve for weld parameter set N1. The weld stages are defined as follows; Cd = conditioning, B-O = burn-off, T = transition, Cs = consolidation, WS = weld stall.

In the mean weld of parameter set N1, the conditioning time was 0.62 s. This was followed by an instant transition into burn-off, which occurred between 0.62 s and 1.25 s. The average upset rate during burn off was 0.26 mm/s. The transition between burn-off and consolidation occurred between 1.25 s and 1.67 s, after which there was a linear upset rate of 1.47 mm/s until a weld time of 2.37 s during conditioning. The weld completed after 2.72 s, with a total upset of 1.67 mm.

## 5.5.2 Microstructure evolution during conditioning

Due to the high rate of data acquired and processed in these experiments, the conditioning stage was divided into three regions, denoted start, middle and end. The microstructural data recorded during the start of conditioning is presented in Figure 5.25.

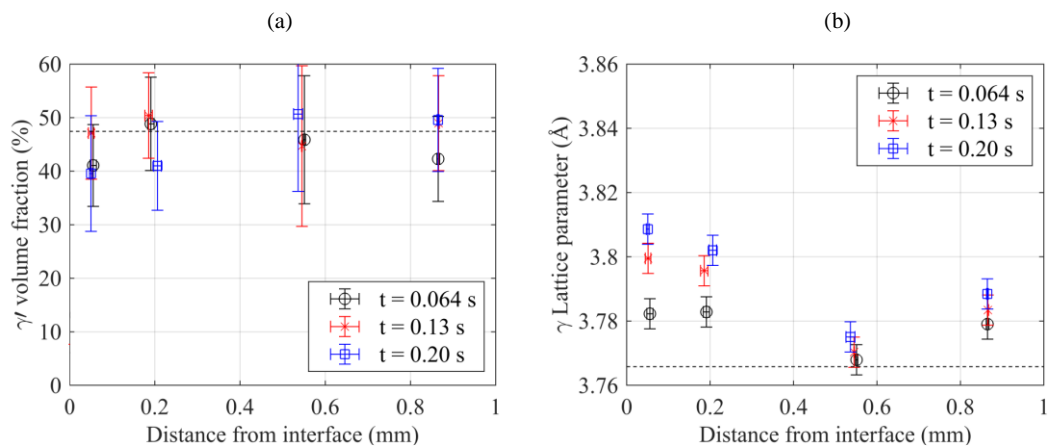


**Figure 5.25:** Microstructure evolution during the start of conditioning for weld parameter set N1. (a)  $\gamma'$  volume fraction, (b)  $\gamma$  lattice parameter.

During the first 0.20 s of conditioning, there was no clear evidence of  $\gamma'$  dissolution. Whilst there appears to be a reduction in  $\gamma'$  volume fraction at  $t = 0.20$  s, the parent volume fraction still falls within the error bars of this measurement. This is supported by the fact that the lattice parameter did not exceed 3.81 Å. However, there was a clear increase in the lattice parameter between each successive time point at positions within 0.2 mm of the contact interface. This indicates that there was some heat generation within this region.

Interestingly, at the three time points recorded during the start of conditioning, there was a consistent minimum in the lattice parameter approximately 0.55 mm from the contact interface. This may simply be an anomalous result, however it may indicate that some compressive strain is present as the values at this position did not fit the trend produced by the three remaining positions.

The microstructure evolution recorded during the middle stage of conditioning is presented in Figure 5.26. It is seen that at a weld time of 0.27 s, dissolution of the  $\gamma'$

has occurred, both at the interface and also 0.2 mm from the interface. The lattice parameter data supports this with an increase above 3.81 Å seen close to the contact interface, indicating temperatures above 850 °C and thus a driving force for  $\gamma'$  dissolution.

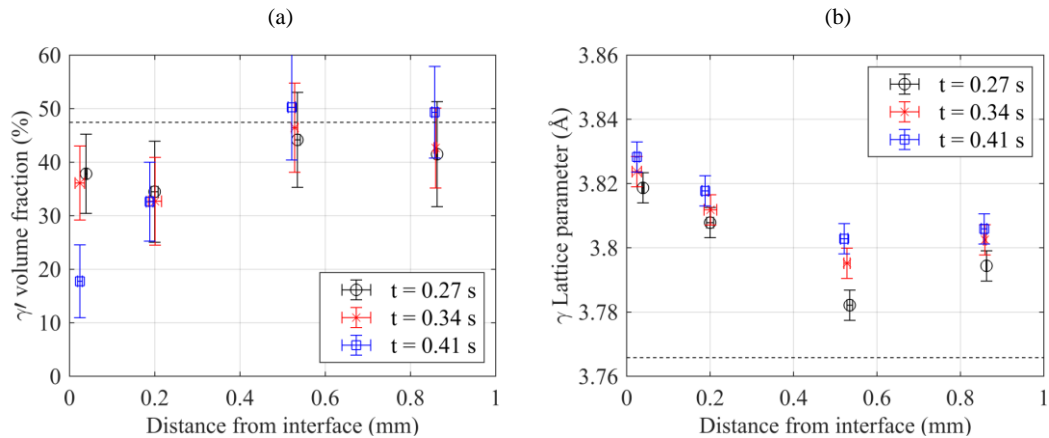


**Figure 5.26:** Microstructure evolution during the middle stage of conditioning for weld parameter set N1. (a)  $\gamma'$  volume fraction, (b)  $\gamma$  lattice parameter.

Between 0.27 s and 0.34 s, there was little change in the  $\gamma'$  volume fraction data. However, the lattice parameter again showed an increase across the range of positions measured, showing continued heat generation at the interface, and conduction of this heat axially through the specimens. By t = 0.41 s, significant dissolution of the  $\gamma'$  phase can be seen at the contact interface. This coincided with a lattice parameter value of 3.828 Å, or an estimated temperature of approximately 1100 °C. The remaining  $\gamma'$  volume fraction of 18.2 % at the contact interface indicates that all tertiary and most of the secondary  $\gamma'$  had been dissolved from the microstructure.

The minima which was present in the lattice parameter approximately 0.55 mm from the contact interface in the early stage of conditioning was still present at a weld time of 0.27 s. This possibly shows a large amount of plastic compressive strain at the edge of the in-situ HAZ. However, throughout the middle of conditioning this value was seen to increase, and by t = 0.41 s, the axial profile of the lattice parameter appeared consistent with the expected thermal profile.

The microstructural data recorded during the final stage of conditioning is presented in Figure 5.27. Throughout this time, the increase in lattice parameter was much smaller than in the early and middle stages of conditioning, which is coincident with the small change in volume fraction which was observed. Whilst the value of lattice parameter slightly exceeded  $3.81 \text{ \AA}$  at distances in excess of  $0.5 \text{ mm}$  from the contact interface at a weld time of  $0.62 \text{ s}$ , there was no significant evidence of  $\gamma'$  dissolution at these points. It appears likely that as the lattice parameter is not significantly above  $3.81 \text{ \AA}$ , the temperature was only slightly above  $850 \text{ }^\circ\text{C}$ , causing only a small driving force for dissolution. Additionally, the three time points plotted in Figure 5.27 span a time of  $0.14 \text{ s}$ . As dissolution of  $\gamma'$  is a diffusion-based transformation, this short time would limit the amount of  $\gamma'$  dissolution which could occur.

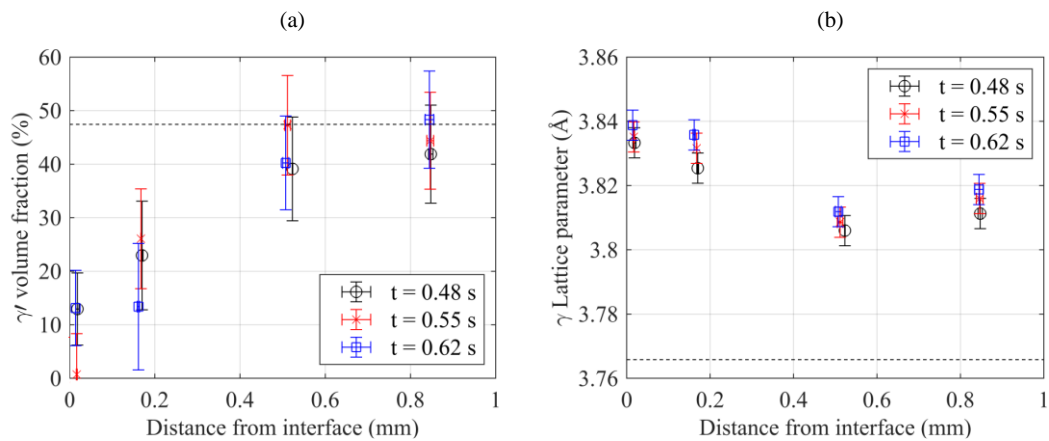


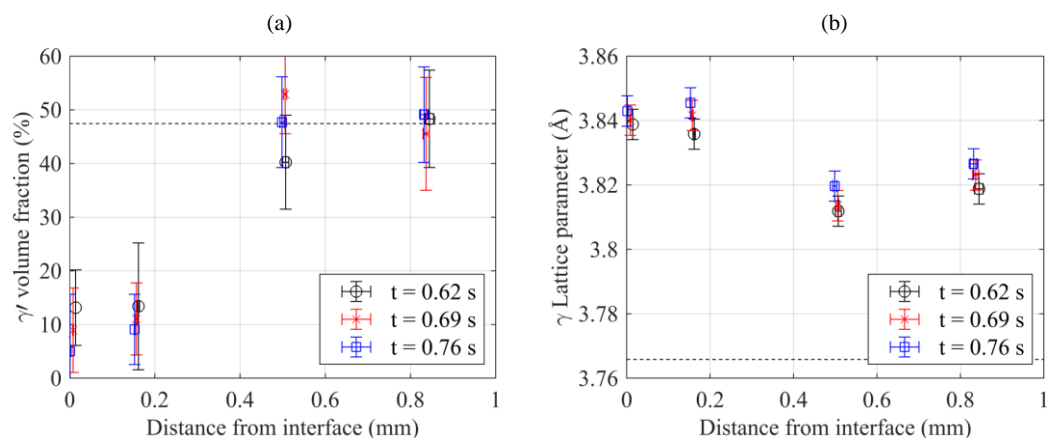
**Figure 5.27:** Microstructure evolution during the end stage of conditioning for weld parameter set N1. (a)  $\gamma'$  volume fraction, (b)  $\gamma$  lattice parameter.

The diffraction data presented during conditioning proves the hypothesis that the conditioning stage exists until there is a sufficient volume of material which has reduced in strength to permit mechanical deformation via upset. Therefore, it can be concluded that as the microstructure controls the strength of the material, the microstructure also controls the behaviour of the process during IFW.

### 5.5.3 Microstructure evolution during burn-off

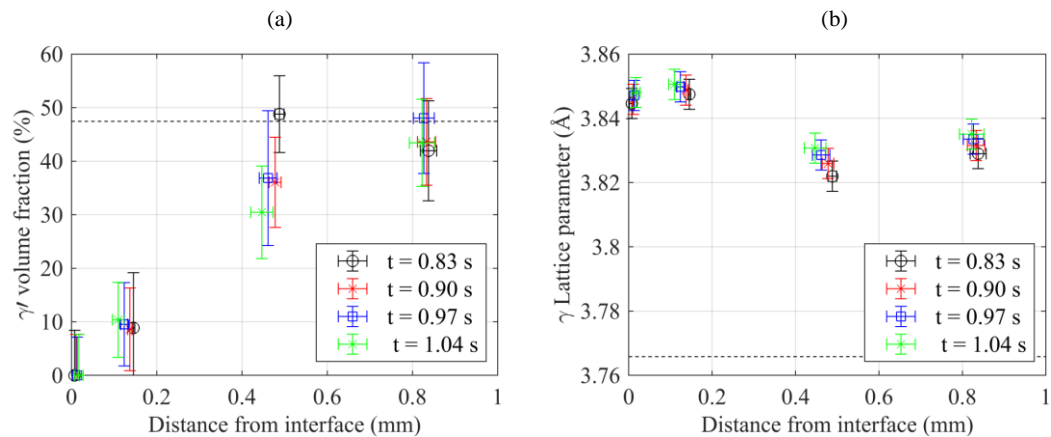
It is commonly assumed that during burn-off, there is a steady-state profile in the axial microstructure, in which the heat input offsets the steady-state upset which occurs. To assess whether this is true, the burn-off stage present between 0.62 and 1.25 s was divided into three sections, and the evolution of microstructure evaluated for each.

The microstructure evolution during the early period of burn-off is presented in Figure 5.28. The  $\gamma'$  volume fraction appears to be steady-state throughout this time. An increase in lattice parameter values is observed, likely indicating an increase in temperature across the specimens. At a weld time of 0.76 s, the lattice parameter was in excess of 3.82 Å further from the interface, indicating temperatures in excess of 950 °C. At these points, however, there was no significant evidence of  $\gamma'$  dissolution. There are two possible causes for this. As the specimens were upsetting at an average rate of 0.26 mm/s during this time, locations which measurements were taken from would have previously been further from the interface, where temperatures would be lower. Hence, the thermal history of the point must be accounted for when assessing whether  $\gamma'$  dissolution was likely to occur. Another possible explanation for the increasing lattice parameter would be the presence of tensile strain, which would expand the lattice, however this is unlikely given the compressive nature of IFW.



**Figure 5.28:** Microstructure evolution during the early stage of burn-off for weld parameter set N1. (a)  $\gamma'$  volume fraction, (b)  $\gamma$  lattice parameter.

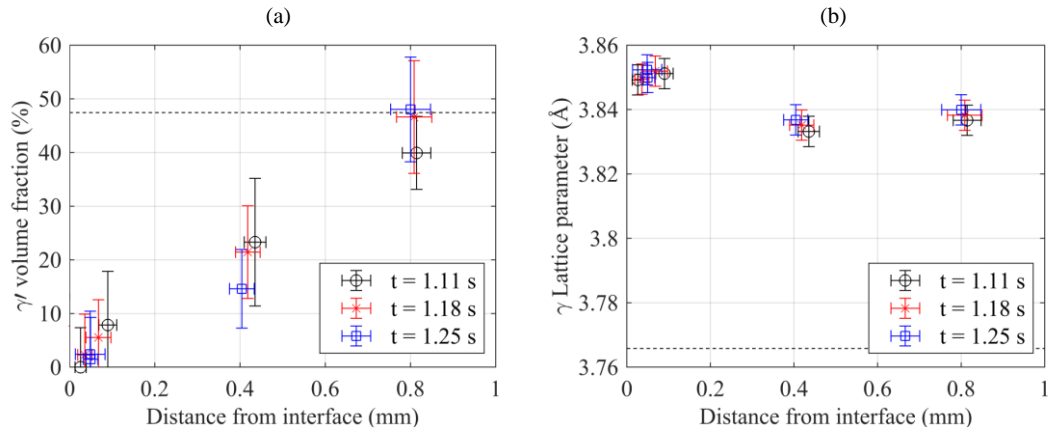
Figure 5.29 presents the microstructural evolution during the middle period of burn-off. As the spread of axial measurement locations increased due to upset, it becomes clear that a zone in which  $\gamma'$  dissolution was occurring was present during burn off, with an approximate axial length of 0.5 mm. Outside of this zone, the  $\gamma'$  volume fractions were close to parent values.



**Figure 5.29:** Microstructure evolution during the middle period of burn-off for weld parameter set N1. (a)  $\gamma'$  volume fraction, (b)  $\gamma$  lattice parameter.

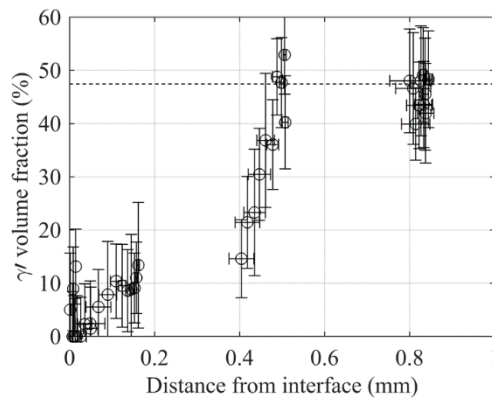
The evolution of lattice parameter data does not match up with the  $\gamma'$  volume fraction data. Again, the lattice parameter was seen to increase with time. By a time of 1.04 s, the lattice parameter recorded outside of the dissolved zone was 3.833 Å. If it is assumed there was no strain present at this location, this would estimate a temperature of 1100 °C. This temperature would likely produce a large driving force for dissolution of  $\gamma'$ . As no dissolution of  $\gamma'$  can be seen in the  $\gamma'$  volume fraction data, it must be assumed that the method used to evaluate the sensitivity of lattice parameter to temperature was not appropriate. Repeat welds were performed with in-situ thermocouple measurements to assess the thermal response and these will be presented at the end of this section.

Figure 5.30 shows the microstructure evolution throughout the final stage of burn-off. Again, the  $\gamma'$  volume fraction data proves the hypothesis that a steady-state axial profile in microstructure was present throughout burn-off. A small increase in the lattice parameter is observed outside of the  $\gamma'$  dissolved zone with increasing time.



**Figure 5.30:** Microstructure evolution during the final period of burn-off for weld parameter set N1. (a)  $\gamma'$  volume fraction, (b)  $\gamma$  lattice parameter.

To prove the hypothesis that the axial profile of microstructure was steady-state during burn-off, the  $\gamma'$  volume fraction data recorded for all time points during burn off were collated and plotted in Figure 5.31. Again, it is seen that the microstructure evolution dictates the process response, with a consistent axial profile in  $\gamma'$  volume fraction throughout burn-off permitting a constant burn-off rate.



**Figure 5.31:** All  $\gamma'$  volume fraction data acquired during steady-state burn-off.

Whilst there are some positions from which diffraction images were not recorded ( $z = 0.2 - 0.4$  mm,  $z = 0.5 - 0.8$ mm) due to the limited amount of upset which occurred during burn-off, the  $\gamma'$  dissolved zone can still be clearly defined. It appears that the axial length of the zone was 0.5 mm, outside of which the  $\gamma'$  volume fraction values were close to parent values. Within the  $\gamma'$  dissolved zone, there was a steep gradient

from parent  $\gamma'$  volume fraction at  $z = 0.5$  mm to 15 %  $\gamma'$  volume fraction at  $z = 0.4$  mm. Between the interface and  $z = 0.4$  mm, it appears that the  $\gamma'$  volume fraction was roughly consistent, which indicates the presence of a zone fully denuded of secondary and tertiary  $\gamma'$ . Whilst some diffraction images recorded close to the interface provided a  $\gamma'$  volume fraction of 0 %, it must be noted that the  $\gamma'$  volume fraction cannot be accurately measured at values below 10 % due to the effects of noise at this acquisition rate.

#### 5.5.4 Microstructure evolution during the transition from burn-off to consolidation

When analysing the mean weld upset for parameter set N1, there is a clear transition between the low upset rate seen during burn-off and the increased upset rate produced during consolidation. To assess the driving forces behind this transition, this transition stage was divided into two sections, and the microstructure evolution of both sections evaluated. Figure 5.32 presents the microstructural evolution during the early transition.

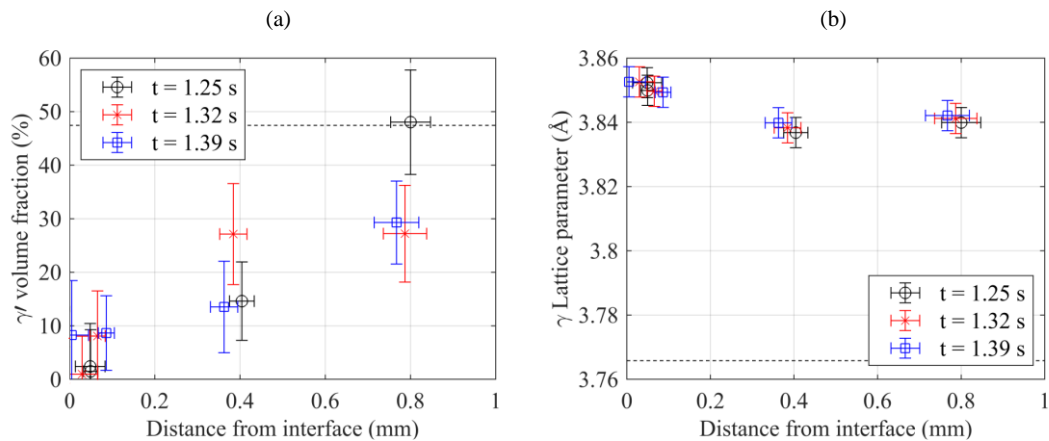


**Figure 5.32:** Microstructure evolution during the early period of transition between burn-off and consolidation for weld parameter set N1. (a)  $\gamma'$  volume fraction, (b)  $\gamma$  lattice parameter.

In Figure 5.32a, there is a clear reduction in  $\gamma'$  volume fraction seen at positions around  $z = 0.8$  mm between  $t = 1.25$  s (end of burn-off) and  $t = 1.32$  s. However, there was no significant change in the lattice parameter recorded at these locations during this time. It is hypothesised that the material outside of the dissolved zone increased in temperature during burn-off, due to the low upset rate which was produced during this stage. At the end of burn-off, the material outside of the zone was subjected to temperatures close to those which would permit dissolution of  $\gamma'$ . The continued energy input and limited removal of material from the interface eventually caused dissolution of  $\gamma'$  outside of the dissolved zone, increasing the size of this.

Microstructure evolution data recorded during the second half of the transition stage is presented in Figure 5.33. It is clear during this time range that a larger region in which  $\gamma'$  dissolution was present had formed. Unfortunately, there were no data points far enough from the contact interface to fully define the size of this, but the trend in data available can be used to estimate this is somewhere in the region of 0.8 – 1.4 mm in axial length.

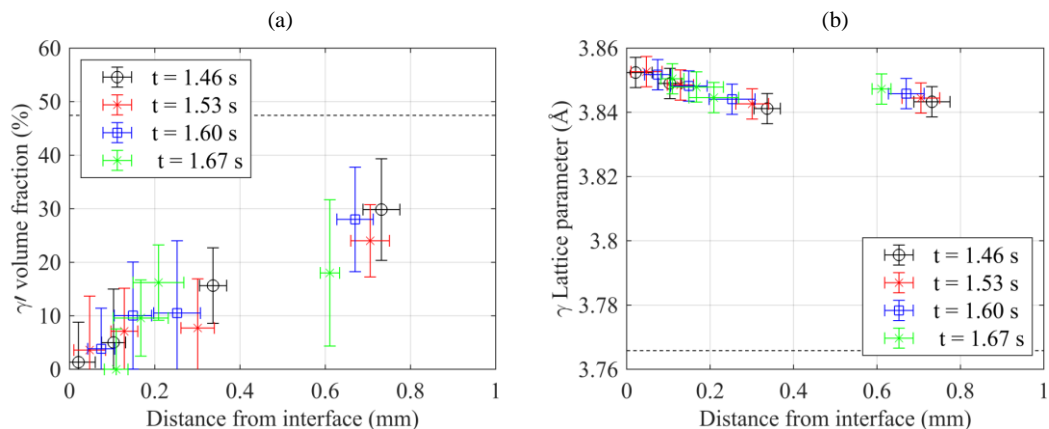


**Figure 5.33:** Microstructure evolution during the end of the transition between burn-off and consolidation for weld parameter set N1. (a)  $\gamma'$  volume fraction, (b)  $\gamma$  lattice parameter.

The lattice parameters presented in Figure 5.33b show an interesting trend. Between the contact interface and  $z = 0.4$ mm, the axial profile of the lattice parameter showed the expected trend with temperature, by which the maximum value was present at the interface and the value decreased with distance from the interface. However, the

measurements recorded between  $z = 0.6$  mm and  $z = 0.8$  mm are larger than those acquired from distances 0.2 – 0.4 mm from the interface. Data recorded at positions between 0.6 and 0.8 mm appear to be consistent with the edge of the dissolved zone, as the  $\gamma'$  volume fraction data showed an increase throughout this region. This may indicate large amounts of plastic compressive strain around the contact interface.

### 5.5.5 Microstructure evolution during consolidation

The mean weld of parameter set N1 exhibited a consolidation region which had an average upset rate of 1.47 mm/s from  $t = 1.67$  s to  $t = 2.37$  s. This large range of time points allows the consolidation stage to be split into three separate regions. Processed diffraction data acquired during the early portion of consolidation is presented in Figure 5.34.

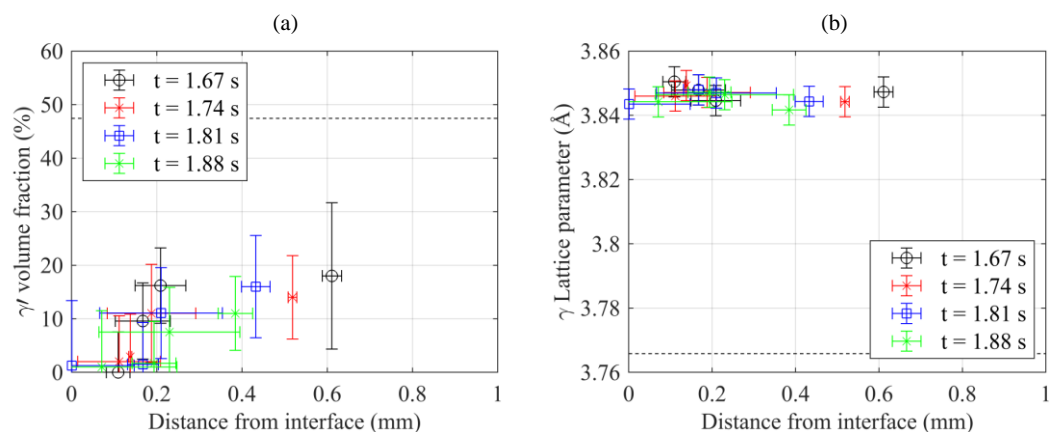


**Figure 5.34:** Microstructure evolution during the start of consolidation for weld parameter set N1. (a)  $\gamma'$  volume fraction, (b)  $\gamma$  lattice parameter.

It can be seen in Figure 5.34a that the microstructure profile displayed at the end of the transition appeared to remain during consolidation. This shows that similar behaviour to burn-off may be exhibited, where a steady-state microstructure is produced during regions of linear upset-rates. There is an interesting artefact present in the lattice parameter data, where the axial profile of this was linear and constant throughout the range of positions and times from which measurements were taken.

It would be expected that during consolidation, where the upset rate is largest, that the axial profile of temperature would show the steepest gradient, due to the large amount of cooler material being brought into the interface under the large upset rate. It is unlikely that the temperatures between the interface and  $z = 0.6$  mm were consistent during the early stage of consolidation. Therefore, it appears likely that there were compressive strains present near the interface which reduced the lattice parameter in this region. With increasing distance from the contact interface, these strains would reduce, and thus the thermal and mechanical effects would offset one another to provide a linear constant profile of lattice parameter.

Microstructural evolution data recorded during the middle portion of consolidation is presented in Figure 5.35. The volume fraction data shows no clear trend with time, confirming that the microstructure remained steady-state during the constant upset rate portion of consolidation. However, a clear reduction in the lattice parameter values can be observed over this time range, which is likely to indicate that a reduction in temperature occurred across the axial range of positions from which measurements were taken. It is likely this reduction in temperature was caused by the large upset rate, with colder material being pushed into the interface zone.

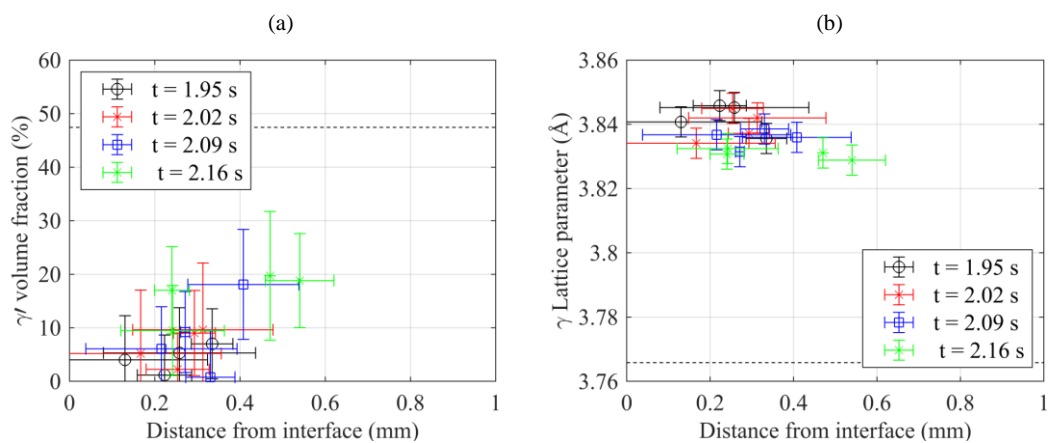


**Figure 5.35:** Microstructure evolution during the middle period of consolidation for weld parameter set N1. (a)  $\gamma'$  volume fraction, (b)  $\gamma$  lattice parameter.

Whilst the thermal history of these points was sufficient provide a consistent  $\gamma'$  volume fraction during this time range, the reduction in overall temperature indicates the evolution of consolidation. It is likely that the influx of successively colder material

into the dissolved zone would eventually cause material to be pushed into the zone which contains an increased volume fraction of  $\gamma'$ . The increased strength of this material will subsequently reduce the upset rate, alongside resisting the shear deformation at the contact interface. The resistance to shear would cause a sharp increase in the energy input rate, as it would act as a braking force at the interface.

To assess whether this hypothesis regarding the microstructural behaviour controlling the physical response of the process at the end of the weld is correct, microstructural evolution data from the end of the conditioning stage is presented in Figure 5.36.

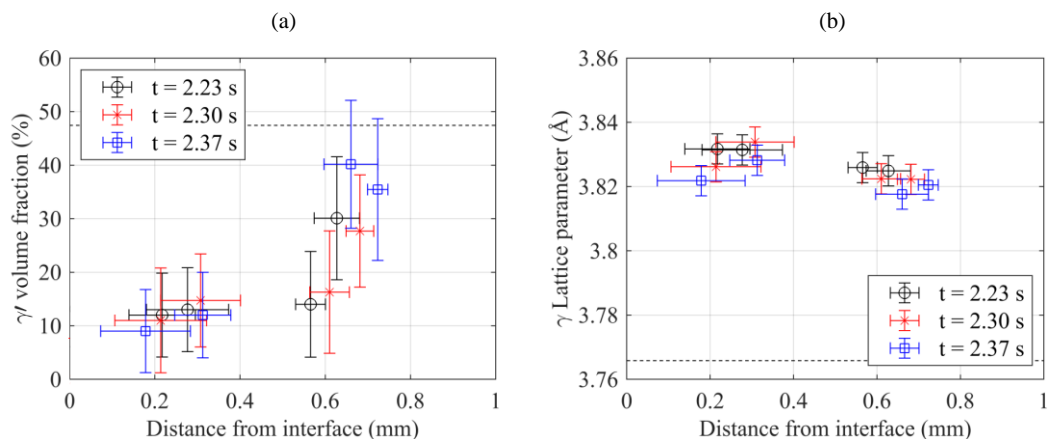


**Figure 5.36:** Microstructure evolution during the end of consolidation for weld parameter set N1. (a)  $\gamma'$  volume fraction, (b)  $\gamma$  lattice parameter.

In Figure 5.36a, measurements were taken from a broad enough axial range to clearly define the size of the zone in which  $\gamma'$  had been dissolved. Despite this region appearing larger in the early stage of conditioning, it can be defined that the approximate axial length of the region was 0.7 mm. This data is of great interest, specifically when compared with the microstructural data acquired during burn-off. The axial length of the  $\gamma'$  dissolved zone during burn-off was in the region of 0.5 mm, which permitted an upset rate of 0.26 mm/s. This is much lower than the upset rate of 1.25 mm/s which was measured during consolidation.

One would expect that an increased energy input rate would have occurred during consolidation, in order to permit this rate of deformation. However, the average energy input rate during consolidation was only 50 % of that measured during burn-off. This shows that the upset rate which occurs is extremely sensitive to the size of the region

in which significant  $\gamma'$  dissolution has occurred, with a 40 % increase in the zone length providing an increase in upset rate of approximately 600 %.

This is not the only factor controlling the upset rate, however. It becomes clear when analysing this data that the microstructure outside of this zone clearly has an effect on the deformation behaviour of the weld. For instance, the burn-off stage occurs early in the weld, when high temperatures are relatively localised around the contact interface due to the limited time for conduction of heat axially through the specimens. On the contrary, consolidation occurs later in the weld, when heat generated at the interface throughout the process was conducted through the specimens. Therefore, there is an increased temperature outside of the  $\gamma'$  dissolved zone. When the material outside of the zone is pushed inwards due to upset, a smaller increase in temperature is required to cause dissolution of  $\gamma'$  and maintain the size of the zone, when compared with burn-off.

In Figure 5.36b, there is a clear reduction in lattice parameter between 2.23 s and 2.37 s, which indicates that there was a reduction in temperature across the specimen. This is in agreement with the trend seen in Figure 5.35b, likely validating the hypothesis that the reduction in temperature will begin the process of stalling the weld.

Similar to burn-off, where the upset rate was linear, all the  $\gamma'$  volume fraction data acquired during consolidation can be plotted together to accurately define the microstructural profile present during this stage of the weld. This data is presented in Figure 5.37. The dissolved zone present during consolidation shares some similarities with that of the burn-off stage. Again, there is a steep gradient on the outer edge of the zone, occurring between 0.6 mm and 0.7 mm during consolidation. Between the contact interface and  $z = 0.6$  mm, the volume fractions present in the diffraction data would suggest full dissolution of secondary and tertiary  $\gamma'$  occurred throughout consolidation. Unfortunately, it cannot be confirmed whether complete dissolution of primary  $\gamma'$  occurred close to the contact interface, due to the inability to accurately resolve  $\gamma'$  volume fractions below 10 %. However, it can be said that complete dissolution of primary  $\gamma'$  is unlikely with an upset rate in the order of 1.47 mm/s, due to the large amount of material ejected and the requirement for increased time at elevated temperatures to fully dissolve these larger precipitates.

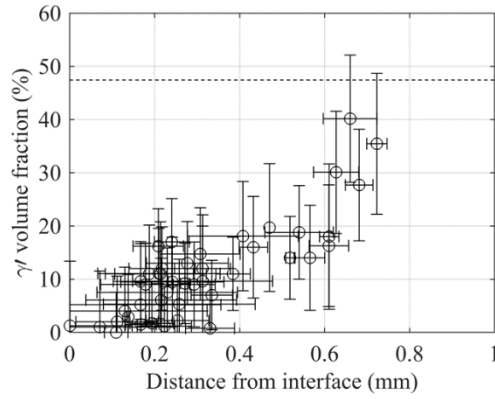


**Figure 5.37:** All  $\gamma'$  volume fraction data acquired during steady-state consolidation.

### 5.5.6 Microstructure evolution during weld stall

Weld stall has been defined as the short stage of an inertia friction weld which occurs between the end of the linear upset rate portion of consolidation, and the end of the weld by which the rotational velocity reaches zero. Whilst this stage would commonly be defined as part of consolidation, the acquisition rate of diffraction data recorded during this study allows for this stage to be analysed separately. Microstructural evolution data from the start of weld stall is presented in Figure 5.38.

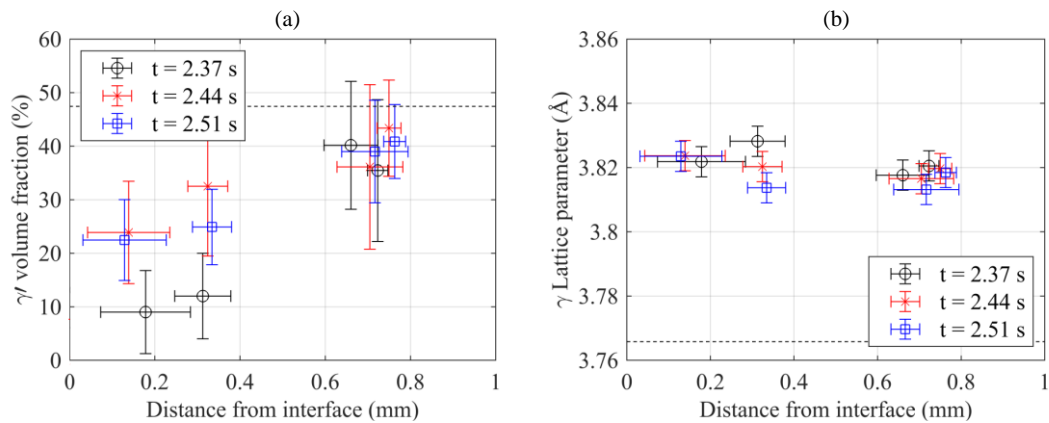


**Figure 5.38:** Microstructure evolution during the start of weld stall for weld parameter set N1. (a)  $\gamma'$  volume fraction, (b)  $\gamma$  lattice parameter.

A weld time of 2.37 s coincides with the last data point recorded during the linear upset region of consolidation. In Figure 5.38a, it can be clearly seen that the end of consolidation is caused by an influx of material with increased  $\gamma'$  volume fraction,

which is likely to be at a lower temperature. This agrees with the lattice parameter data from the middle and end of consolidation, in which a general reduction in temperature across the specimens was observed.

The microstructural evolution data acquired during the end of weld stall is plotted in Figure 5.39. Throughout weld stall there is a decreasing upset rate, which is seen in Figure 5.39a as there is little evolution in the  $\gamma'$  volume fraction during the last 0.14 s of welding. Again, a reduction in lattice parameter is observed which highlights the reduction of temperatures which occurred throughout the specimens.

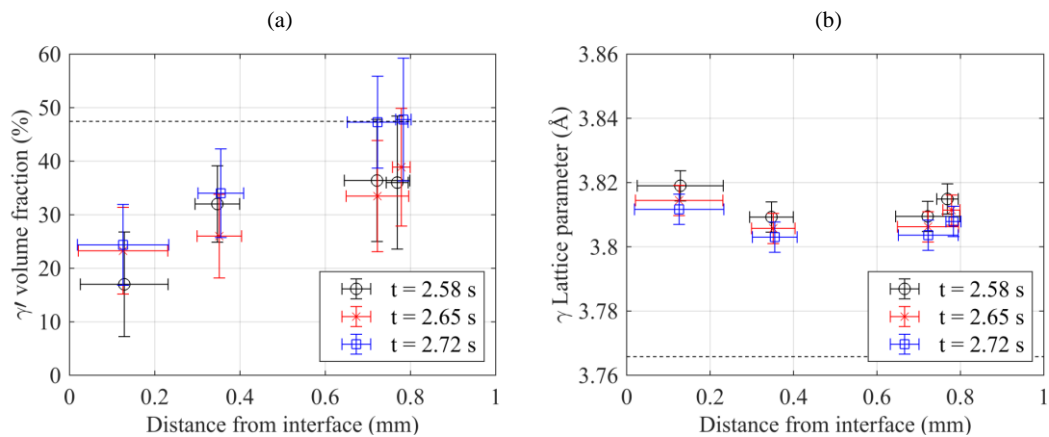


**Figure 5.39:** Microstructure evolution during the end of weld stall for weld parameter set N1. (a)  $\gamma'$  volume fraction, (b)  $\gamma$  lattice parameter.

An interesting observation to make through this analysis is the variation in the microstructure profile between burn-off, consolidation and at the end of welding. Despite there being a clear HAZ present at the end of the weld, this had a much smaller axial size than those observed during welding. Additionally, the  $\gamma'$  volume fractions across the HAZ at the end of the process were larger than those observed during burn-off and consolidation.

### 5.5.7 Thermal validation of diffraction data

To validate the evolution of lattice parameters observed in the in-situ X-ray diffraction measurements, in-situ thermocouple measurements have been recorded during validation welds of parameter set N1. Type K thermocouples were spot-welded to the fixture specimen at distances 0.72 mm and 1.2 mm from the contact interface. The thermocouple spot sizes were measured to have an approximate diameter of 0.6 mm, which provides an uncertainty of  $\pm 0.3$  mm in the positional measurements from which temperatures were recorded due to the large thermal gradients which are known to exist in the IFW process, and thus would exist across the thermocouple spot.

First, the validation weld outputs have been compared against the mean weld data for parameter set N1. This allows for analysis of the repeatability of the validation welds compared to the welds performed during the in-situ diffraction experiments. Additionally, the difference in the upset response has been used to evaluate positional error of the thermocouple position when compared with diffraction results. The comparison of weld outputs for the thermocouple validation welds is presented in Figure 5.40.

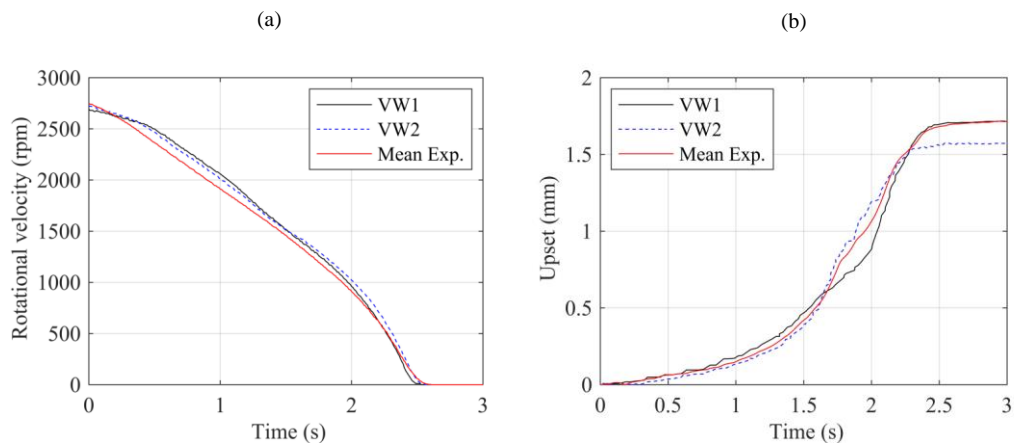


**Figure 5.40:** Weld output data from the validation welds compared with the mean experimental weld. (a) rundown, (b) upset.

It can be seen in Figure 5.40a that the rundown curves of the validation welds are consistent with that of the mean experimental weld, with there being minimal variation in weld duration or the rundown profile. In Figure 5.40b, the upset response of the

validation welds is seen to have excellent agreement with the mean experimental weld upset curve. The maximum difference in the upset response occurs at the end of welding, where validation weld 2 had a total upset which was 6.06 % lower than that of the mean experimental weld.

The thermocouple positions have been measured in a similar manner to the beam position. Here, both specimens were assumed to deform symmetrically about the weld interface and therefore the upset profile was used to calculate the evolution of the thermocouple relative to the contact interface. The thermocouple positions throughout IFW are presented in Figure 5.41.

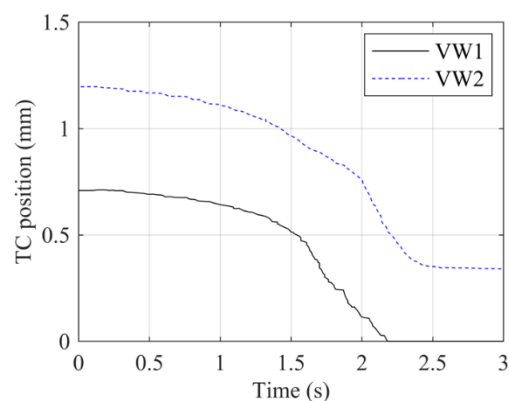


**Figure 5.41:** Thermocouple positions relative to the contact interface for the two validation welds performed.

The thermocouple readings measured from the two validation welds are presented in Figure 5.42. It is observed that despite the different positions of the thermocouples, the temperature measurements recorded by both were similar for the first 0.25 s of welding. Beyond this, it is clear that the thermocouple measurement from validation weld 1 was recorded from a position closer to the contact interface, as the heating rate and peak temperatures were both larger in this case.

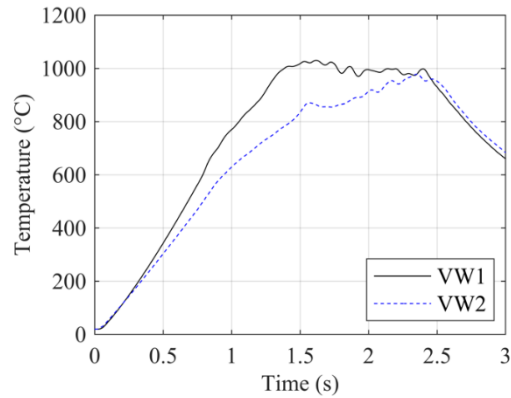


**Figure 5.42:** Thermocouple measurements recorded during the two repeat welds performed.

To analyse the thermal response throughout IFW, diffraction data has been extracted at weld times of 0.34 s, 0.9 s, 1.46 s, 2.02 s, 2.72s. These times coincide with the middle of the conditioning, burn-off, transition and consolidation stages, alongside the time at which the weld was completed.

For each point in time, the lattice parameters evaluated from the in-situ synchrotron diffraction experiments are presented at the axial positions from which they were recorded. At the same points in time, thermocouple readings have been extracted and Figure 5.23 has been used to evaluate the lattice parameter due to thermal expansion. The thermocouple readings have been presented at their interface-relative axial positions. Positional error bars have been defined in the thermocouple positions from the thermocouple spot size, and the difference in upset response compared to the mean weld. Finite element models have been used to predict the axial thermal profile at the time point at which temperatures were recorded to define the uncertainty in temperature due to uncertainty in positional measurements. The uncertainty in the temperature measurements have also been evaluated in the predicted lattice parameters. The thermocouple measurements and calculated thermal lattice parameters are presented for the middle of the conditioning stage in Figure 5.43.

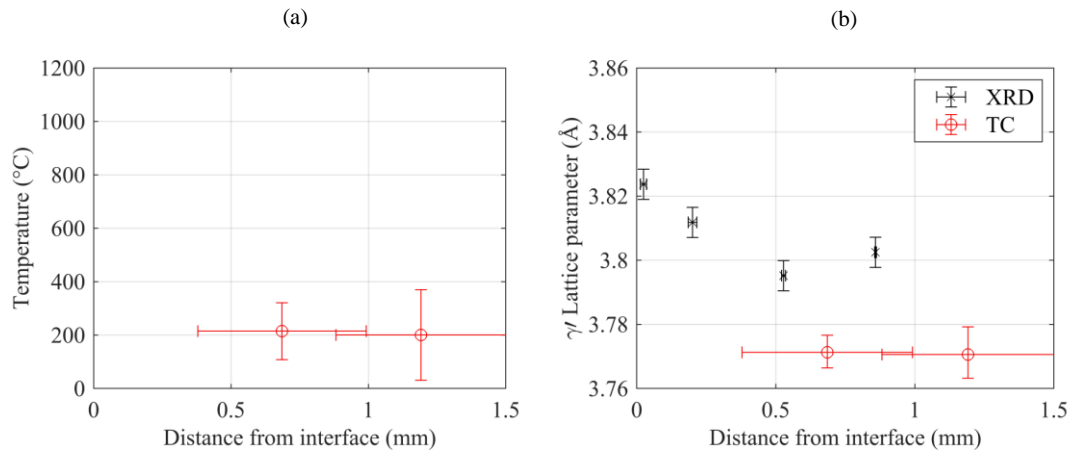


**Figure 5.43:** Thermal validation of diffraction data for the middle of the conditioning stage. (a) temperature readings, (b) calculated thermal lattice parameter.

At a weld time of 0.34 s, it can be observed that the positions at which thermal measurements were taken were too far from the interface to measure any significant thermal effects. The insufficient time for conduction of heat generated at the contact interface produced temperatures in the region of 200 °C.

The thermal lattice parameters calculated in Figure 5.43b show good agreement with the XRD data for positions between 0 and 0.6 mm. However, the XRD measurement at a position 0.85 mm from the contact interface is much larger than the predicted thermal lattice parameter from the thermocouple measurements. This suggests that a large amount of mechanical strain is present within this region. However, the fact that the lattice parameters evaluated from the diffraction data were larger than those evaluated from thermal measurements suggests tensile mechanical strain. This is unexpected given the compressive nature of the IFW process. 5.44a.

Figure 5.44 presents the temperature measurements and predicted thermal lattice parameters for the middle of the burn-off stage. Here, significant conduction of the heat generated at the contact interface can be observed in Figure 5.44a. Figure 5.44b shows a similar trend to Figure 5.43b, when the thermocouple predicted thermal lattice parameters are compared with the XRD measurements. Again, the thermocouple predictions appear to agree well with data recorded at positions between 0 and 0.5 mm from the contact interface. The weld lattice parameter recorded at a position 0.8 mm

from the contact interface was again much larger than the thermal predictions. This again suggests the presence of tensile mechanical strain.

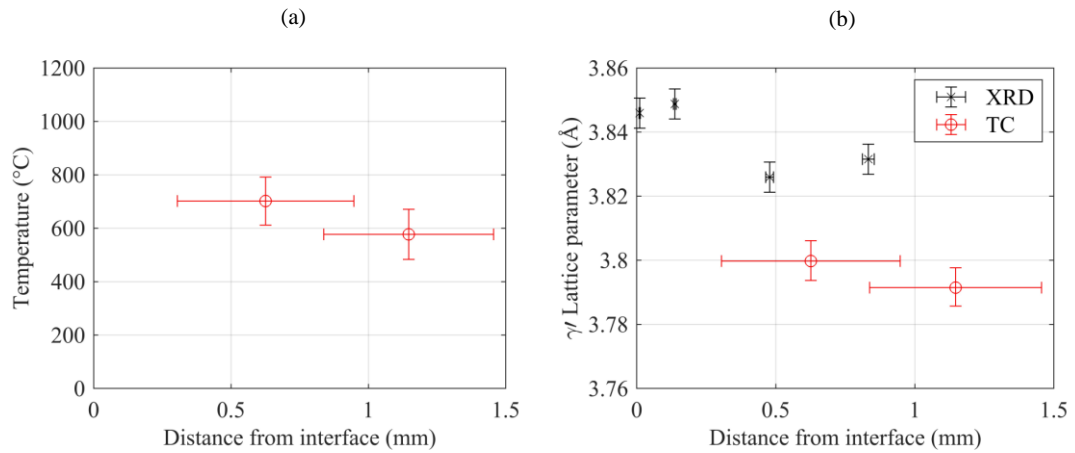


**Figure 5.44:** Thermal validation of diffraction data for the middle of the burn-off stage. (a) temperature readings, (b) calculated thermal lattice parameter.

Figure 5.45 presents the thermocouple data acquired during the middle of the transition from burn-off to consolidation. A combination of the increased time for conduction of heat generated at the contact interface and the movement of thermocouples closer to the contact interface due to upset is observed due to the increase in temperature seen at this time.

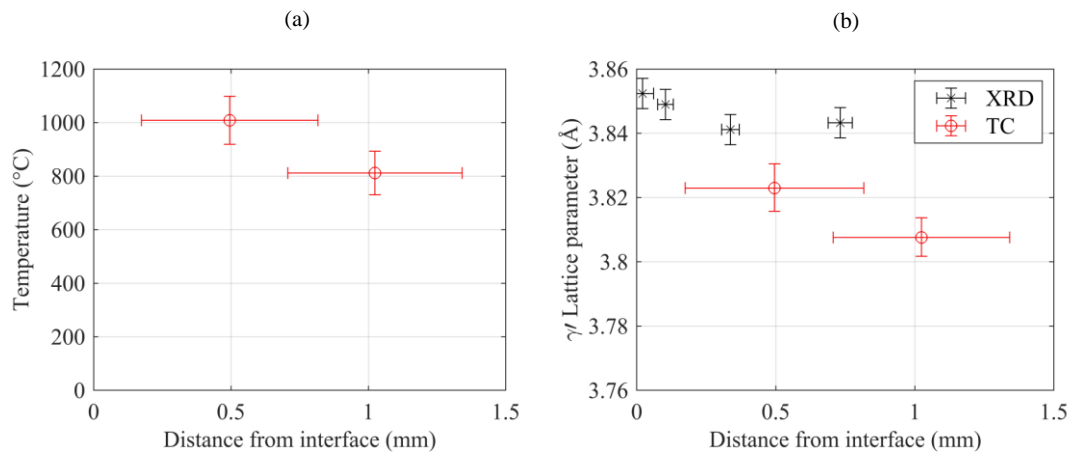


**Figure 5.45:** Thermal validation of diffraction data for the middle of the transition from burn-off to consolidation. (a) temperature readings, (b) calculated thermal lattice parameter.

Figure 5.45b presents the same trend as seen so far throughout the process, where the lattice parameter evaluated furthest from the contact interface during IFW shows a large discrepancy with the thermal predictions of lattice parameter. Again, this highlights the presence of tensile mechanical strain within this region. However, it should be noted that the difference between in-situ weld lattice parameter and thermal predicted lattice parameter was smaller in this case when compared to conditioning and burn-off.

The thermocouple data and predicted thermal lattice parameters are presented in Figure 5.46. In Figure 5.46b, it can be observed that there is a consistent trend in which the XRD evaluated lattice parameters are larger than those predicted due to thermal effects alone. This suggests that there was a large mechanical influence on the microstructure throughout the axial length of the specimens, as the thermal measurements alone cannot account for the increase in lattice parameter observed during this stage of the weld.

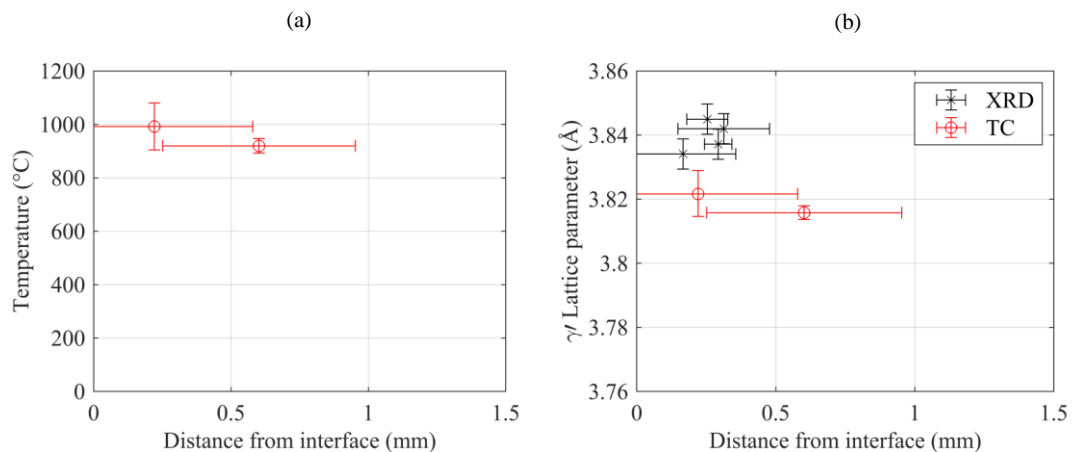


**Figure 5.46:** Thermal validation of diffraction data for the middle of the consolidation stage. (a) temperature readings, (b) calculated thermal lattice parameter.

Figure 5.47 presents the temperature data recorded during weld stall, alongside the predictions of lattice parameters due to thermal expansion. Figure 5.47b shows an excellent agreement between thermally predicted lattice parameters and those measured during the in-situ diffraction experiments. This shows that there is little mechanical effect on the microstructure at the end of the weld, which is to be expected.

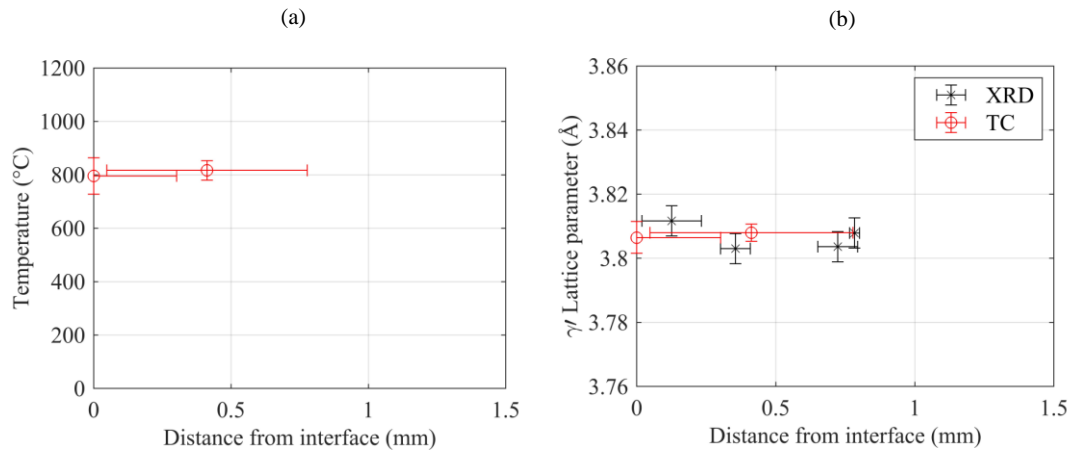


**Figure 5.47:** Thermal validation of diffraction data at weld stall. (a) temperature readings, (b) calculated thermal lattice parameter.

The validation welds in which spot-welded thermo-couples were implemented to acquire thermal evolution data have been used to predict the lattice parameter due to thermal expansion which occurs during the process. These predictions have been compared with the lattice parameters evaluated from in-situ diffraction images. For conditioning, burn-off, and the transition to consolidation, the thermal lattice parameter predictions showed good agreement with the lattice parameters recorded during IFW at positions close to the interface.

Throughout these three weld stages, there was a clear mechanical strain present at distances further from the interface. It should be noted that at these positions, no dissolution of the  $\gamma'$  phase was observed as presented previously in this chapter. Therefore, it is hypothesised that this tensile mechanical strain observed here may be due to the interaction between the  $\gamma$  phase and  $\gamma'$  precipitates, as it is not observed in diffraction images in which  $\gamma'$  dissolution has occurred.

In the consolidation phase, the in-situ diffraction results produced lattice parameters much larger than the thermal predictions, indicating the presence of a large mechanical strain. Whilst this was only observed close to the interface, due to the small positional range over which data was acquired during this time, it is expected this effect occurs further from the interface also.

At the end of the process, the in-situ measurements of lattice parameter showed excellent agreement with the thermal predictions. This is logical as the deformation had stopped at this time, and so no mechanical influence would be expected. Therefore, the lattice parameters observed via in-situ diffraction would be controlled primarily by the temperatures as the specimens cooled after the process finished.

## 5.6 Sensitivity of microstructure evolution to process parameters

To understand the sensitivity of microstructure evolution to weld input parameters, direct comparisons were made between the microstructure evolution for welds of different process parameters. Due to the large amounts of data recorded in these experiments, data has only been evaluated from the start, middle and end of each weld stage.

### 5.6.1 Sensitivity to weld pressure

The first comparison made is between the two parameter sets with low initial rotational velocity, N1 and N2. Here, parameter set N1 had a much larger weld pressure than N2. The mean weld upset curves are presented in Figure 5.48, alongside the defined stages analysed in these comparisons.

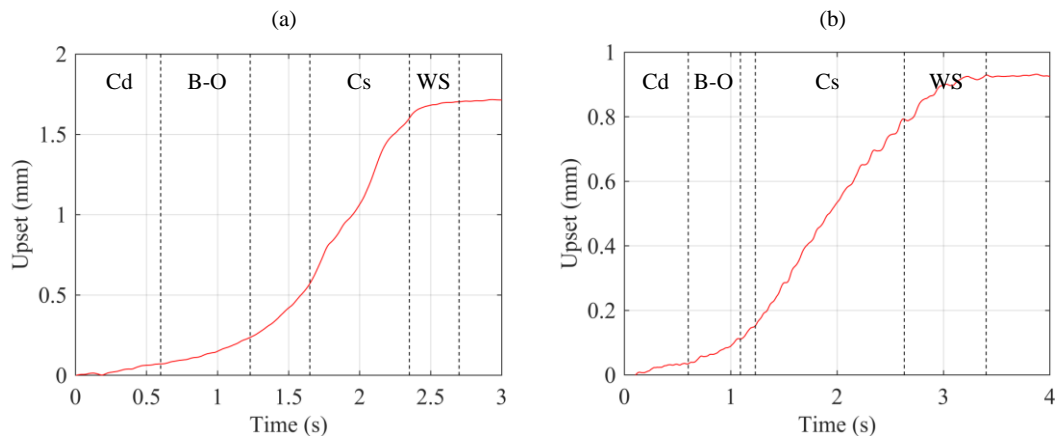
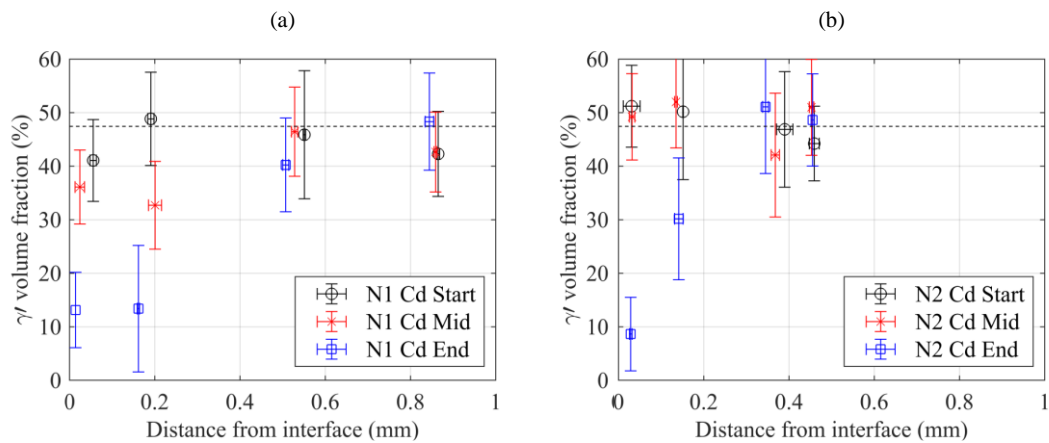


**Figure 5.48:** Mean upset data for the low speed welds with defined weld stages. (a) N1 – high pressure, (b) N2 – low pressure.

Both low speed welds have identical conditioning time. The high pressure variant (N1) had a longer burn-off stage with increased upset rate during this stage, due to the faster energy input rate. The higher rate of energy input is also seen in the increased upset rate produced by the consolidation stage of the high pressure welds. The increased energy input rate produced by high pressure welds resulted in a shorter weld duration.

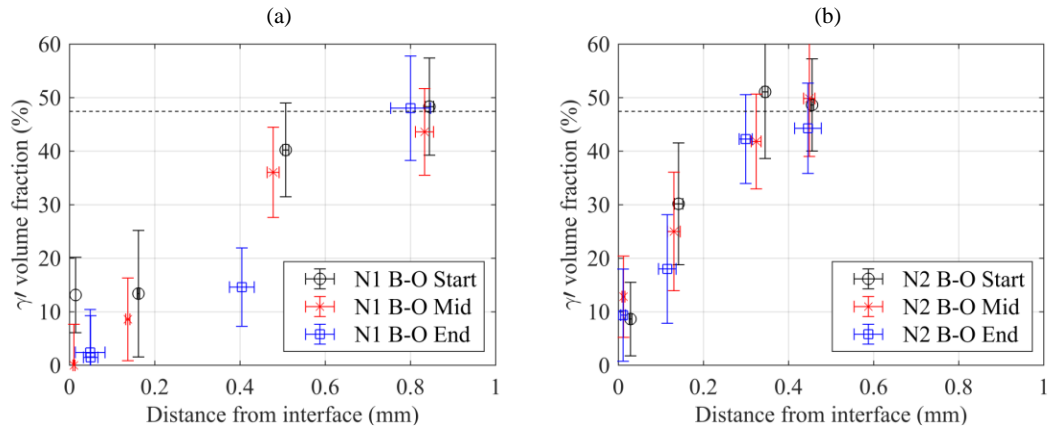
It should be noted here that there was an outlier in weld parameter set N2, with weld N2, P4 providing insufficient upset. However, the upset profile of this weld aligns with the mean data during conditioning and burn-off, and so this weld will only be treated separately during consolidation and weld stall.

The microstructure evolution during conditioning of low speed welds is presented in Figure 5.49. It can be seen that dissolution of  $\gamma'$  began earlier in the high pressure welds, due to the increased energy input rate under the increased mechanical loading. Furthermore, the increased pressure produced a broader  $\gamma'$  dissolved zone at the end of conditioning, due to the increased heat generation and conduction. The full set of microstructure evolution for parameter set N2 is available in Appendix A1.



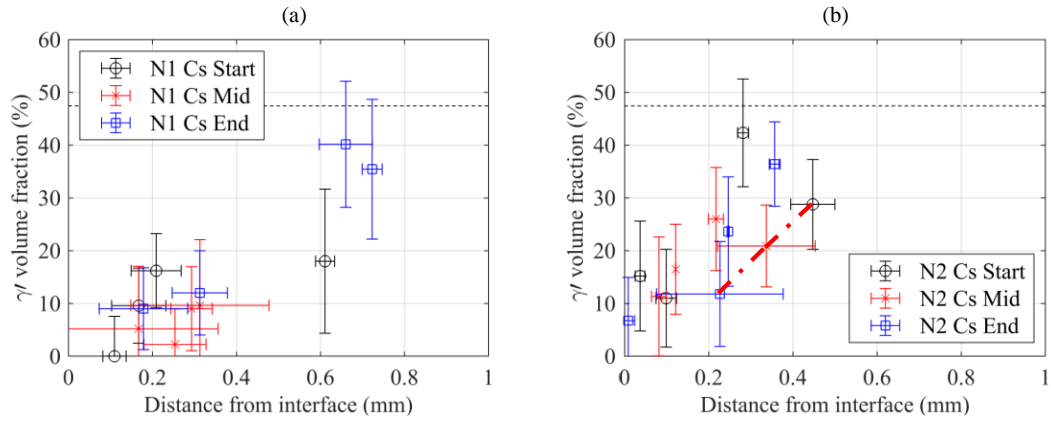
**Figure 5.49:**  $\gamma'$  volume fraction evolution during conditioning of the low speed welds. (a) N1 – high pressure, (b) N2 – low pressure.

Figure 5.50 presents the  $\gamma'$  volume fraction evolution for the burn-off stage of the low speed welds. Both welds exhibited a steady-state axial profile of  $\gamma'$  volume fraction during conditioning. The broader zone presenting  $\gamma'$  dissolution in the high pressure welds appears to permit the increased upset rate during burn-off of these welds.



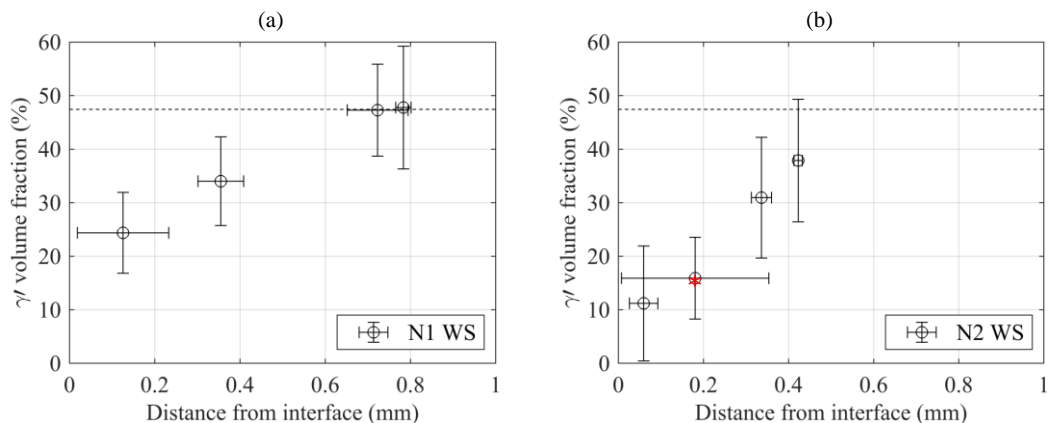
**Figure 5.50:**  $\gamma'$  volume fraction evolution during the burn-off stage of the low speed welds. (a) N1 – high pressure, (b) N2 – low pressure.

In Figure 5.51, the microstructure evolution during consolidation is presented. Here, the reduced upset of weld N2, P4 can be clearly noticed, with the data points recorded during this weld appearing to show a broader zone of  $\gamma'$  dissolution. It becomes clear in Figure 5.51b that weld N2, P4 did not provide insufficient upset due to the microstructural evolution, but more likely due to a poor mechanical response from the welding machine. It is hypothesised that increased friction between the weld carriage and tie bars may have occurred during this weld, as the microstructural profile produced would permit the same upset rate as the remaining three welds from parameter set N2.



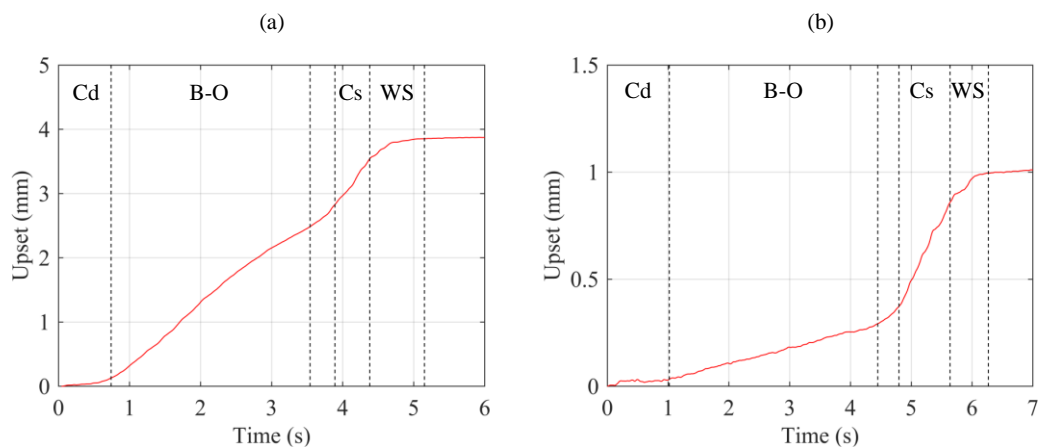
**Figure 5.51:**  $\gamma'$  volume fraction evolution during the consolidation stage of the low speed welds. (a) N1 – high pressure, (b) N2 – low pressure. The data points joined by a dashed red line in Figure 5.51b are those of weld N2, P4, in which a reduced total upset occurred.

Figure 5.52 presents the  $\gamma'$  volume fraction profiles produced at weld stall for both low speed welds. The welds with increased pressure produced a broader HAZ at the end of the process. However, the low pressure welds had a reduced  $\gamma'$  volume fraction at the contact interface at the end of welding. This is logical considering the total energy input of both weld parameter sets was consistent, and the reduced upset of the low pressure welds. As less mechanical deformation occurred, the material close surrounding the interface in welds of parameter set N2 would be subjected to an increased temperature for a longer time, resulting in increased dissolution of  $\gamma'$ .



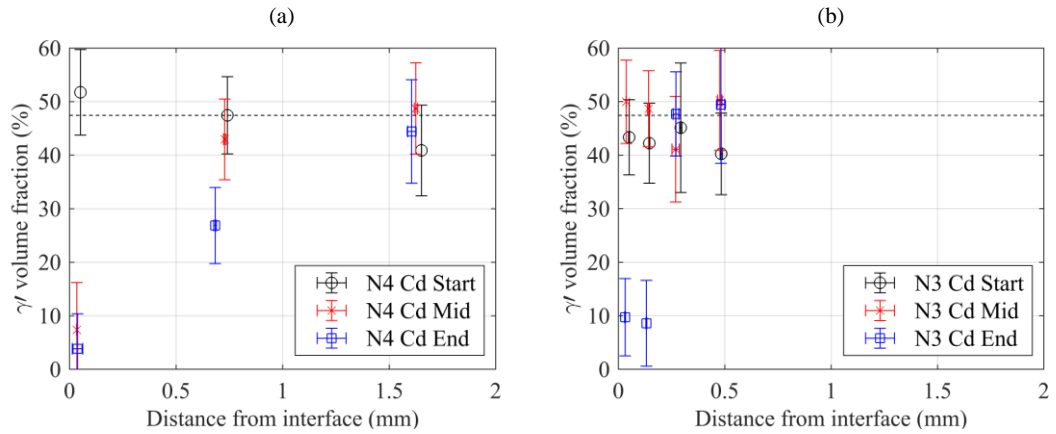
**Figure 5.52:**  $\gamma'$  volume fraction at the weld stall of the low speed welds. (a) N1 – high pressure, (b) N2 – low pressure. The data point overlaid with a red \* in Figure 5.52b is that of weld N2, P4, in which a reduced total upset occurred.

Next, the high speed welds are compared to assess their sensitivity to the weld pressure. Here, comparisons will be drawn between the low speed and high speed behaviour. The mean upset curves for parameter sets N4 and N3 are presented in Figure 5.53. It is observed that the low pressure variant produced an increased conditioning duration, which would be expected due to the slower energy input rate. The increased energy input rate in the high pressure weld produced a much higher burn-off rate. Similarly, the upset rate during conditioning was also larger in the high pressure weld. Again, the high pressure weld had a shorter duration due to the increased energy input rate.



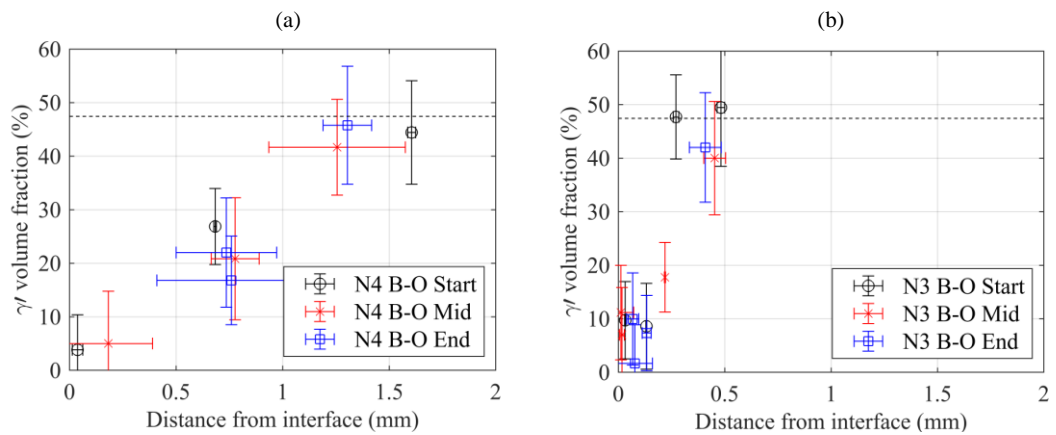
**Figure 5.53:** Mean upset data for the high speed welds with defined weld stages. (a) N4 – high pressure, (b) N3 – low pressure.

The microstructure evolution throughout conditioning of the high speed welds is provided in Figure 5.54. Similar to the low speed welds, the high pressure variant showed that dissolution of the  $\gamma'$  phase began earlier during conditioning than the low pressure counterpart. Additionally, the high pressure welds produced a much larger zone with reduced  $\gamma'$  volume fraction.



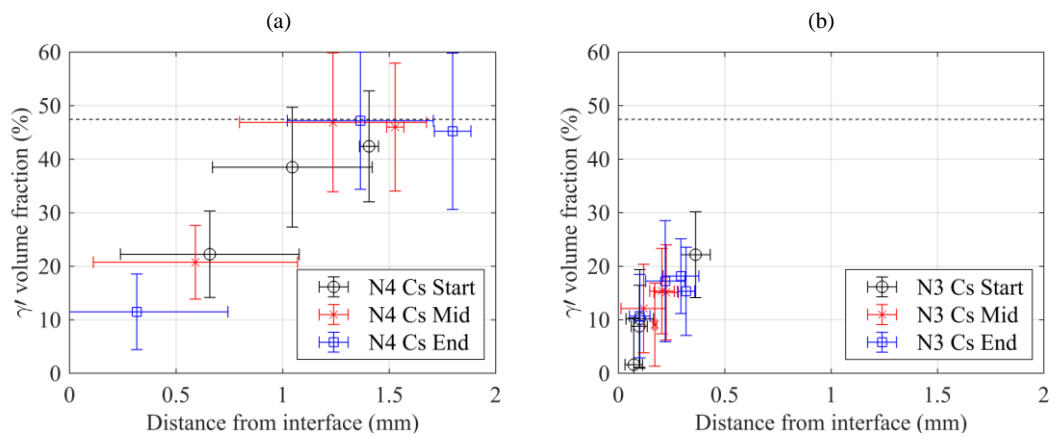
**Figure 5.54:**  $\gamma'$  volume fraction evolution during conditioning of the high speed welds. (a) N4 – high pressure, (b) N3 – low pressure.

Figure 5.55 presents the evolution of  $\gamma'$  volume fraction during burn-off for both high speed weld parameter sets. It is seen that a broader  $\gamma'$  dissolved zone of approximately  $z = 1$  mm was produced by the high pressure welds to permit the average burn-off rate of 0.84 mm/s. On the contrary, the narrow dissolved zone produced by the low pressure welds ( $z = 0.25$  mm) allowed for a much lower burn-off rate of 0.08mm/s. The full set of microstructure evolution for parameter sets N3 and N4 are available in Appendix A2 and A3, respectively.



**Figure 5.55:**  $\gamma'$  volume fraction evolution during the burn-off stage of the high speed welds. (a) N4 – high pressure, (b) N3 – low pressure.

In Figure 5.56, the  $\gamma'$  volume fraction evolution during consolidation of both high speed weld parameter sets is presented. Unfortunately, the large positional error bars on the high speed data make it difficult to define the size of the dissolved zone during conditioning of welds of parameter set N4. Additionally, the small axial range of data measurements for welds of parameter set N3 do not permit an accurate measurement of the dissolved zone in these welds. However, it is clear that between burn-off and consolidation, the zone became larger in low pressure welds, as the  $\gamma'$  volume fraction 0.25mm from the interface reduces from parent values in Figure 5.55b, to approximately 18 % in Figure 5.56b



**Figure 5.56:**  $\gamma'$  volume fraction evolution during the consolidation stage of the high speed welds. (a) N4 – high pressure, (b) N3 – low pressure.

The axial profile of  $\gamma'$  volume fraction for both high speed welds at the end of the process is presented in Figure 5.57. Due to insufficient axial data, the size of the HAZ at the end of weld N4 cannot be accurately defined. However, it is clear that there was a HAZ of length  $z = 0.5$  mm present in the low pressure welds. In both high speed welds, the  $\gamma'$  volume fraction is similar at the contact interface. This was not seen in the low speed welds, as the low speed, high pressure weld showed an increased interface  $\gamma'$  volume fraction when compared with its low pressure counterpart.

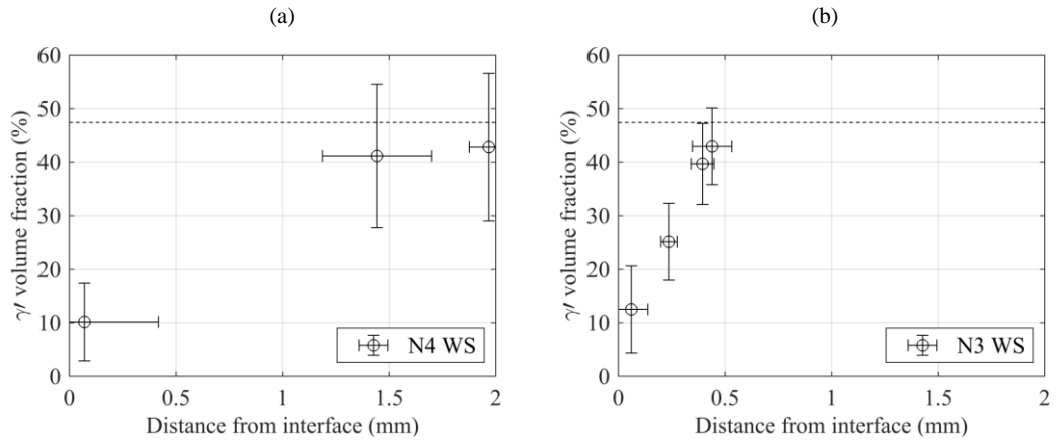
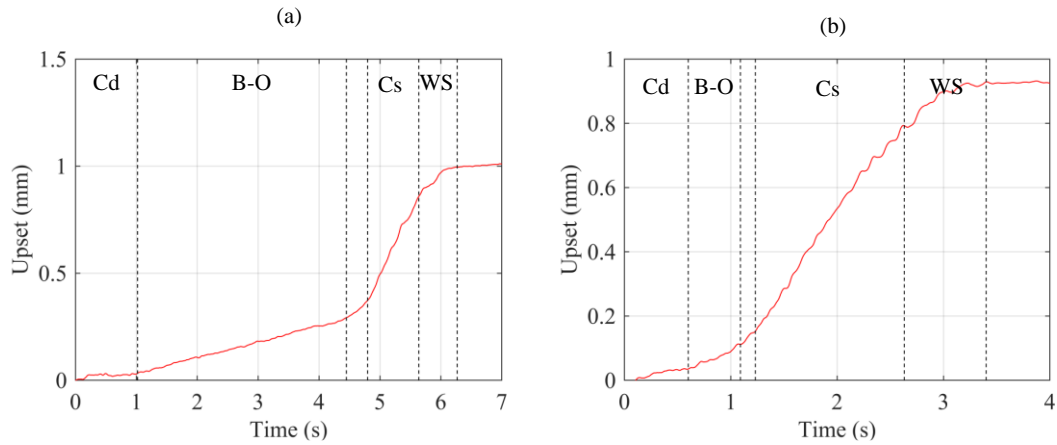


**Figure 5.57:** Axial profile of  $\gamma'$  volume fraction at the end of the high speed welds. (a) N4 – high pressure, (b) N3 – low pressure.

Through comparison of all welds, there were some clear trends defined. In both cases, the high pressure welds showed the onset of  $\gamma'$  dissolution occurring earlier during conditioning, due to the increased frictional heat generation at high pressures. In the high pressure welds, this increased energy input continued to produce broader zones in which the microstructure was changed significantly from parent values. These broader zones of softer material permitted the increased upset rates during burn-off and consolidation seen in the high pressure welds.

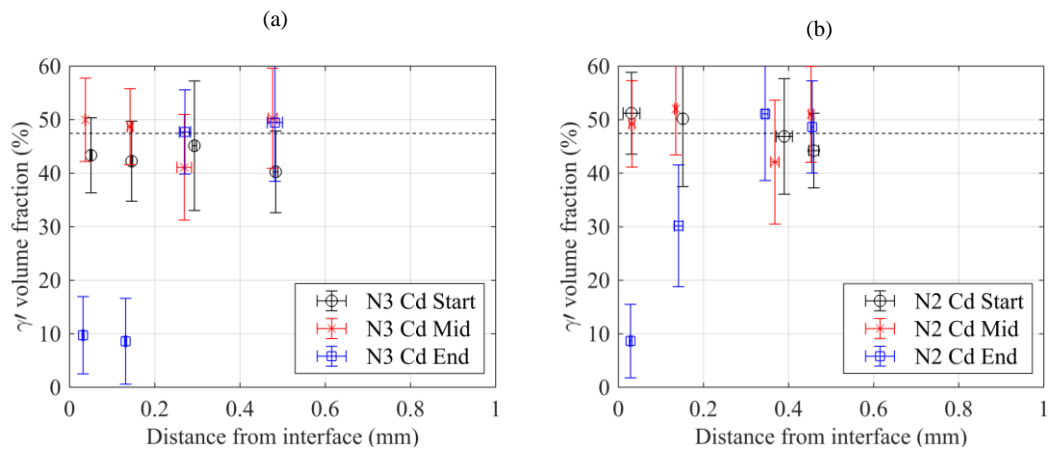
### 5.6.2 Sensitivity to initial rotational velocity

Comparing the microstructural evolution with welds of identical weld pressure allows for an assessment of the sensitivity of the microstructural evolution to the initial rotational speed, or total energy input. First, welds with low weld pressure, parameter sets N3 and N2 are compared. The mean upset data for these weld parameter sets are presented in Figure 5.58 alongside the defined stages of each weld.



**Figure 5.58:** Mean upset data for the low pressure welds with defined weld stages. (a) N3 – high speed, (b) N2 – low speed.

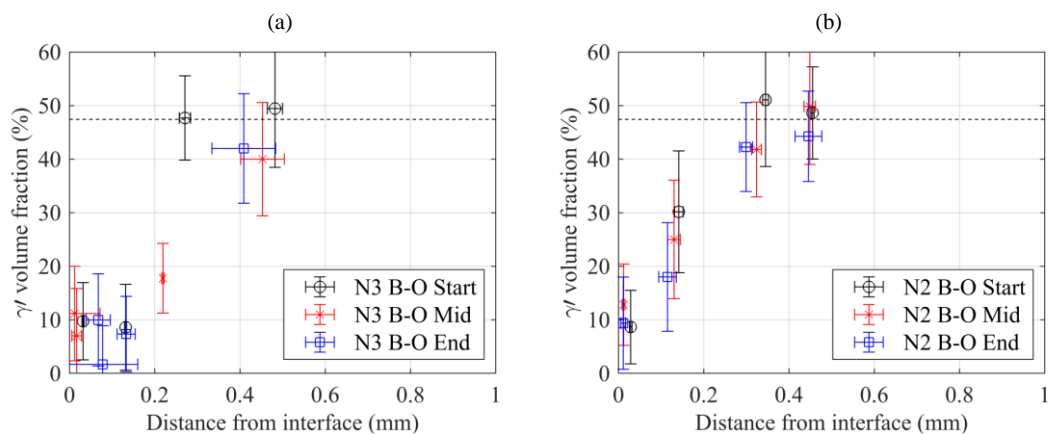
When comparing the mean upset curves, it can be seen that the high speed weld had a longer conditioning time. This was followed by a longer burn-off stage with increased burn-off rate due to the larger energy input rate. The high speed weld also had an increased upset rate during consolidation. Due to the increased amount of total energy available for mean weld N3, the weld duration was significantly longer.



**Figure 5.59:** Axial profile of  $\gamma'$  volume fraction during conditioning of the low pressure welds. (a) N3 – high speed, (b) N2 – low speed.

The evolution of the  $\gamma'$  volume fraction during the conditioning stage of the low pressure welds is presented in Figure 5.59. Both sets of input parameters showed no dissolution of  $\gamma'$  at the start or middle of conditioning, with the  $\gamma'$  volume fraction only decreasing towards the end of the conditioning stage. Interestingly, the size of the zone with reduced  $\gamma'$  volume fraction appears to be approximately the same size for both welds. However, it can be seen that the increased rotational velocity (and total weld energy) provided by the increased velocity provided a larger energy input rate during this stage, as the  $\gamma'$  volume fraction from welds of parameter set N3 showed increased dissolution of  $\gamma'$  at a distance of 0.15 mm from the contact interface.

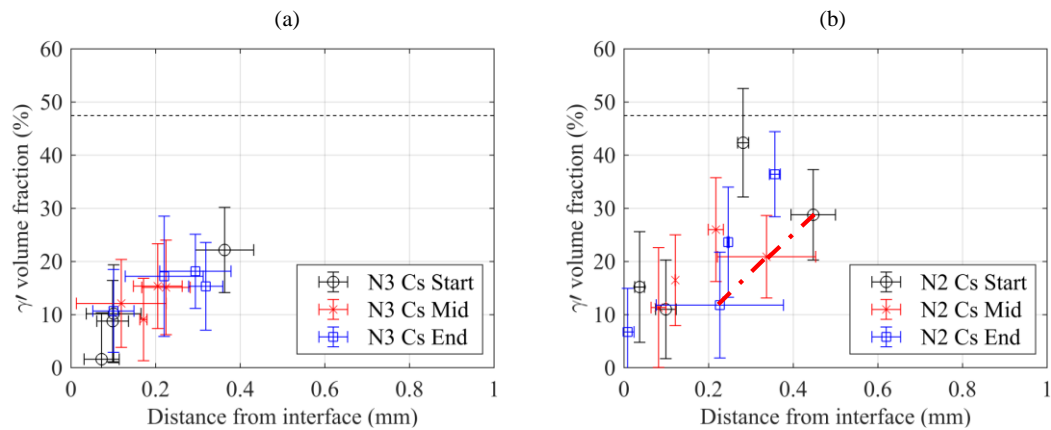
In Figure 5.60, the microstructure evolution of low pressure welds is presented for the burn-off stage of the process. It is observed that the axial  $\gamma'$  volume fraction profiles produced during conditioning were preserved throughout burn-off. Additionally, the axial length of the dissolved zone was approximately the same for both low pressure welds. This aligns with the similar upset rates produced by the welds during burn-off. The mean burn-off rates were 0.08 mm/s and 0.15 mm/s, respectively, for mean welds N3 and N2. This again shows the sensitivity of the burn off rate to the width of the  $\gamma'$  dissolved zone.



**Figure 5.60:** Axial profile of  $\gamma'$  volume fraction during the burn-off stage of the low pressure welds. (a) N3 – high speed, (b) N2 – low speed.

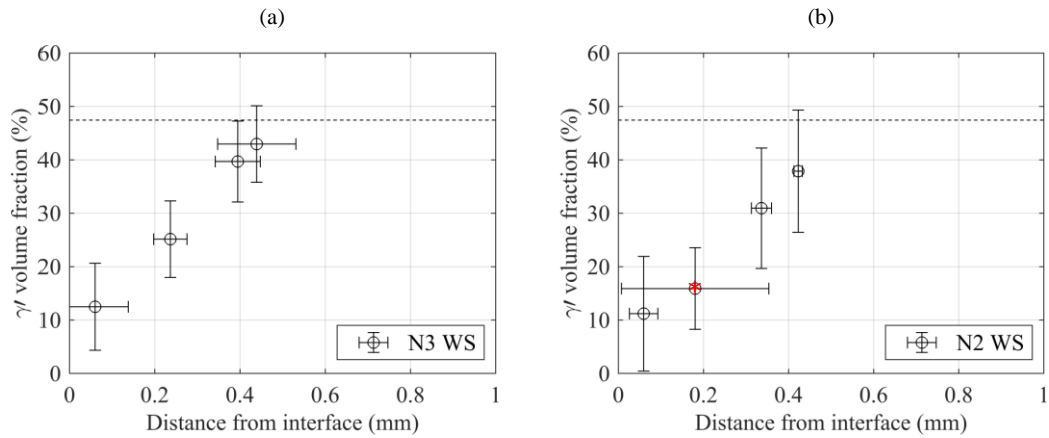
In Figure 5.61, the axial profiles of  $\gamma'$  volume fraction throughout consolidation of the low pressure welds is presented. Whilst the size of the dissolved zone cannot be accurately defined for the high speed welds (N3), it is clear that the zone was larger

when increased initial rotational velocity was used. When comparing the upset rates during conditioning of both weld sets, the 0.58mm/s rate produced by the high speed welds was greater than the 0.45 mm/s rate calculated from the low speed welds. This confirms that the dissolved zone from N3 was larger than that of N2 during the consolidation stage, as it permitted an increased upset rate.



**Figure 5.61:** Axial profile of  $\gamma'$  volume fraction during the consolidation stage of the low pressure welds. (a) N3 – high speed, (b) N2 – low speed. The data points joined by a dashed red line in Figure 5.61b are those of weld N2, P4, in which a reduced total upset occurred.

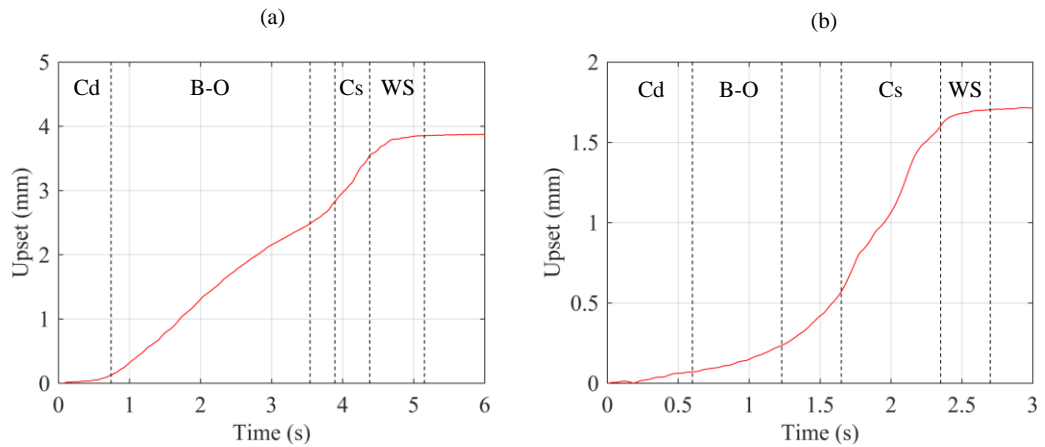
The axial profile of  $\gamma'$  volume fraction at the end of the process is presented for both low pressure welds in Figure 5.62. It appears that the HAZ present at the end of welding was similar for both welds, which is interesting due to the different macro-scale process behaviour produced by the two sets of welds. It is very likely that the HAZ is extremely dependent on the consolidation phase, with the volume of material ejected having a large effect on the material which remains once the process is complete. The upset rates during consolidation for both sets of low pressure welds were not drastically different, producing average rates of 0.45 mm/s and 0.58 mm/s. This assists the explanation of the similar HAZ profiles produced by the two sets of input parameters.



**Figure 5.62:** Axial profile of  $\gamma'$  volume fraction produced at the end of welding for the low pressure welds. (a) N3 – high speed, (b) N2 – low speed. The data point overlaid with a red \* in Figure 5.62b is that of weld N2, P4, in which a reduced total upset occurred.

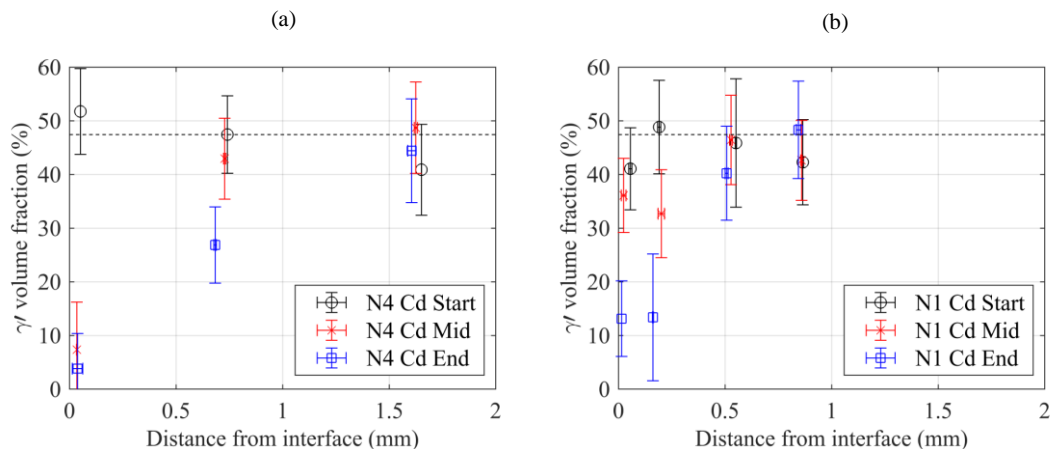
The high pressure welds were compared in the same nature to assess the sensitivity of microstructural response to the initial rotational velocity. Here, comparisons will be made between the trends seen in the low pressure and high pressure behaviour, to assist the understanding of process sensitivity. The mean upset curves are presented in Figure 5.63 for both high pressure welds.

Figure 5.63 shows that the conditioning duration for mean weld N4 was longer than that of mean weld N1. The increased initial rotational velocity produced a much larger upset rate during burn-off and a longer burn-off duration. Similar to the low pressure welds, both high pressure welds produced similar upset rates during consolidation, with values of 1.43 mm/s and 1.47 mm/s respectively for mean welds N4 and N1.



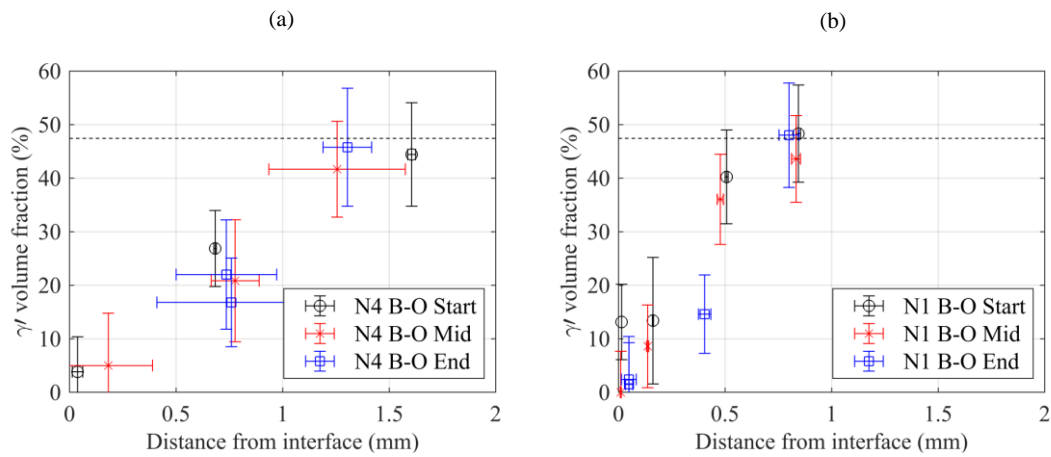
**Figure 5.63:** Mean upset data for the high pressure welds with defined weld stages. (a) N4 – high speed, (b) N1 – low speed.

The microstructural evolution which occurred during conditioning of both sets of high pressure welds is presented in Figure 5.64. It is observed that both high pressure welds showed dissolution of  $\gamma'$  around the contact interface during the middle portion of the conditioning stage. The effect of the increased energy input rate due to the larger initial rotational velocity can be seen in weld parameter set N4, as a larger  $\gamma'$  dissolved zone is produced at the end of conditioning.



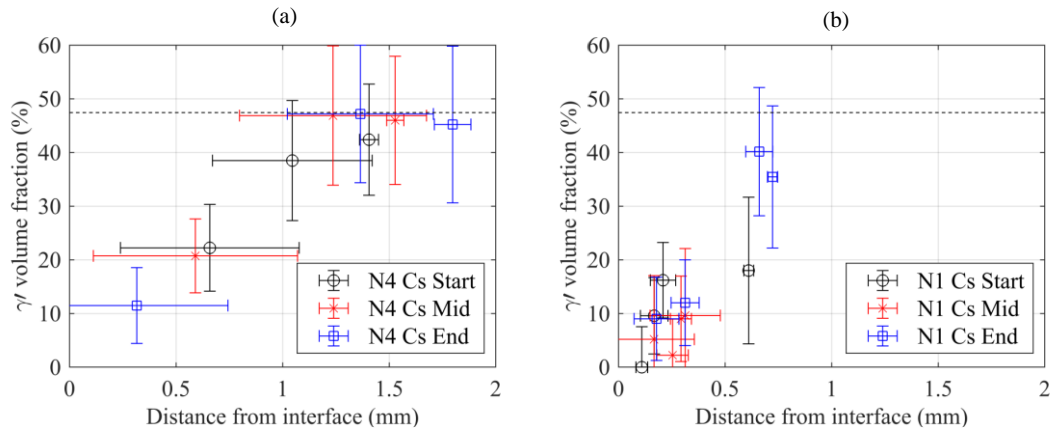
**Figure 5.64:** Axial profile of  $\gamma'$  volume fraction during conditioning of the high pressure welds. (a) N4 – high speed, (b) N1 – low speed.

In Figure 5.65, the microstructure evolution of the high pressure welds during the burn-off stage is presented. Both welds showed a steady-state microstructure evolution during burn-off, consistent with the linear upset rates produced during these stages. Mean weld N1 had a burn-off rate of 0.26 mm/s, while the upset rate of mean weld N4, was much larger, at 0.84 mm/s. As expected, the size of the dissolved zone was much larger in weld N4 during burn-off, permitting this increased upset rate.



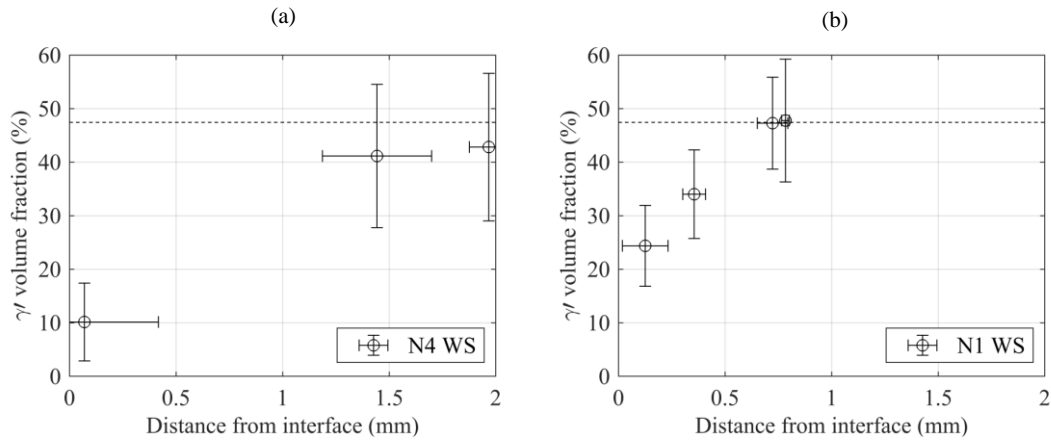
**Figure 5.65:** Axial profile of  $\gamma'$  volume fraction during the burn-off stage of the high pressure welds. (a) N4 – high speed, (b) N1 – low speed.

Figure 5.66 displays the microstructure evolution for both sets of high pressure weld parameter sets during consolidation. For weld parameter N4, there was little change between the burn-off profile and consolidation profile. However, this was to be expected considering the similar upset rates produced by the two stages. For the low speed welds, there was a clear increase in the  $\gamma'$  dissolved zone size from 0.5 mm during burn-off and 0.7 mm during consolidation, which aligns with the change in upset rate from 0.26 mm/s to 1.46mm/s between these two weld stages.



**Figure 5.66:** Axial profile of  $\gamma'$  volume fraction during the consolidation stage of the high pressure welds. (a) N4 – high speed, (b) N1 – low speed.

The axial profile of the  $\gamma'$  volume fraction at the end of both sets of high pressure welds is provided in Figure 5.67. Due to an insufficient range of axial data measurements in parameter set N4, the size of the HAZ at the end of the weld cannot be accurately measured. However, it can be seen that the interface volume fraction was much lower in the case of increased rotational velocity. It is believed that despite the two sets of parameters producing similar upset rates during consolidation, the increased total energy input in the high speed welds produced an increased amount of heat input and axial conduction throughout the specimen. Therefore, even with a high upset rate during consolidation, there was a more prominent HAZ in the high speed welds due to the fact that material further from the interface had been subjected to increased temperatures for longer durations.



**Figure 5.67:** Axial profile of  $\gamma'$  volume fraction for high pressure welds at the end of the process. (a) N4 – high speed, (b) N1 – low speed.

### 5.6.3 Assessment of microstructural control of macro-scale process behaviour

Through the analysis of the microstructure evolution during IFW of various sets of process parameters, it has become clear that there is a relationship between the size of the region which is denuded of  $\gamma'$  and the rate of axial deformation of material through upset. This is a logical trend, as the dissolution of  $\gamma'$  reduces the strength of the superalloy, permitting deformation at lower mechanical loads. Therefore, with a larger region of material which is reduced in strength, an increased rate of deformation can exist.

To assess the trends in the relationship between microstructural response and macro-scale upset behaviour, the  $\gamma'$  dissolved zone was measured from in-situ measurements during burn-off and consolidation. These have been plotted against the respective burn-off rates and consolidation upset rates which occurred during the mean weld of each parameter set. The relationship between  $\gamma'$  dissolved zone size and burn-off rate is presented in Figure 5.68. There appears to be a linear trend visible in the relationship between  $\gamma'$  dissolved zone width and burn-off rate, where the increased size of the zone permitted an increased burn-off rate.

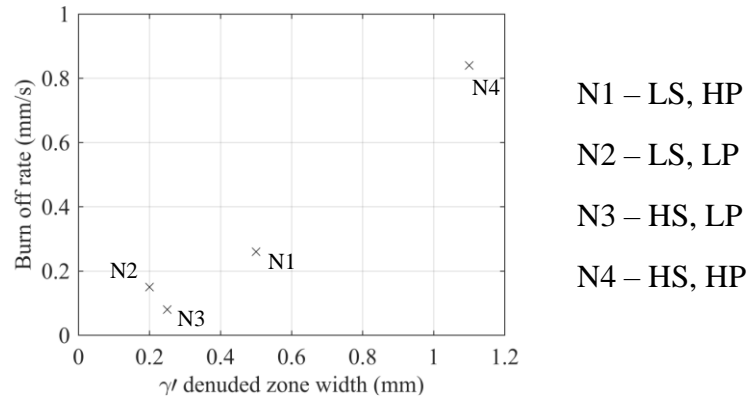


**Figure 5.68:** Relationship between the measured width of the  $\gamma'$  dissolved zone during burn-off and the burn-off rate for each weld parameter set.

The relationship between the  $\gamma'$  dissolved zone size during consolidation and the consolidation upset rate measured from each weld parameter set is presented in Figure 5.69. Here, there is no clear trend which links all the weld data. However, by adding trend lines connecting the points with identical input parameters, understanding of the behaviour which occurs can be developed.

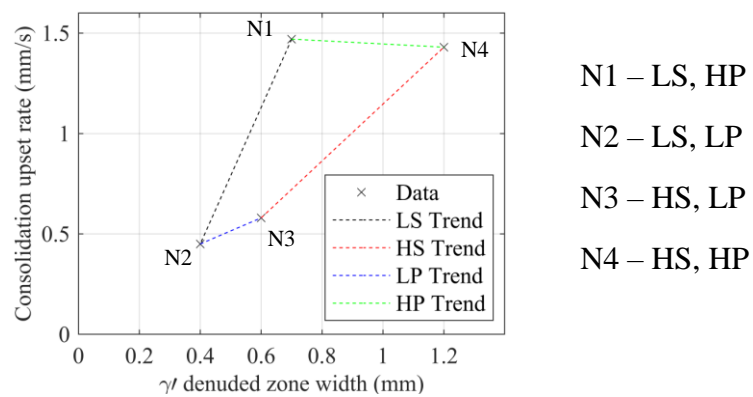


**Figure 5.69:** Relationship between the measured width of the  $\gamma'$  dissolved zone during consolidation and the consolidation upset rate for each weld parameter set.

When comparing the low pressure and high pressure trends, it is clear that an increase in weld pressure will cause a large increase in consolidation upset rate, with only a small increase in dissolved zone size measured for this change in parameters. When comparing the low speed and high speed trends, it can be seen that increasing the initial

rotational velocity will cause an increased dissolved zone size, but with little increase to the consolidation upset rate.

It is known via ex-situ metallurgical analyses that at constant pressure, increased initial rotational velocity will produce a larger HAZ. The data presented in Figure 5.69 goes some way to presenting the cause of this. As increasing the initial rotational velocity is shown to produce a wider  $\gamma'$  dissolved zone, a large 'in-situ HAZ' would be created in this case. As the consolidation upset rate does not increase proportionally with this, there is insufficient upset to eject from at the contact interface, which in turn would produce the larger HAZ seen in welds of increased rotational velocity.

To provide a direct comparison between the size of the  $\gamma'$  dissolved zone throughout the process for the four sets of weld parameters, the microstructure evolution data has been investigated at the start, middle and end of each weld stage for each set of process parameters. Despite these stages having different durations for each set of process parameters, they have been presented relative to the process to allow for a direct comparison.

For each point in time, the axial profile of  $\gamma'$  volume fraction has been extracted. A second order polynomial has been fit to the diffraction data points closest to the interface, and it has been ensured in each case that the minimum of this polynomial occurs at the contact interface. The axial position at which this polynomial intersects the parent  $\gamma'$  volume fraction of 47.43 % has been measured for each image to allow for an estimation of the  $\gamma'$  dissolved zone or 'in-situ HAZ'. It is acknowledged here that there are errors in both the positional measurements and the  $\gamma'$  volume fractions measured by Rietveld refinement. However, to allow for comparison between weld parameters, these have not been included in this study.

An example case from the end of conditioning stage of weld parameter set N1 is presented in Figure 5.70. Here, the size of the  $\gamma'$  dissolved zone was measured as 0.56 mm.

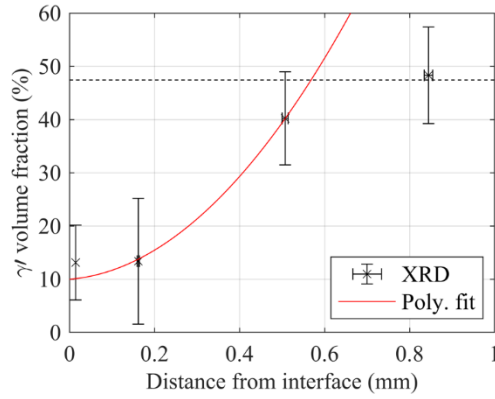


**Figure 5.70:** Polynomial fitting of the relationship between axial position and  $\gamma'$  volume fraction for the measurement of the  $\gamma'$  dissolved zone at the end of conditioning of weld parameter set N1.

This operation has been performed for the data acquired for each set of weld parameters at the start, middle and end of each weld stage, and is presented in Figure 5.71. It can be seen that weld parameter set N2 has the smallest  $\gamma'$  dissolved zone width throughout the process, which is logical given these welds utilised the lowest combination of weld parameters. The conditioning behaviour of both low pressure welds was similar, however it can be seen that through burn-off and consolidation the size of the  $\gamma'$  dissolved zone increased for the case with increased initial rotational velocity.

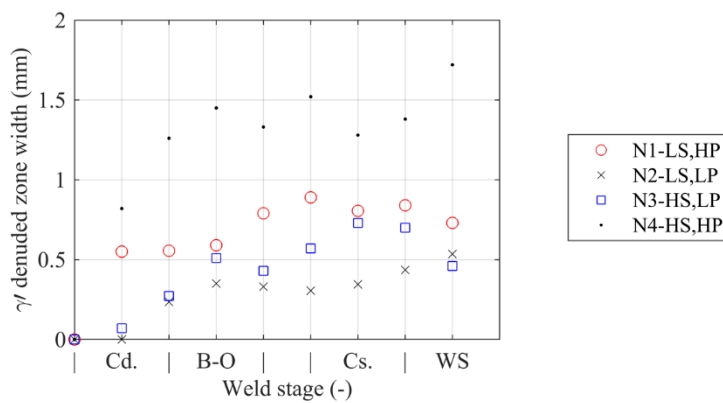


**Figure 5.71:** Size of the  $\gamma'$  dissolved zone relative to the IFW process for the four sets of weld parameters investigated in this study.

The high speed, high pressure combination of weld parameters produced the widest  $\gamma'$  dissolved zone both during the process and at the end of the process. Additionally, the values of  $\gamma'$  dissolved zone width throughout IFW were much larger than those produced by the three remaining parameter sets.

It would be logical to conclude that the low pressure welds produce the least detriment to the microstructure in the as-welded condition during IFW. However, it must be noted that these welds also produced the smallest upset values. Therefore, there may be issues regarding the amount of mixing that has occurred between the two specimens, which would result in a weaker weld joint. There is a compromise which must be made regarding optimal joint strength in the as-welded condition and the detriment to the microstructure produced by the process parameters. However, investigating this trade-off is beyond the scope of the work presented here.

## 5.7 Conclusions

The in-situ synchrotron diffraction experiments performed for IFW of RR1000 have successfully quantified the microstructure evolution during the process for the first time, providing insights into the behaviour of Nickel-based superalloys during IFW that have not been available before. It was proven through comparison of welds with different weld parameters that the microstructure evolution has some control of the macroscale physical response of the process, as a clear relationship between the size of the  $\gamma'$  dissolved zone and burn-off rate exists.

It was quantified that the conditioning phase exists until a zone containing sufficient dissolution of  $\gamma'$  is present about the contact interface. This dissolved zone appeared to be steady-state during burn-off, proving that the combination of heat input, thermal history and mechanical deformation offset one another during this stage. It is hypothesised that burn-off acts as a second conditioning phase for material outside of the  $\gamma'$  dissolved zone, increasing the temperatures in this region until sufficient  $\gamma'$  dissolution can occur and the size of the  $\gamma'$  dissolved zone can expand.

Expansion of the  $\gamma'$  dissolved zone permits an increased upset rate during the consolidation stage. Throughout the region of consolidation in which the upset rate is constant, the microstructure measured in these experiments again appeared to be steady-state. The large upset rate present during consolidation brings cooler material into the  $\gamma'$  dissolved zone, which eventually does not have the thermal history required to permit  $\gamma'$  dissolution. At this point there is a large increase in strength about the interface, which rapidly reduces the upset rate and additionally causes the weld to stall.

However, IFW is a highly coupled problem in which there is a balance between the thermal, mechanical and microstructural components which control the evolution of the process. In this study, the thermal and microstructural fields have been investigated in great detail. The mechanical component has been included within this analysis, but this has primarily been linked to the interface friction behaviour and subsequent heat generation due to changes in weld pressure. There are clear and logical trends presented in the data within this chapter that show the mechanical influence on macroscale process behaviour, such as the high-pressure welds having increased total upset and upset rates in both burn-off and consolidation stages. However, there are some artefacts which cannot be described purely from the thermal and microstructural

fields, such as the transition from burn-off to consolidation. Here, the thermal and microstructural fields have been analysed to show that they may have some influence on this transition, but it is acknowledged that this is most likely to be significantly affected by the mechanical behaviour.

## Chapter 6

# Cellular Automata Modelling of Microstructure

## Evolution During IFW

### 6.1 Introduction

The production of a numerical modelling approach to evaluate the microstructure of Nickel-based superalloys during IFW aims to reduce the requirement for experimental trials. A fully validated model which correctly predicts the physics of microstructure evolution would have the ability to predict optimised process parameters in which there is minimal detriment to the weld zone microstructure and mechanical properties.

Cellular Automata (CA) models have been produced which evaluate the diffusion of elements between two phases, in this case  $\gamma$  and  $\gamma'$ . The models are linked to the CALPHAD approach using thermodynamic reference tables and the local equilibrium approach to evaluate the phase composition of a cell based on the current atomic composition.

Alongside the equilibrium values of phase composition, the CA models require thermal history data. The temperature data is used to evaluate chemical potentials and atomic mobilities which are the driving forces for atomic diffusion, and thus dissolution of the  $\gamma'$  phase. Here, Finite Element Analysis (FEA) has been implemented as a means of calculating the thermal evolution of weld specimens.

## 6.2 Finite element analysis

Finite Element Analysis (FEA) has been implemented to model the macro-scale process outputs and temperature evolution during inertia friction welding of the Nickel-based superalloy RR1000. The four sets of process parameters used in the synchrotron diffraction experiments have been evaluated using FEA.

FEA was performed using the commercial software DEFORM. This software is commonly used in industry and amongst the wider IFW research community and has been proven to produce accurate results when the macro-scale outputs and thermal histories are compared with experimental data.

The material data for RR1000 was provided in the form of tabulated flow stress data. In this data, the flow stress (yield stress) values are defined as functions of temperature, strain and strain rate. Similar material data has been used in the literature and has been proven to produce accurate results [100]. However, implementation of this material data for finite element modelling of IFW at the geometries used in the synchrotron diffraction experiments showed to produce low total upset values when compared with experimental data.

The in-situ experimental data evaluating the microstructure evolution of RR1000 IFWs has shown that the axial profile of  $\gamma'$  volume fraction occurs over extremely small length scales. For validation of the numerical modelling results, the upset profile must be as accurate as possible when compared with experimental data, as the thermal measurements are recorded at relative distances from the interface for consistency with the experimental data.

As an example, assume that XRD data has been evaluated from a weld at position  $z$  relative to the interface at a weld time of  $t$ . If the FE model underpredicts the upset exhibited by the experimental welds, there are two problems presented. Firstly, it can be questioned whether it is correct to take thermal data from a consistent position  $z$  at time  $t$  from the FEA model, given the fact that the model has not correctly mapped the mechanical behaviour of the weld. This can be overcome by evaluating the positional error from the difference in upset in both cases, however given the small length scales in which the microstructure evolution was observed in the experimental data, there is a large risk that these would be extremely large relative to the region in which the

microstructure is altered due to the process behaviour. The second problem which arises is the fact that the thermal history of the weld is largely dependent on the upset. If the model underpredicts the experimental upset value, there is insufficient deformation and thus insufficient removal of material from the interface. Therefore, the material surrounding the interface would be subjected to additional heat generation at the contact interface, which may produce temperatures larger than the values produced experimentally.

To improve the upset response produced by FEA models, the material model has been fit to a power law which describes the temperature and rate dependence of flow stress values. The power law can be described by four parameters. These parameters have been input into an optimisation routine which runs the finite element model prior to comparing the upset produced by the model with the experimental upset. The Matlab function *lsqnonlin* has been implemented to assist optimisation of the material parameters.

### **6.2.1 Assessment of process outputs**

The outputs of the DEFORM model for the baseline (BL) and optimised (Opt.) cases for all welds are presented in Figure 6.1. The material data produced by the optimisation is presented in Figure 6.2 for each weld parameter set.

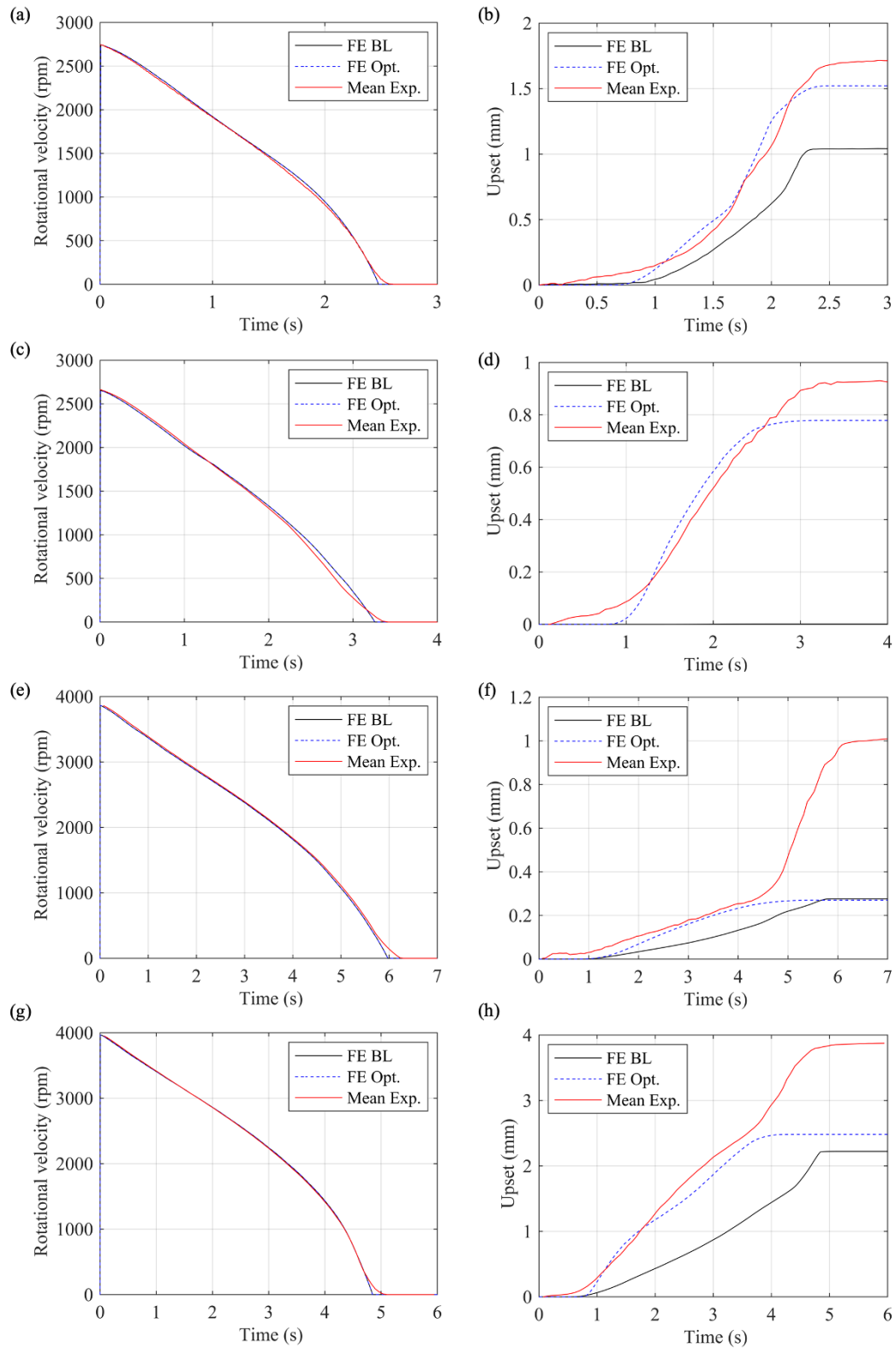


**Figure 6.1:** Outputs of the baseline and optimised DEFORM FE models compared with the experimental mean weld data. (a) N1 rundown, (b) N1 upset, (c) N2 rundown, (d) N2 upset, (e) N3 rundown, (f) N3 upset, (g) N4 rundown, (h) N4 upset.

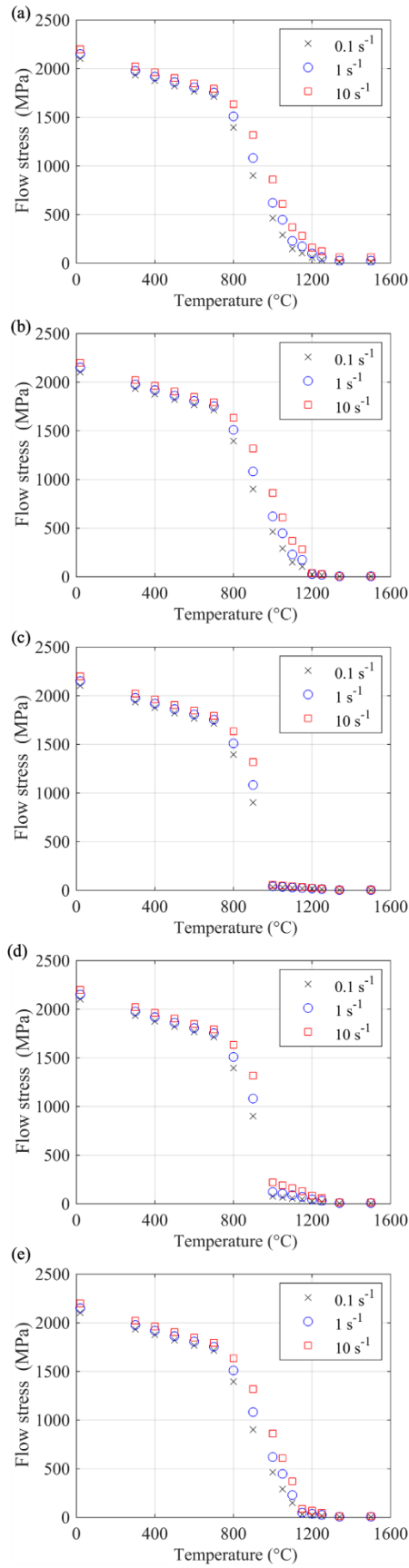


**Figure 6.2:** Flow stress input data produced by the optimisation routine (a) Baseline, (b) N1 optimisation, (c) N2 optimisation, (d) N3 optimisation, (e) N4 optimisation.

In Figure 6.1 it can be seen that the rundown curves were identical for both baseline and optimised cases as these were calculated from experimentally defined friction coefficient data. The rundown curves produced by the FE models were consistent with the experimental rundown data, and so it can be assumed within reason that the energy input was correct in both models, for all parameter sets.

It is observed that for all welds, there was a slight difference in deceleration at the end of the process when the model was compared with the experimental data. This occurred due to the averaging performed on the four experimental welds. Due to the fact that this difference occurred at the end of the process, this did not have any significant impact on the energy input into the weld.

For parameter set N1, it is observed that the baseline DEFORM model provided a reasonable representation of the weld. The total upset was underestimated by approximately 39 % compared to the mean experimental weld of parameter set N1. It is clear in this case that the flow stress values in the baseline material model are too large, as insufficient deformation has occurred.

After optimisation, the FEA model had a total upset which was only 11% lower than that of the mean experimental weld. Additionally, the upset profile produced by the optimisation of the material model was extremely consistent with that of the mean experimental weld. Throughout the process, the maximum difference in upset between the optimised FE model and the mean experimental weld was 0.21 mm, which occurred at a weld time of 2 s. This difference presents a maximum positional error of 0.105 mm in the thermal histories extracted from the FE model at this time in the weld, due to the fact both specimens are assumed to deform symmetrically about the contact interface.

The peak stress values produced through optimisation of the material model for parameter set N1 in Figure 6.2b show that the optimisation procedure only produced a small reduction in flow stress values at temperatures in excess of 1200 °C, which is logical given the fact that the baseline material model produced a reasonable representation of the upset response.

For welds of parameter set N2, the original material model produced a negligible amount of upset. The total upset of the base FE model was 0.0012 mm, compared to the 0.91 mm of upset produced by the experimental weld.

After optimisation, the total upset produced by the FE model was 0.78 mm. This underestimated the total weld upset by 14.3 %. However, it can be clearly seen that the upset profile, and particularly the rate of consolidation upset, are extremely similar. The maximum difference between the optimised FE model and mean experimental weld was 0.13 mm, which occurred at the end of the weld. For weld times prior to 2.5 s, the maximum difference in upset was 0.058 mm, which occurred at a weld time of 0.89 s. This shows that throughout the majority of the weld duration, the positional error in temperatures extracted from the FE model was no larger than 0.029 mm.

The peak stress data for the optimised material model for weld parameter set N2 in Figure 6.2c shows the optimisation routine produced a large reduction in flow stress values at temperatures greater than 900 °C. Given the fact that the baseline material model produced negligible upset when modelling weld parameter set N2, a large reduction in flow stress values was expected in order to permit plastic deformation.

When comparing the upset of the original DEFORM model and the mean experimental weld for parameter set N3 (Figure 6.1f), it can be seen that the FE model underestimated the total weld upset by 73 %, again highlighting the fact that the yield strengths in the material model were larger than those produced by the material in the experimental case.

After optimisation, the total upset value did not differ much from the total upset in the base DEFORM model. However, there was a much better representation of the linear burn-off region produced by FEA when the optimised material model was used.

It is clear in this case that the tabular material data which is used in these DEFORM models is incapable of representing the results seen in the experimental data. It is expected that material data which is in some way representative of microstructure (for example, heating rate dependent volume fraction data or grain recrystallisation behaviour) would provide a much better representation of the mechanical behaviour of this weld parameter set. However, development and validation of a new material model for FEA is beyond the scope of this work.

Due to the inability of the optimised material model to represent the large consolidation upset rate in this data, the positional error of thermal data extracted from the FE model in this region would subsequently be extremely large. In this case, the positional error was up to 0.37 mm during consolidation due to the 0.74 mm difference

in total upset. However, during conditioning and burn off, the maximum positional error in the optimised FE model was 0.024 mm, which occurred at a weld time of 1.4 s.

Similar to weld parameter set N2, a large reduction in flow stress values at temperatures in excess of 900 °C was produced by the optimisation routine for weld parameter set N3 (Figure 6.2c). However, it should be noted when comparing the optimised material models for parameter sets N2 and N3 that in the case of N3, the material model retained some strength at temperatures 1000 °C and greater. This difference appears small but this slight difference in yield strength was the cause of the material model accurately representing the low rate burn-off observed in welds of parameter set N3.

The outputs of the baseline and optimised material models implemented in DEFORM are presented for parameter set N4 in Figure 6.1g-h. The base FE model produced a total upset which was 43 % lower than that of the mean experimental weld. The optimisation procedure produced a material model which provided a total upset of 2.48 mm, which was still 36 % lower than that of the experimental upset.

Similar to weld parameter set N3, it is observed here that neither material model can accurately represent large consolidation upset rate which occurs at the end of these high-speed welds. This again suggests that an improved material model which is closely linked to microstructural data may be required in order to accurately represent the mechanical deformation of welds of this parameter set.

Despite this, the optimised material model shows good agreement with the mean experimental weld during conditioning and burn-off. Throughout these two stages of the weld, the maximum difference in upset between the optimised model and experimental data was 0.28 mm, at a weld time of 1.56 s. When accounting for the symmetrical deformation of the specimens, this produces a maximum positional error of 0.14 mm when evaluating the thermal response of the FE model.

Similar to weld parameter set N1, a very small reduction in flow stress values was produced by the optimisation routine at temperatures greater than 1150 °C for parameter set N4 (Figure 6.2e). When comparing the product of the optimisation routine for all four parameter sets, there are clear trends in the behaviour relative to the process parameters. Low pressure welds N2 and N3 both required a large reduction

in flow stresses at lower temperatures in order to permit more accurate modelling of the upset response. On the contrary, high pressure welds N1 and N3 produced more accurate upset responses with much smaller changes in the material model.

There are two possible causes for this. The high pressure welds were shown in the previous chapter to produce the highest energy input rates. Therefore, temperatures in these models will reach peak values much faster than in the low pressure welds and additionally, a larger region of material will reach these peak temperatures. Hence, changes to the material data near these peak temperatures influence the plasticity response for a much larger volume of material in the high pressure welds. Secondly, the high pressure welds utilise a larger axial loading to produce upset. Therefore, smaller changes to the flow stress are required to permit plasticity under these more prominent loading conditions.

### **6.2.2 Analysis of thermal response**

Optimisation of the tabular material data used in DEFORM FE models has shown to greatly increase the accuracy of the macro-scale deformation behaviour. However, the thermal response of the FE models cannot be assumed to be correct. To validate the thermal response of the FE models, temperature data has been extracted from the optimised FE model of parameter set N1 and compared with thermocouple data from validation welds.

Two validation welds have been performed for weld parameter set N1. These welds were performed with a type K thermocouple spot welded to the outer diameter of the fixture specimen. The desired thermocouple positions were measured as 0.72 mm and 1.2 mm from the initial contact interface. The spot size for both thermocouples was approximately 0.6 mm.

The weld data for the validation welds was compared with the mean weld outputs for parameter set N1, to assess whether the behaviour of these welds was similar. This is presented in Figure 6.3. It is observed that the rundown curves of both validation welds were consistent with that of the mean XRD weld, and so it can be assumed that the deceleration and therefore energy input rates were consistent in these cases. The validation welds produced total upsets of 1.57 mm and 1.71 mm respectively.

Additionally, the upset profiles of these welds were close to that of the mean weld. The difference in upset profiles have been used to define time-dependent positional errors at the locations at which temperature measurements were recorded. These upset-based positional errors have been summed with the radius of the thermocouple spot, in order to define a total positional error in the thermocouple readings.

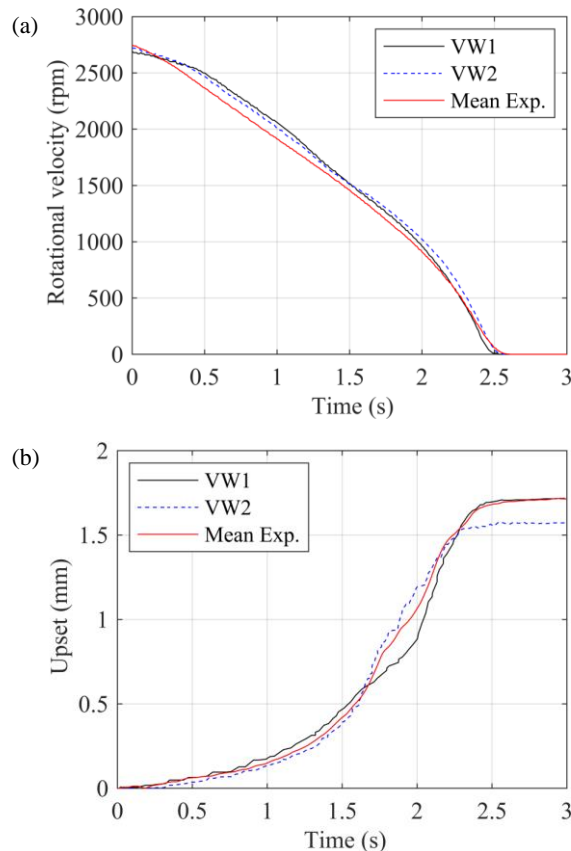


**Figure 6.3:** Process outputs of the validation welds compared with the mean experimental weld. (a) Rundown, (b) Upset.

In Figure 6.4, the thermocouple measurements for validation weld 1 (VW1) have been presented alongside the thermal history of the optimised finite element model for the same location. Here, the temperature errors in the thermocouple data have been defined from the temperature gradient present over the positional error, which have been evaluated from the finite element model. The temperature error from the finite element model has been evaluated in a similar manner, by which the positional error due to the upset response of the finite element model when compared to the mean weld has been calculated at each time, and the thermal gradient across this positional range

evaluated. To allow for these errors to be accurately assessed, temperature data from the thermocouple readings and the FE model have been evaluated at increments of 0.2 s.

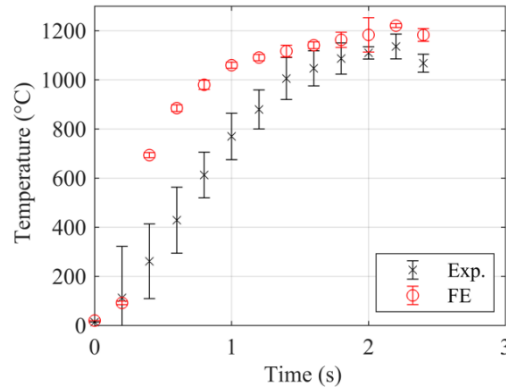


**Figure 6.4:** Thermocouple measurements from validation weld 1 presented alongside FEA temperature values at consistent axial positions.

It can be seen in Figure 6.4 that the FE model produced a much larger heating rate than measured by the thermocouple. This difference is logical as the FE simulation is modelling an ideal solution, in which there are two parallel weld faces which are perfectly aligned, such that when they come into contact, heat is generated instantly at the contact interface and conducted axially through the specimens. There may be slight misalignment between the weld specimens, and there may also be slight imperfections in the surface finish at the interface of these specimens. When the specimens come into contact, there is likely a short time period in which the weld specimen faces grind against one another, removing material from the interface until specimen faces are completely in contact and heat is generated around the whole circumference of the specimens. Therefore, it is logical that the heat generation in the experimental case would lag slightly behind that of the FE simulation.

It can also be seen in Figure 6.4 that the maximum temperature produced by the FE simulation was approximately 100 °C larger than that seen in the experimental results. This difference can be explained when analysing the path of the thermocouple. The position of the thermocouple relative to the interface moves at a speed of  $u(t)/2$  until it reaches the contact interface. In reality, the thermocouple will never reach the interface due to the flash formation which is expelled outwards from interface. It is

instead likely that the thermocouple becomes trapped under the flash collar, and therefore the positions at which temperatures are recorded are actually some small distance from the contact interface. Hence, the thermocouple readings are lower than those recorded from the mid-wall of the FE model as these readings can be evaluated from the contact interface. It has been observed that there is very little thermal gradient radially across the specimens in FEA. Therefore, temperatures have been extracted from the mid-wall of the weld specimen to allow for direct comparison with in-situ synchrotron diffraction data.

It is expected that the true temperature which is exhibited by the experimental weld likely sits somewhere between these two values. FE is limited in the fact it cannot account for the initial contact period of the weld; however, it offers benefits such that it can be used to evaluate temperatures from locations which cannot be probed experimentally. The experimental thermocouple data offers the benefit that the delay in heat generation due to initial contact behaviour can be measured, however there are limitations in how close to the interface a thermocouple can record temperature data from due to the formation of flash.

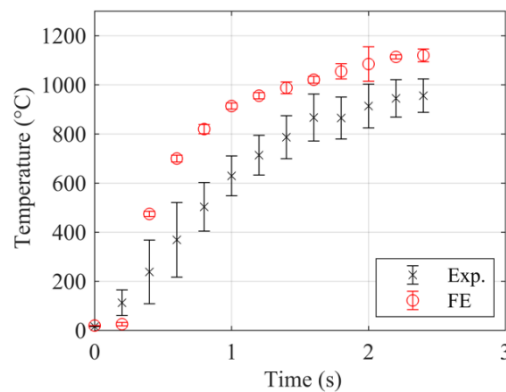


**Figure 6.5:** Thermocouple measurements from validation weld 2 presented alongside FEA temperature values at consistent axial positions.

The thermocouple measurements for VW2 are presented alongside the FE model thermal data in Figure 6.5. Here, the initial thermocouple position was 1.2 mm from the contact interface, and FE temperature data has been extracted at a consistent position. Again, it is observed that the FE model produces a faster heating rate than seen experimentally, due to the fact that the initial contact region is not accounted for

in the FE model. Once the temperature appears to level out after  $t = 1.5$  s, there is a difference of approximately 200 °C between the FE model and the experimental data. This difference is approximately double that of the case in which the thermocouple was positioned 0.72mm from the initial contact interface. It is expected that the difference between experimental and modelling data at positions close to the interface are lower due to the fact that there is a 'peak temperature' which will occur in IFW. At temperatures in excess of 1200 °C, it is expected that the  $\gamma$ ' phase will fully dissolve, reducing the strength of the material significantly. This softer material will be expelled from the interface as flash, bringing colder material into the contact interface. The colder material is then heated at the contact interface and the process continues. Therefore, there is a peak temperature in the process whereby the material close to the interface is reduced in strength enough to be expelled as flash. Due to this, temperature measurements close to the interface are likely to be closer to the FE value due to this peak temperature, as there is essentially an upper limit of the temperature at which upset is inevitable. Further from the interface, such as in the case of VW2, the difference in temperature is likely to be larger as the problem is not bound by that upper limit of temperature.

It is clear that there is a significant difference in the thermal response measured experimentally using thermocouples and those evaluated using finite element methods. The difficulty in recording thermocouple measurements with geometries of this scale propose further issues as they produce a large source of error in the experimental temperature measurements.

The two methods used to analyse the thermal evolution of weld specimens have benefits, however, they both have their own respective drawbacks. Thus, it cannot be said with confidence that either method is better than the other. Typically, experimental data would be more reliable in this case, but the large thermocouple spot size relative to the specimen geometry leads to large thermal gradients across the thermocouple spot. As neither method of evaluating the temperature history produced by IFW shows any significant benefit over the other, temperature data from both cases were tested in the CA model for the ternary system.

### 6.3 1D Finite difference

Cellular Automata offers a sturdy foundation for the numerical modelling of thermodynamic atomic diffusion. The use of local cell neighbourhoods lends itself well to the reliance of gradients in atomic concentration and chemical potential for the evaluation of the diffusion problem. Furthermore, the correct physics can be applied to the model as an unlimited number of predefined fundamental equations which control the evolution of the system can be linked to the evolution of the state variables. When modelling in 1 dimension, the CA approach reduces to the Finite Difference (FD) method

#### 6.3.1 Binary Ni-Al system

To ensure that the appropriate physics of thermodynamic diffusion of elements have been applied here, a simple test case has been investigated as detailed in the methodology. The results produced by the 1D FD model were compared with the results produced by the DICTRA diffusion module. Thermodynamic equilibrium values of chemical potential and atomic mobility are presented in Appendix B1.

This investigation is inspired by the analyses performed by Tancret *et al.*, in which a single precipitate was subjected to various heating rates and the  $\gamma'$  dissolution kinetics measured [97]. For consistency with the literature data, the binary Ni-Al system has been used with an atomic weight of 9 % Aluminium. A single  $\gamma'$  precipitate of 1  $\mu\text{m}$  radius has been included in the model. The equilibrium  $\gamma'$  volume fraction has been defined by Thermo-Calc and applied to the model, such that the total system has a radius which produces the equilibrium volume fractions in the system. Four heating rates have been applied to the precipitate; 1  $^{\circ}\text{C/s}$ , 10  $^{\circ}\text{C/s}$ , 100  $^{\circ}\text{C/s}$  and 1000  $^{\circ}\text{C/s}$ . Whilst this data is available in the literature, the simulations have been performed in the latest version of DICTRA to make use of the latest thermodynamic and mobility databases. In these models, the start temperature was set to 1000  $^{\circ}\text{C}$  for consistency with the literature, and the maximum temperature was set to 1370  $^{\circ}\text{C}$  as melting of the alloy is not of interest here.

The results of the 1D CA simulations are presented alongside the DICTRA model results in Figure 6.6. Here, all controllable aspects have been kept consistent in both

models, such as the zero flux boundary conditions and identical cell/element sizes. It is observed that the 1D binary CA model produced excellent results when compared with the results produced by the DICTRA simulations. The difference in  $\gamma'$  volume fraction produced by the two models did not exceed 3 % at any temperature or heating rate tested in this study.

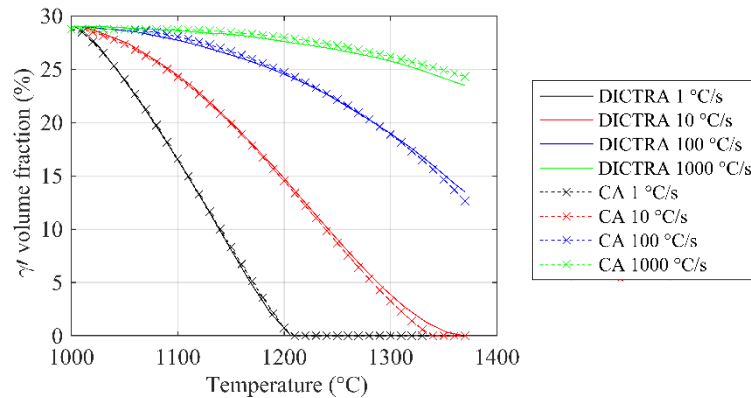


**Figure 6.6:** Verification of the CA model through comparison of  $\gamma'$  dissolution kinetics with the DICTRA diffusion module.

It should be noted here that DICTRA has a large advantage over the CA modelling approach, due to how it handles the interface in moving boundary simulations such as these. The solver calculates the interface velocity at the time step, and then adds a node to track the exact distance the interface moves in that time step.

This is not as simple in the CA model. To accurately track the position of the  $\gamma/\gamma'$  interface, the region modelled must be finely discretised. Otherwise, clear steps are present in the  $\gamma'$  volume fraction data as the interface shifts between cells if the distance between cells is large. To avoid this, smaller cells are used. However, in cases such as this, there is a small region in which diffusion is occurring close to the interface. Meanwhile, the state variables must still be evaluated and updated for all cells. At distances further from the phase interface, where gradients in concentration and chemical potential are low, a lot of computational time is spent performing calculations which have negligible effect on the solution.

Generally, this doesn't cause many issues. When the concentration gradient is zero, there is no diffusion. However, when there is a small gradient and a diffusive flux is

present, the time step then becomes dependent on this flux alongside those at the interface. As the concentration gradient is very low in these regions, this causes a very small time step due to the fact that the time step is limited such that the direction of the concentration gradient cannot change in any single time step.

When comparing the two models, the computational time of the 1D DICTRA model is approximately 5 % of that of the CA model, highlighting that it is much more computationally efficient than the CA solution.

The main aim of this modelling work is to produce a numerical model which can represent atomic diffusion and phase transformations over a 2D microstructure representation, such that the effects of the multiple diffusive gradients from multiple precipitates can be analysed to assess how these may affect the precipitate dissolution. This cannot be done in DICTRA due to the fact it is limited to 1 dimension. The true benefit of CA modelling comes when analysing the capabilities at the 2D model, and the fact that multiple precipitates can be modelled, with various sizes and positions across two axes.

### **6.3.2 Ternary Ni-Al-Cr system**

Expansion of the alloy system to a ternary system with the inclusion of the Chromium element allows for a better representation of the RR1000 Nickel-based superalloy used in the synchrotron diffraction experiments. It is known that in superalloys, Chromium is often the element with the slowest diffusivity [98], and hence the rate of  $\gamma'$  dissolution is dependent on the diffusivity of Chromium. Thermodynamic equilibrium values of chemical potential and atomic mobility are presented in Appendix B2.

For the ternary Ni-Cr-Al alloy, both 1D and 2D cellular automata models have been produced. The 1D model works in a similar manner to that of the binary system, in which a single precipitate is modelled. Here, the single precipitate has been used to model three different precipitate radii; 0.48  $\mu\text{m}$ , 0.125  $\mu\text{m}$  and 12.5 nm. These are the measured mean radii for primary and secondary  $\gamma'$  measured via SEM, and an estimate of the average tertiary  $\gamma'$  radius evaluated from literature values [16].

To verify the results produced for the ternary model, the primary  $\gamma'$  precipitate has been modelled in 1D and various heating rates have been applied. The dissolution of the  $\gamma'$  precipitate has been compared with results produced by DICTRA. Here, the heating rates are applied from temperatures of 1000 °C to 1290 °C, as this composition begins to melt at 1294 °C. This is shown in Figure 6.7.

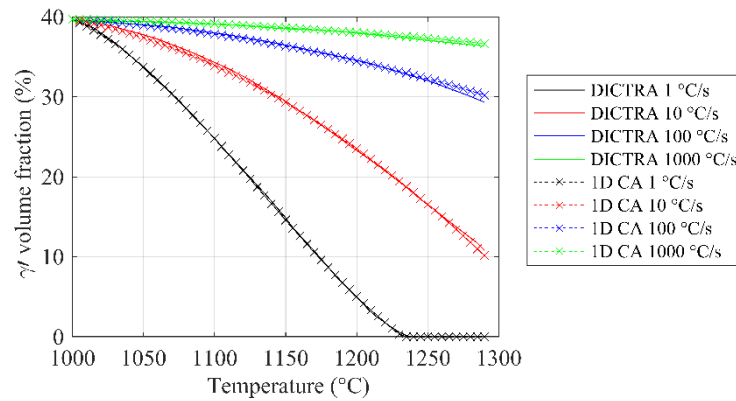


**Figure 6.7:** Verification of the CA model for the ternary alloy system through comparison of  $\gamma'$  dissolution kinetics with the DICTRA diffusion module.

It can be seen in Figure 6.7 that there is a strong agreement between the  $\gamma'$  volume fraction evolution produced by the 1D model and the DICTRA simulations. Similar to the binary case, the difference in  $\gamma'$  volume fraction at any point, and for any heating rate, does not exceed 3%.

Each precipitate is subjected to a thermal history which has been extracted from FEA at weld times consistent with regions of interest which were analysed in the synchrotron diffraction investigation. Thermal histories have been extracted at various axial distances from the contact interface, in accordance with the range of axial distances measured in the experimental studies.

The dissolution of each precipitate is modelled due to the thermal history it is subjected to. The  $\gamma'$  volume fraction is then normalised such that the starting  $\gamma'$  volume fraction is in accordance with the phase fraction of that precipitate size in the parent material. In the 1D study, there is no coupling between the precipitates, and therefore it is logical to expect that the  $\gamma'$  volume fractions are underestimated when compared with diffraction data.

The aim of this study is to provide a fast solution in which the evolution of the parent microstructure can be evaluated due to the thermal response of the IFW process. These will then be compared with the 2D CA model to assess whether there are benefits to modelling the full parent microstructure in 2 dimensions.

As an example, temperatures were extracted from the FE model for weld parameter set N1 (LS, HP) at a weld time of 0.62 s, which is consistent with the end of conditioning seen in the mean experimental weld. Axial positions of 0, 0.5 and 1.0 mm have been defined, and the temperature history of these points has been extracted from the FE model as presented in Figure 6.8.

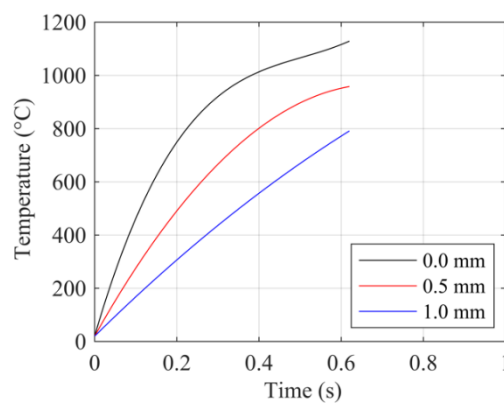


**Figure 6.8:** Thermal history data extracted from the FEA model for three axial locations at a weld time of 0.62 s for IFW of weld parameter set N1.

In Figure 6.8, it can be seen that closer to the contact interface, the temperatures experienced are higher. Therefore, it would be logical to expect that positions closer to the interface would show increased dissolution of  $\gamma'$  due to the fact that they have been subjected to increased temperatures for a longer duration.

In Figure 6.9, the outputs of the 1D ternary CA model are presented for each of the thermal histories provided in Figure 6.8. In Figure 6.9a, it can be seen that the temperatures experienced by the point at the contact interface were large enough to cause dissolution of all three precipitate sizes. Within the first 0.62 s, the tertiary  $\gamma'$  phase has almost completely dissolved at the contact interface. Additionally, a significant amount of secondary  $\gamma'$  dissolution had occurred, with only 13.8 % of the original 28.8 % volume fraction of secondary  $\gamma'$  remaining at  $t = 0.62$ s. After a weld

time of 0.62 s, some primary  $\gamma'$  dissolution had occurred, however due to the large size of these precipitates, a significant volume of primary  $\gamma'$  was not dissolved in this short time. At a weld time of 0.62 s, the total  $\gamma'$  volume fraction had reduced to 23.6 %, which is approximately half of the value present in the parent material.

Figure 6.9b presents the  $\gamma'$  dissolution kinetics represented by the 1D CA model at a weld time of 0.62 s and a position 0.5 mm from the contact interface. At this position, the temperatures experienced were lower than those at the contact interface, and so less dissolution of the  $\gamma'$  precipitates occurred. It is observed in this case that the primary  $\gamma'$  precipitate did not dissolve at all. Approximately 4 % of the secondary  $\gamma'$  volume fraction was dissolved, and the volume fraction of tertiary  $\gamma'$  was reduced to 5.3 %. The total  $\gamma'$  volume fraction present at 0.62 s was 39.8 %.

In Figure 6.9c, the  $\gamma'$  volume fraction evolution for a point 1 mm from the contact interface at a weld time of 0.62 s is displayed. At this position, it is clear that the temperature history presented in Figure 6.8 was not high enough at any point to provide a driving force for atomic diffusion and subsequent  $\gamma'$  dissolution. The data in Figure 6.9c shows that no precipitate size experienced any dissolution in the first 0.62 s of the process.

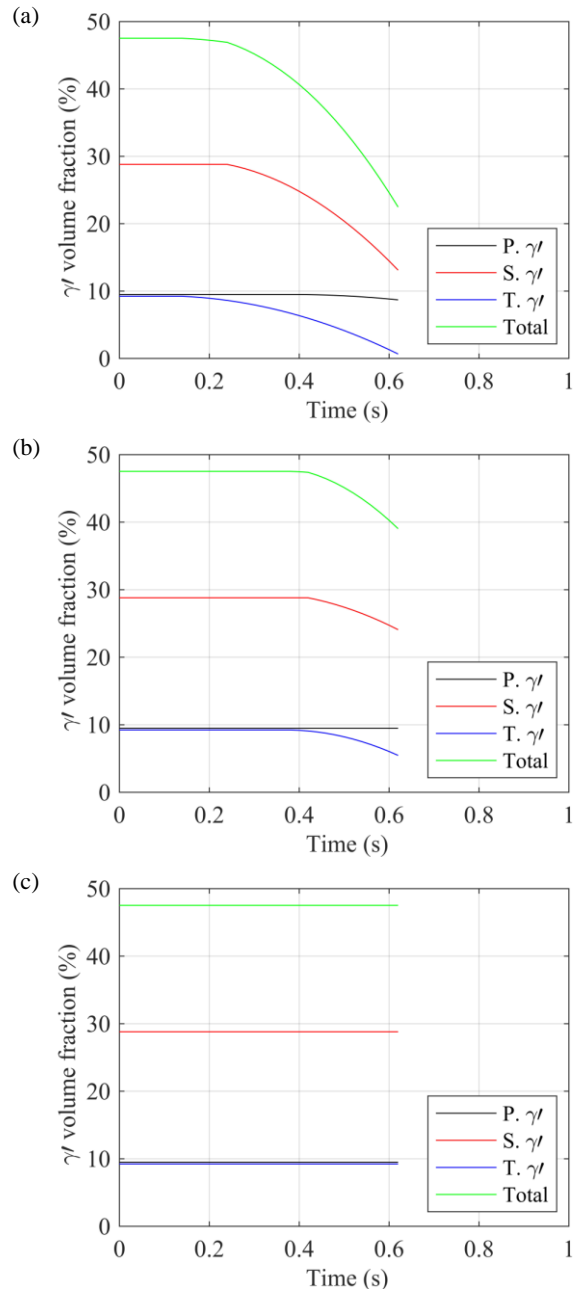


**Figure 6.9:** Combined results of the 1D CA simulation for temperatures extracted from FEA modelling of weld parameter set N1 at  $t = 0.62$  s. (a)  $z = 0$  mm, (b)  $z = 0.5$  mm, (c)  $z = 1$  mm.

The results presented in Figure 6.9 can be plotted in a different manner. By presenting the total  $\gamma'$  volume fraction with the axial position from which the data was evaluated, consistent data can be produced for comparison with the in-situ synchrotron diffraction results.

Figure 6.10 displays the experimental synchrotron diffraction data acquired for weld parameter set N1 at the end of conditioning ( $t = 0.62$ ). Alongside this, two sets of CA model results are presented. Firstly, FEA temperatures have been extracted at positional increments of 0.25 mm and input into the CA model, as shown above. The second set of CA results are evaluated using the thermal histories measured by the in-situ thermocouple validation welds.

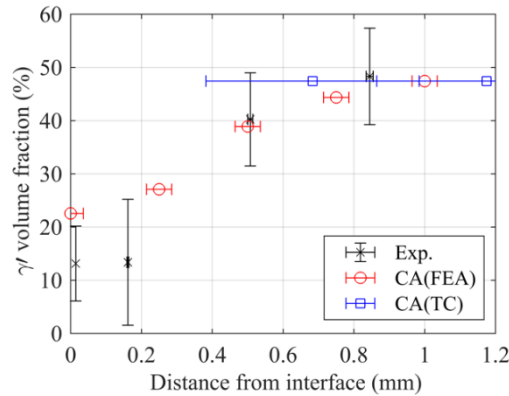


**Figure 6.10:** Comparison of microstructure evolution data evaluated from in-situ synchrotron diffraction and cellular automata models for weld parameter set N1 at  $t = 0.62$  s.

In general, the results produced by the combination of finite element and cellular automata modelling show good agreement with the in-situ diffraction data. Close to the interface, the CA model over-estimates the  $\gamma'$  volume fraction, showing that insufficient dissolution of this phase has occurred in the model. This is an unexpected result given that the temperature histories evaluated using FEA are expected to be larger than the experimental temperatures due to the inability to model initial part contact effects accurately. Additionally, the 1D CA model is limited in the fact that it can only model a single precipitate, hence dissolution-retarding effects from neighbouring precipitates are not represented. Therefore, it would be expected that the 1D CA model would overestimate the amount of  $\gamma'$  dissolution occurring in this case.

In Figure 6.10, the CA model shows no dissolution occurring when the thermocouple temperature data is input. However, given the positions of the thermocouples at this weld time, this is to be expected.

The results of CA models are compared with experimental data for the end of burn-off in weld parameter set N1 in Figure 6.11. Again, the general trend produced by FEA and CA models shows good agreement with the experimental data. At a time of 1.25s, the CA model now shows excellent agreement with the experimental data at positions close to the interface. However, at a distance 0.5 mm from the contact interface, the CA model now overestimates the amount of  $\gamma'$  dissolution when compared with experimental data. It is also likely that the CA model values at distances of 0.75 mm and 1.0 mm are overestimating  $\gamma'$  dissolution also, although these results appear to fall within the error bars of the experimental data.

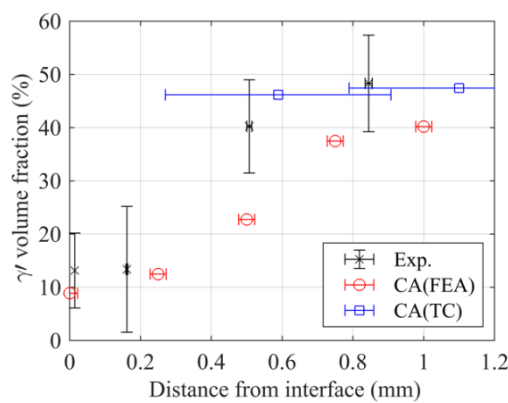


**Figure 6.11:** Comparison of microstructure evolution data evaluated from in-situ synchrotron diffraction and cellular automata models for weld parameter set N1 at  $t = 1.25$  s.

During the analysis of the synchrotron diffraction results, it was hypothesised that the temperature is localised about the interface such that a steady-state axial profile of microstructure was present during the steady-state burn-off stage. If this is in fact a physical occurrence, then it is clear that the FE model does not accurately represent this, as  $\gamma'$  dissolution is seen in the CA model at distances in excess of 0.5 mm from the contact interface.

In Figure 6.11, the thermocouple data input into the CA model shows a small amount dissolution occurring at a distance 0.57 mm from the interface. However, as there is not yet data closer to the interface, where a significant amount of dissolution can occur, this cannot yet be fully compared with the FEA results.

The outputs of the CA model are presented in Figure 6.12 for the end of the consolidation stage of weld parameter set N1. It was hypothesised earlier in the chapter that the true thermal evolution of the weld likely sits somewhere between the results produced from in-situ thermocouple measurements and finite element model outputs. This can be seen in Figure 6.12 when comparing the experimental  $\gamma'$  volume fraction data with the outputs of the CA models.

Using FE output temperatures in the CA model, the results produced show good agreement with the synchrotron diffraction data. In general, the results from the CA(FEA) approach tend to lie at the lower bound of the  $\gamma'$  volume fraction error bars produced experimentally. In comparison, the CA(TC) model outputs appear to reside towards the top of the  $\gamma'$  volume fraction error bars. This likely highlights the fact that the true temperature evolution occurs is somewhere between the FEA and thermocouple values produced.

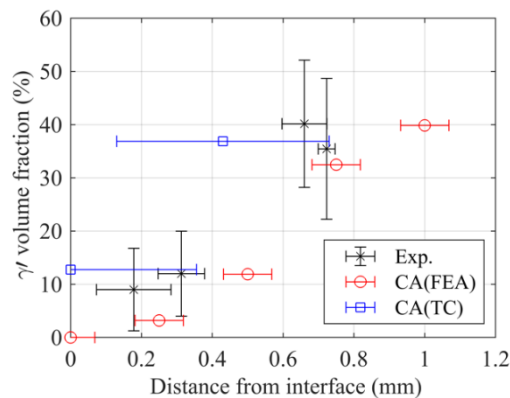


**Figure 6.12:** Comparison of microstructure evolution data evaluated from in-situ synchrotron diffraction and cellular automata models for weld parameter set N1 at  $t = 2.37$  s.

It is clear that neither FEA nor thermocouple temperature values offer a significant benefit over the other. However, in-situ thermocouple experiments are costly in terms of time. Additionally, they are susceptible to large uncertainties in this case given the fact the thermocouple spot size is reasonably large when compared with the thermal gradient produced during IFW of this specimen geometry. Therefore, FEA temperature data has been used as input data for the CA model for the three remaining sets of process parameters.

For the remaining weld parameter sets, comparisons between the results obtained by 1D CA modelling have been compared with the experimental data at the end of the three main stages of the IFW process; conditioning, burn-off and consolidation.

The results of the CA model for weld parameter set N2(LS, LP) are presented in Figure 6.13. At the end of conditioning, Figure 6.13a shows that there is reasonable agreement between the CA models and experimental data. Dissolution of the  $\gamma'$  phase is localised about the contact interface in the first 0.62 s of welding. The exact size of the  $\gamma'$  dissolved zone cannot be experimentally defined due to the axial resolution of diffraction data, however both data sets agree that this is between 0.2 mm and 0.4 mm in length. At the contact interface, the CA model underpredicts the volume of  $\gamma'$  dissolved during conditioning. This is not expected given the fact that the thermal data from FEA is likely to overestimate the temperatures experienced in the real weld. This may highlight that thermal effects alone do not control the dissolution of  $\gamma'$ . Close to the interface, where strain and strain rates are high due to mechanical deformation, there may be an additional driving force for  $\gamma'$  dissolution given the mechanical energy applied.

At the end of burn-off, the experimental and numerical results are in good agreement, as shown in Figure 6.13b. Again, the CA model underestimates the  $\gamma'$  dissolution at positions extremely close to the interface, which may highlight the presence of additional driving forces for microstructure evolution in the experimental case.

A similar trend is seen in at the end of consolidation for weld parameter set N2, as presented in Figure 6.13c. The two data sets again show comparable results. Additionally, the  $\gamma'$  volume fraction evaluated at the contact interface now falls within the error bars of the experimental data. However, this point lies towards the upper limit of the experimental uncertainty. Comparing these results with those of parameter set N1 shows different behaviour in the CA models. For parameter set N1, the  $\gamma'$  volume fraction produced by the CA models tended to reside towards the lower limit of the uncertainty in the experimental data. This was attributed to the overestimation in temperature generation due to the inability of the FE process to model effects such as initial contact behaviour which are present in reality. However, for parameter set N2, the  $\gamma'$  volume fractions evaluated by the CA model tended to lie towards the upper limit of experimental uncertainty, particularly at axial positions close to the interface.

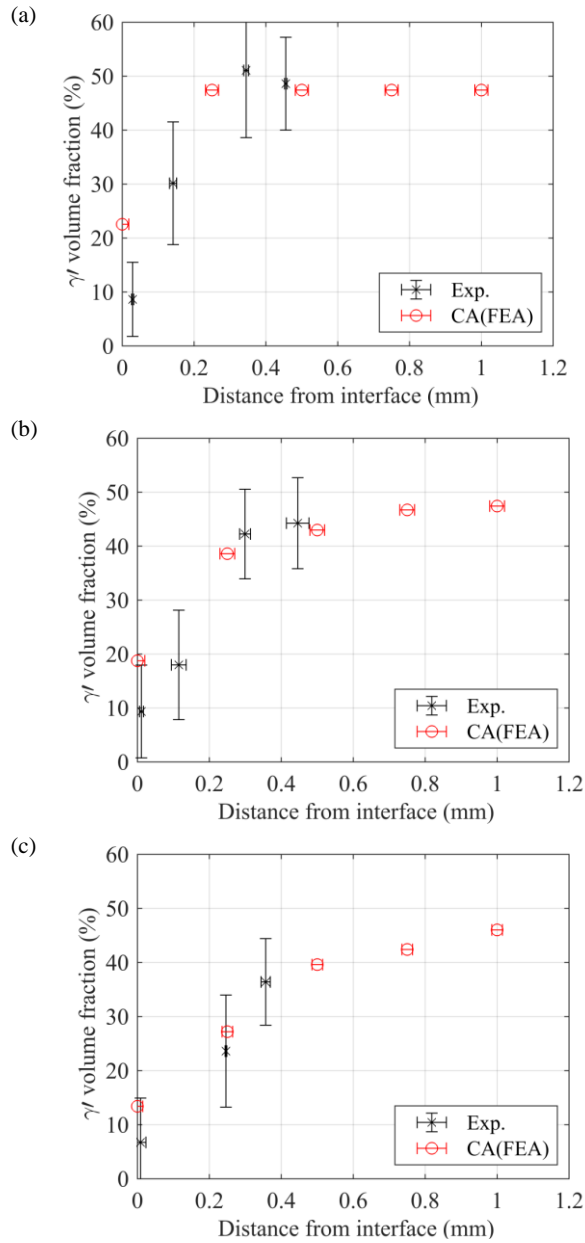


**Figure 6.13:** Comparison of  $\gamma'$  volume fraction data evaluated from in-situ synchrotron diffraction and cellular automata models for weld parameter set N2. (a) End of conditioning. (b) End of burn-off. (c) End of consolidation.

A possible explanation for this behaviour is incorrect thermal conductivity data. In welds of parameter set N2, the total upset is approximately 60 % of that of parameter set N1. Therefore, the removal rate of material from the interface is generally lower. As the material is ejected from the interface at a slower rate, there is an increased

reliance on thermal conductivity data to correctly evaluate the thermal response of the weld.

It may be possible that when modelling welds of parameter set N2, the thermal conductivity data was too high. Thus, heat generated at the interface was conducted axially through the specimens at a rate higher than that present experimentally. This would have resulted in reduced temperatures at the interface, and increased temperatures further from the interface, when compared with the true values.

The same issue would be present in FE models of weld parameter set N1, as the thermal conductivity was consistent throughout all FE modelling. However, in the case of parameter set N1, the interface material removal rate is larger, due to the greater total upset and shorter weld duration. Therefore, the effects of conduction are less dominant due to the fact that material further from the interface will be brought closer to the interface, and thus the heat source, due to the increased upsetting.

The results produced by the CA model for IFW using parameter set N3 (HS, LP) are presented alongside the diffraction data at consistent weld times in Figure 6.14. For this parameter set, there is a consistent over-estimation of the size of the  $\gamma'$  dissolved zone produced by the CA model. It can be observed that the thermal histories present at the contact interface at the end of the three weld stages produce significant dissolution of  $\gamma'$ , which is consistent in both experimental and numerical modelling data sets. However, further from the interface, at distances greater than 0.4 mm, the CA model calculates a much greater reduction in  $\gamma'$  volume fraction than is observed in the experimental results.

This may again be linked to the thermal conductivity defined in the material model. Similar to welds of parameter set N2, parameter set N3 produced a reasonably low total upset of 1.01 mm in the mean experimental data. Further to this, the long burn-off region observed permitted an upset of 0.3 mm at a weld time of 4.5 s. This presents an opportunity for the conduction of heat to dominate the thermal evolution, due to the low upset rate exhibited during the majority of the weld duration.

However, for this weld parameter set, the results produced by the CA model are extremely inaccurate when compared with experimental values. It is extremely unlikely that inaccuracies in the thermal conductivity data would cause such a large misevaluation of the thermal histories and thus  $\gamma'$  volume fraction evolution.

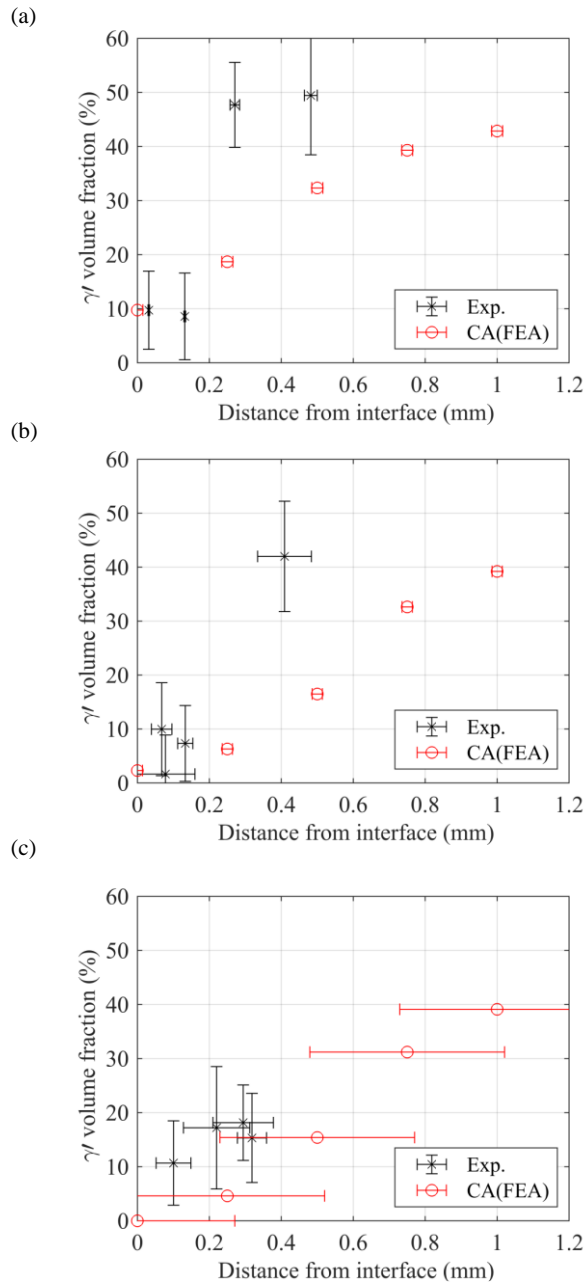


**Figure 6.14:** Comparison of  $\gamma'$  volume fraction data evaluated from in-situ synchrotron diffraction and cellular automata models for weld parameter set N3. (a) End of conditioning. (b) End of burn-off. (c) End of consolidation.

For this weld parameter set, the finite element model failed to produce the consolidation stage seen in the experimental welds. Therefore, it can be said that the process physics were not correctly represented. While the deformation produced by the finite element model correctly represented the burn-off stage of the experimental

weld, it is clear that the consolidation, burn-off and conditioning stages are not clearly observed in the finite element upset profile.

It is possible that the optimisation procedure performed here has altered the physics of the process modelled, through modification of the material model. The transformation from the initial material model to the optimised model has reduced the yield stress values, permitting plastic flow of material under smaller loads. This additional plasticity may cause viscoplastic heating, which in turn could act as another source of heat generation close to the contact interface. It is possible that the combination of frictional heat generation and viscoplastic heating may cause increased temperatures throughout the specimens, due to the larger amount of temperature generated. The increased temperatures would then permit increased dissolution of  $\gamma'$  in the CA model, as observed here.

However, if this is the source of the error in the CA modelling results for this parameter set, it would be expected that a similar trend would be seen across all models, as the optimisation of the material model has reduced the yield stress in all cases, to permit increased upset. Additionally, this effect would expect to be more pronounced in the high pressure cases, due to the greater amount of plastic flow required to permit larger amounts of mechanical upset. This has not been observed in the cases investigated so far, which makes the inaccurate response of the CA model in this case incredibly difficult to understand.

Another possible source of this error may be due to the increased weld duration of parameter set N3. No numerical solution can be completely accurate when compared with experimental results due to effects such as boundary condition assumptions and discretisation which must be performed in order to produce numerical models. Any errors introduced due to effects such as these would increase over time, and it may be possible that these have led to the increased dissolution seen in Figure 6.14.

To assess these possible sources of error, the CA modelling results for weld parameter set N4 (HS, HP) are presented in Figure 6.15. Similar to parameter set N3, this weld parameter set produced a longer weld duration. Additionally, the finite element model also failed to correctly represent the consolidation stage of the weld, and so it can also be stated that the model did not correctly replicate the physics of the process.

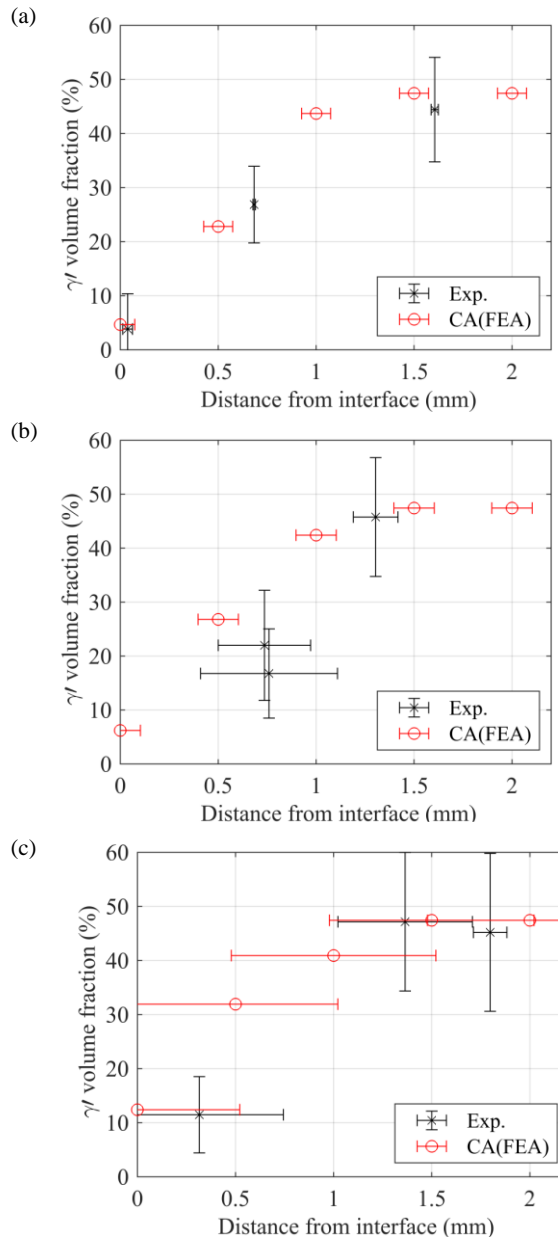


**Figure 6.15:** Comparison of  $\gamma'$  volume fraction data evaluated from in-situ synchrotron diffraction and cellular automata models for weld parameter set N4. (a) End of conditioning. (b) End of burn-off. (c) End of consolidation.

The results produced by the CA model for weld parameter set N4 show the opposite trend to parameter set N3. Here, the  $\gamma'$  volume fractions produced by the CA model appear to slightly underestimate the amount of  $\gamma'$  dissolution which occurred in the experimental case. Therefore, any additional viscoplastic heating or compounding of errors due to increased simulation times cannot be defined as the cause for the poor results produced by the CA model for parameter set N3.

The 1D CA model has been shown to produce an accurate representation of  $\gamma'$  volume fraction evolution for three of the four weld parameter sets investigated in this study. The inaccurate results produced by the model for parameter set N3 have been analysed, but comparison with other weld parameter sets appears to disprove the majority of hypothesis regarding the possible sources of error in the numerical modelling approach.

Modelling of three individual precipitates to provide a representation of the  $\gamma'$  volume fraction evolution of different precipitate sizes appears to show that the  $\gamma'$  dissolution behaviour present in inertia friction welding can be feasibly explained by thermodynamic atomic diffusion. There are some cases, particularly early in the weld process and close to the contact interface, in which the  $\gamma'$  phase fraction produced by the CA model was larger than the experimental values, and here it is hypothesised that there may be some strain energy contribution to the driving force for  $\gamma'$  dissolution in reality.

However, the 1D models utilised here are formed on the basis that the precipitates, and the atomic concentration gradients produced at the  $\gamma/\gamma'$  interfaces during  $\gamma'$  dissolution, do not interact. In reality, the random distribution of precipitates means that neighbouring precipitates do occur at times. To fully assess whether thermal modelling of atomic diffusion and  $\gamma'$  dissolution is an accurate method of evaluating the microstructure evolution, the effects of closely neighbouring precipitates on the  $\gamma'$  dissolution kinetics must be evaluated through implementation of a 2D model.

## 6.4 2D Cellular automata

The 2D implementation of the cellular automata model allows for the  $\gamma'$  dissolution characteristics to be evaluated with the inclusion of neighbouring precipitates and local concentration gradients which may reduce the driving force for atomic diffusion and  $\gamma'$  dissolution.

As a point of verification, the same heating rate tests have been performed for a single precipitate modelled in using the 2D CA approach. Here, the primary  $\gamma'$  precipitate size was simulated with four heating rates, and the dissolution profiles compared with DICTRA, as shown in Figure 6.16.

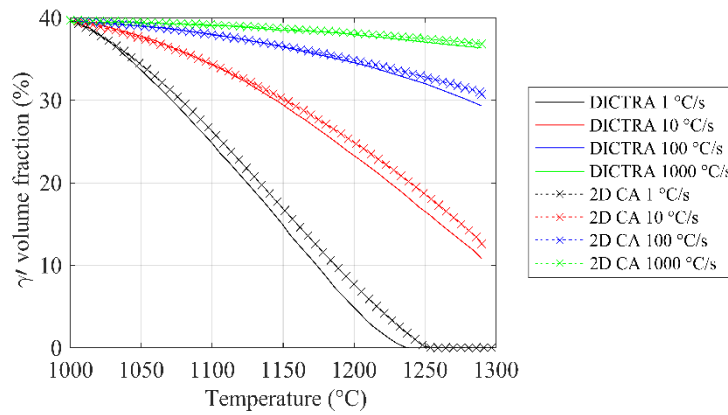


**Figure 6.16:** Verification of the 2D CA model through comparison of  $\gamma'$  dissolution kinetics with the DICTRA diffusion module.

It is observed in Figure 6.16 that the 2D model produced less accurate results when compared with the 1D model. The  $\gamma'$  dissolution kinetics appear to be least accurate at lower heating rates, with the higher heating rate models producing reasonable results. The inaccurate response in this case is expected to be due to the Von Neumann neighbourhood used in the 2D CA model, as only the north, south, east and west neighbours are included in the calculation. Therefore, gradients in concentration and chemical potential the diagonal directions were not evaluated for input into the diffusion equation, which in turn reduced the rate at which the precipitates dissolved. However, from FEA it is known that the heating rates are extremely high, and the process durations are extremely short. Therefore, heating rates of 1 °C/s and 10 °C/s

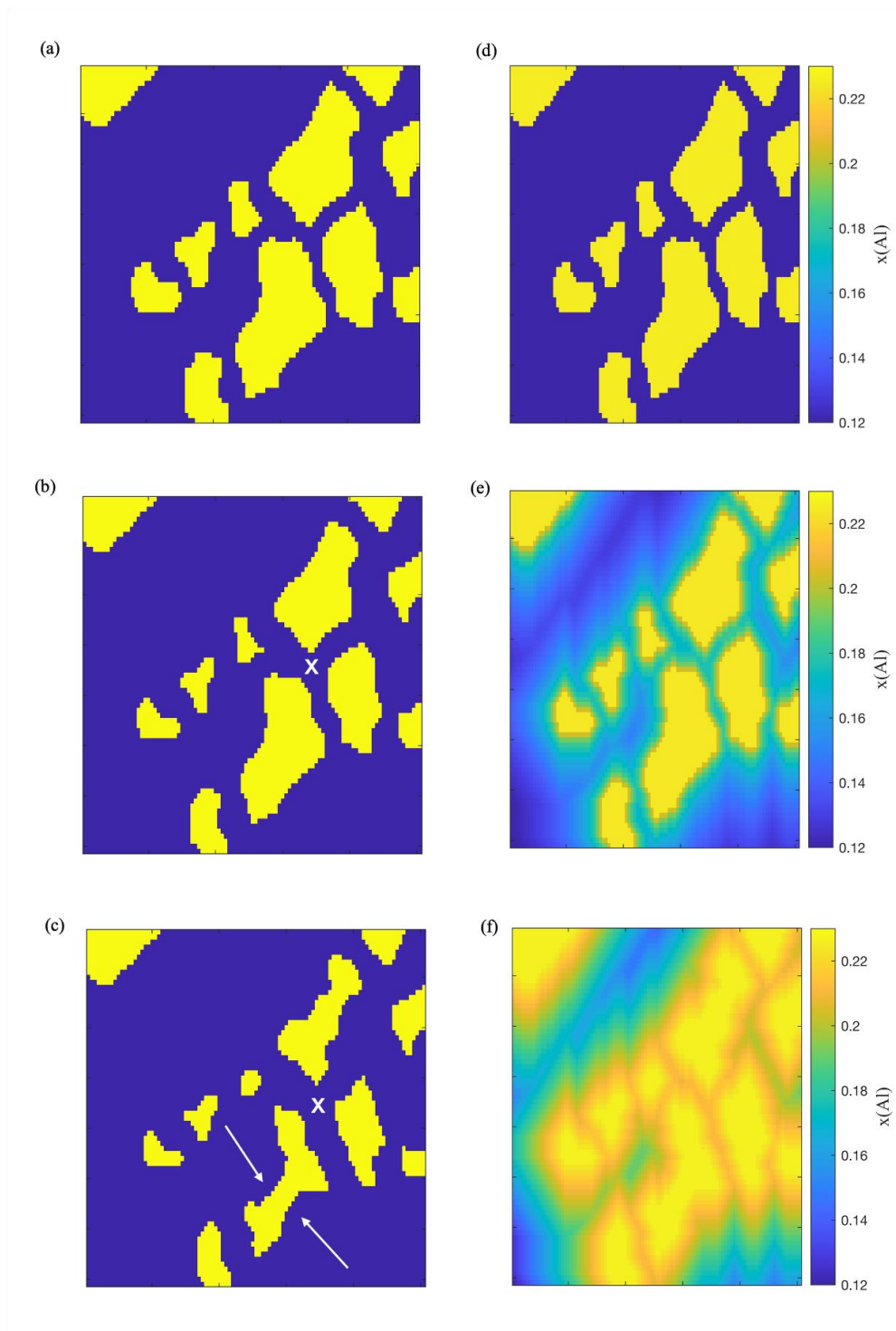
are not of particular relevance here. When modelling high heating rates, the CA model showed good agreement with the 1dimensional DICTRA simulations. Therefore, this approach can be used to model the  $\gamma'$  dissolution kinetics which occur in IFW.

Figure 6.17 presents a region of the 2D CA model, in which a cluster of secondary  $\gamma'$  precipitates are observed. The thermal history modelled in this case was extracted from weld parameter set N1, where the axial position 0.5 mm from the contact interface at the end of burn-off was defined as the point of interest.

Figure 6.17a shows the parent material, prior to dissolution of  $\gamma'$ . A region x has been labelled between the cluster of precipitates, as this is a site in which local enrichment of Aluminium is expected to occur, thus slowing dissolution of the precipitate. The distribution of Aluminium in the parent material is provided in Figure 6.17d.

The CA model at a weld time of 0.7 s is presented in Figure 6.17b. Here, the cluster of precipitates have started to dissolve uniformly. Due to the close proximity of the precipitates, there is not a large region for the  $\gamma'$ -forming Aluminium to dissolve through, allowing for the concentration gradient to be maintained. Thus, the concentration of Aluminium increases around point x, providing a smaller concentration gradient and a reduced driving force for dissolution. It is observed in Figure 6.17e that the local concentration of Aluminium at point x is approximately 0.19.

In Figure 6.17c, the microstructure at a weld time of 1.25 s is presented. Here, it can be seen that precipitate dissolution in the region surrounding point x is limited. However, when observing the precipitate to the right of point x, it can be seen that the ideal dissolution behaviour is present, as shown by the arrows.



**Figure 6.17:** A small region of the microstructure modelled in the 2D CA model highlighting the benefits of 2D modelling. (a) Parent microstructure at  $t = 0$  s. (b) Weld microstructure at  $t = 0.7$  s. (c) Weld microstructure at  $t = 1.5$  s. (d-f) Show the corresponding distribution of Aluminium for the microstructures in (a-c).

The atomic fraction of the  $\gamma'$  forming element Aluminium at position  $x$  has been extracted from the 2D CA model and the evolution of this plotted over the time simulated. This is presented in Figure 6.18 alongside the equilibrium atomic fraction of Aluminium in the  $\gamma'$  and  $\gamma$  phases.

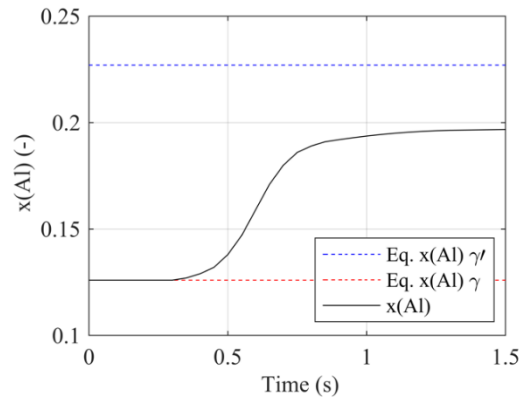


**Figure 6.18:** The evolution of the atomic fraction of Aluminium at position  $x$  in the simulation presented in Figure 6.17.

In Figure 6.18, it is observed that the atomic fraction of Aluminium is consistent with that of equilibrium  $\gamma$ , as defined for the parent microstructure. At approximately 0.3 s, the temperature in the model is high enough to produce diffusion of Aluminium out of the  $\gamma'$  phase and into the surrounding matrix. It can be seen that the dissolution of the three precipitates surrounding position  $x$  causes a rapid local enrichment of Aluminium between 0.5 s and 0.8 s. After 0.8 s, the gradients in chemical potential and concentration between point  $x$  and the surrounding precipitates are much lower, and so the driving forces for precipitate dissolution in this region are reduced significantly. This is observed by the slower increase in Aluminium atomic fraction present at position  $x$  after 0.8 s of welding.

To assess the effect of the local concentrations on the dissolution kinetics, the 2D CA model has been implemented for weld parameter set N1. Here, the 2D model has been evaluated at consistent weld times and positions as the 1D model for direct comparison.

The results produced by the 1D and 2D CA models at the end of conditioning of weld parameter set N1 are presented in Figure 6.19. It can be observed that at this weld

time, modelling the microstructure evolution in 2D offers little benefit over the faster 1D approximation.

During the first 0.62 s, the dissolution kinetics do not appear to be inhibited by neighbouring precipitates. This is logical given the fact that the early period of dissolution is modelled in this case. Here, there is limited time for concentration gradients around neighbouring precipitates to affect one another and slow the dissolution rate. Hence, the dissolution kinetics of  $\gamma'$  can be modelled representatively using the 1D approximation. At positions close to the interface, the 2D model produces a slightly lower volume fraction than the 1D model. This is thought to occur due to the fact that the 2D model represents a range of secondary  $\gamma'$  precipitate sizes as opposed to the mean secondary  $\gamma'$  precipitate radius modelled in the 1D approximation. The smaller secondary  $\gamma'$  precipitates dissolve faster due to their smaller size.

The largest difference between 1D and 2D model outputs occurs at a distance 0.5 mm from the interface. Here, the  $\gamma'$  volume fraction produced by the 2D model is approximately 3 % lower than that of the 1D model. It is thought that this difference is mainly caused by the linear approximation of tertiary  $\gamma'$  dissolution occurring between 850 and 1000 °C. In the 2D case, the temperature of 960 °C estimates that the tertiary  $\gamma'$  volume fraction is reduced to only 2 %. The 1D CA approximation for this time and position shows that approximately 5 % of the tertiary  $\gamma'$  volume fraction remains in the 1D model (Figure 6.9b).

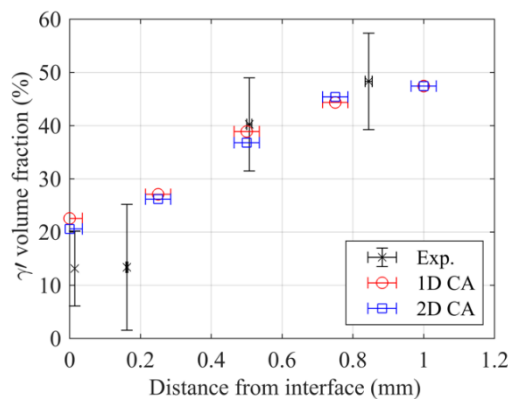


**Figure 6.19:** Comparison of microstructure evolution data evaluated from in-situ synchrotron diffraction and cellular automata models for weld parameter set N1 at  $t = 0.62$  s.

Figure 6.20 presents the comparison of 1D and 2D CA models evaluated from thermal FEA data from weld parameter set N1 at the end of burn off ( $t = 1.25$  s). In this case, it can be seen that the weld duration modelled is long enough for the effects of neighbouring precipitates and local concentration to affect the solution. There is a clear trend in which the 2D CA model produces a larger  $\gamma'$  volume fraction than the 1D CA model, particularly at positions close to the interface. Here, the 2D model begins to represent the reduction in  $\gamma'$  dissolution rate due to an increased concentration in  $\gamma'$  forming elements in the surrounding matrix, which are present due to dissolution of nearby precipitates.

At  $z = 0.75$  mm, it is observed that the 2D CA model estimates an increased amount of  $\gamma'$  dissolution compared to the 1D CA model. This is again due to the approximation made regarding dissolution of tertiary  $\gamma'$ .

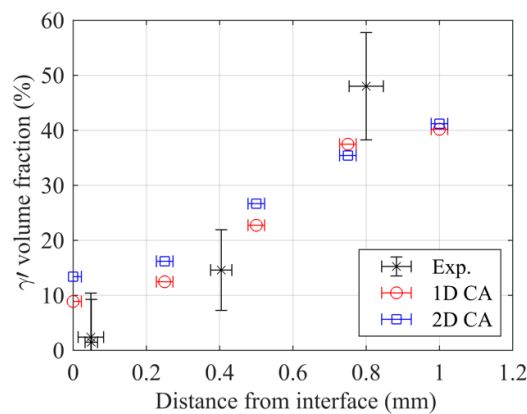


**Figure 6.20:** Comparison of microstructure evolution data evaluated from in-situ synchrotron diffraction and cellular automata models for weld parameter set N1 at  $t = 1.25$  s.

Figure 6.21 presents the comparison of CA modelling approaches for weld parameter set N1 at the end of consolidation. Here, the benefits of modelling the full 2D microstructure can be seen, as the 2D CA model estimates a  $\gamma'$  volume fraction which is approximately 10 % larger than that of the 1D simulation, due to the effects of precipitate clustering seen in the microstructure.

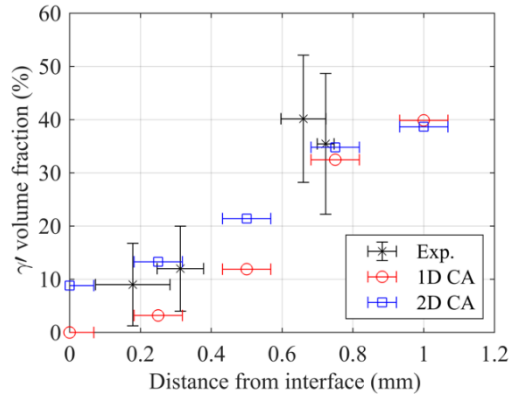


**Figure 6.21:** Comparison of microstructure evolution data evaluated from in-situ synchrotron diffraction and cellular automata models for weld parameter set N1 at  $t = 2.37$  s.

Further from the interface, the difference in the results produced by 1D and 2D CA models is reduced due to the reduction in total dissolution which occurs due to the thermal histories at these locations. With limited dissolution of  $\gamma'$ , there is a limited effect of the local concentration of  $\gamma'$  forming elements in the surrounding matrix to impact the dissolution behaviour of neighbouring precipitates.

Analysing Figure 6.21, it can be seen that both 1D and 2D CA models produce accurate results. This is in part due to the large uncertainty provided by the experimental approach. It can be said that both models offer benefits to modelling the dissolution of  $\gamma'$  in RR1000. The 1D model approximation provides a reasonable estimate of  $\gamma'$  dissolution kinetics with a shorter computational time than the 2D model. However, the 2D model offers a more representative evaluation of the real microstructure.

## 6.5 Conclusions

A Cellular Automata (CA) numerical modelling methodology has been developed and used alongside Finite Element Analysis (FEA) to evaluate the ability of numerical models to estimate the  $\gamma'$  dissolution kinetics which occur due to the temperature histories present in the IFW process.

Through implementation of a commonly used FEA approach, it has been observed that inaccurate mechanical outputs produced by a validated material model. This highlights a possible change of process physics or an increased sensitivity to heating rate at reduced geometries which tabular material data cannot account for. Optimisation of the material data used in FEA has allowed for an increase in accuracy in the outputs modelled when compared with experimental data, however it is questioned whether this approach may possibly introduce errors into the procedure.

There are other possible approaches to modelling material data, which may offer increased accuracy in macro-scale process outputs than the tabular material data used in this study, such as coupled microstructure-mechanical constitutive models. However, development and validation of new material models is beyond the scope of this research.

It has been presented that through calculation of thermodynamic atomic diffusion and application of the local equilibrium approach, the dissolution of  $\gamma'$  during IFW can be well represented. In general, the numerical modelling results produced by three of the four weld parameter sets investigated in this study showed good agreement with the in-situ synchrotron diffraction data.

Both 1D and 2D CA models have been evaluated. The 1D model offers a faster solution while the 2D model produces a more accurate representation. The test case presented showed that both 1D and 2D numerical modelling approaches produced an accurate response when compared with experimental diffraction results.

## Chapter 7

### Conclusions

#### 7.1 Conclusions

In-situ synchrotron diffraction experiments have been implemented for the IFW process providing novel insight into the microstructure evolution which occurs during the process. For IFW of steel, the transformation of parent ferrite to high-temperature austenite has been captured in great detail, with both positional and temporal resolution. Additionally, the evolution of the HAZ and TMAZ have been observed and quantified throughout the process. It was observed through validation welds that the transformation to austenite occurs below the equilibrium phase transformation temperature. The mechanical contribution to the phase transformation in the TMAZ was evaluated and it was shown that the strains present during IFW were large enough to assist this non-equilibrium phase transformation.

For the Nickel-based superalloy RR1000, the localised dissolution of  $\gamma'$  precipitates has been quantified about the contact interface. Four sets of weld parameters have been investigated to assess the sensitivity of the dissolution of  $\gamma'$  precipitates to design changes in the weld parameters.

The understanding of microstructure evolution obtained through this novel experimental approach has provided a great level of detail which has not been seen in the conventional ex-situ analyses performed. For the first time, the microstructure evolution has been quantitatively investigated and it has been revealed that this has some control over the macro-scale process physics which are observed. The thermal and microstructural components of this highly coupled process have been assessed to show that during conditioning and burn-off, these factors control the duration of the conditioning phase and the upset rate produced during burn off. This investigation also showed that there is a relationship between the size of the HAZ produced during welding, and the rate of upset during the consolidation phase. However, analysis of the mechanical strains during this weld stage concluded that the process was not controlled purely by thermal and microstructural evolution.

The weld parameters implemented in this study were shown to produce discrete trends in the microstructure produced both during and after the process, offering novel information regarding the relationship between macroscale process outputs and HAZ width that may be used to determine optimal process parameters.

FEA analysis has been investigated as a method for modelling the macroscale process outputs produced by IFW, and the thermal histories of the weld specimens. The currently implemented tabular material data has been shown to be incapable of correctly representing the mechanical upset produced when IFW is performed on small weld geometries.

An optimisation procedure was implemented to improve the mechanical response produced by FEA, but this too was limited. For two sets of weld parameters, the optimisation procedure produced a material model which could accurately represent the experimental upset measurements. However, for welds performed with larger initial rotational velocities, the material model could not represent the consolidation stage of welding after the optimisation.

Cellular Automata has been investigated as a means of evaluating the microstructure evolution which occurs due to the thermal loading produced during IFW. These models utilised thermal history data extracted from FEA to calculate the diffusion of elements which occur between the  $\gamma$  and  $\gamma'$  phases. The models were coupled with CALPHAD via 'lookup tables' which allowed for implementation of the local equilibrium approach to update the phase composition based on local element concentrations.

A ternary Ni-Al-Cr alloy system has been produced to represent the multicomponent alloy RR1000 and this has been applied to 1D and 2D CA. The 1D form does not model coupling of precipitate interactions during dissolution, and therefore was shown to overpredict the amount of dissolution of  $\gamma'$  which occurred when compared with experimental data. The 2D model utilised a digital material representation of primary and secondary  $\gamma'$  precipitates, thus modelling the coupling between these. The 2D model was shown to represent the precipitate interactions well, where localised increases in  $\gamma'$ -forming elements in the matrix was observed which inhibited further dissolution of precipitates in the direction of the localised concentration.

## 7.2 Suggestions for future work

There are some areas in which additional research would further enhance the understanding of microstructure evolution which can be characterised using these techniques. Trends have been shown to exist between the microstructure evolution and macro-scale process response, but there are stages within IFW in which the thermal and microstructural evolution alone cannot describe the process physics. More complete understanding of the coupled thermal, mechanical and microstructural effects on deformation mechanisms is required to fully understand the relationship between these controlling factors and the process response. Defining trends between the thermal and mechanical loads applied to a material, the microstructure produced by these, and the deformation observed due to large shear loading would enrich the results presented in this work. Such data could be linked to the behaviour observed during IFW to further analyse the relationships between temperature, mechanical loading, microstructure and deformation mechanics.

Further to this, there are simple amendments to the IFW machine used in this research would allow for increased weld energies and axial loading. This would permit welding of larger weld specimens with increased contact areas. It is expected that welding of samples with 3 mm wall thickness, as opposed to the 1 mm wall thickness used in this study, would produce a process response similar to larger scale weld geometries which are of interest in industry. The small wall thickness used in the investigations here were more susceptible to misalignment and imperfections in the contact surface. Increasing the weld wall thickness would greatly reduce the impact of these effects.

Furthermore, the uncertainties in volume fractions characterised in the in-situ diffraction experiments were relatively large. However, this was offset by the high acquisition rate at which data was collected for analysis. Development of beamlines in the future will allow for greater X-ray beam fluxes, which will allow for acquisition of more coherent diffraction patterns at the same acquisition rate. These patterns would be less influenced by the background noise allowing for more accurate characterisation of phase fractions.

Tabular material data has been shown to produce accurate results in FEA modelling of RR1000 IFWs at larger geometries. In the investigations performed here, it has been observed that the tabular material data is insufficient for modelling smaller weld

geometries where the thermal and mechanical conditions are more extreme. Whilst this is an isolated case for now, future alloy systems which exhibit higher strengths at elevated temperatures will require larger thermal and mechanical loads to join. Therefore, it is suggested that the development of a coupled microstructure-mechanical constitutive material model would be of benefit for modelling welding of future alloy systems.

The CA models developed in this thesis have shown good agreement with the experimental data. However, it has been observed in experimental studies that there are large mechanical loads present during the process. For IFW of BS1407 steel, the mechanical loading was shown to be large enough to permit the formation of non-equilibrium austenite at temperatures below the transformation temperature. Additionally, there was a large mechanical force driving the evolution of the consolidation stage observed during IFW of RR1000, which may be likely to also act as a driving force for  $\gamma'$  dissolution in the microstructure. The CA models developed in this work have only accounted for the thermal driving forces for phase transformations. Characterisation of the mechanical loads present during IFW would allow for an assessment of whether these produce a significant energy to permit non-equilibrium phase transformations.

## References

- [1] A. J. A. Mom, "Introduction to gas turbines," in *Modern Gas Turbine Systems: High Efficiency, Low Emission, Fuel Flexible Power Generation*, Woodhead Publishing Series in Energy, 2013, pp. 3–20.
- [2] R. J. Mitchell, J. A. Lemsky, R. Ramanathan, H. Y. Li, K. M. Perkins, and L. D. Connor, "Process development & microstructure & mechanical property evaluation of a dual microstructure heat treated advanced Nickel disc alloy," *Proc. Int. Symp. Superalloys*, no. March 2016, pp. 347–356, 2008.
- [3] N. Wang, S. Mokadem, M. Rappaz, and W. Kurz, "Solidification cracking of superalloy single- and bi-crystals," *Acta Mater.*, vol. 52, pp. 3173–3182, 2004.
- [4] L. Rakoczy *et al.*, "Characterization of  $\gamma'$  precipitates in cast Ni-Based superalloy and their behaviour at high-homologous temperatures studied by TEM and in situ XRD," *Materials (Basel)*, vol. 13, no. 10, 2020.
- [5] A. P. Mouritz, "Superalloys for gas turbine engines," in *Introduction to Aerospace Materials*, A. P. Mouritz, Ed. Woodhead Publishing, 2012, pp. 251–267.
- [6] T. M. Pollock and S. Tin, "Nickel-Based Superalloys for Advanced Turbine Engines: Chemistry, Microstructure and Properties," *J. Propuls. Power*, vol. 22, no. 2, pp. 361–374, 2006.
- [7] R. C. Reed, *The Superalloys - Fundamentals and Applications*. Cambridge: Cambridge University Press, 2006.
- [8] F. I. Versnyder and M. E. Shank, "The development of columnar grain and single crystal high temperature materials through directional solidification," *Mater. Sci. Eng.*, vol. 6, no. 4, pp. 213–247, 1970.
- [9] J. Lacaze and A. Hazotte, "Directionally Solidified Materials : Gas Turbines," *Textures Microstruct.*, vol. 13, no. December 1989, pp. 1–14, 1990.
- [10] H. Fecht and D. Furrer, "Processing of Nickel-base superalloys for turbine engine disc applications," *Adv. Eng. Mater.*, vol. 2, no. 12, pp. 777–787, 2000.

- [11] W. Eisen, "Powder metallurgy Superalloys," *Mater. World*, vol. 4, pp. 22–24, 1992.
- [12] Z. W. Huang, H. Y. Li, G. Baxter, S. Bray, and P. Bowen, "Electron microscopy characterization of the weld line zones of an inertia friction welded superalloy," *J. Mater. Process. Technol.*, vol. 211, pp. 1927–1936, 2011.
- [13] M. P. Jackson and R. C. Reed, "Heat treatment of UDIMET 720Li: The effect of microstructure on properties," *Mater. Sci. Eng. A*, vol. 259, no. 1, pp. 85–97, 1999.
- [14] R. J. Mitchell, M. C. Hardy, M. Preuss, and S. Tin, "Development of  $\gamma'$  morphology in P/M rotor disc alloys during heat treatment," *Proc. Int. Symp. Superalloys*, no. February 2016, pp. 361–370, 2004.
- [15] P. A. J. Bagot *et al.*, "An Atom Probe Tomography study of site preference and partitioning in a Nickel-based superalloy," *Acta Mater.*, vol. 125, pp. 156–165, 2017.
- [16] Y. Q. Chen *et al.*, "Measurement of size-dependent composition variations for gamma prime ( $\gamma'$ ) precipitates in an advanced Nickel-based superalloy," *Ultramicroscopy*, vol. 144, pp. 1–8, 2014.
- [17] N. D'Souza, W. Li, C. Argyrakis, G. D. West, and C. D. Slater, "On the Evolution of Primary Gamma Prime Precipitates During High Temperature and High Strain Rate Deformation and Subsequent Heat Treatment in the Ni-Based Superalloy, RR1000," *Metall. Mater. Trans. A Phys. Metall. Mater. Sci.*, vol. 50, no. September, 2019.
- [18] A. Harte *et al.*, "The effect of solid solution and gamma prime on the deformation modes in Ni-based superalloys," *Acta Mater.*, vol. 194, pp. 257–275, 2020.
- [19] D. M. Collins, B. D. Conduit, H. J. Stone, M. C. Hardy, G. J. Conduit, and R. J. Mitchell, "Grain growth behaviour during near- $\gamma'$  solvus thermal exposures in a polycrystalline Nickel-base superalloy," *Acta Mater.*, vol. 61, no. 9, pp. 3378–3391, 2013.

- [20] I. A. Choudhury and M. A. El-Baradie, "Machinability of Nickel-base super alloys: A general review," *J. Mater. Process. Technol.*, vol. 300, no. 3–4, pp. 278–284, 1998.
- [21] S. Sravan Sashank, S. Rajakumar, R. Karthikeyan, and D. S. Nagaraju, "Weldability, Mechanical Properties and Microstructure of Nickel Based Super Alloys: A review," *E3S Web Conf.*, vol. 184, pp. 1–6, 2020.
- [22] O. A. Ojo, "Intergranular liquation cracking in heat affected zone of a welded Nickel based superalloy in as cast condition," *Mater. Sci. Technol.*, vol. 23, no. 10, pp. 1149–1155, 2007.
- [23] A. Wang *et al.*, "Effects of heat treatment on microstructure and high-temperature tensile properties of Nickel-based single-crystal superalloys," *Mater. Res. Express*, vol. 6, no. 12, 2019.
- [24] O. A. Ojo, N. L. Richards, and M. C. Chaturvedi, "Contribution of constitutional liquation of gamma prime precipitate to weld HAZ cracking of cast Inconel 738 superalloy," *Scr. Mater.*, vol. 50, no. 5, pp. 641–646, 2004.
- [25] G. M. M.B. Henderson , D. Arrell , M. Heobel, R. Larsson, "Nickel-Based Superalloy Welding Practices for Industrial Gas Turbine Applications M.B. Henderson , D. Arrell , M. Heobel\*, R. Larsson and G. Marchant + +," *Sci. Technol. Weld. Join.*, vol. 9, no. 1, pp. 1–14, 2004.
- [26] L. Zai, G. You, X. Tong, Y. Ding, X. Xu, and Q. Liu, "Microstructure and Mechanical Properties of Inertia-Friction-Welded Fe–Cr–Ni–Mo High-Strength Steel," *Steel Res. Int.*, vol. 91, no. 9, pp. 1–12, 2020.
- [27] M. D. Tumuluru, "Parametric Study of Inertia Friction Welding for Low Alloy Steel Pipes.," *Weld. J. (Miami, Fla)*, vol. 63, no. 9, pp. 5–10, 1984.
- [28] F. Daus, H. Y. Li, G. Baxter, S. Bray, and P. Bowen, "Mechanical and microstructural assessments of RR1000 to IN718 inertia welds - Effects of welding parameters," in *Materials Science and Technology*, 2007, vol. 23, no. 12, pp. 1424–1432.
- [29] W. Guo, G. You, G. Yuan, and X. Zhang, "Microstructure and mechanical properties of dissimilar inertia friction welding of 7A04 aluminum alloy to

- AZ31 magnesium alloy,” *J. Alloys Compd.*, vol. 695, pp. 3267–3277, 2017.
- [30] M. Kessler, S. Suenger, M. Haubold, and M. F. Zaeh, “Modeling of upset and torsional moment during inertia friction welding,” *J. Mater. Process. Technol.*, vol. 227, pp. 34–40, 2016.
- [31] D. W. Mahaffey, O. N. Senkov, R. Shivpuri, and S. L. Semiatin, “Effect of Process Variables on the Inertia Friction Welding of Superalloys LSHR and Mar-M247,” *Metall. Mater. Trans. A Phys. Metall. Mater. Sci.*, vol. 47, no. 8, pp. 3981–4000, 2016.
- [32] O. N. Senkov, D. W. Mahaffey, D. J. Tung, W. Zhang, and S. L. Semiatin, “Efficiency of the Inertia Friction Welding Process and Its Dependence on Process Parameters,” *Metall. Mater. Trans. A Phys. Metall. Mater. Sci.*, vol. 48, no. 7, pp. 3328–3342, 2017.
- [33] O. N. Senkov, D. W. Mahaffey, and S. L. Semiatin, “Effect of process parameters on process efficiency and inertia friction welding behavior of the superalloys LSHR and Mar-M247,” *J. Mater. Process. Technol.*, vol. 250, no. April, pp. 156–168, 2017.
- [34] L. Chen, W. Y. Li, and J. L. Li, “Effect of rotation speed on temperature field and axial shortening of inertia friction welded GH4169 joints by numerical simulation,” *J. Shanghai Jiaotong Univ.*, vol. 16, no. 3, pp. 277–280, 2011.
- [35] F. F. Wang, W. Y. Li, J. L. Li, and A. Vairis, “Process parameter analysis of inertia friction welding Nickel-based superalloy,” pp. 1909–1918, 2014.
- [36] R. P. Turner, D. Howe, B. Thota, R. M. Ward, H. C. Basoalto, and J. W. Brooks, “Calculating the energy required to undergo the conditioning phase of a titanium alloy inertia friction weld,” *J. Manuf. Process.*, vol. 24, pp. 186–194, 2016.
- [37] R. P. Turner, B. Perumal, Y. Lu, R. M. Ward, H. C. Basoalto, and J. W. Brooks, “Modeling of the Heat-Affected and Thermomechanically Affected Zones in a Ti-6Al-4V Inertia Friction Weld,” *Metall. Mater. Trans. B Process Metall. Mater. Process. Sci.*, vol. 50, no. 2, pp. 1000–1011, 2019.
- [38] W. Liu, F. Wang, X. Yang, and W. Li, “Upset prediction in friction welding

- using radial basis function neural network,” *Adv. Mater. Sci. Eng.*, vol. 2013, 2013.
- [39] M. Preuss, J. W. L. Pang, P. J. Withers, and G. J. Baxter, “Inertia Welding Nickel-Based Superalloy : Part I . Metallurgical Characterization,” *Metall. Mater. Trans. A*, vol. 33, no. October, pp. 3215–3225, 2002.
- [40] M. Preuss, P. J. Withers, and G. J. Baxter, “A comparison of inertia friction welds in three Nickel base superalloys,” *Mater. Sci. Eng. A*, vol. 437, no. 1, pp. 38–45, 2006.
- [41] O. Roder, J. Albrecht, and G. Lu, “Microstructure and mechanical properties of an inertia friction welded INCOLOY alloy 909 – INCONEL alloy 718 joint for rotating applications,” vol. 23, pp. 171–177, 2006.
- [42] Z. W. Huang *et al.*, “Inertia Friction Welding Dissimilar Nickel-Based Superalloys Alloy 720Li to IN718,” *Metall. Mater. Trans. A*, vol. 38, no. July, pp. 1608–1620, 2007.
- [43] R. Moat, M. Karadge, M. Preuss, S. Bray, and M. Rawson, “Phase transformations across high strength dissimilar steel inertia friction weld,” *J. Mater. Process. Technol.*, vol. 204, no. 1–3, pp. 48–58, 2008.
- [44] E. Taban, J. E. Gould, and J. C. Lippold, “Dissimilar friction welding of 6061-T6 aluminum and AISI 1018 steel : Properties and microstructural characterization,” *Mater. Des.*, vol. 31, no. 5, pp. 2305–2311, 2010.
- [45] O. N. Senkov, D. W. Mahaffey, S. L. Semiatin, and C. Woodward, “Site-Dependent Tension Properties of Inertia Friction-Welded Joints Made From Dissimilar Ni-based Superalloys,” vol. 24, no. March, pp. 1173–1184, 2015.
- [46] M. Eckert, “Max von Laue and the discovery of X-ray diffraction in 1912,” *Ann. Phys.*, vol. 524, no. 5, pp. 83–85, 2012.
- [47] W. H. Bragg, “The Reflection of X-Rays by Crystals. (II.),” *Proc. R. Soc. A*, vol. 89, no. 610, pp. 246–248, 1913.
- [48] H. Winick and A. Bienenstock, *Synchrotron Radiation Research.*, vol. 28. 1978.

- [49] G. Margaritondo and R. Meuli, “Synchrotron radiation in radiology: Novel X-ray sources,” *Eur. Radiol.*, vol. 13, no. 12, pp. 2633–2641, 2003.
- [50] R. L. Owen, J. M. Holton, C. Schulze-Briese, and E. F. Garman, “Determination of X-ray flux using silicon pin diodes,” *J. Synchrotron Radiat.*, vol. 16, no. 2, pp. 143–151, 2009.
- [51] R. Jenkins, “X-Ray Analysis,” in *Encyclopedia of Physical Science and Technology (Third Edition)*, Third Edit., Academic Press, 2003, pp. 887–902.
- [52] H. Van Swygenhoven and S. Van Petegem, “In-situ mechanical testing during X-ray diffraction,” *Mater. Charact.*, vol. 78, pp. 47–59, 2013.
- [53] IUCr, “Online Dictionary of Crystallography.” [Online]. Available: <https://dictionary.iucr.org/Brilliance>. [Accessed: 13-Mar-2021].
- [54] J. D. Brock and M. Sutton, “Materials science and X-ray techniques,” *Mater. Today*, vol. 11, no. 11, pp. 52–55, 2008.
- [55] ESRF, “Questions & Answers.” [Online]. Available: <https://www.esrf.eu/about/ask-an-expert/questions-answers>. [Accessed: 14-Mar-2021].
- [56] N. Baimpas, M. Drakopoulos, T. Connolley, and X. Song, “A feasibility study of dynamic stress analysis inside a running internal combustion engine using synchrotron X-ray beams research papers,” *J. Synchrotron Radiat.*, vol. 20, pp. 316–323, 2013.
- [57] J. W. Elmer, T. A. Palmer, and J. Wong, “In situ observations of phase transitions in Ti-6Al-4V alloy welds using spatially resolved x-ray diffraction,” *J. Appl. Phys.*, vol. 93, no. 4, pp. 1941–1947, 2003.
- [58] J. W. Elmer, T. A. Palmer, S. S. Babu, W. Zhang, and T. Debroy, “Phase transformation dynamics during welding of Ti – 6Al – 4V,” *J. Appl. Phys.*, vol. 95, no. 12, pp. 8327–8339, 2004.
- [59] J. Wong, T. Ressler, and J. W. Elmer, “Dynamics of phase transformations and microstructure evolution in carbon ± manga- nese steel arc welds using time-resolved synchrotron X-ray diffraction research papers,” *J. Synchrotron Radiat.*, vol. 10, pp. 154–167, 2003.

- [60] H. J. Stone, M. J. Peet, H. K. D. H. Bhadeshia, P. J. Withers, S. S. Babu, and E. D. Specht, "Synchrotron X-ray studies of austenite and bainitic ferrite," *Proc. R. Soc. A Math. Phys. Eng. Sci.*, vol. 464, no. 2092, pp. 1009–1027, 2008.
- [61] A. Kromm, T. Kannengiesser, and J. Gibmeier, "In Situ Studies of Phase Transformation and Residual Stresses in LTT Alloys During Welding Using Synchrotron Radiation," in *In-situ Studies with Photons, Neutrons and Electrons Scattering*, I., Berlin: Springer-Verlag Berlin Heidelberg, 2010, pp. 13–26.
- [62] C. Kenel *et al.*, "In situ investigation of phase transformations in Ti-6Al-4V under additive manufacturing conditions combining laser melting and high-speed micro-X-ray diffraction," *Sci. Rep.*, vol. 7, no. 1, pp. 1–10, 2017.
- [63] D. W. Brown *et al.*, "In-Situ High-Energy X-ray Diffraction During a Linear Deposition of 308 Stainless Steel via Wire Arc Additive Manufacture," *Metall. Mater. Trans. A Phys. Metall. Mater. Sci.*, vol. 51, no. 3, pp. 1379–1394, 2020.
- [64] P. Wang, K. K.; Nagappan, "Transient Temperature Distribution in Inertia Welding of Steels," *Weld. Res. Suppl.*, vol. 49, no. 9, pp. 419s-426s, 1970.
- [65] V. R. Dave, M. J. Cola, and G. N. A. Hussien, "Heat Generation in the Inertia Welding of Dissimilar Tubes," *Weld. Res. Suppl.*, vol. 80, no. October, pp. 246–252, 2001.
- [66] V. Balasubramanian, Y. Li, T. Stotler, J. Crompton, and W. Soboyejo, "An Energy Balance Method for the Numerical Simulation of Inertia Welding An Energy Balance Method for the Numerical Simulation of," *Mater. Manuf. Process.*, vol. 14, no. 5, pp. 755–773, 1999.
- [67] E. Moal, A; Massoni, "Finite element simulation of the inertia welding of two similar parts," *Eng. Comput.*, vol. 12, no. 6, pp. 497–512, 1995.
- [68] L. D'Alvise, E. Massoni, and S. J. Walløe, "Finite element modelling of the inertia friction welding process between dissimilar materials," *J. Mater. Process. Technol.*, vol. 126, pp. 387–391, 2002.

- [69] L. Fu, L. Y. Duan, and S. G. Du, “Numerical Simulation of Inertia Friction,” *Weld. Res.*, vol. March, pp. 65–70, 2003.
- [70] C. J. Bennett, T. H. Hyde, and P. H. Shipway, “A transient finite element analysis of thermoelastic effects during inertia friction welding,” *Comput. Mater. Sci.*, vol. 50, no. 9, pp. 2592–2598, 2011.
- [71] L. B. Yang, J. Gebelin, R. C. Reed, L. B. Yang, J. Gebelin, and R. C. Reed, “Modelling of inertia welding of IN718 superalloy Modelling of inertia welding of IN718 superalloy,” vol. 0836, no. June, 2017.
- [72] C. J. Bennett, T. H. Hyde, and E. J. Williams, “Modelling and simulation of the inertia,” *Proc. Inst. Mech. Eng. Part L J. Mater. Des. Appl.*, vol. 221, pp. 275–284, 2007.
- [73] C. J. Bennett, M. M. Attallah, M. Preuss, P. H. Shipway, T. H. Hyde, and S. Bray, “Finite Element Modeling of the Inertia Friction Welding of Dissimilar High-Strength Steels,” 2013.
- [74] O. Iracheta, C. J. Bennett, and W. Sun, “A sensitivity study of parameters affecting residual stress predictions in finite element modelling of the inertia friction welding process,” *Int. J. Solids Struct.*, vol. 71, pp. 180–193, 2015.
- [75] W. J. Boettinger, J. A. Warren, C. Beckermann, and A. Karma, “Phase-field simulation of solidification,” *Annu. Rev. Mater. Sci.*, vol. 32, pp. 163–194, 2002.
- [76] B. Nestler, H. Garcke, and B. Stinner, “Multicomponent alloy solidification: Phase-field modeling and simulations,” *Phys. Rev. E - Stat. Nonlinear, Soft Matter Phys.*, vol. 71, no. 4, pp. 1–6, 2005.
- [77] G. Abrivard, E. P. Busso, S. Forest, and B. Appolaire, “Phase field modelling of grain boundary motion driven by curvature and stored energy gradients. Part I: Theory and numerical implementation,” *Philos. Mag.*, vol. 92, no. 28–30, pp. 3618–3642, 2012.
- [78] I. Singer-Loginova and H. M. Singer, “The phase field technique for modeling multiphase materials,” 2008.
- [79] L. Sieradzki, L. Madej, and M. Carlo, “A perceptive comparison of the

- cellular automata and Monte Carlo techniques in application to static recrystallization modeling in polycrystalline materials,” *Comput. Mater. Sci.*, vol. 67, pp. 156–173, 2013.
- [80] T. M. Rodgers, J. D. Madison, V. Tikare, and M. C. Maguire, “Predicting Mesoscale Microstructural Evolution in Electron Beam Welding,” *Jom*, vol. 68, no. 5, pp. 1419–1426, 2016.
- [81] T. M. Rodgers, J. D. Madison, and V. Tikare, “Simulation of metal additive manufacturing microstructures using kinetic Monte Carlo,” *Comput. Mater. Sci.*, vol. 135, pp. 78–89, 2017.
- [82] X. Zhan, Y. Wei, and Z. Dong, “Cellular automaton simulation of grain growth with,” vol. 8, no. 1999, pp. 1–8, 2008.
- [83] H. Yin, S. D. Felicelli, and L. Wang, “Simulation of a dendritic microstructure with the lattice Boltzmann and cellular automaton methods,” *Acta Mater.*, vol. 59, no. 8, pp. 3124–3136, 2011.
- [84] Y. X. Liu, Y. C. Lin, H. Bin Li, D. X. Wen, X. M. Chen, and M. S. Chen, “Study of dynamic recrystallization in a Ni-based superalloy by experiments and cellular automaton model,” *Mater. Sci. Eng. A*, vol. 626, pp. 432–440, 2015.
- [85] A. Zinoviev, O. Zinovieva, V. Ploshikhin, V. Romanova, and R. Balokhonov, “Evolution of grain structure during laser additive manufacturing. Simulation by a cellular automata method,” *Mater. Des.*, vol. 106, pp. 321–329, 2016.
- [86] D. A. Zaitsev, “A generalized neighborhood for cellular automata,” *Theor. Comput. Sci.*, vol. 666, pp. 21–35, 2017.
- [87] T&A Precision, “BS1407 Technical Specifications.” [Online]. Available: [https://www.silversteel.co.uk/catalog/view/theme/silversteel/documents/BS1407 Technical Specifications.pdf](https://www.silversteel.co.uk/catalog/view/theme/silversteel/documents/BS1407%20Technical%20Specifications.pdf). [Accessed: 18-Mar-2020].
- [88] J.-O. Andersson, T. Helander, L. Hoglund, P. Shi, and B. Sundman, “THERMO-CALC & DICTRA, Computational Tools For Materials Science,” *Calphad*, vol. 26, no. 2, pp. 273–312, 2002.

- [89] RLS, “GTS35 / GTS45 Gear Tooth Sensor Data Sheet,” 2017. [Online]. Available:  
[https://www.rls.si/de/fileuploader/download/download/?d=0&file=custom%2Fupload%2FGTSD01\\_03.pdf](https://www.rls.si/de/fileuploader/download/download/?d=0&file=custom%2Fupload%2FGTSD01_03.pdf).
- [90] TE Connectivity, “FC23 Compression Load Cell,” 2020. [Online]. Available:  
[https://www.te.com/commerce/DocumentDelivery/DDEController?Action=showdoc&DocId=Data+Sheet%7FFC23%7FA8%7Fpdf%7FEnglish%7FENG\\_DS\\_FC23\\_A8.pdf%7FCAT-FSE0002](https://www.te.com/commerce/DocumentDelivery/DDEController?Action=showdoc&DocId=Data+Sheet%7FFC23%7FA8%7Fpdf%7FEnglish%7FENG_DS_FC23_A8.pdf%7FCAT-FSE0002). [Accessed: 16-Mar-2020].
- [91] E. J. Payton, P. J. Phillips, and M. J. Mills, “Semi-automated characterization of the  $\gamma'$  phase in Ni-based superalloys via high-resolution backscatter imaging,” *Mater. Sci. Eng. A*, vol. 527, no. 10–11, pp. 2684–2692, 2010.
- [92] M. Basham *et al.*, “Data Analysis Workbench (DAWN),” *J. Synchrotron Radiat.*, vol. 22, pp. 853–858, 2015.
- [93] B. H. Toby and R. B. Von Dreele, “GSAS-II: The genesis of a modern open-source all purpose crystallography software package,” *J. Appl. Crystallogr.*, vol. 46, no. 2, pp. 544–549, 2013.
- [94] D. Yu, Y. Chen, L. Huang, and K. An, “Tracing phase transformation and lattice evolution in a TRIP sheet steel under high-temperature annealing by real-time in situ neutron diffraction,” *Crystals*, vol. 8, no. 9, p. 360, 2018.
- [95] A. Sarkar, P. Mukherjee, P. Barat, T. Jayakumar, S. Mahadevan, and S. K. Rai, “Lattice misfit measurement in inconel 625 by X-ray diffraction technique,” *Int. J. Mod. Phys. B*, vol. 22, no. 23, pp. 3977–3985, 2008.
- [96] L. Onsager, “Reciprocal Relations in Irreversible Processes. I.,” *Phys. Rev.*, vol. 37, pp. 405–426, 1956.
- [97] F. Tancret, “Thermo-Calc and DICTRA simulation of constitutional liquation of gamma prime ( $\gamma'$ ) during welding of Ni base superalloys,” vol. 41, pp. 13–19, 2007.
- [98] Y. Chen, E. M. Francis, M. Preuss, and S. J. Haigh, “On the diffusion mechanisms of fine-scale  $\gamma'$  in an advanced Ni-based superalloy,” *MATEC Web Conf.*, vol. 14, no. August, 2014.

- [99] A. Ramesh and S. N. Melkote, "Modeling of white layer formation under thermally dominant conditions in orthogonal machining of hardened AISI 52100 steel," *Int. J. Mach. Tools Manuf.*, vol. 48, no. 3–4, pp. 402–414, 2008.
- [100] B. Grant, M. Preuss, P. J. Withers, G. Baxter, and M. Rowson, "Finite element process modelling of inertia friction welding advanced Nickel-based superalloy," *Mater. Sci. Eng. A*, vol. 513–514, no. C, pp. 366–375, 2009.

## Appendix A

# Microstructure Evolution of RR1000 During IFW Using Weld Parameter Sets N2, N3 and N4

### A1. Microstructure evolution during weld parameter set N2

Note: Weld N2, P4 has been omitted here due to the insufficient upset produced.

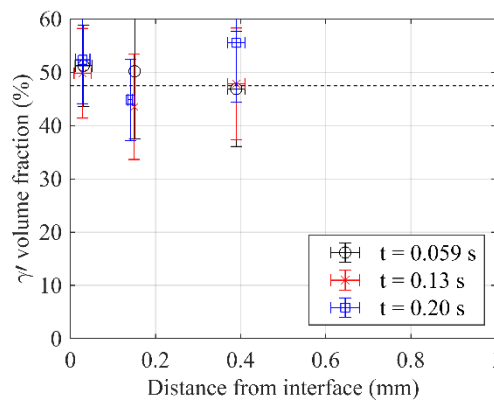


**Figure A.1:** Microstructure evolution during conditioning for weld parameter set N2.

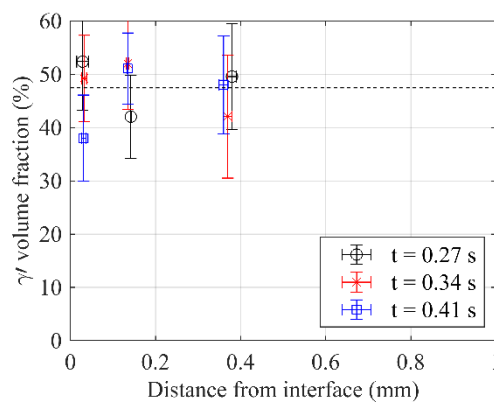


**Figure A.2:** Microstructure evolution during conditioning for weld parameter set N2.

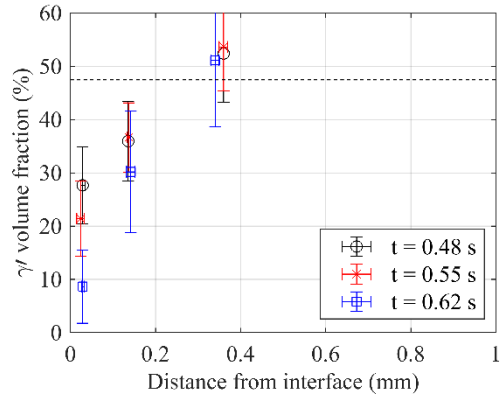


**Figure A.3:** Microstructure evolution during conditioning for weld parameter set N2.

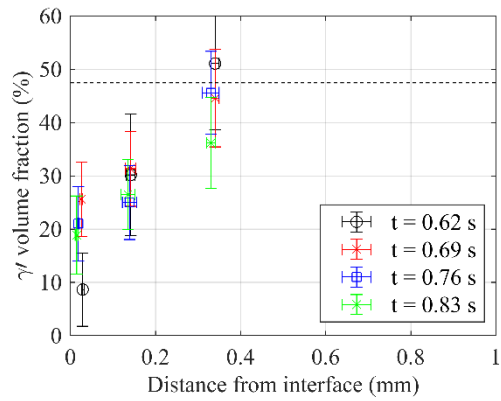


**Figure A.4:** Microstructure evolution during burn-off for weld parameter set N2.

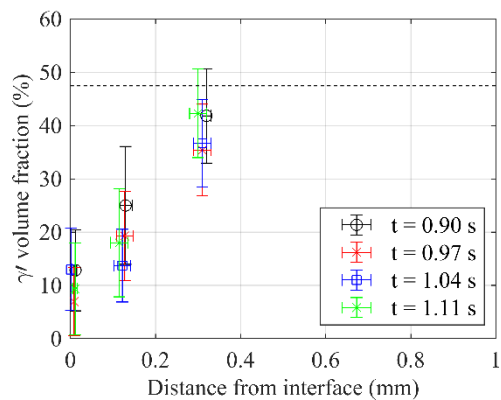


**Figure A.5:** Microstructure evolution during burn-off for weld parameter set N2.

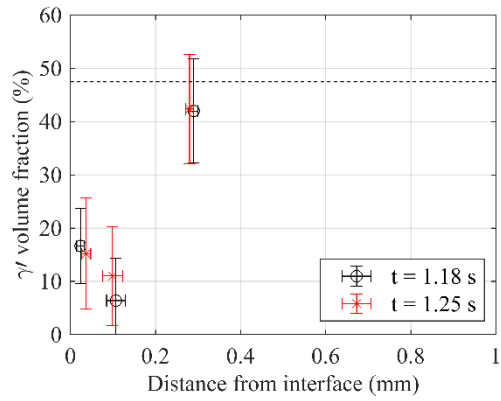


**Figure A.6:** Microstructure evolution during the transition from burn-off to consolidation for weld parameter set N2.

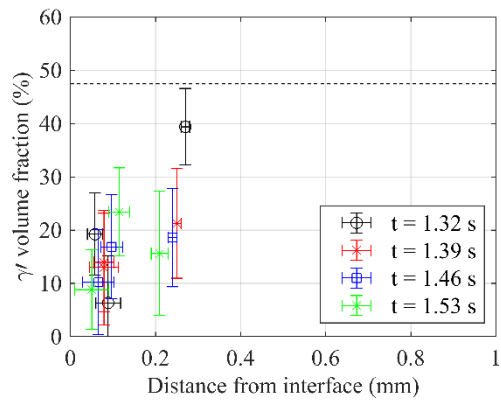


**Figure A.7:** Microstructure evolution during consolidation for weld parameter set N2.

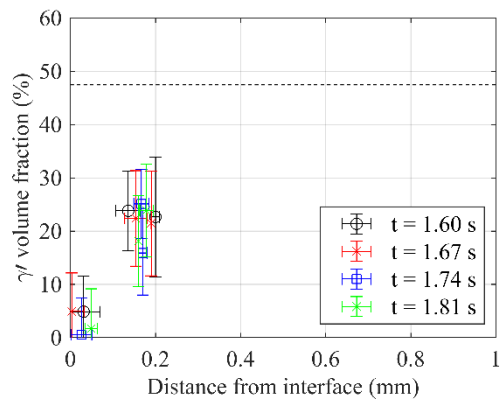


**Figure A.8:** Microstructure evolution during consolidation for weld parameter set N2.

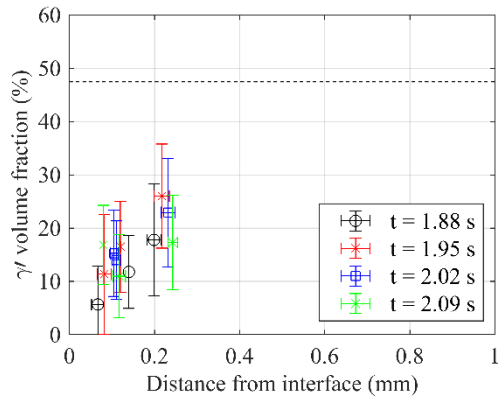


**Figure A.9:** Microstructure evolution during consolidation for weld parameter set N2.

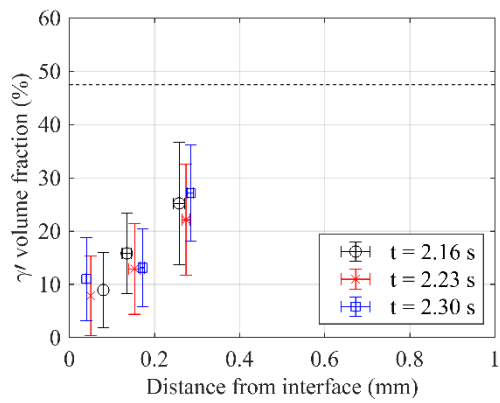


**Figure A.10:** Microstructure evolution during consolidation for weld parameter set N2.

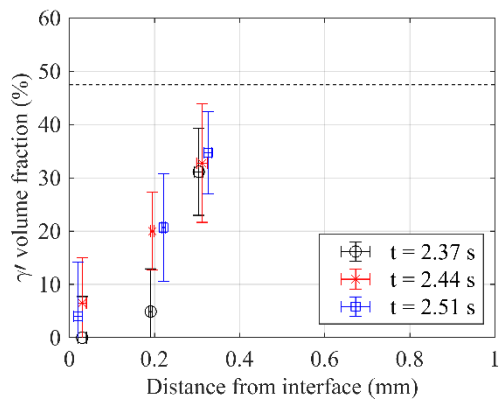


**Figure A.11:** Microstructure evolution during consolidation for weld parameter set N2.

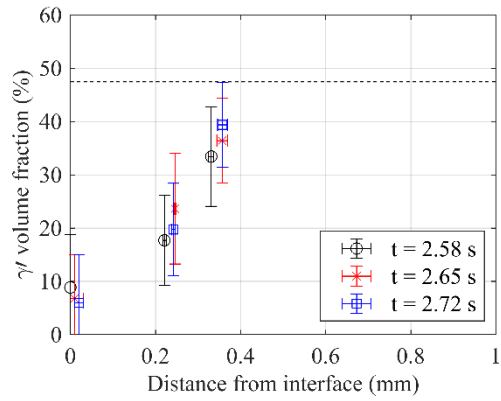


**Figure A.12:** Microstructure evolution during consolidation for weld parameter set N2.

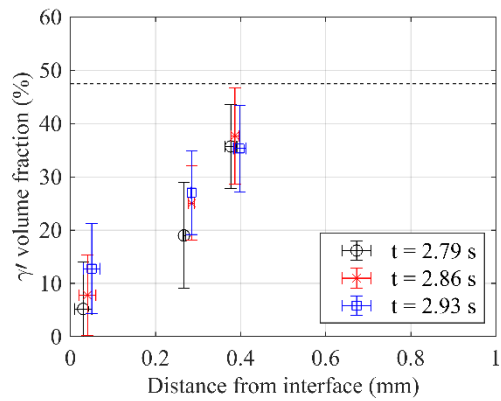


**Figure A.13:** Microstructure evolution during weld stall for weld parameter set N2.

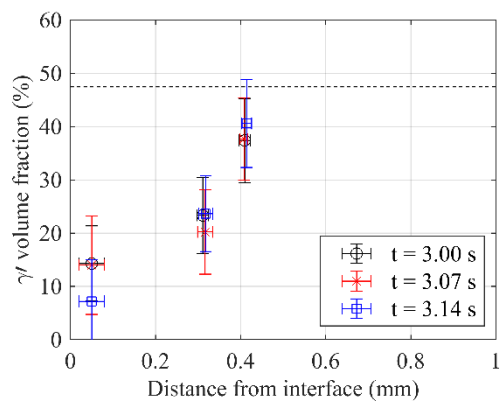


**Figure A.14:** Microstructure evolution during weld stall for weld parameter set N2.

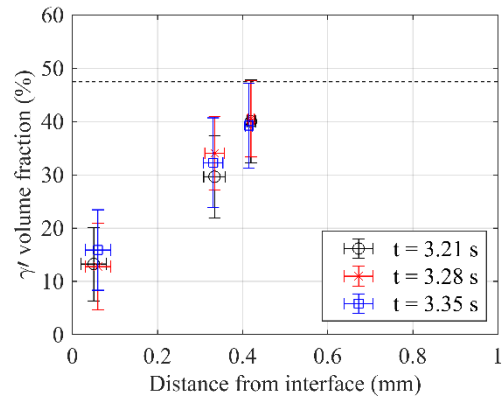


**Figure A.15:** Microstructure evolution during weld stall for weld parameter set N2.

## A2. Microstructure evolution during weld parameter set N3

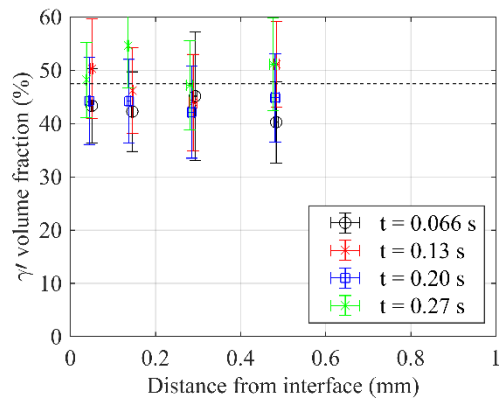


Figure A.16: Microstructure evolution during conditioning for weld parameter set N3.

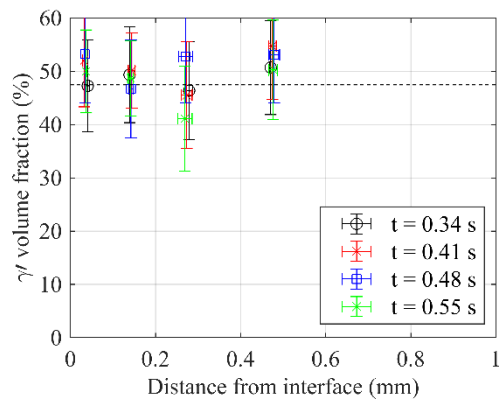


Figure A.17: Microstructure evolution during conditioning for weld parameter set N3.

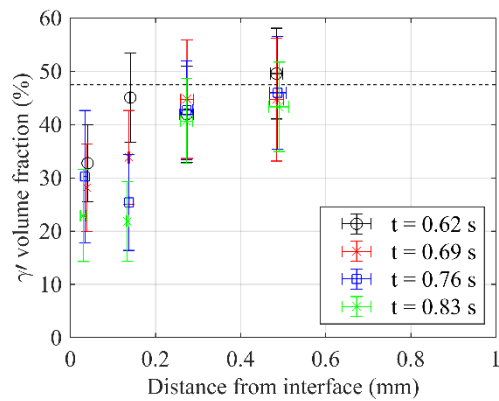
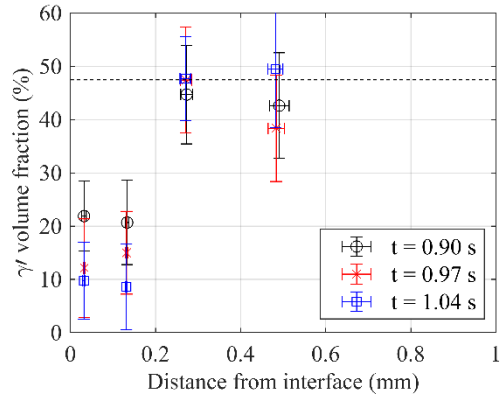
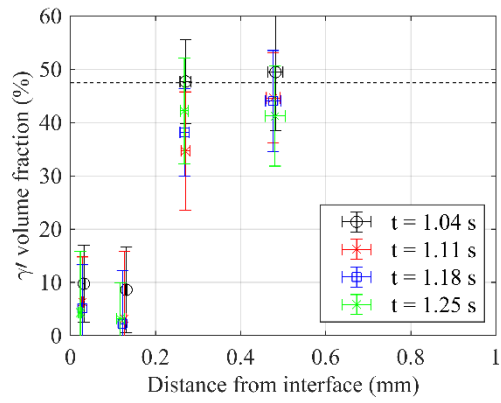


Figure A.18: Microstructure evolution during conditioning for weld parameter set N3.



**Figure A.19:** Microstructure evolution during conditioning for weld parameter set N3.



**Figure A.20:** Microstructure evolution during burn-off for weld parameter set N3.

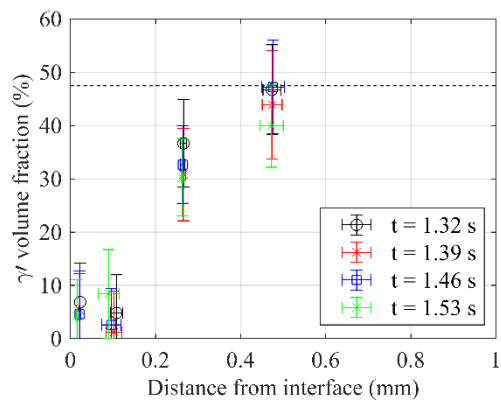


**Figure A.21:** Microstructure evolution during burn-off for weld parameter set N3.

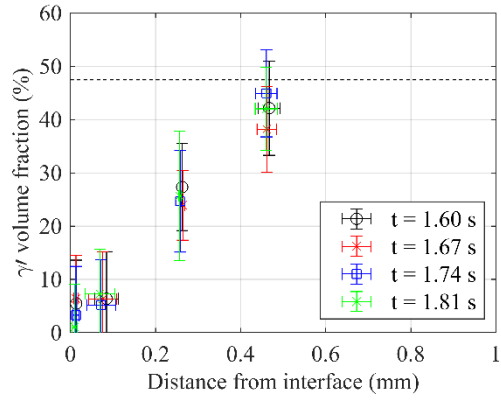


**Figure A.22:** Microstructure evolution during burn-off for weld parameter set N3.

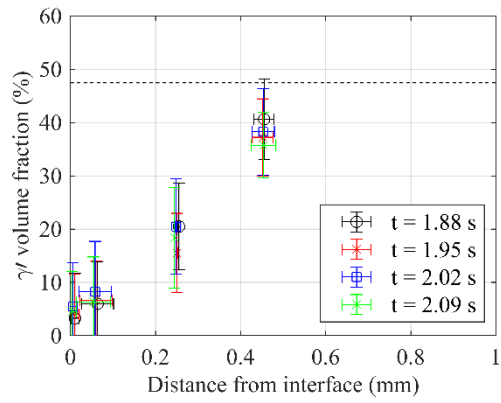


**Figure A.23:** Microstructure evolution during burn-off for weld parameter set N3.

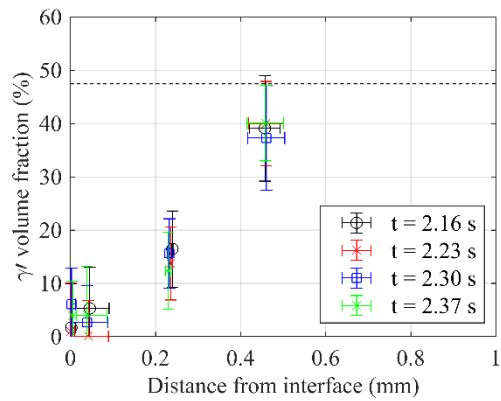


**Figure A.24:** Microstructure evolution during burn-off for weld parameter set N3.

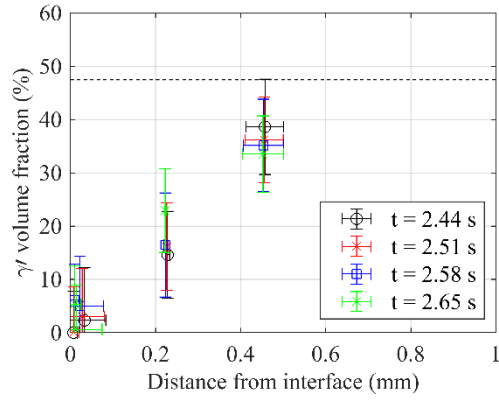


**Figure A.25:** Microstructure evolution during burn-off for weld parameter set N3.

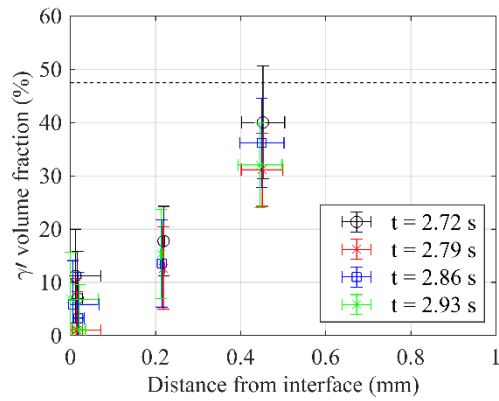


**Figure A.26:** Microstructure evolution during burn-off for weld parameter set N3.

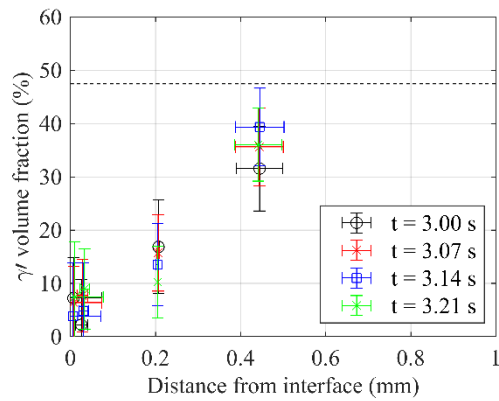


**Figure A.27:** Microstructure evolution during burn-off for weld parameter set N3.

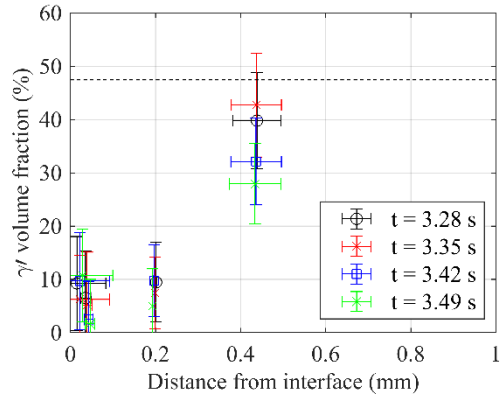


**Figure A.28:** Microstructure evolution during burn-off for weld parameter set N3.

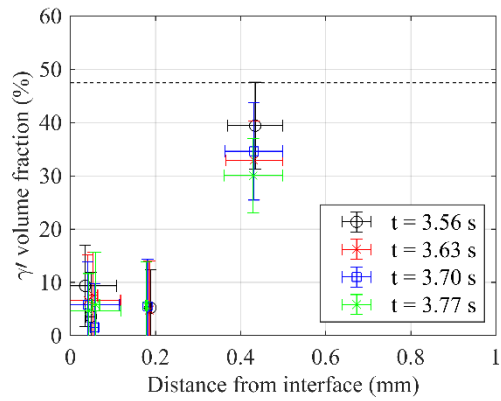


**Figure A.29:** Microstructure evolution during burn-off for weld parameter set N3.

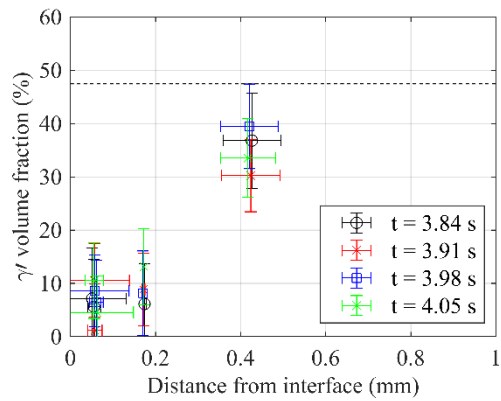


**Figure A.30:** Microstructure evolution during burn-off for weld parameter set N3.

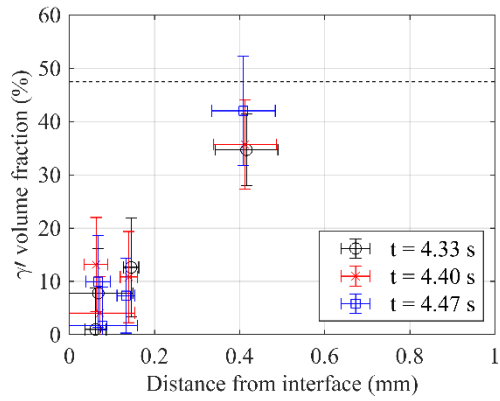


**Figure A.31:** Microstructure evolution during burn-off for weld parameter set N3.

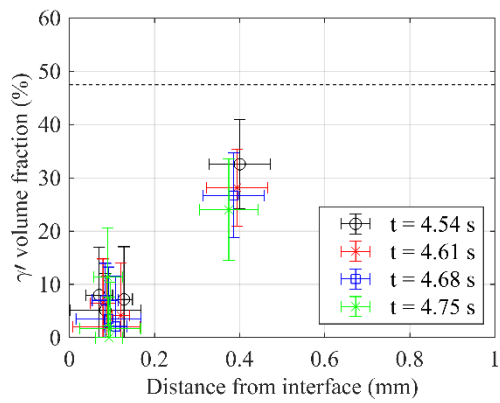


**Figure A.32:** Microstructure evolution during the transition from burn-off to consolidation for weld parameter set N3.

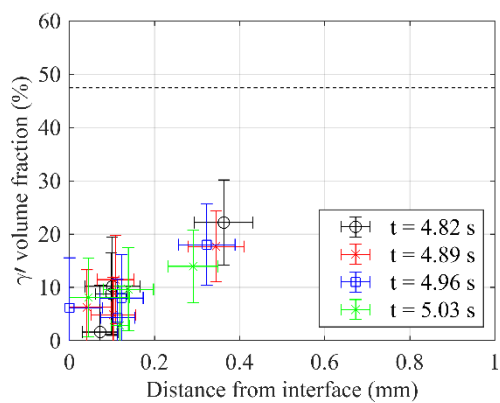


**Figure A.33:** Microstructure evolution during consolidation for weld parameter set N3.

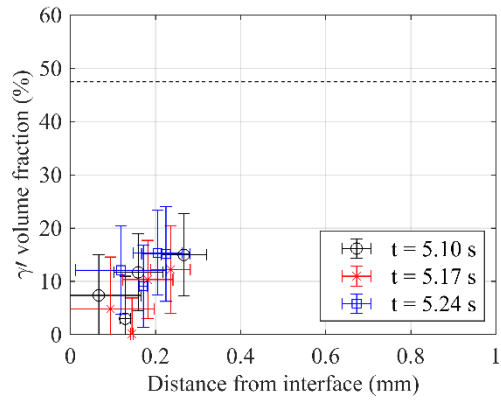


**Figure A.34:** Microstructure evolution during consolidation for weld parameter set N3.

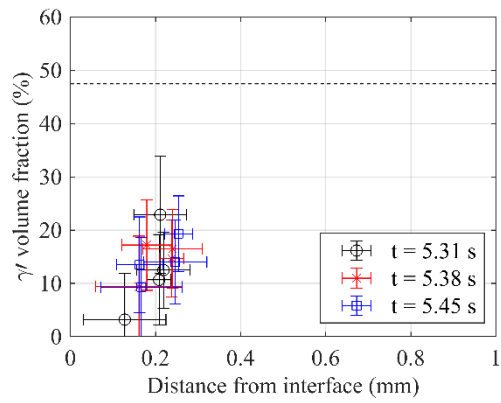


**Figure A.35:** Microstructure evolution during consolidation for weld parameter set N3.

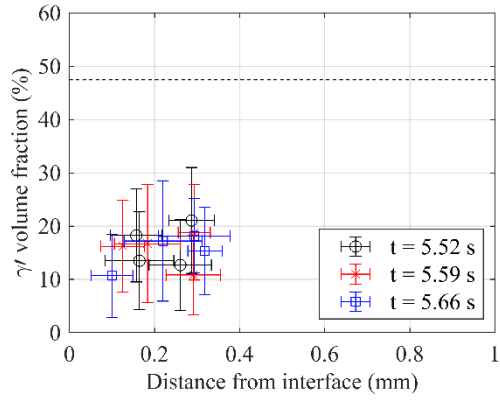


**Figure A.36:** Microstructure evolution during consolidation for weld parameter set N3.

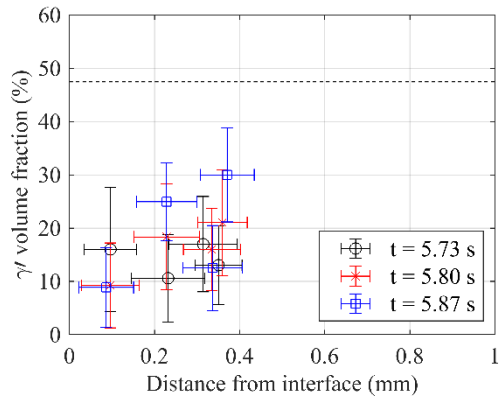


**Figure A.37:** Microstructure evolution during weld stall for weld parameter set N3.

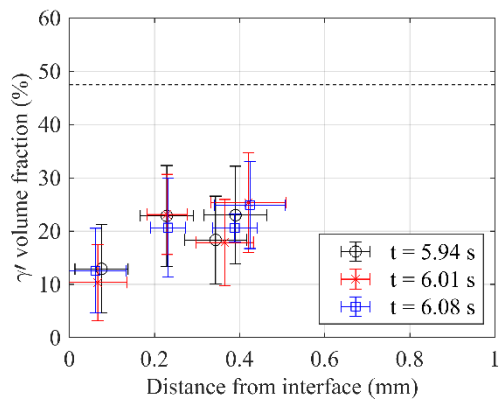


**Figure A.38:** Microstructure evolution during weld stall for weld parameter set N3.

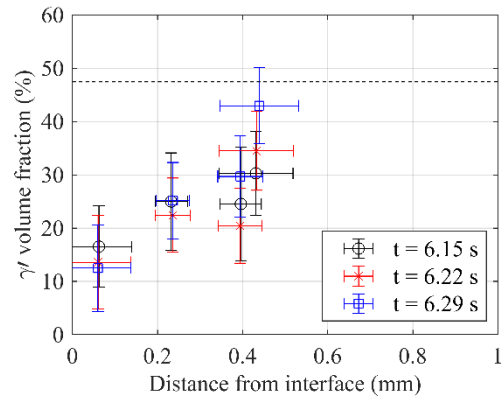


**Figure A.39:** Microstructure evolution during weld stall for weld parameter set N3.

### A3. Microstructure evolution during weld parameter set N4

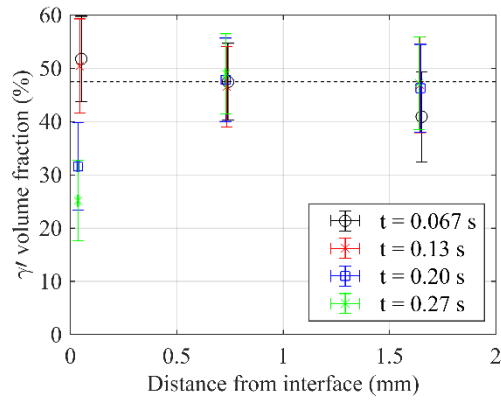


Figure A.40: Microstructure evolution during conditioning for weld parameter set N4.

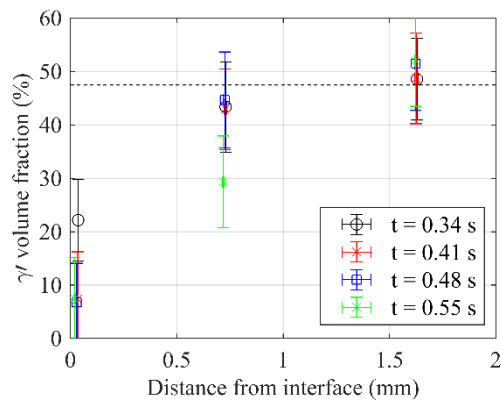


Figure A.41: Microstructure evolution during conditioning for weld parameter set N4.

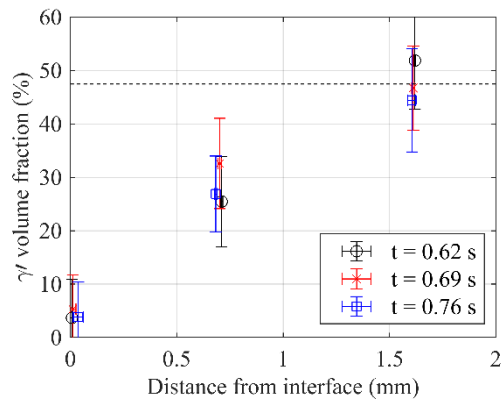
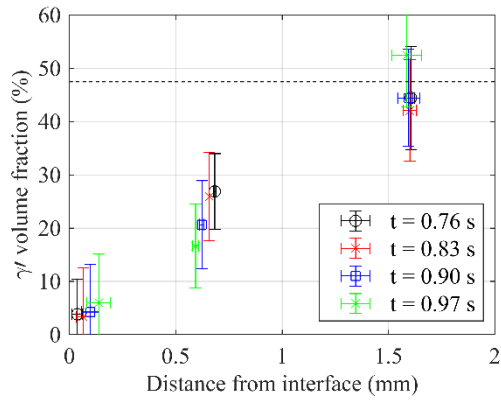
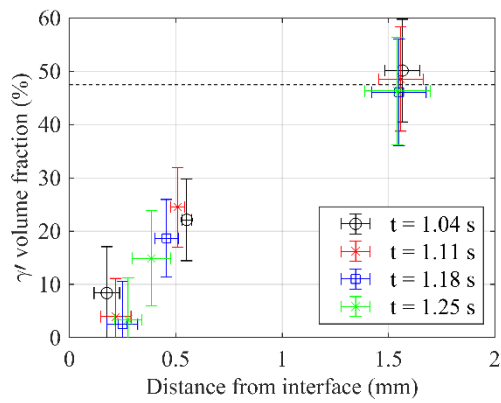


Figure A.42: Microstructure evolution during conditioning for weld parameter set N4.



**Figure A.43:** Microstructure evolution during burn-off for weld parameter set N4.



**Figure A.44:** Microstructure evolution during burn-off for weld parameter set N4.

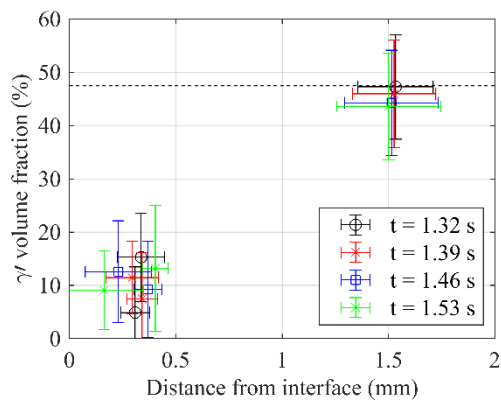


**Figure A.45:** Microstructure evolution during burn-off for weld parameter set N4.

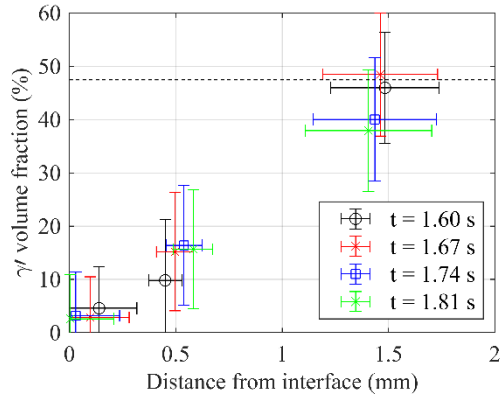


**Figure A.46:** Microstructure evolution during burn-off for weld parameter set N4.

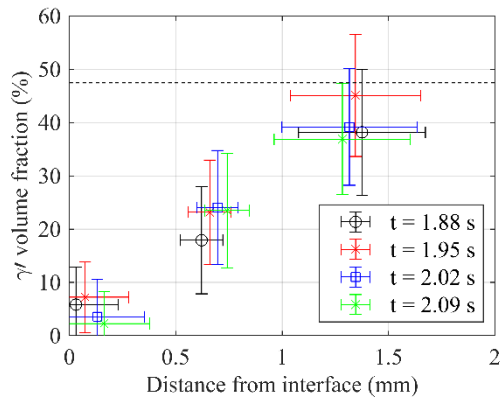


**Figure A.47:** Microstructure evolution during burn-off for weld parameter set N4.

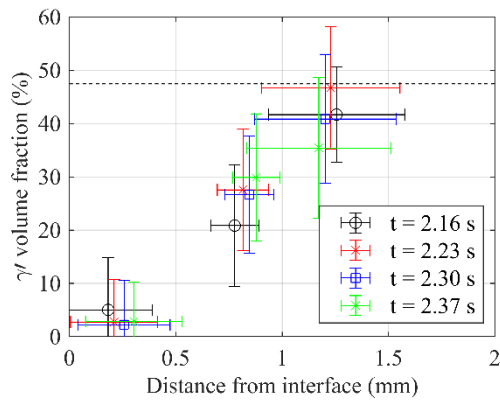


**Figure A.48:** Microstructure evolution during burn-off for weld parameter set N4.

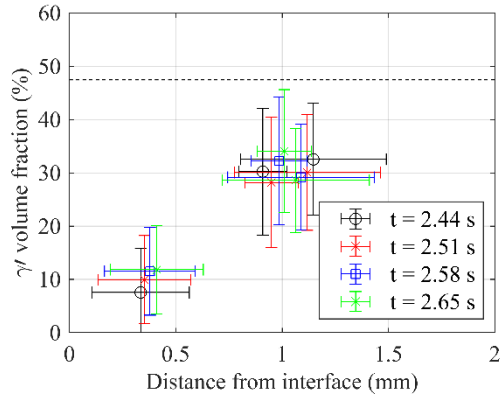


**Figure A.49:** Microstructure evolution during burn-off for weld parameter set N4.

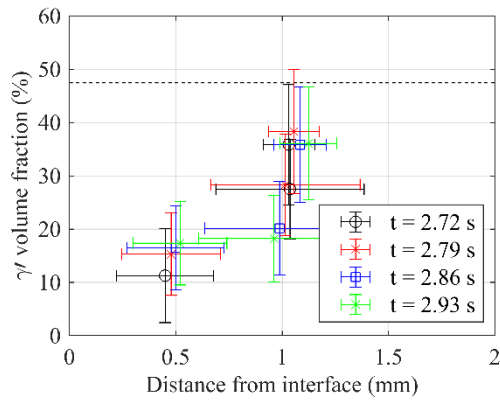


**Figure A.50:** Microstructure evolution during burn-off for weld parameter set N4.

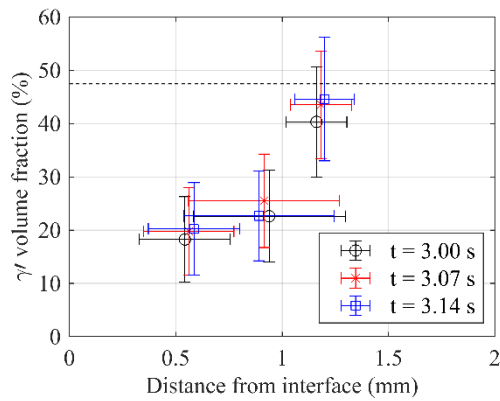


**Figure A.51:** Microstructure evolution during burn-off for weld parameter set N4.

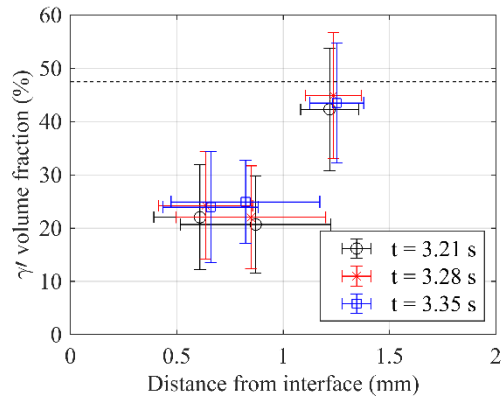


**Figure A.52:** Microstructure evolution during burn-off for weld parameter set N4.

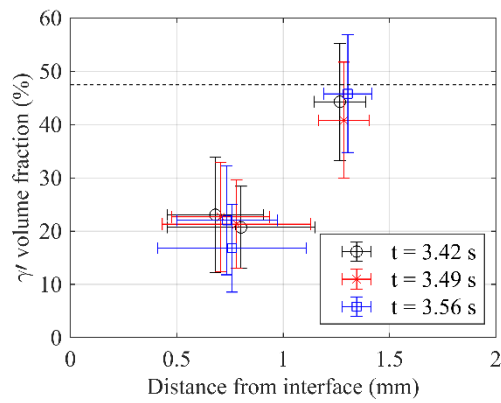


**Figure A.53:** Microstructure evolution during burn-off for weld parameter set N4.

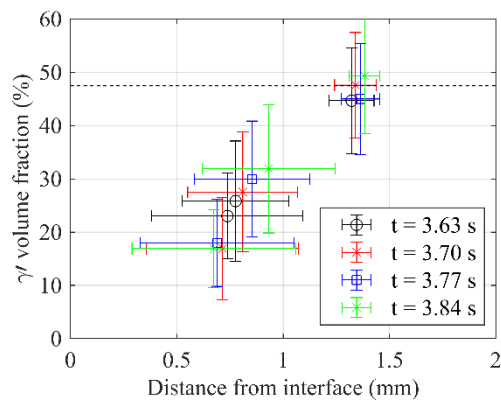


**Figure A.54:** Microstructure evolution during the transition from burn-off to consolidation for weld parameter set N4.

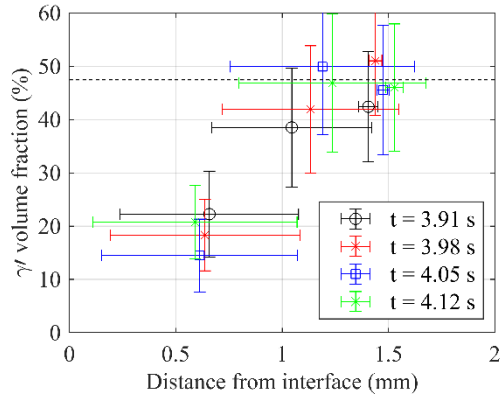


**Figure A.55:** Microstructure evolution during consolidation for weld parameter set N4.

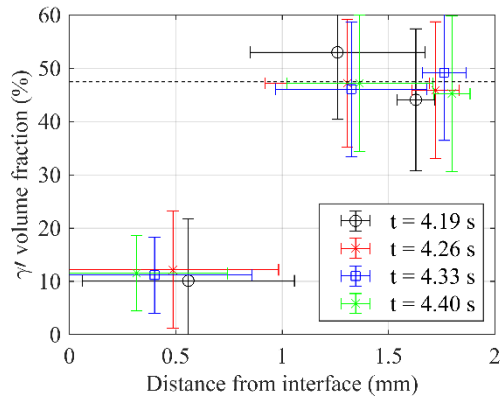


**Figure A.56:** Microstructure evolution during consolidation for weld parameter set N4.

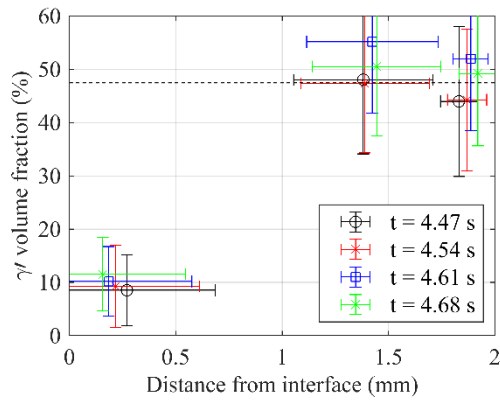


**Figure A.57:** Microstructure evolution during weld stall for weld parameter set N4.

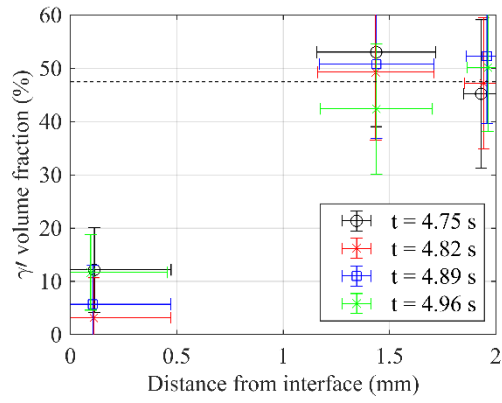


**Figure A.58:** Microstructure evolution during weld stall for weld parameter set N4.

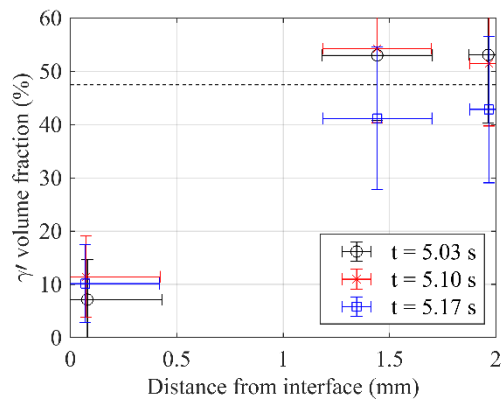


**Figure A.59:** Microstructure evolution during weld stall for weld parameter set N4.

## Appendix B

### Reference Input Data for CA Models

#### B1. Binary Ni-Al system

**Table B.1:** Chemical potential of Aluminium at a range of Al mole fractions (columns) and temperatures in °C (rows).

	<b>0</b>	<b>0.05</b>	<b>0.1</b>	<b>0.15</b>	<b>0.2</b>	<b>0.25</b>
<b>1000</b>	-411323.5	-220887.9	-206041	-191103.3	-189253.3	-180395.3
<b>1020</b>	-415563.9	-222198.9	-207300.1	-192383.8	-189752.7	-181162.8
<b>1040</b>	-419813.5	-223519.6	-208569.1	-193674.1	-190251.2	-181935.8
<b>1060</b>	-424072.1	-224849.8	-209847.8	-194974.1	-190748.4	-182714.4
<b>1080</b>	-428339.7	-226189.4	-211135.9	-196283.7	-191244	-183498.5
<b>1100</b>	-432616.1	-227538.3	-212433.5	-197602.6	-191737.6	-184288.2
<b>1120</b>	-436901.3	-228896.3	-213740.2	-198930.8	-192228.6	-185083.6
<b>1140</b>	-441195.2	-230263.4	-215056.1	-200268.1	-192716.9	-185884.8
<b>1160</b>	-445497.6	-231639.3	-216381	-201614.5	-193201.9	-186692
<b>1180</b>	-449808.5	-233024	-217714.7	-202969.6	-193683.1	-187505.4
<b>1200</b>	-454127.9	-234417.4	-219057.1	-204333.6	-194160.2	-188325.3
<b>1220</b>	-458455.5	-235819.4	-220408.2	-205706.1	-194632.6	-189151.8
<b>1240</b>	-462791.4	-237229.7	-221767.7	-207087.2	-195099.7	-189985.3
<b>1260</b>	-467135.3	-238648.5	-223135.6	-208476.6	-195561	-190826.1
<b>1280</b>	-471487.3	-240075.4	-224511.9	-209874.4	-196015.8	-191674.6
<b>1300</b>	-475847.3	-241510.5	-225896.2	-211280.3	-196524.8	-192531
<b>1320</b>	-480215.1	-242953.6	-227288.7	-212694.3	-197991.2	-193395.7
<b>1340</b>	-484590.7	-244404.6	-228689.1	-214116.2	-199465.7	-194269
<b>1360</b>	-488973.9	-245863.4	-230097.3	-215546.1	-200947.9	-195151
<b>1380</b>	-493364.8	-247330	-231513.4	-216983.7	-202438	-197471.1
<b>1400</b>	-497763.2	-248804.2	-232937.1	-218429	-209015.6	-198977.3

**Table B.2:** Chemical potential of Nickel at a range of Al mole fractions (columns) and temperatures in °C (rows).

	<b>0</b>	<b>0.05</b>	<b>0.1</b>	<b>0.15</b>	<b>0.2</b>	<b>0.25</b>
<b>1000</b>	-64104.7	-64744.3	-65946.33	-68088.78	-68423.02	-71241.93
<b>1020</b>	-65600.5	-66247.89	-67453.59	-69592.74	-70072.84	-72803.74
<b>1040</b>	-67107.03	-67762.21	-68971.56	-71107.42	-71738.28	-74379.77
<b>1060</b>	-68624.18	-69287.14	-70500.14	-72632.7	-73419.46	-75969.99
<b>1080</b>	-70151.86	-70822.59	-72039.23	-74168.48	-75116.47	-77574.37
<b>1100</b>	-71689.97	-72368.46	-73588.73	-75714.67	-76829.47	-79192.87
<b>1120</b>	-73238.4	-73924.64	-75148.53	-77271.17	-78558.58	-80825.46
<b>1140</b>	-74797.06	-75491.05	-76718.56	-78837.88	-80303.98	-82472.08
<b>1160</b>	-76365.87	-77067.6	-78298.72	-80414.73	-82065.85	-84132.7
<b>1180</b>	-77944.73	-78654.19	-79888.92	-82001.61	-83844.38	-85807.25
<b>1200</b>	-79533.56	-80250.75	-81489.08	-83598.45	-85639.82	-87495.69
<b>1220</b>	-81132.28	-81857.19	-83099.12	-85205.16	-87452.41	-89197.95
<b>1240</b>	-82740.79	-83473.42	-84718.94	-86821.67	-89282.45	-90913.97
<b>1260</b>	-84359.03	-85099.38	-86348.49	-88447.89	-91130.26	-92643.67
<b>1280</b>	-85986.92	-86734.98	-87987.67	-90083.75	-92996.21	-94386.98
<b>1300</b>	-87624.38	-88380.14	-89636.42	-91729.17	-94865.36	-96143.85
<b>1320</b>	-89271.34	-90034.8	-91294.66	-93384.08	-96509.01	-97914.22
<b>1340</b>	-90927.72	-91698.89	-92962.32	-95048.42	-98162.07	-99698.04
<b>1360</b>	-92593.47	-93372.33	-94639.34	-96722.1	-99824.49	-101495.3
<b>1380</b>	-94268.51	-95055.06	-96325.64	-98405.08	-101496.2	-103015.2
<b>1400</b>	-95952.77	-96747.01	-98021.16	-100097.3	-101975.7	-104962.3

**Table B.3:** Atomic mobility of Aluminium at a range of Al mole fractions (columns) and temperatures in °C (rows).

	<b>0</b>	<b>0.05</b>	<b>0.1</b>	<b>0.15</b>	<b>0.2</b>	<b>0.25</b>
<b>1000</b>	1.79E-19	1.62E-19	1.56E-19	1.61E-19	1.62E-19	1.72E-19
<b>1020</b>	2.61E-19	2.35E-19	2.27E-19	2.33E-19	2.36E-19	2.49E-19
<b>1040</b>	3.76E-19	3.39E-19	3.26E-19	3.34E-19	3.39E-19	3.57E-19
<b>1060</b>	5.35E-19	4.82E-19	4.63E-19	4.73E-19	4.81E-19	5.06E-19
<b>1080</b>	7.54E-19	6.79E-19	6.50E-19	6.63E-19	6.77E-19	7.17E-19
<b>1100</b>	1.05E-18	9.46E-19	9.05E-19	9.20E-19	9.42E-19	9.86E-19
<b>1120</b>	1.45E-18	1.31E-18	1.25E-18	1.27E-18	1.30E-18	1.36E-18
<b>1140</b>	1.99E-18	1.79E-18	1.70E-18	1.72E-18	1.77E-18	1.85E-18
<b>1160</b>	2.70E-18	2.42E-18	2.30E-18	2.33E-18	2.40E-18	2.50E-18
<b>1180</b>	3.63E-18	3.25E-18	3.09E-18	3.11E-18	3.22E-18	3.38E-18
<b>1200</b>	4.84E-18	4.34E-18	4.11E-18	4.14E-18	4.29E-18	4.44E-18
<b>1220</b>	6.40E-18	5.73E-18	5.43E-18	5.45E-18	5.66E-18	5.85E-18
<b>1240</b>	8.41E-18	7.52E-18	7.12E-18	7.13E-18	7.42E-18	7.65E-18
<b>1260</b>	1.10E-17	9.80E-18	9.26E-18	9.25E-18	9.66E-18	9.94E-18
<b>1280</b>	1.42E-17	1.27E-17	1.20E-17	1.19E-17	1.25E-17	1.30E-17
<b>1300</b>	1.82E-17	1.63E-17	1.54E-17	1.53E-17	1.60E-17	1.64E-17
<b>1320</b>	2.33E-17	2.08E-17	1.96E-17	1.95E-17	2.04E-17	2.09E-17
<b>1340</b>	2.96E-17	2.64E-17	2.48E-17	2.46E-17	2.57E-17	2.64E-17
<b>1360</b>	3.73E-17	3.33E-17	3.13E-17	3.09E-17	3.22E-17	3.33E-17
<b>1380</b>	4.69E-17	4.18E-17	3.92E-17	3.87E-17	4.02E-17	4.13E-17
<b>1400</b>	5.85E-17	5.21E-17	4.88E-17	4.81E-17	4.90E-17	5.12E-17

**Table B.4:** Atomic mobility of Nickel at a range of Al mole fractions (columns) and temperatures in °C (rows).

	<b>0</b>	<b>0.05</b>	<b>0.1</b>	<b>0.15</b>	<b>0.2</b>	<b>0.25</b>
<b>1000</b>	3.59E-20	6.03E-20	1.03E-19	1.81E-19	1.94E-19	2.77E-19
<b>1020</b>	5.37E-20	8.97E-20	1.53E-19	2.65E-19	2.91E-19	4.11E-19
<b>1040</b>	7.94E-20	1.32E-19	2.22E-19	3.82E-19	4.33E-19	6.01E-19
<b>1060</b>	1.16E-19	1.91E-19	3.20E-19	5.46E-19	6.36E-19	8.69E-19
<b>1080</b>	1.68E-19	2.74E-19	4.56E-19	7.72E-19	9.24E-19	1.27E-18
<b>1100</b>	2.40E-19	3.89E-19	6.43E-19	1.08E-18	1.33E-18	1.76E-18
<b>1120</b>	3.39E-19	5.46E-19	8.97E-19	1.50E-18	1.89E-18	2.47E-18
<b>1140</b>	4.74E-19	7.60E-19	1.24E-18	2.06E-18	2.66E-18	3.43E-18
<b>1160</b>	6.57E-19	1.05E-18	1.70E-18	2.80E-18	3.72E-18	4.73E-18
<b>1180</b>	9.03E-19	1.43E-18	2.30E-18	3.77E-18	5.16E-18	6.59E-18
<b>1200</b>	1.23E-18	1.94E-18	3.10E-18	5.04E-18	7.08E-18	8.73E-18
<b>1220</b>	1.66E-18	2.60E-18	4.14E-18	6.69E-18	9.65E-18	1.17E-17
<b>1240</b>	2.22E-18	3.46E-18	5.48E-18	8.80E-18	1.31E-17	1.56E-17
<b>1260</b>	2.96E-18	4.58E-18	7.20E-18	1.15E-17	1.75E-17	2.07E-17
<b>1280</b>	3.90E-18	6.01E-18	9.40E-18	1.49E-17	2.34E-17	2.79E-17
<b>1300</b>	5.11E-18	7.83E-18	1.22E-17	1.92E-17	3.09E-17	3.54E-17
<b>1320</b>	6.64E-18	1.01E-17	1.57E-17	2.46E-17	3.93E-17	4.59E-17
<b>1340</b>	8.58E-18	1.30E-17	2.01E-17	3.14E-17	4.98E-17	5.91E-17
<b>1360</b>	1.10E-17	1.66E-17	2.55E-17	3.97E-17	6.26E-17	7.57E-17
<b>1380</b>	1.41E-17	2.11E-17	3.22E-17	4.99E-17	7.84E-17	9.23E-17
<b>1400</b>	1.78E-17	2.67E-17	4.05E-17	6.24E-17	8.32E-17	1.15E-16

## B2. Ternary Ni-Al-Cr system

**Table B.5:** Chemical potential values for the three elements in the parent composition of  $\gamma$ .

Temperature (°C)	$\mu_{\text{Ni}}$	$\mu_{\text{Al}}$	$\mu_{\text{Cr}}$
800	-64295.583	-153618.13	-35455.195
820	-65844.886	-154072.26	-36952.702
840	-67393.865	-154580.59	-38485.599
860	-68907.199	-155561.8	-40021.313
880	-70392.915	-156987.8	-41542.799
900	-71890.163	-158424.91	-43076.132
920	-73398.814	-159872.91	-44621.223
940	-74918.74	-161331.61	-46177.995
960	-76449.821	-162800.84	-47746.369
980	-77991.939	-164280.4	-49326.277
1000	-79544.979	-165770.12	-50917.652
1020	-81108.831	-167269.85	-52520.431
1040	-82683.389	-168779.43	-54134.557
1060	-84268.547	-170298.69	-55759.976
1080	-85864.206	-171827.5	-57396.637
1100	-87470.267	-173365.7	-59044.493
1120	-89086.636	-174913.17	-60703.502
1140	-90713.22	-176469.76	-62373.623
1160	-92349.929	-178035.34	-64054.819
1180	-93996.677	-179609.8	-65747.056
1200	-95653.379	-181193	-67450.302
1220	-97319.952	-182784.82	-69164.531
1240	-98996.316	-184385.15	-70889.715
1260	-100682.39	-185993.88	-72625.831
1280	-102378.11	-187610.9	-74372.859
1300	-104083.38	-189236.09	-76130.78

**Table B.6:** Chemical potential values for the three elements in the parent composition of  $\gamma'$ .

Temperature (°C)	$\mu_{Ni}$	$\mu_{Al}$	$\mu_{Cr}$
800	-64943.956	-151730.34	-35002.664
820	-66233.466	-152952.84	-36671.868
840	-67522.826	-154212.77	-38389.547
860	-68809.15	-155500.24	-40193.085
880	-70100.061	-156799.49	-42061.429
900	-71404.432	-158104.45	-43946.307
920	-72722.398	-159414.27	-45847.983
940	-74054.117	-160728.04	-47766.754
960	-75399.779	-162044.82	-49702.958
980	-76759.6	-163363.6	-51656.982
1000	-78133.83	-164683.31	-53629.273
1020	-79522.746	-166002.83	-55620.347
1040	-80926.931	-167296.92	-57680.191
1060	-82349.228	-168561.58	-59799.854
1080	-83791.148	-169805.31	-61952.604
1100	-85253.892	-171025.22	-64138.214
1120	-86738.689	-172218.46	-66356.453
1140	-88246.78	-173382.3	-68607.078
1160	-89779.41	-174514.18	-70889.834
1180	-91337.795	-175611.74	-73204.498
1200	-92923.099	-176672.94	-75550.864
1220	-94536.402	-177696.11	-77928.813
1240	-96178.671	-178680.03	-80338.353
1260	-97850.725	-179624	-82779.67
1280	-99553.228	-180527.85	-85253.183
1300	-101286.67	-181391.95	-87759.586